Exploring and Controlling Phenazine Biosynthesis with Chemical and Structural Biology

Von der Fakultät für Lebenswissenschaften

der Technischen Universität Carolo-Wilhelmina zu Braunschweig

zur Erlangung des Grades

einer Doktorin der Naturwissenschaften (Dr. rer. nat.)

genehmigte

D i s s e r t a t i o n

von Christina Diederich
aus Bad Hersfeld

Exploring and Controlling Phenazine Biosynthesis with Chemical and Structural Biology

Von der Fakultät für Lebenswissenschaften

der Technischen Universität Carolo-Wilhelmina zu Braunschweig

zur Erlangung des Grades

einer Doktorin der Naturwissenschaften (Dr. rer. nat.)

genehmigte

D i s s e r t a t i o n

von Christina Diederich
aus Bad Hersfeld

1. Referent:	Prof. Dr. Wulf Blankenfeldt
2. Referentin:	Prof. Dr. Anett Schallmey
eingereicht am:	13.03.2017
mündliche Prüfung (Disputation) am:	30.06.2017
Druckjahr	2018

Vorveröffentlichungen der Dissertation

Teilergebnisse aus dieser Arbeit wurden mit Genehmigung der Fakultät für Lebenswissenschaften, vertreten durch den Mentor der Arbeit, in folgenden Beiträgen vorab veröffentlicht:

Publikationen

Diederich, C., Leypold, M., Breinbauer, R. & Blankenfeldt, W.: Biosynthese der Phenazine. *Nachrichten aus der Chemie* **2014** Oct 2, 62(10): 975-980.

Diederich, C., Leypold, M., Breinbauer, R. & Blankenfeldt, W.: Aus zwei mach eins: die Biosynthese der Phenazine. *BioSpektrum* **2016**, 22(02): 137-139.

Diederich, C.*, Leypold, M.*, Culka, M.*, Weber, H., Breinbauer, R.#, Ullmann, G. M.# & Blankenfeldt, W.#: Mechanisms and Specificity of Phenazine Biosynthesis Protein PhzF. *Sci. Rep*. **2017** Jul 24; 7(1): 6272.

** Diese Autoren haben in gleichem Maße zu der Veröffentlichung beigetragen* # Korrespondenzautoren

Tagungsvorträge

Diederich, C., Leypold, M., Breinbauer, R. & Blankenfeldt, W.: Kinetic isotope effects in the phenazine biosynthetic protein PhzF from *Pseudomonas fluorescens* – An enzymatic approach. 16th Heart of Europe Bio-Crystallography Meeting, Hipping, Österreich, September 2013

Posterbeiträge

Diederich, C., Leypold, M., Ullmann, G. M., Breinbauer, R. & Blankenfeldt, W.: Is the phenazine biosynthetic protein PhzF catalysing a rare pericyclic reaction? 6th International PhD symposium of the HZI International Graduate School for Infection Research, Helmholtz-Zentrum für Infektionsforschung (HZI), Braunschweig, Deutschland, Dezember 2013

Diederich, C., Pletz, J., Breinbauer, R. & Blankenfeldt, W.: Synthetic PhzB product analogs as inhibitors of a key step in phenazine biosynthesis. 22nd Annual Conference of the German Crystallographic Society (DGK), Berlin, Deutschland, März 2014

Diederich, C., Pletz, J., Breinbauer, R. & Blankenfeldt, W.: Triggering self-intoxication – Inhibition of Phenazine Biosynthesis using synthetic PhzB Product Analogs. 5th Murnau Conference on Structural Biology, Murnau am Staffelsee, Deutschland, September 2014

Diederich, C., Pletz, J., Breinbauer, R. & Blankenfeldt, W.: Triggering self-intoxication – Inhibition of Phenazine Biosynthesis using synthetic PhzB Product Analogs. DKFZ/KTK/HZI Joint PhD Retreat "Core Elements of Academic Drug Discovery", Hofgeismar, Deutschland, Oktober 2014

Diederich, C., Pletz, J., Breinbauer, R. & Blankenfeldt, W.: Synthetic PhzB product analogs as inhibitors of a key step in phenazine biosynthesis. 7th International PhD symposium of the HZI International Graduate School for Infection Research, Helmholtz-Zentrum für Infektionsforschung (HZI), Braunschweig, Deutschland, Dezember 2014

Diederich, C., Leypold, M., Culka, M., Ullmann, G. M., Breinbauer, R. & Blankenfeldt, W.: The phenazine biosynthetic protein PhzF - Investigating the nature of its isomerization reaction. 24th Enzyme Mechanisms Conference, Galveston, Texas, Vereinigte Staaten von Amerika, Januar 2015

Für meinen Paps

« Puisque nos dieux et nos espoirs ne sont plus que scientifiques, pourquoi nos amours ne le deviendraient-ils pas également ? »

- *L'Eve Future*, Auguste Villiers de l'Isle-Adam

Index

List of abbreviations

- 1-OH-PHZ: 1-hydroxy-phenazine
- 2-OH-PCA: 2-hydroxy-phenazine-1-carboxylic acid
- 2-OH-PHZ: 2-hydroxy-phenazine
- 2ACHCA: 2-amino-cyclohexanecarboxylic acid
- 3OCHCA: 3-oxo-cyclohexanecarboxylic acid
- 5-Me-PCA: *N*-5-methyl-phenazine-1-carboxylic acid
- A_λ: absorbance at the wavelength λ
- AA: anthranilic acid
- ADIC: 2-amino-2-deoxyisochorismate
- AGA: *D*-alanyl-griseoluteiic acid
- AHCDC : 6-amino-5-hydroxy-2,4-cyclohexadiene-1-carboxylic acid
- AMP: adenosine monophosphate
- AOCHC: 6-amino-5-oxo-2-cyclohexene-1-carboxylic acid
- APS: ammonium persulfate
- AS: anthranilate synthase
- ATP: adenosine triphosphate
- BESSY: Berlin Electron Storage Ring Society for Synchrotron Radiation
- bp: base pair
- CD: circular dichroism
- *cf*.: *confer*
- CPL: circularly polarized light
- CV: column volume
- DAHP: 3-deoxy-*D*-arabino-heptulosonic acid 7-phosphate
- DAP: diaminopimelate epimerase
- DESY: Deutsches Elektronen-Synchrotron
- DHHA: *trans*-2*S*,3*S*-dihydro-3-hydroxyanthranilic acid
- DHPCA: dihydro-phenazine-1-carboxylic acid
- DHPDC: dihydro-phenazine-1,6-dicarboxylic acid
- DMSO: dimethyl sulfoxide
- DNA: deoxyribonucleic acid
- dNTP: deoxy nucleoside triphosphate
- DPF: Dortmund Protein Facility
- ε_λ: extinction coefficient at the wavelength λ
- E4P: *D*-erythrose-4-phosphate
- EDTA: ethylenediaminetetraacetic acid
- ESRF: European Synchrotron Radiation Facility
- *et al*.: *et alii*
- FAD: flavin adenine dinucleotide
- FEM: feature enhanced map
- FMN: flavin mononucleotide
- FT: Fourier transformation
- GATase1: type-I glutamine amidotransferase
- H_2-DHHA: 2,3,4,5-tetrahydro-3-hydroxy anthranilic acid
- HEPES: *4*-(*2*-hydroxyethyl)-*1*-piperazineethanesulfonic acid
- HHPDC: hexahydro-phenazine-1,6-dicarboxylic acid
- HIPS: Helmholtz Institute for Pharmaceutical Research Saarland
- HZI: Helmholtz Centre for Infection Research

- IC_{50}: half maximal inhibitory concentration
- IR: infrared
- ITC: isothermal titration calorimetry
- IQS: integrated quorum sensing
- FPLC: fast protein liquid chromatography
- IPTG: isopropyl-β-*D*-1-thiogalactopyranoside
- LB-medium/-agar: Luria-Bertani-medium/-agar
- LED: light emitting diode
- M63-medium: minimal medium 63 = low osmolarity medium
- MPI: Max Planck Institute
- MR: molecular replacement
- MST: a) menaquinone, siderophore, tryptophan synthase-like
  b) microscale thermophoresis
- MWCO: molecular weight cut-off
- NADH: reduced nicotinamide adenine dinucleotide
- *N*-AHL: *N*-acyl-*L*-homoserine lactone
- NMR: nuclear magnetic resonance
- OD_{600}: optical density at 600 nm
- *p.a.*: *pro analysis*
- PAGE: polyacrylamide gel electrophoresis
- PCA: phenazine-1-carboxylic acid
- PCR: polymerase chain reaction
- PCN: phenazine-1-carboxamide
- PDB: protein data bank
- PDC: phenazine-1,6-dicarboxylic acid
- PEG: polyethylene glycol
- PEP: phosphoenol pyruvate
- PHZ: phenazine
- PMSF: phenylmethylsulfonyl fluoride
- PPGAS-medium: proteose peptone glucose ammonium salt-medium (rhamnolipid promoting medium)
- PSI: Paul Scherrer Institute
- PQS: *Pseudomonas* quinolone signal
- PYO: pyocyanin
- QS: quorum sensing
- *q.v.*: *quod vide*
- ROS: reactive oxygen species
- RT-PCR: reverse transcription polymerase chain reaction
- SAD/MAD: singe/multiple wavelength anomalous dispersion
- SAM: *S*-adenosyl methionine
- SDS: sodium dodecyl sulfate
- SIR/MIR: singe/multiple isomorphous replacement
- SIRAS/MIRAS: singe/multiple isomorphous replacement with anomalous scattering
- SLS: Swiss Light Source
- SOD: superoxide dismutase
- TB-medium: terrific broth-medium
- TEMED: *N,N,N',N'*-tetramethylethylenediamine
- TEV: tobacco etch virus
- THPCA: tetrahydro-phenazine-1-carboxylic acid

- TLS: translation/libration/screw
- T_M: melting temperature
- TRIS: tris(hydroxymethyl)aminomethane
- TS: transition state
- UHPLC ultra high performance liquid chromatography
- UV: ultraviolet
- WT: wild type

According to the recommendations of the *International Union of Pure and Applied Chemistry* (IUPAC) and of the *International Union of Biochemistry and Molecular Biology* (IUB) amino acids are abbreviated with one letter code.

Summary

Phenazines are secondary metabolites of bacterial and archaeal origin. Involved in a variety of redox reactions yielding reactive oxygen species, phenazines exhibit a broad-spectrum antibiotic activity and a high potency as virulence factors. As such, their biosynthesis has been studied extensively in recent years leading to the structural and functional characterization of most enzymes (PhzA-G) responsible for biosynthesis of the common phenazine scaffold. Yet, some details of the associated reaction mechanisms remained elusive. This study aimed at answering remaining questions about the potentially unique catalytic mechanism of the isomerase PhzF, the role, and significance of PhzAB heterodimerization and at the development of PhzB-specific inhibitors.

This work contributed to a deeper understanding of the individual steps employed by the isomerase PhzF to convert DHHA, the last stable intermediate of phenazine biosynthesis, to a reactive ketamine. Measurement of kinetic isotope effects lent evidence that initial abstraction of a non-acidic proton is the rate-limiting step of catalysis. Together with computational data from collaborators, the complete catalytic cycle of this enzyme could be elucidated. It could also be shown that the substrate specificity of PhzF is narrow and one substrate analog revealed weak inhibitory potency, thus constituting a promising starting point for future drug-development studies.

Analysis of the catalytic activity of PhzBB homodimers and PhzAB heterodimers using a newly developed enzymatic assay revealed similar efficiency of both dimer forms. Together with thermal stability data from CD-measurements showing that heterodimers are as stable as PhzBB homodimers, these results indicate that PhzAB heterodimers might be prevalent *in vivo*. This hypothesis is further supported by quantitative RT-PCR data from collaborators and as such might explain why pseudomonads, which carry genes encoding for PhzA and PhzB, are such efficient phenazine producers.

New synthetic compounds, termed "phenazistatins" or "mavericks", were characterized regarding their inhibitory potency towards the potential drug target PhzB. To this aim, an *in vitro* assay was developed and employed for screening of more than 80 compounds. Combining ITC binding data, crystal structures and *in cellulo* activity data, a detailed structure activity relationship could be drawn and potent inhibitors identified.

1. Introduction

1.1. Phenazines

1.1.1. Background

Phenazines are small nitrogen-containing heterocyclic pigments, which occur in all colors of the rainbow. To date more than 180 naturally occurring phenazine derivatives have been identified (Dictionary of Natural Products, Taylor & Francis Group, available at dnp.chemnetbase.com). Yet, these pigments do not only show a high abundance in the biological world, but can be obtained via synthetic routes as well. Including all synthetic compounds, such as the first synthetic dye Mauveine (Hübner, 2006) or the common pH-indicator neutral red, the number of phenazine derivatives increases to over 6000 (Laursen and Nielsen, 2004). In the environment, more than 50 different organisms, such as *Burkholderia* species, Streptomycetaceae, Brevibacteriaceae, Enterobacteriaceae and most notably *Pseudomonas* species, were identified to produce and secrete the colorful, aromatic metabolites (Figure 1; Turner and Messenger, 1986).

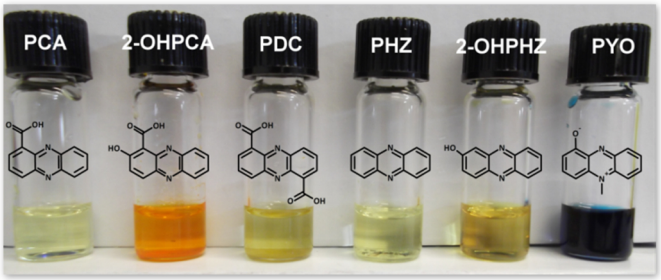

Figure 1: Phenazine pigments and their corresponding chemical structures. Different phenazines exhibit different colors when dissolved in DMSO. From left to right: phenazine-1-carboxylic acid (PCA), 2-hydroxy-phenazine-1-carboxylic acid (2-OH-PCA), phenazine-1,6-dicarboxylic acid (PDC), phenazine (PHZ), 2-hydroxy-phenazine (2-OH-PHZ) and pyocyanin (PYO).

Recently, phenazines, specifically a membrane-bound methanophenazine, were also discovered in the archaeon *Methanosarcina mazei* Gö1, showing that phenazines are important secondary metabolites present in different domains of life (Abken *et al*., 1998). Over the last decades, *Pseudomonas spp*. were the best studied of all phenazine producers, in particular because one representative, *Pseudomonas aeruginosa*, moved more and more into the focus of attention. As an opportunistic human pathogen, it causes severe nosocomial infections in immunocompromised patients (Jimenez *et al*., 2012). This pathogen, *i.e.* its primarily produced phenazine, the blue pigment pyocyanin, also originally led to discovery of phenazines over 150 years ago. Articles in the medical literature of the mid-19th century reported on infected wounds covered with "blue pus"

(for review Blankenfeldt and Parsons, 2014). In 1859, the French pharmacist Mathurin-Joseph Fordos was able to isolate the pigment responsible for the characteristic color. He called it "pyocyanin", a combination of the Greek words for "pus" (πύσ) and "cyan" (κυανό; Fordos, 1859 and 1860). A few years later, also the organism producing this pigment was discovered. Then called *Bacillus pyocyaneus*, it is nowadays known as *Pseudomonas aeruginosa* (Gessard, 1882). Research on the colored pigments continued and led to the classification of pyocyanin as a phenazine in 1924 (Wrede and Strack, 1924) and finally, in 1938, to its structural elucidation as a 5-*N*-methyl-1-hydrophenazinium betaine (Hillemann, 1938). Since, multiple phenazines from a variety of different bacteria were discovered and further characterized.

1.1.2. Mode of action – The diverse biological functions of phenazines

Phenazines are proposed to play multiple roles in the metabolic pathways of their producing organisms (Scheme 1).

First, the small secondary metabolites are toxic to a broad range of organisms like bacteria, fungi or algae and thus provide a competitive advantage for space and resources in nature (Toohey *et al*., 1965). Furthermore, the phenazine pyocyanin was identified as an important virulence factor in human infections (Lau *et al*., 2004; Pierson and Pierson, 2010; Rada and Leto, 2013).

Recently, it was also discovered that phenazines are involved in the primary metabolism of their producer and therefore are crucial for its survival, *e.g*. by acting as respiratory pigments in the lower layers of biofilms (Price-Whelan *et al*., 2007). Phenazines were also found to enhance iron acquisition (Cox, 1986; Hernandez *et al*., 2004) and even to serve as terminal signaling molecules in the *quorum sensing*–network (Dietrich *et al*., 2006).

Most of these functions are based on the redox-properties of phenazines. Phenazines are proposed to diffuse over or insert into membranes where they act as reducing agents of molecular oxygen and as such are directly involved in uncoupling of the oxidative phosphorylation, which in turn leads to the endogenous generation of reactive oxygen species, in particular superoxide radicals ($^{\bullet}O_2^-$) or hydrogen peroxide (H_2O_2).

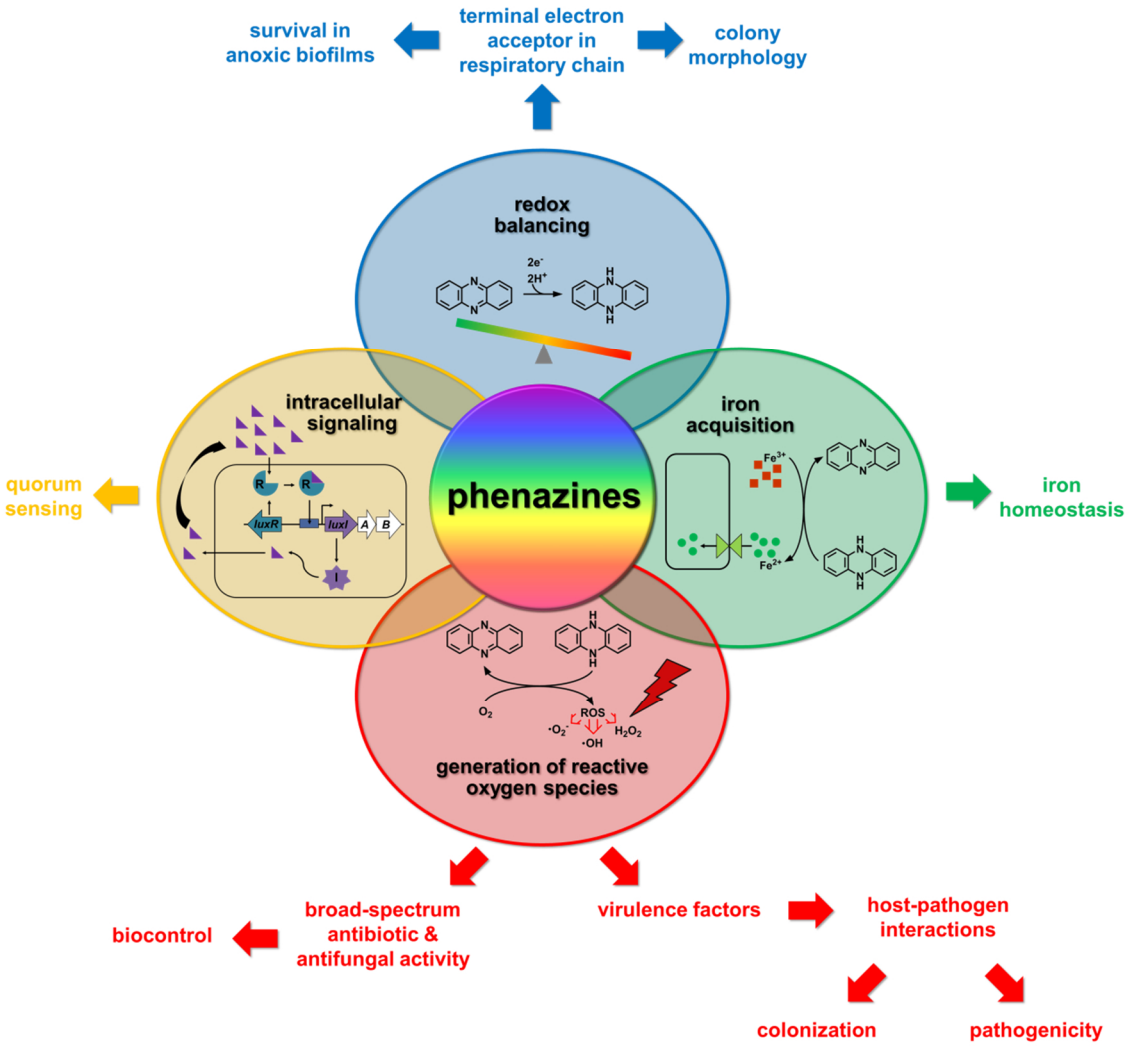

Scheme 1: The diverse roles of phenazines as secondary metabolites.
Graphical representation of different molecular functions phenazines exhibit in their source organism and its environment. Most of these functions rely on the redox properties of the heterocyclic phenazine core.

As these toxic radicals are causing irreversible oxidation of DNA or proteins and major damage to cellular structures such as lipid bilayers, the broad-range antibiotic activity of phenazines and the role of pyocyanin as an important virulence factor are easily explained. Yet, these properties render phenazines also harmful to their source organism. Hence, *e.g*. in *P. aeruginosa,* a higher activity of superoxide dismutases (SOD) can be observed. Likewise, phenazines were identified to upregulate the expression of PA2274, a hypothetical monooxygenase potentially involved in redox control, and of the efflux pump MexGHI-OmpD, potentially protecting the phenazine producing strain from self-intoxication (Sakhtah *et al*., 2016). In some phenazine producers, such as *Pantoea agglomerans*, also specific phenazine resistance proteins (EhpR) were identified (Giddens *et al*., 2002; Yu *et al*., 2011).

Despite these detrimental effects caused by phenazines, their biosynthesis also strongly contributes to the survival of the organism, *e.g*. in biofilms. Under the local anaerobic conditions, molecular oxygen is not available for maintaining glycolysis by reoxidation of NADH; instead, phenazines can serve as electron shuttles in these subzones by taking up electrons from NADH. These electrons might then be transported to the surface of the biofilm either via a phenazine relay, in which the electrons are repeatedly transferred to other phenazines until the aerobic zones are reached, or the reduced pigments directly diffuse to the surface where they get reoxidized by oxygen (Sakhtah *et al*., 2016).
Additionally, phenazines are involved in iron homeostasis. On the one hand, they were found to downregulate the expression of genes involved in the ferric iron (Fe^{3+}) uptake (Dietrich *et al*., 2006), on the other hand, they are able to oxidize ferric iron to ferrous iron (Fe^{2+}) thus facilitating its acquisition (Cox, 1986; Hernandez *et al*., 2004).

All these findings not only underline the importance of phenazine pigments for their producers, but also even more emphasize the necessity to further study and characterize these secondary metabolites and their production to gain a better understanding of the multifaceted roles they fulfill especially in infections by pathogenic phenazine producing bacteria such as *P. aeruginosa.*

1.2. Phenazine biosynthesis

1.2.1. The *phz*-operon

Comparison of phenazine-producing bacterial strains led to identification of a conserved gene cluster responsible for biosynthesis of phenazine-1-carboxylic acid (PCA) and phenazine-1,6-dicarboxylic acid (PDC) (Pierson and Thomashow, 1992; Pierson and Pierson, 1996; Mavrodi *et al*., 1998). This cluster, called *phz*-operon, is comprised of at least five genes, *phzCDEFG*, essential for the basal biosynthetic pathway. Most phenazine producers possess at least one additional conserved "core" biosynthesis gene termed *phzB.* This gene, as well as the highly homologous gene *phzA*, seems not to be required for PCA or PDC synthesis, yet is able to greatly enhance the levels of these two "core" phenazines *in vitro* (Mavrodi *et al*., 1998; McDonald *et al.*, 2001). However, *in vivo*, *e.g.* in the phenazine producer *P. agglomerans,* expression of the *phzB*-gene seems to be absolutely essential for phenazine biosynthesis (Giddens *et al*., 2002).

As anticipated by the structural diversity of phenazines from different bacteria, many of the biosynthetic clusters contain operon extensions or additional genes somewhere else in the genome for downstream modifications of the two "precursor" phenazines PCA or PDC, leading to strain-specific derivatives. Moreover, auto resistance genes, such as *ehpR* from *P. agglomerans*, or regulators like *phzI* and *phzR* are often located adjacent to the "core" biosynthesis genes (Scheme 2).

The opportunistic pathogen *P. aeruginosa* represents a peculiarity among the phenazine-producing bacteria. This organism contains two *phz*-operons, which are highly homologous (98.3 % in strain PAO1) and both contribute to PCA production in this bacterium. It was discovered that these two operons underlie not only a complex regulatory network (*q.v.* 1.2.4.), but also exhibit cross-regulation under certain conditions (Cui *et al*., 2016).

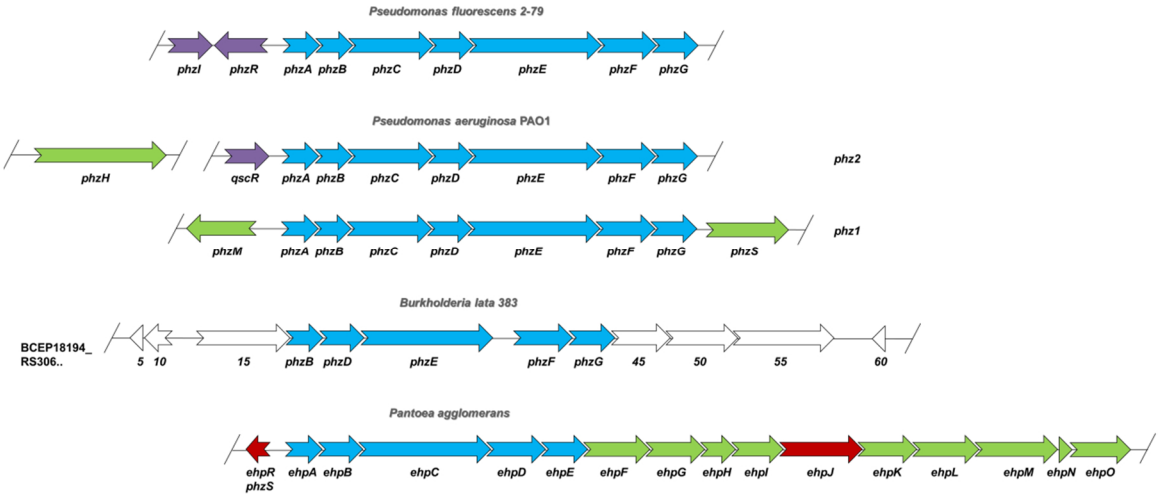

Scheme 2: The *phz*-operon in different species.
Most of the phenazine-producing organisms possess a conserved gene cluster, which encodes the enzymes of the biosynthetic pathway. Besides the "core" biosynthesis genes (▭), genes involved in further modifications of the basic scaffold (▭), regulation of the pathway (▭) or self-resistance (▭) are organized in the so-called *phz*-operon. For some bacterial species, the roles of some of the gene products are still unknown (▭).

As mentioned before, phenazines were also discovered in archaea. However, these organisms lack the characteristic *phz*-operon. Hence, it is not clear, which pathway archaea use to generate phenazines or if the essential phenazine scaffold is obtained from other external sources (Abken *et al*., 1998; Deppenmeier *et al*., 2002).

1.2.2. The "core" biosynthesis pathway

After identification of the genes involved in phenazine biosynthesis in 1996 and 1998 (Pierson and Pierson, 1996; Mavrodi *et al*., 1998), further characterization of this pathway was initiated at the molecular level. Over the past two decades, the role of all essential "core" biosynthesis enzymes could be elucidated (for review: Blankenfeldt and Parsons, 2014). It was established that phenazine biosynthesis proceeds via the shikimic acid pathway and finally branching from the biosynthetic pathway of aromatic amino acids at the stage of chorismate (Ingledew and Campbell, 1969). In fact, already in 1972, two groups could show that phenazines are built from two molecules of chorismic acid (Calhoun *et al*., 1972; Longley *et al*., 1972).

Accordingly, PhzC was shown to be homologous to DAHP (3-deoxy-*D*-arabino-heptulosonic acid 7-phosphate) synthases and to catalyze the formation of DAHP from *D*-erythrose-4-phosphate (E4P) and phosphoenol pyruvate (PEP) (McDonald *et al*., 2001). DAHP is further converted via shikimic acid to chorismic acid by other enzymes of the shikimic acid pathway (Scheme 3). As mentioned before, chorismic acid represents the last common precursor of phenazines and aromatic amino acids. While for amino acid biosynthesis chorismate is converted either to anthranilic acid (AA) or to prephenate yielding tryptophan and tyrosine/phenylalanine respectively, in phenazine biosynthesis the homodimeric, intertwined two-domain enzyme PhzE converts chorismate to 2-amino-2-deoxyisochorismate (ADIC) (Li *et al*., 2011).

PhzE facilitates this reaction by establishing an intramolecular channel that connects the N-terminal menaquinone, siderophore, tryptophan synthase-like (MST) domain with the C-terminal type-I glutamine amidotransferase (GATase1) domain. In the latter domain, glutamine is hydrolyzed to glutamate leading to generation of free ammonia, which is transferred directly to the active site of the MST-domain in the second monomer, where it is used for conversion of chorismate to ADIC. Interestingly, PhzE was found to be related to anthranilate synthases (AS), yet, despite a very similar organization of the active site residues, PhzE seems not to catalyze the subsequent elimination of pyruvate that leads to generation of AA by these AS (Li *et al*., 2011).

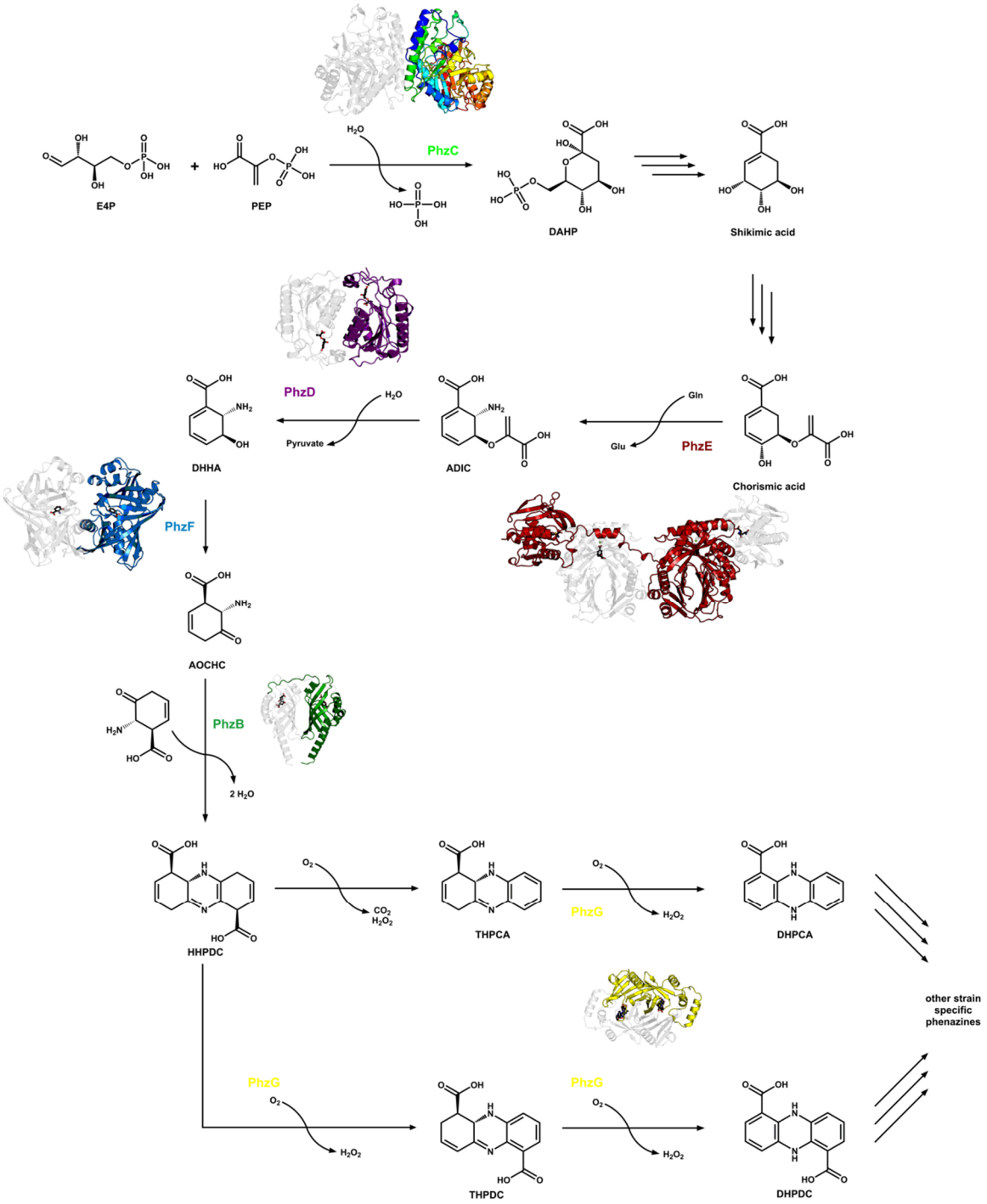

Scheme 3: Overview of the "core" phenazine biosynthesis leading to production of the two phenazine precursors DHPCA and DHPDC.
Phenazine biosynthesis branches from the shikimic acid pathway at the stage of chorismic acid. The first specific phenazine biosynthesis enzyme is PhzE, which catalyzes the conversion of chorismate to ADIC. Subsequently, ADIC is cleaved by the isochorismatase PhzD yielding DHHA. DHHA represents the last stable intermediate of the pathway. After its PhzF-catalyzed isomerization, the reactive ketamine AOCHC undergoes condensation assisted by PhzB. The final steps are comprised of multiple uncatalyzed and PhzG-dependent oxidation reactions leading to the two phenazine precursors DHPCA and DHPDC.

The next step in the biosynthetic pathway is comprised of a hydrolysis reaction whereupon ADIC is converted to *trans*-2*S*,3*S*-dihydro-3-hydroxyanthranilic acid (DHHA;

Scheme 3). The α/β-hydrolase PhzD cleaves ADIC via a general acid-base catalysis involving a conserved aspartic acid and a lysine residue. This catalysis follows again an unusual mechanism, *i.e*. other structurally similar enzymes facilitate such reactions in a metal-dependent fashion and via formation of a covalent intermediate (Parsons *et al*., 2003).

Subsequently, DHHA is converted to the highly reactive amino ketone 6-amino-5-oxo-2-cyclohexene-1-carboxylic acid (AOCHC) by the isomerase PhzF (Blankenfeldt *et al*., 2004; Parsons *et al*., 2004a; a more detailed description of this enzyme and its proposed catalytic mechanism can be found in paragraph 1.3.1.).

In order to prevent unwanted side reactions of this ketone, the dimeric enzyme PhzB, which is structurally similar to enzymes from the Δ^5-3-ketosteroid isomerase/nuclear transport factor 2 family was found to accelerate the otherwise spontaneous head-to-tail condensation of two identical AOCHC molecules (Ahuja *et al*., 2008; for further details please see paragraph 1.3.2.).

Finally, PhzG, a FMN-dependent monooxygenase and the last enzyme of the "core" biosynthesis, is catalyzing different oxidative steps leading to formation of PCA or PDC in their reduced dihydro-state (Scheme 3). Two recent studies showed that PhzG is, similar to other enzymes of the biosynthetic pathway, a homodimeric enzyme. Structurally related to pyridoxine-5'-phosphate oxidase (PdxH), it contains an essential FMN-cofactor in its active site, which is formed by residues from both monomeric chains (Parsons *et al*., 2004b; Xu *et al*., 2013). The study by Xu *et al.* (2013) also revealed that PhzG can oxidize different tricyclic intermediates. It either directly binds the reaction product of PhzB-catalysis, hexahydro-phenazine-1,6-dicarboxylic acid (HHPDC), or a downstream product of this catalysis, tetrahydro-phenazine-1-carboxylic acid (THPCA). In the former case PhzG catalyzes two subsequent oxidations leading to dihydro-phenazine-1,6-dicarboxylic acid (DHPDC) as final product. In the other case, THPCA, which results from spontaneous, uncatalyzed oxidative decarboxylation of HHPDC, is converted to dihydro-phenazine-1-carboxylic acid (DHPCA).

The fact that PhzG can catalyze oxidations leading to two different products of the same biosynthetic pathway is unusual and can be explained best by the relative activities of

PhzG and the two preceding enzymes PhzF and PhzB. Since the final catalytic steps require oxygen, also the availability of oxygen might play a crucial role in PCA or PDC biosynthesis.

1.2.3. Synthesis of more complex, strain specific phenazine derivatives

As mentioned before, over 180 naturally occurring phenazine derivatives have been identified. All derive from the two precursors DHPCA or DHPDC, which are the final products of the "core" biosynthetic pathway (Scheme 4).

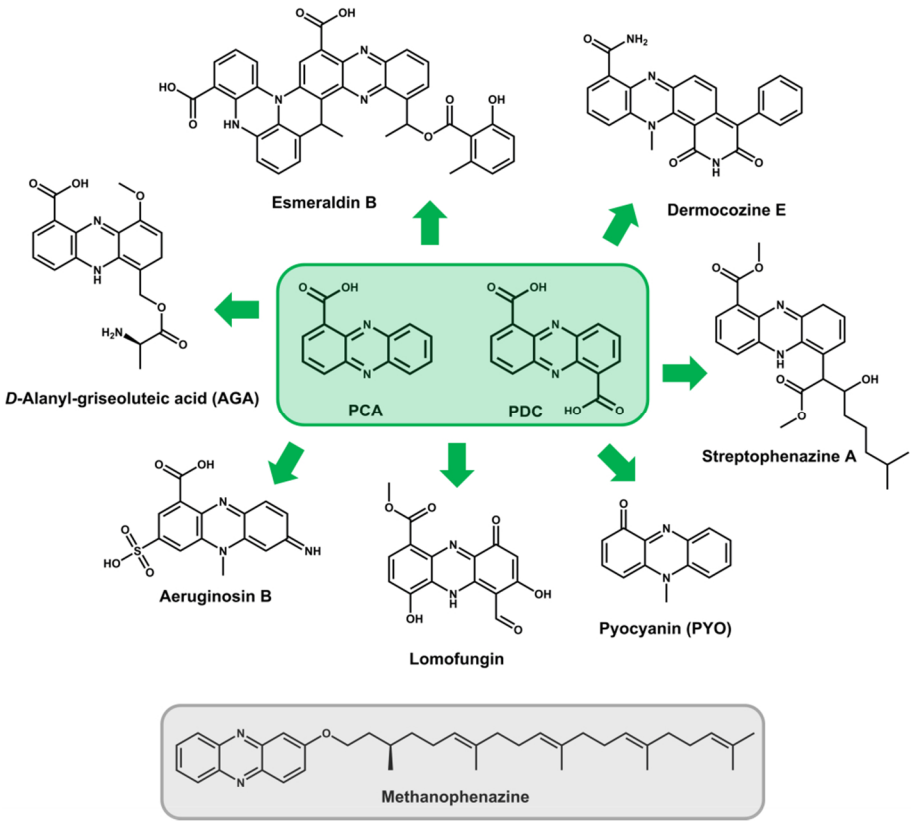

Scheme 4: The variety of naturally occurring phenazines from different bacterial or archaeal organisms. All different phenazines, except the archaeal methanophenazine (gray), whose biosynthesis is unknown to date, are based on the two precursors PCA and PDC (green).

Yet, to generate strain specific phenazines further enzymes are necessary to modify the basic phenazine scaffolds (Scheme 5). *P.* aeruginosa for instance possesses the two genes *phzM* and *phzS* adjacent to their "core" biosynthetic operon *phz1* as well as a third DHPCA-modifying gene, *phzH*, localized upstream of the *phz2*-operon (Chin-A-Woeng *et al.*, 2001a, 2001b).

PhzM is a methyltransferase catalyzing the SAM-dependent methylation of DHPCA leading to formation of *N*-5-methyl-phenazine-1-carboxylic acid (5-Me-PCA). This intermediate was recently found to regulate its own transport by the MexGHI-OmpD

efflux pump (Sakhtah *et al*., 2016).

In a subsequent reaction, 5-Me-PCA is converted to pyocyanin by the FAD-dependent monooxygenase PhzS, which uses NADH and molecular oxygen. PhzS can also directly convert DHPCA, which leads to formation of 1-hydroxy-phenazine (1-OH-PHZ; Scheme 5; Gohain *et al*., 2006; Greenhagen *et al*., 2008).

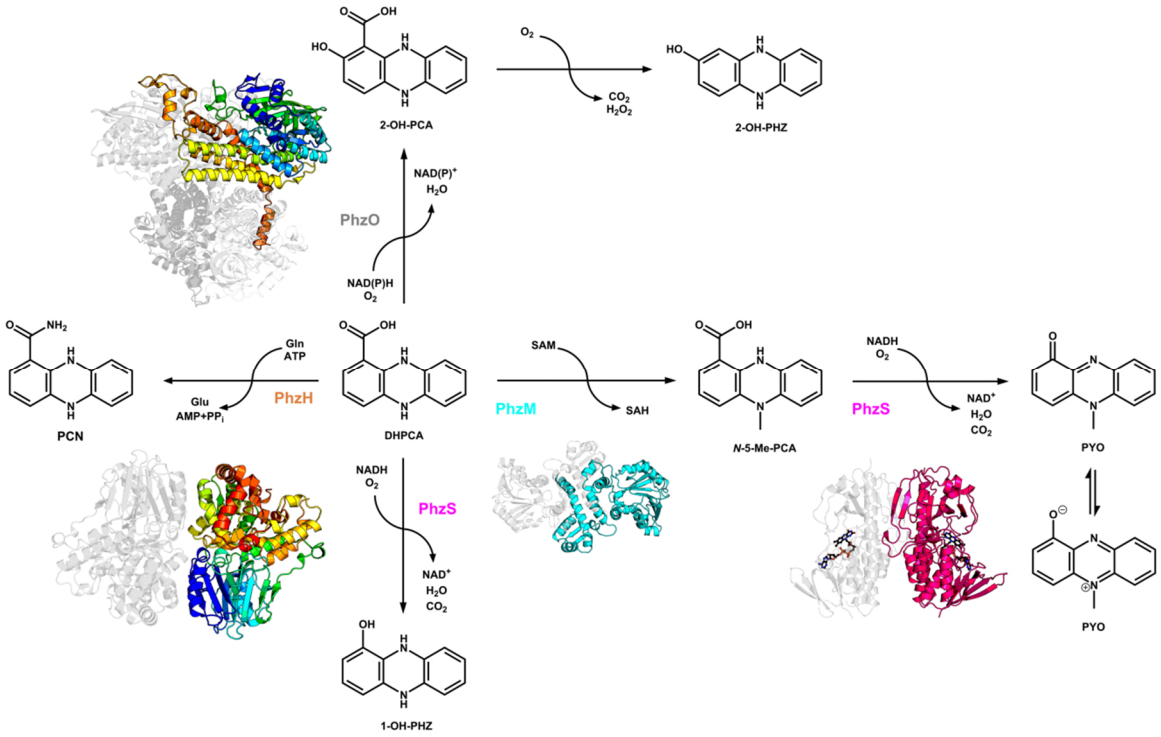

Scheme 5: Overview of alternative phenazine modifying pathways.
Starting from DHPCA, different phenazine modifying enzymes convert this precursor to strain specific phenazines. PhzH is converting DHPCA to PCN using ATP hydrolysis as energy and glutamine as ammonium source. PhzM is an SAM-dependent enzyme leading to formation of 5-Me-PCA that can be converted, similarly to DHPCA, by PhzS using NADH and molecular oxygen leading to formation of pyocyanin and 1-OH-PHZ respectively. PhzO is catalyzing a similar reaction leading to 2-OH-PCA that, after oxidative decarboxylation, forms 2-OH-PHZ.

Another monooxygenase termed PhzO, which can *e.g*. be found in *P. aureofaciens*, catalyzes a similar oxidation of DHPCA to 2-hydroxy-PCA, which spontaneously reacts further to form 2-OH-PHZ (Scheme 5; Delaney *et al*., 2001).

The product of the *phzH* gene is a transamidase, which catalyzes the glutamine and ATP-dependent synthesis of phenazine-1-carboxamide (PCN; Chin-A-Woeng *et al*. 2001b).

Other bacteria, such as *Streptomyces spp*., produce even more complex phenazines like griseoluteiic acid or esmeraldins (Scheme 4; Rui *et al*., 2012). Their biosynthesis pathways contain a variety of additional modifying enzymes.

1.2.4. Everything under control – Regulation of phenazine biosynthesis by QS

Phenazines are important bacterial and archaeal secondary metabolites (*q.v*. 1.1.2.). As such, it is no surprise that their biosynthesis is tightly regulated. In pseudomonads this regulation mainly depends on the so-called quorum sensing (QS) network (Pierson *et al*., 1994; Wood *et al*., 1997). Quorum sensing in general enables bacteria to regulate gene expression of their secondary metabolism according to environmental conditions and to coordinate the behavior of the entire cell population (for review: Lee and Zhang, 2015; Papenfort and Bassler, 2016).

In the most simple case, as it can be found *e.g*. in *P. fluorescens* 2-79, two genes, encoding for a so-called autoinducer synthase (PhzI) and a transcription regulator (PhzR), are necessary for QS control of phenazine biosynthesis. Both proteins belong to a QS system that uses *N*-acyl-*L*-homoserine lactones (*N*-AHL) as signaling molecules/autoinducer (Fuqua *et al*., 1994). In *P. aeruginosa* however, the network is more complex. So far, four quorum sensing pathways have been identified, which are hierarchically arranged but also highly interconnected. The two major networks, the LasI/LasR- and the RhlI/RhlR-system, also rely on *N*-AHLs as signaling molecules. In addition, there is the specific *Pseudomonas* quinolone signal (PQS) system, which plays an important regulatory role in phenazine biosynthesis, and the recently discovered integrated quorum sensing (IQS) system, which is triggered under limiting phosphate concentrations (for review: Lee and Zhang, 2015; Papenfort and Bassler, 2016).

Quorum sensing is population density dependent, hence, only when the size of the population is large enough, the intracellular level of the signaling molecule reaches a certain threshold, binds to the receptor and activates the expression of genes under QS control.

Interestingly, also phenazines themselves, especially the virulence factor pyocyanin, seem to serve as signaling molecules by reducing the redox-sensitive transcription activator SoxR and thus activating gene expression *e.g*. of PA2274, which might be involved in redox control (Dietrich *et al*., 2006).

1.3. Unique reactions of phenazine biosynthesis

1.3.1. PhzF catalyzes DHHA isomerization by a suprafacial-[1,5]-hydrogen shift

The phenazine biosynthetic pathway is characterized by some unique reaction mechanisms, *e.g*. the metal-independent hydrolysis of ADIC by the isochorismatase PhzD (Parsons *et al*., 2003). The isomerization of DHHA, the product of this hydrolysis and the last stable intermediate of the pathway, seems to proceed via an unusual reaction as well. Previous studies showed that the homodimeric isomerase PhzF catalyzes the conversion of DHHA to the reactive ketamine AOCHC (Blankenfeldt *et al*., 2004; Parsons *et al*., 2004a).

In agreement with anterior predictions, crystal structures of PhzF (Figure 2) confirmed that the enzyme is structurally related to DapF, a diaminopimelate epimerase first characterized in *Hemophilus influenza* (Cirilli *et al*., 1998; Lloyd *et al*., 2004).

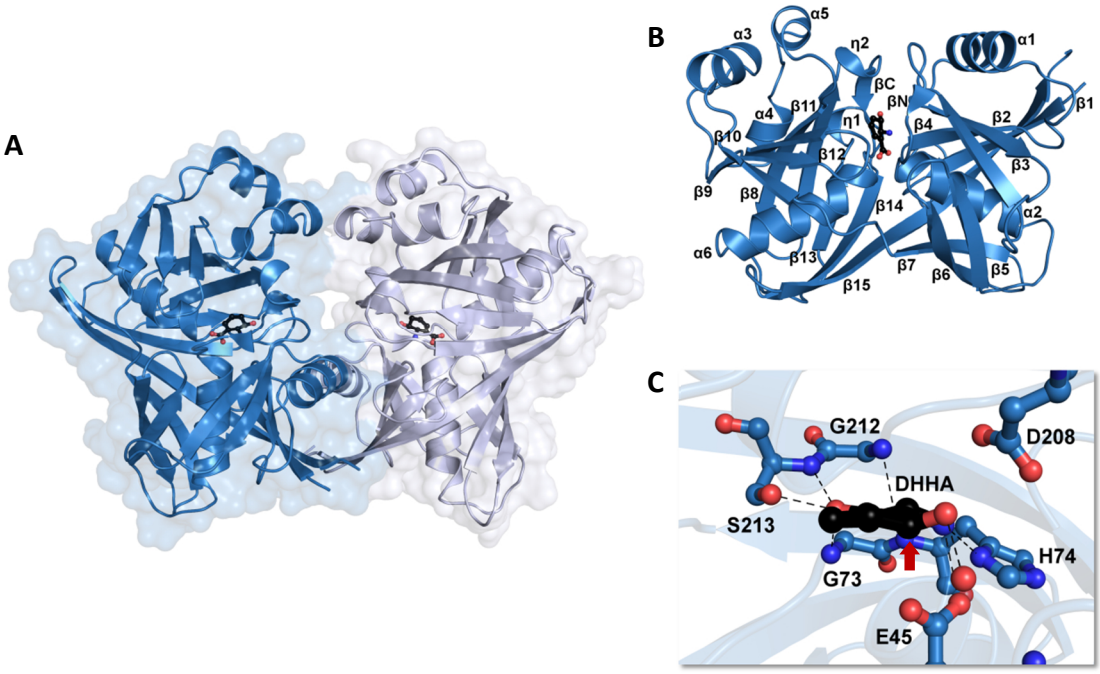

Figure 2: Structure and active site of the isomerase PhzF.
A Overall topology of the dimeric biological assembly of PhzF shown as cartoon and surface (transparent) representation. The individual chains are colored in **blue** (chain A) and light blue (chain B) respectively. The natural substrate DHHA is shown as ball and stick representation in **black**. **B** The PhzF monomer depicted with its secondary structure elements. **C** Close-up on the active site of PhzF in complex with DHHA. The active site residues as well as the ligand are shown as balls and sticks colored as described above. The important hydrogen bonds are highlighted (- - -) and the arrow (⬆) indicates the location of the C3 proton that is abstracted during catalysis.

A PhzF monomer (Figure 2B) is built up by two very similar domains each comprised of approximately 130 amino acids, which might have arisen from ancient gene duplication. The two domains share a very similar topology characterized by a central α-helix (α_2 and

α_6) that is wrapped in an eight-stranded β-sheet. One of these β-strands (β_{15}) is larger and spans into both domains. Additionally, each domain is flanked by small helices (α_1 and α_3-α_5), a short β-strand (β_N and β_C), and a 3_{10}-helix (η_1 and η_2). The substrate binding site is located at the interface of the domains at the bottom of a central cleft with the two positive central helix dipoles pointing towards it (Blankenfeldt *et al*., 2004). In contrast to DapF, PhzF lacks the two important catalytic cysteine residues in the active site. Instead, based on a complex structure with the substrate DHHA, E45 could be identified as catalytic residue. It stabilizes the substrate together with the side chains of H74, D208 and S213 as well as the backbone amides of G73, H74 and G212 and a water molecule, which together provide an extensive hydrogen-bonding network (Figure 2C). Mutagenesis studies confirmed the crucial role of E45, as variants, in which this residue is replaced by an alanine or glutamine, completely lose catalytic activity *(*Blankenfeld*t et al.*, 2004).

The essential role of residue E45 indicates a catalytic mechanism potentially involving a proton/hydrogen transfer whereupon the C3-proton of DHHA has to migrate to position C1. This [1,5]-hydrogen shift could follow two potential reaction mechanisms: a) a general acid-base catalysis or b) a sigmatropic reaction via a pericyclic intermediate.

The first mechanistic hypothesis involves direct contribution of residue E45 as a general base, which initiates the proton abstraction that is followed by rearrangement of the π-system of the substrate. The proton is then transferred to position C1, leading to formation of an enol, which subsequently tautomerizes stereospecifically to the respective ketone. As the migrating proton is predicted to be non-acidic, a high energy barrier can be expected for its initial abstraction.

Furthermore, NMR measurements carried out in D_2O revealed full recycling of the migrating proton without solvent exchange. Assuming that in a classical acid-base catalyzed reaction, possibly involving solvent molecules, incorporation of a solvent deuterium at position C1 is expected, this suggests that E45 is not directly involved in proton abstraction. Consequently, both findings render a classical acid-base catalyzed mechanism less likely, but offer the possibility of another mechanistic route, *i.e*. a sigmatropic [1,5]-hydrogen shift. Sigmatropic reactions are pericyclic reactions, which proceed in a concerted manner and are characterized by a cyclic geometry of the transition state (TS; Blankenfeldt *et al*., 2004). A pericyclic mechanism is further supported

by structural data of phenazine biosynthesis enzymes downstream of PhzF (Ahuja *et al*., 2008; Xu *et al*., 2013), which, in complex with their respective substrates, revealed *R*-configuration of the proton at the position equivalent to C1 in DHHA. As this stereochemistry would only be observed if de- and reprotonation of DHHA occur on the same side of the central 1,3-cyclohexadiene ring, these structures further indicate a suprafacial [1,5]-hydrogen shift following a sigmatropic rearrangement.

In fact, pericyclic reactions have already been described in enzyme catalysis. Among these, the [3,3] Claisen rearrangement of chorismate to prephenate catalyzed by chorismate mutases is probably known best (Burschowsky *et al*., 2014). Another example is the asynchronous [1,5] prototropic fragmentation found in PchB, an isochorismate pyruvate lyase from *P. aeruginosa*, which catalyzes the elimination of pyruvate from isochorismate (DeClue *et al*., 2005). However, a sigmatropic [1,5]-hydrogen shift as suggested for PhzF has not been reported so far.

Subsequently to the PhzF-catalyzed isomerization of DHHA, the reactive amino ketone product AOCHC undergoes head-to-tail condensation via a double Schiff base reaction leading to formation of the tricyclic phenazine scaffold (Blankenfeldt *et al*., 2004). As the amino ketone is very reactive, potentially harmful side reactions have to be prevented. It could be shown that PhzB is able to catalyze this reaction, however a slow, but significant uncatalyzed auto condensation of two AOCHC molecules could be observed as well (Ahuja *et al.*, 2008).

1.3.2. PhzB accelerates AOCHC self-condensation leading to formation of the phenazine scaffold

Subsequent to PhzF catalysis, another key step of the biosynthesis pathway is the two-fold condensation of two identical ketamine precursors leading to formation of the characteristic tricyclic phenazine scaffold. Although this step can proceed spontaneously and without further assistance of an enzyme in solution, PhzB was found to accelerate the bimolecular reaction several-fold (Ahuja *et al.*, 2008). In fact, deletion of the respective gene from *P. agglomerans* (*ephA*) led to drastic impairment of phenazine production, suggesting that enzyme catalysis of this step is crucial for successful biosynthesis *in vivo* (Giddens *et al.*, 2002).

Several crystal structures of PhzB from *Burkholderia lata* 383 (synonym: *Burkholderia cepacia* R18194) and *Pseudomonas fluorescens* 2-79 as well as biochemical studies provided a deeper insight into substrate binding and the mechanistic details of the enzyme catalyzed reaction (Ahuja *et al.*, 2008; Blankenfeldt *et al.*, unpublished).

The structural studies identified PhzB as a small dimeric enzyme belonging to the Δ^5-3-ketosteroid isomerase/nuclear transport factor 2 family (Figure 3).

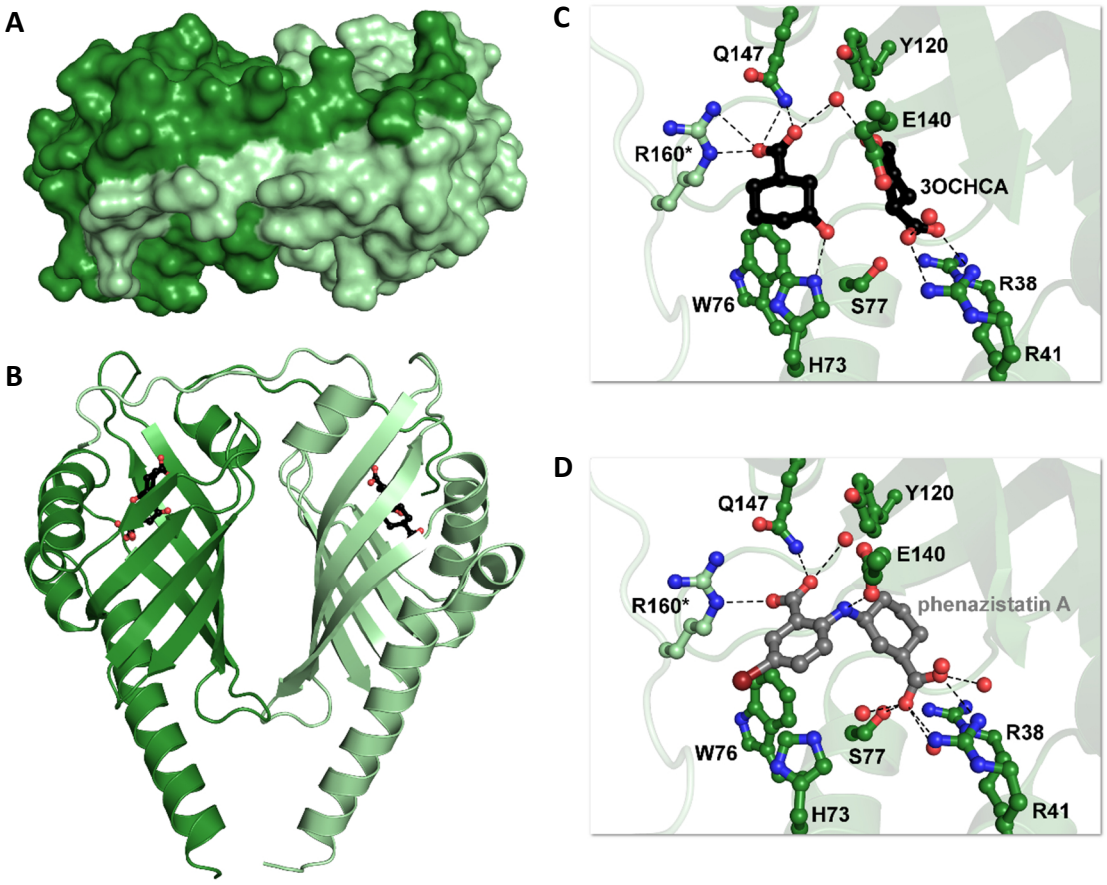

Figure 3: Structure and active site of the phenazine biosynthesis protein PhzB.
A Surface representation of Phz(A)/B from *B. cepacia* R18194 showing the arm-to-arm exchange between the C-termini of two monomers. The individual chains are colored in **forest** (chain A) and palegreen (chain B) respectively. **B** Overall topology of the dimeric biological assembly of Phz(A)/B shown as cartoon representation in similar colors as described before. Four molecules of the substrate analog 3OCHCA (3-oxo-cyclohexanecarboxylic acid) bound to the active site of PhzB are shown as ball and stick representation in **black**. **C** and **D** Close-ups on the active site of *Bc*Phz(A)/B in complex with either two molecules of the substrate analog 3OCHCA (**C**) or a potential PhzB-inhibitor called phenazistatin A (**D**). The active site residues as well as the ligands are shown as balls and sticks colored as described above or in gray for phenazistatin A. The important hydrogen bonds are highlighted (- - -).

A remarkable feature of the obligate dimer is the arm-exchange of the two C-termini (Figure 3A), which act as flexible lids shielding the active site from the solvent. The exchange was found to be essential for activity as truncations in this region led to a drastic decrease or even full abrogation of enzymatic activity (Ahuja *et al.*, 2008).

A closer look at the active site explains this observation: PhzB provides a large cavity for binding of two, chemically identical substrate molecules, formed by residues from both monomers (Figure 3C). The first substrate molecule binds deep inside this cavity and is stabilized via its carboxylic acid moiety through a hydrogen-bonding network, which is mainly provided by a conserved arginine (R41). The binding site for the second substrate is located closer to the surface. The C-terminal arginine of the other monomer (R160*) is directly involved in binding and orienting the ligand, again by coordinating its carboxylate. Consequently, the two substrate molecules are perfectly oriented towards each other to facilitate catalysis. Two consecutive nucleophilic attacks by the 2-amino-groups lead to formation of a double Schiff base intermediate and release of two water molecules. After further rearrangements, the heterocyclic product HHPDC is formed. The active site residues E140, as well as H73 and S77 are involved in protonation and stabilization of the two different anionic intermediates (Ahuja *et al*., 2008).

Surprisingly, phenazine producing pseudomonads feature a second, 70 % identical copy of PhzB, termed PhzA (Mavrodi *et al*., 1998). Yet, the function of this protein is unclear. Although depletion of the encoding gene leads to reduced PCA production, PhzA was found to be inactive in the condensation reaction (Ahuja *et al*., 2008). This finding can be explained by two mutations of the active site, where two residues involved in PhzB-catalysis, H73 and S77, are replaced by leucines. In addition, a crystal structure of PhzA from *P. fluorescens* 2-79 revealed a dimeric organization, which does not feature the arm-exchange found to be indispensable for catalysis (Ahuja *et al*., 2008). Nevertheless, due to the high sequence as well as structural similarity, it was proposed that both proteins could form heterodimers. Indeed, a crystal structure of PhzAB confirmed this hypothesis (Figure 4; Blankenfeldt *et al*., unpublished).

However, the actual function of PhzA or PhzAB remains elusive, although it was suggested that heterodimer formation might be advantageous under substrate-limiting conditions when the substrate concentration is too low to occupy all four binding sites of an active homodimer (Ahuja *et al.*, 2008).

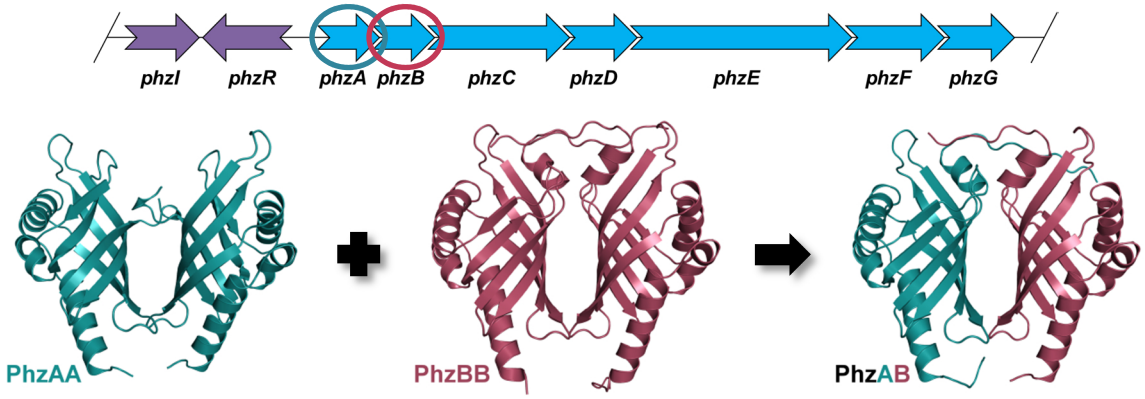

Figure 4: PhzAB heterodimerization in *Pseudomonas fluorescens* 2-79.
Top: Schematic representation of the *phz*-operon from *P. fluorescens* 2-79 with the genes encoding for PhzA and PhzB highlighted in deepteal (○) and raspberry (○) respectively. **Bottom**: Schematic representation of PhzAB heterodimerization as indicated by the crystal structures of dimeric PhzA (**deepteal**) and dimeric PhzB (**raspberry**) and the PhzAB heterodimer (colored accordingly).

The unique role of PhzB in phenazine biosynthesis renders it an interesting drug target. In the first place, enzyme inhibition could lead to reduced levels of phenazine virulence factors. In addition, inhibition of the PhzB-catalyzed condensation reaction might trigger self-intoxication of the producing bacteria by accumulation of the reactive ketamine substrate. Studies of PhzB catalysis already provided various synthetic substrate and product analogs, which served as mechanistic probes (Mentel *et al.*, 2009a). Some of these compounds revealed high affinity binding to the enzyme in the µM-range. As such, these ligands constitute promising starting points for further inhibitor development.

2. Research Objectives

Phenazines are small, nitrogen-containing heterocyclic pigments. They exhibit versatile and sometimes pivotal roles in the primary and secondary metabolism of their producing organisms such as the human nosocomial pathogen *P. aeruginosa*. Biosynthesis of these important metabolites is carried out by the products of at least five highly conserved genes, *phz(B)CDEFG*, clustered in the *phz*-operon. Among the peculiar catalytic mechanisms employed in the pathway, the two reactions leading to formation of the tricyclic phenazine scaffold are of special scientific and/or therapeutic interest and therefore constituted the focus of this study, which aimed at:

1. The elucidation of the basic principles of the PhzF-catalyzed DHHA isomerization

The isomerase PhzF converts *trans*-2*S*,3*S*-dihydro-3-hydroxyanthranilic acid (DHHA) into a highly reactive ketamine. Previous data revealed that this isomerization requires a suprafacial [1,5]-shift of a non-acidic proton within the π-system of the substrate, followed by immediate stereospecific keto-enol tautomerization (Blankenfeldt *et al*., 2004), yet the molecular details of the mechanism remained unclear.

2. The analysis of the occurrence of PhzAB heterodimerization and its relevance for phenazine biosynthesis

Following DHHA isomerization, two molecules of the ketamine product undergo diagonal-symmetrical condensation leading to generation of the tricyclic phenazine scaffold. Due to the high reactivity of the ketamine, this reaction can occur spontaneously, it is however significantly accelerated by PhzB (Ahuja *et al*., 2008). Interestingly, an additional gene in the *phz*-operon of pseudomonads encodes a second, highly homologous copy of PhzB, termed PhzA. This protein is inactive in the condensation reaction, but, as revealed by a crystal structure, can form heterodimers with PhzB (Blankenfeldt *et al*., unpublished). Despite the structural insights, the physiological relevance and role of these dimers remained elusive.

3. The development of specific PhzB-inhibitors to modulate phenazine biosynthesis

In addition to the potentially special dimerization behavior of Phz(A)/B, the enzyme could be a promising drug target as its inhibition is supposed to cause accumulation of the highly

reactive ketamine substrate. Elevated levels of this substrate might promote unspecific side reactions and consequently trigger self-intoxication of the phenazine-producing bacteria.

Altogether, by combining the information obtained from different types of experiments, such as enzymatic activity assays, biophysical binding studies and X-ray crystal structure analysis, this study provides a deeper insight into two unique steps of phenazine biosynthesis. A profound understanding of the generation of these virulence factors is essential for identification of new potential drug targets and allows further rational drug design to interfere with this important metabolic pathway and eventually fight infectious diseases caused by phenazine producing pathogens.

3. Methods & Materials

3.1. Theoretical Section

This section deals with the basic theory of the most important biochemical and biophysical methods used in this study.

3.1.1. Steady-state enzyme kinetics

Enzymes are essential components in all biological systems and understanding their function can provide a deeper insight into the function and regulation of the whole system. Enzymes, in contrast to other proteins, are molecular catalysts that can accelerate the rate of a (bio)chemical reaction in both, forward (substrate to product) and reverse (product to substrate), direction, typically at different rates. A simple and rapid way to study this activity is the performance of steady-state kinetic experiments. The experimental setup constitutes the determination of initial reaction rates under the assumption that at the beginning of the experiment each enzyme molecule repeatedly binds one substrate and catalyzes its turnover. A prerequisite for this assumption is that substrate is available in large excess (at least fivefold) compared to the enzyme. In this case, the concentration change of unbound substrate over time is negligible, *i.e.* the concentration of free substrate [S] is equal to the total substrate concentration [S_T] ([S]≈[S_T]), which leads to a linear dependency. At the same time, almost no product will be present at this point and thus will not interfere with the monitored reaction. Under these conditions the Michaelis-Menten theory applies, *i.e.* that the rate of the enzyme-catalyzed reaction is proportional to the concentration of the enzyme-substrate complex (equation 1).

$$v = \frac{k_{cat}[E_T][S]}{K_M + [S]} \quad \text{where } k_{cat}[E_T] = v_{max} \qquad \textbf{(1)}$$

with

v	rate of the reaction
k_{cat}	apparent first order rate-constant, independent of enzyme concentration
[E_T]	total enzyme concentration
[S]	substrate concentration in the equilibrium
K_M	Michaelis-constant ≡ substrate concentration at $v_{max}/2$
v_{max}	maximal rate of reaction at a specific enzyme concentration ≡ saturation

In practice, the depletion of substrate or the formation of product is followed over a course of time starting from different initial substrate concentrations (Scheme 6). Initial reaction rates are then determined from the linear portion of the resulting plots and in turn plotted as a function of the initial substrate concentrations (Scheme 6).

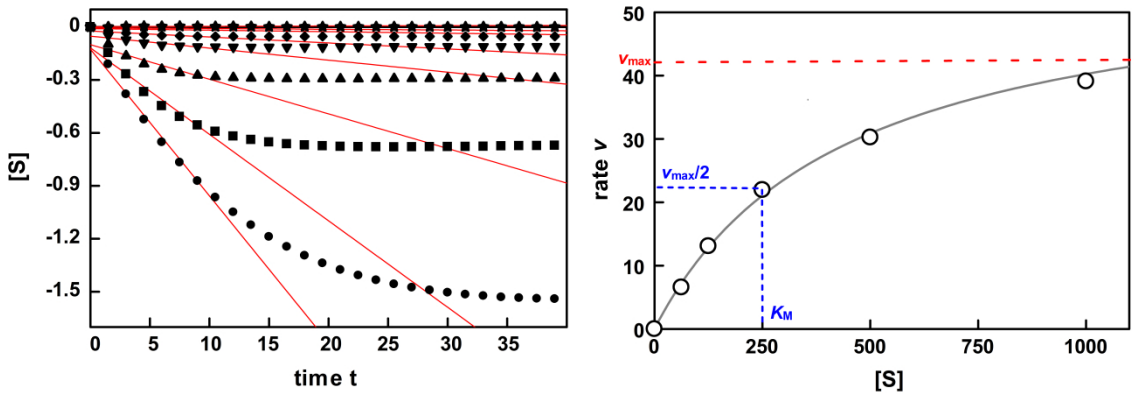

Scheme 6: The principle of steady-state enzyme kinetics.
Left panel: Depletion of a substrate at different concentrations [S] (●,■,▲,▼,◆,★) is followed over time. The slope of the linear portion of the resulting curves is determined (—). **Right panel:** The slopes are equivalent to the initial rates *v* and are plotted over the corresponding initial substrate concentration [S] yielding a Michaelis-Menten plot. The enzyme kinetic parameters v_{max} and K_M are determined by fitting the data via non-linear regression using a Michaelis-Menten model.

Fitting of these data using non-linear regression with equation 1 allows determination of the enzyme and substrate specific parameters k_{cat} and K_M and gives information about enzyme proficiency and substrate specificity. k_{cat} is a measure for the slowest, *i.e*. rate-limiting step of catalysis directly after formation of the productive enzyme-substrate complex. K_M is often interpreted as the apparent "affinity" of the substrate to the enzyme, but it is important to note that it represents a kinetic and not an affinity constant. As such, it is not necessarily identical to the dissociation constant K_D of the enzyme-substrate complex. However, the second order rate-constant k_{cat}/K_M is generally considered as most important because it gives information about substrate specificity, in other words the higher this value the more specific the enzyme.

Steady-state kinetics can be analyzed in different ways, *i.e.* by continuous or end-time readout with different assay probes, such as fluorescence or absorbance. Steady-state kinetics are also applicable, if an enzyme has more than one substrate. In this case, the co-substrate, *e.g.* SAM or NADH, is given in at least tenfold excess and the turnover of the other substrate is studied as described above. Moreover, enzyme inhibitors and their mode of action can be characterized using steady-state kinetics as well. Sometimes, also

the shape of the plot lends information about enzyme specific characteristics; a sigmoidal plot for instance can indicate that the enzyme exhibits cooperativity.

Yet, there are also limitations: Steady-state kinetics do not give information about fundamental rate constants and thus the obtained parameters alone do not allow to dissect a catalytic mechanism in detail and additional experiments are required, *e.g*. binding studies or computational methods.

3.1.2. Studying macromolecular interactions

Most cellular functions rely on macromolecular interactions such as protein-protein, protein-nucleic acid, protein-lipid or protein-small molecule interactions. Understanding the nature of these interactions provides crucial information on the molecular function of the binding partners. Various techniques exist for quantification of the interaction between different binding partners. Each method relies on different special characteristics of the studied molecules and two of these methods are presented in more detail below.

3.1.2.1. Isothermal titration calorimetry

The principle of isothermal titration calorimetry (ITC) is based on the direct measurement of the energetics (heat) of a non-covalent macromolecule-ligand interaction in solution. It allows quantitative characterization of all thermodynamic parameters of macromolecular complex formation such as molar enthalpy (ΔH) and binding/affinity K_A and, based on the relation depicted in equation 2, the molar Gibbs free energy (ΔG) as well as the molar entropy (ΔS):

$$\Delta G = -RT \cdot lnK_A = \Delta H - T \cdot \Delta S \qquad \textbf{(2)}$$

with

ΔG	Gibbs free energy in kcal mol^{-1}
R	ideal gas constant = 8.3144598 J K^{-1} mol^{-1} (= 1.9872036•10^{-3} kcal K^{-1} mol^{-1})
T	temperature in K
K_A	equilibrium constant of binding
ΔH	binding enthalpy in kcal mol^{-1}
ΔS	binding entropy in kcal mol^{-1}

The technique is widely used due to its high sensitivity towards even small changes in the composition of a solution and because it requires no additional labeling or immobilization of one interaction partner.

The experimental setup of a calorimeter (Scheme 7 left panel) constitutes of a sample cell (S) and a reference cell (R) enclosed in an adiabatic jacket. The cells are connected via a temperature sensor, which monitors the temperature difference between them.

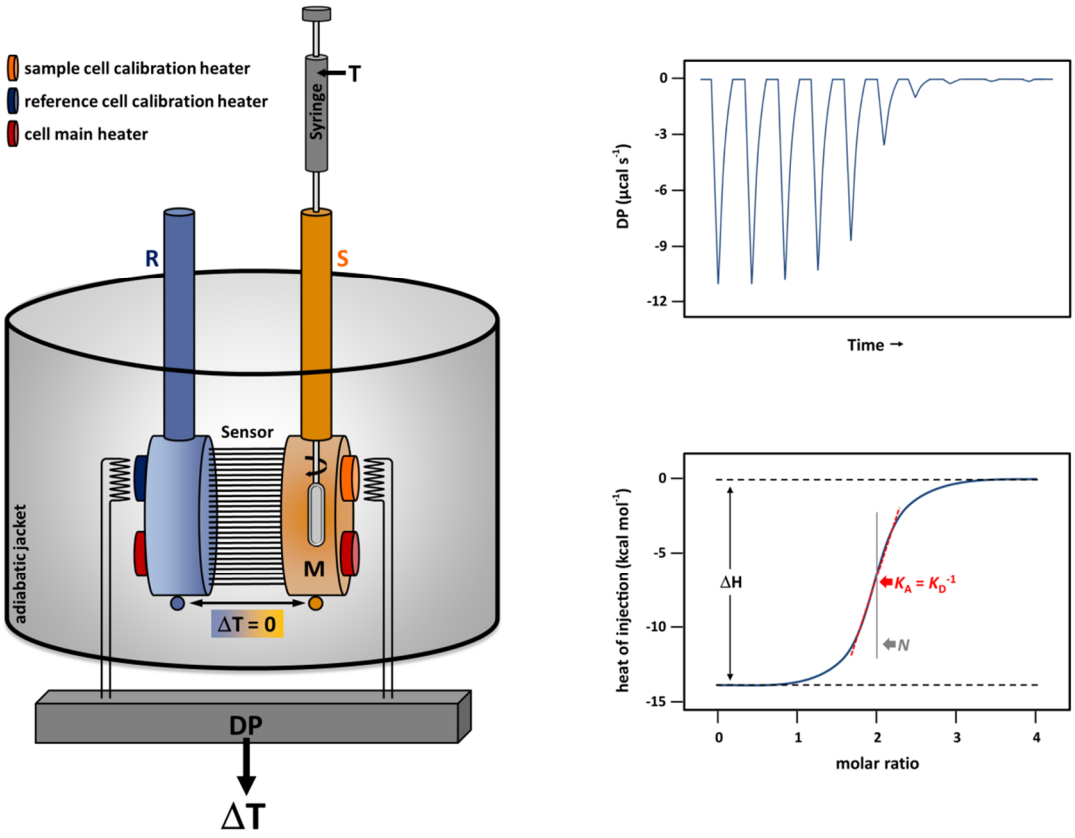

Scheme 7: The principle of isothermal titration calorimetry.
Left panel: An isothermal titration calorimeter consists of an adiabatic jacket, in which the sample (S) and the reference cell (R) are enclosed. Both cells are kept at a constant temperature via the cell main heater (red). The sample cell contains the macromolecule **M** at a certain concentration. Under constant stirring, the titrant **T**, typically ten-times the concentration of the macromolecule, is added to the sample cell via defined volume injections from a syringe. Complex formation **MT** either generates or absorbs heat in the sample cell causing a temperature difference between the sample and the reference cell. To compensate this temperature difference ΔT (ΔT = 0) a differential power **DP** is applied. **Top right panel:** For each individual injection, the DP that is used to keep both cells at equal temperature is recorded over a period of time. **Bottom right panel:** The integral of the DP is plotted against the molar ratio of macromolecule and titrant in the sample cell. The amplitude of the resulting sigmoidal binding curve yields the binding enthalpy ΔH and the position of the inflection point gives information about the binding affinity constant K_A and binding stoichiometry *N*.

At the onset of an ITC experiment both cells are heated to the experimental temperature T, while the reference cell is filled with water or buffer and the sample cell contains the macromolecule M. During the experiment, a defined amount of titrant T (small molecule ligand, protein, or nucleic acid) is added to the sample cell in a series of individual injections. For each injection, the heat that is generated or absorbed upon solvation and especially complex formation is recorded by the differential power (DP) that is applied to keep the temperature difference between the sample and neighboring reference cell

equal to zero (Scheme 7 top right panel). The integral of this power is plotted against the concentration of the titrated ligand versus the macromolecule, *i.e.* their molar ratio. The resulting curve contains information about the binding enthalpy ΔH, which is equal to the amplitude of the curve, as well as the binding affinity K_A and stoichiometry *N* that can be deduced from the position of the inflection point and the shape of the curve (Scheme 7 bottom right panel). The more data points describe this curve, the more accurate the corresponding parameters can be determined. This relation is described by the c-value, which links the macromolecule concentration used in the experiment (M_0) to the expected K_A (= K_D^{-1}; equation 3) and the stoichiometry of complex formation *N*:

$$c = \frac{[M_0]}{K_D} \cdot N \qquad \textbf{(3)}$$

with

$[M_0]$ total/starting concentration of the macromolecule M
K_D dissociation constant

Reliable parameters can typically be obtained with a c-value in the range of 10 to 100.

3.1.2.2. Microscale thermophoresis

Microscale thermophoresis (MST) is a method that records the directed movement of particles, in this case macromolecular complexes, along a defined temperature gradient. Thermophoresis is dependent of the size, charge and hydration shell of the analyzed particle and is thus very sensitive to changes in one or all of these molecular characteristics *e.g.* upon ligand binding (for review Jerabek-Willemsen *et al.*, 2011).

The experimental setup (Scheme 8 left panel) consists in an array of capillaries filled with the analytic solution comprised of a fluorescence-labeled binding partner at constant concentration and its potential interaction partner as serial dilution. Irradiation of these capillaries with an infrared laser creates a locally defined, very steep temperature gradient along which the particles move either towards or out of the heat focus (Scheme 8 top right panel). Typically, the fluorescence signal of an intrinsic (*e.g*. tryptophan) or chemically introduced/linked fluorophore serves as an experimental probe to record movement of the molecules (Scheme 8 bottom right panel).

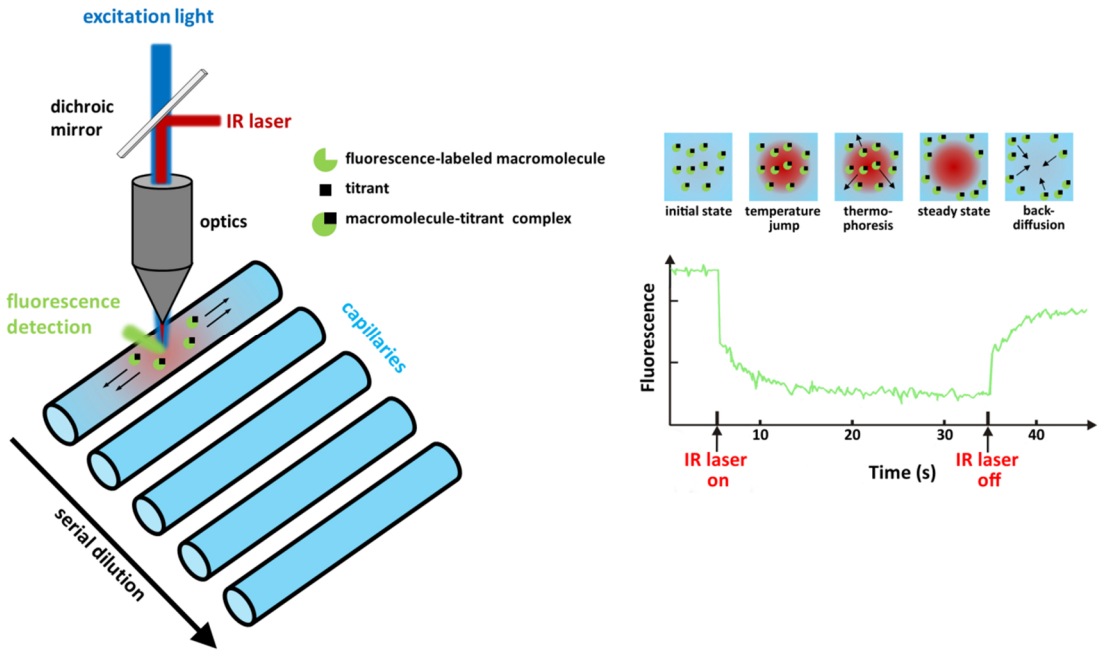

Scheme 8: The principle of microscale thermophoresis.
Capillaries containing a fluorescent-labeled macromolecule (green) at constant concentration and a serial dilution of the interaction partner (■) are irradiated with an infrared laser. This induces a microscopic, steep temperature gradient. The movement of the molecules along the gradient depends on their size, charge, and hydration shell, as such free ligands or macromolecules show a different thermophoretic behavior than macromolecule-ligand complexes. As one of the interaction partners is containing a fluorophore, its movement can be followed using fluorescence spectroscopy. This signal plotted against the ligand/titrant concentration allows determination of the binding parameters. Figure adapted from Jerabek-Willemsen *et al.*(2011).

As mentioned before, macromolecular interactions such as ligand binding influence the size, charge and hydration properties of a particle and hence will lead to differences in the thermophoretic profile between a ligand-bound and unbound state. This information, *i.e.* the fraction of bound [L_B] and free ligand [L_F], together with the knowledge of the concentration of the interaction partners in a titration experiment can be used to derive specific binding parameters from fitting the data to a two-state model as shown in equation 4:

$$[L_B] = \frac{C \cdot [L_F]}{K_D + [L_F]} + B \qquad \textbf{(4)}$$

with

[L_B]	fraction/concentration of ligand bound to the macromolecule
C	capacity/total amplitude of binding ≈ [L_B]/[L_F]
[L_F]	fraction/concentration of free/unbound ligand
K_D	dissociation constant
B	background = thermophoresis in the absence of any ligand

3.1.3. Circular dichroism spectroscopy

Circular dichroism (CD) spectroscopy is a method that allows determination of the secondary structure composition of a protein in solution. The basic principle of this technique is the differential absorbance of left and right circularly polarized light (CPL) by chiral molecules. Since chirality is independent of the orientation of the molecule, randomly oriented samples such as proteins in solution can be measured.

Circularly polarized light arises from the superposition of two linearly polarized electromagnetic waves with perpendicular oscillation and a phase difference of $\pi/2$. The electric field vector of the resulting wave rotates with constant amplitude either clockwise (right CPL) or counterclockwise (left CPL) in the propagation direction of the electromagnetic wave (Bulheller *et al.*, 2007; Figure 5 left panel). When such a circularly polarized wave hits a chiral molecule, the electrons within this molecule absorb the energy and undergo transition from the ground to an excited state (Garab and van Amerongen, 2009). The extent of this excitation (absorbance) depends on the handedness of the polarization (left or right-handed), on the wavelength as well as on the geometry of the chiral molecule.

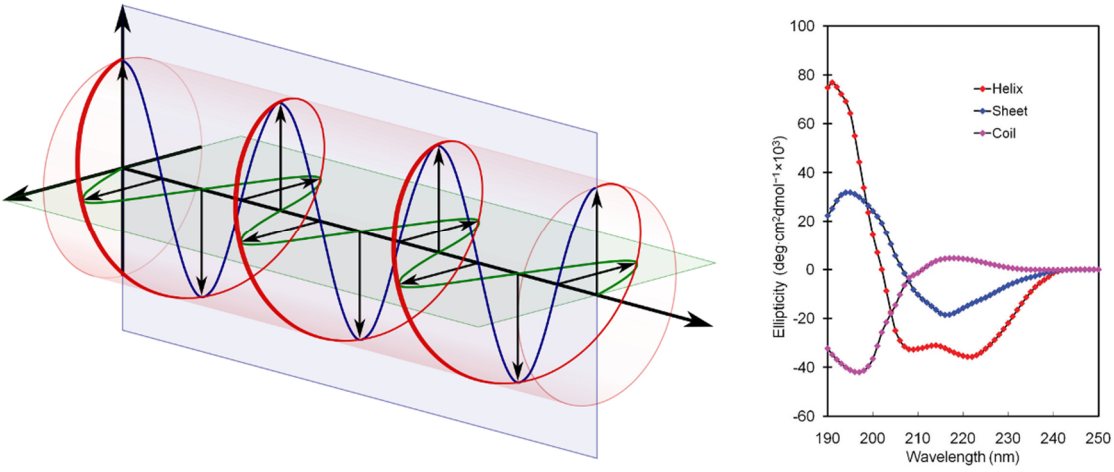

Figure 5: The principle of circular dichroism spectroscopy.
Left panel: Circularly polarized light originates from two perpendicularly oscillating electromagnetic waves that are superposed with a phase difference of $\pi/2$. The resulting electromagnetic wave oscillates with constant amplitude, but the electric field vector rotates in direction of the wave propagation either clockwise (right-handed) or counterclockwise (left-handed). Figure reproduced from https://en.wikipedia.org/wiki/Circular_polarization (2017). **Right panel:** When a circularly polarized wave interacts with proteins in solution, the difference in absorbance of left and right circularly polarized light plotted against the wavelength gives characteristic spectra. The shape of these spectra depends on the geometry of the interacting chiral molecule. In proteins, this geometry is mainly determined by the peptide bond angles and hence different secondary structure elements yield specific spectra. Figure reproduced with permission from Biomolecular Crystallography by Bernhard Rupp, © 2009-2014 Garland Science/Taylor & Francis LLC (Rupp, 2009).

In a typical CD-experiment, the difference in absorption of left and right CPL is recorded over a range of wavelengths - typically ultraviolet (UV) light in the range from 190 to 250 nm. This difference, precisely the difference in the extinction coefficients Δε between left (ε_L) and right (ε_R) CPL is plotted against the corresponding wavelengths and yields the characteristic spectra (Bulheller *et al*., 2007; Figure 5 right panel). As mentioned before, the difference in absorbance also depends on the geometry of the chiral molecule, in proteins this is determined by the specific angles of the peptide backbone and thus explains why different types of secondary structure elements yield specifically shaped CD-spectra (Whitmore and Wallace, 2008; Figure 5 right panel).

3.1.4. Principles of protein X-ray crystallography

The molecular function of a protein is closely linked to its structure. For this reason, determination and analysis of this structure can help to decipher and understand the biological function of a protein. In order to study a molecular structure in detail, information about the precise spatial organization of its atoms is necessary. A way to determine the three-dimensional structure of a protein is X-ray crystallography.

3.1.4.1. Protein crystallization

At the beginning of each macromolecular crystallography experiment stands the crucial step of crystallization. Typically, protein of high purity (≥ 95 %) and in a reasonable high concentration (~10 - 20 mg/mL) is needed to yield initial protein crystals. Protein crystallization however, is an unpredictable process that depends on many variables. In addition to the quality and concentration of the protein sample, a variety of external parameters such as temperature, pH and composition of the precipitant solution influence the desired phase transition of the protein from the liquid to the solid phase. Hence, a successful crystallization experiment often requires extensive screening and optimization to obtain diffraction quality crystals.

The basic principle of protein crystallization is the stepwise reduction of protein solubility in a closed system. To this aim, a protein solution is mixed with precipitants to increase the protein concentration up to the solubility limit leading to formation of a supersaturated, metastable solution (Figure 6 left panel). Phase separation occurs and, if

so-called nuclei form, a controlled self-assembly of protein molecules into a regular and periodic arrangement, in other words crystallization, might be initiated. Different techniques exist to facilitate this phase transition; the most common are vapor-diffusion via sitting- or hanging drop, microbatch, or microdialysis (Figure 6 top right panel).

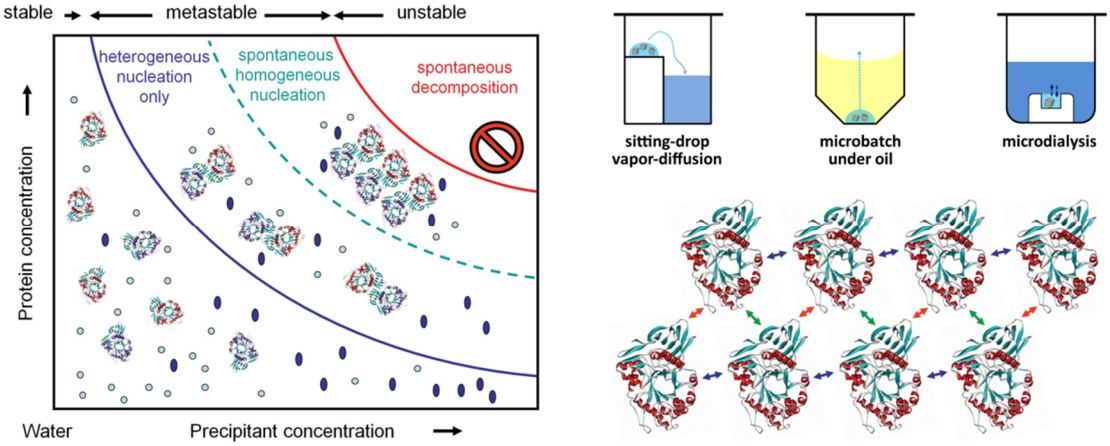

Figure 6: The basic principles of protein crystallization.
Left panel: Different nucleation zones in the protein crystallization diagram. Precipitant molecules are shown as **dark blue** ovals and water molecules as **light blue** circles. At high protein and/or precipitant concentration, the crystallization solution reaches the metastable phase. In this region of the diagram, spontaneous nucleation is only possible at high supersaturation. At lower supersaturation, crystal growth can be supported; however, nucleation requires external seeds. **Top right panel**: Schematic representation of the main macromolecular crystallization methods. **Bottom right panel**: Visualization of intermolecular contacts in a protein crystal. Three different types of interactions are symbolized by **green**, **orange**, and **blue** arrows in this two-dimensional crystalline arrangement. Figure adapted and reproduced with permission from Biomolecular Crystallography by Bernhard Rupp, © 2009-2014 Garland Science/Taylor & Francis LLC.

The former constitutes mixing the protein with precipitant solution typically in a 1:1-ratio. This crystallization drop of about 100 nL up to a few µL, either hanging from a siliconized cover-slip or sitting on a socket, is placed over a reservoir containing the precipitant solution. As the crystallization drop contains only half the precipitant concentration of the reservoir, the closed system tends to compensate this difference by evaporation of water and other volatile ingredients from the drop into the reservoir and thus the concentration of the protein-precipitant mixture increases.

The second method of microbatch crystallization is also based on mixing the protein with precipitant solution, both at high concentration, which leads to immediate formation of a supersaturated solution. In this case, the crystallization drop is enclosed in an isolated environment under a layer of oil. Sometimes, a water permeable oil is used, which allows additional diffusion of water or other organic solvent molecules through the oil phase and hence lead to further concentration of the drop until the metastable phase is reached.

The third technique of microdialysis simply constitutes an exchange of solvent via a membrane. The protein solution is mixed with a precipitant solution, typically of low precipitant concentration, and placed into a microdialysis button. The button is sealed with a membrane that allows only diffusion of water or other small molecules such as ligands. The large proteins as well as high molecular weight polyethylene glycols (PEGs) cannot pass this barrier. The button is placed in a reservoir of high precipitant concentration and, similar to the vapor-diffusion method, the closed system tends to reach equilibrium by diffusion of water from the inner compartment to the outer one. This in turn leads to an increase of the protein concentration in the inner compartment. In all cases, crystal growth is followed over days or weeks until preferably single crystals of regular shape are obtained.

As crystallization is a dynamic process, a grown crystal is always in equilibrium with the supersaturated protein solution and the stability of this equilibrium can be described by the mean molar Gibbs free energy of a system $\bar{G}$ and the molar fraction of the protein x_1 (equation 5):

$$\left(\frac{\partial^2 \bar{G}}{\partial x_1^2}\right) > 0 \qquad \textbf{(5)}$$

As long as this condition is true, the metastable phase remains in equilibrium, but if the protein concentration increases further, the solution becomes highly supersaturated and decomposes spontaneously. At this point, crystallization is no longer possible. If the system however remains in the metastable, supersaturated state, spontaneous formation of crystallization nuclei is possible. In fact, the high concentration of protein molecules multiplies the probability of collisions in a proper orientation and thus enables formation of energetically favorable interactions between them*, i.e.* nucleation sites can form. The bigger these nucleation sites are, the higher their stability and hence the better attachment of additional molecules. As proteins are irregular structures only weak and few, *i.e.* 3-12, intermolecular contacts are typically formed over a surface area of about 200 to 500 Å² (Figure 6 bottom right panel). This causes formation of large voids filled with precipitant solution. In average, these solvent channels make up ~ 50 % of the protein crystal and explain why protein crystals are rather soft in comparison to salt crystals. Nevertheless, these large channels also allow soaking of a protein crystal with different

ligands or even heavy metal derivatives for *de novo*-phasing (see below). Despite their weak character, the intermolecular interactions between protein molecules are very specific and are typically constituted of hydrogen bonds, salt bridges, dipole-dipole interactions, as well as van-der-Waals or hydrophobic interactions. In order to enable periodic assembly of the protein molecules, it is important that the sample is very homogenous to ensure the same interaction scaffold and formation of periodic interactions across the crystal. Flexible surface loops or disordered termini as well as partially degraded protein might represent a problem for crystallization and thus different protein constructs lacking these elements might be necessary for successful crystallization. However, it is also possible that these flexible structure elements become fixed in one specific conformation in the crystal due to crystal packing (specific interactions) and thus present only one of many possible native conformations (in solution). In contrast, the protein core is usually preserved in its native conformation.

3.1.4.2. X-ray diffraction and data collection

Single, regularly shaped protein crystals of about 50 to 500 µm size are generally considered suitable for diffraction experiments. The crystals are harvested from the crystallization drop using a nylon-loop and immediately flash-cooled in liquid nitrogen. Depending on the composition of the crystallization solution, addition of a cryo-protectant might be necessary to avoid formation of crystalline ice as this could lead to destruction of the periodic arrangement of the crystal and diminish its diffraction quality. Typical cryo-protectants are glycerol, sugars, alcohols, or short-chain PEGs. Once the protein crystal is preserved in this way, it can be mounted on a multi-angle goniometer head in front of the X-ray source (Figure 7). During a diffraction experiment, the crystal is constantly cooled by a nitrogen gas stream at 100 K. The X-ray source generates a focused X-ray beam of a defined wavelength that interacts with the crystal causing a characteristic diffraction pattern.

X-rays are electromagnetic waves with energies approximately 10^4-times higher than visible light. In other words, their wavelengths range from 0.1 to 100 Å and as such are of similar dimension as chemical bonds, allowing analysis of molecular details of matter.

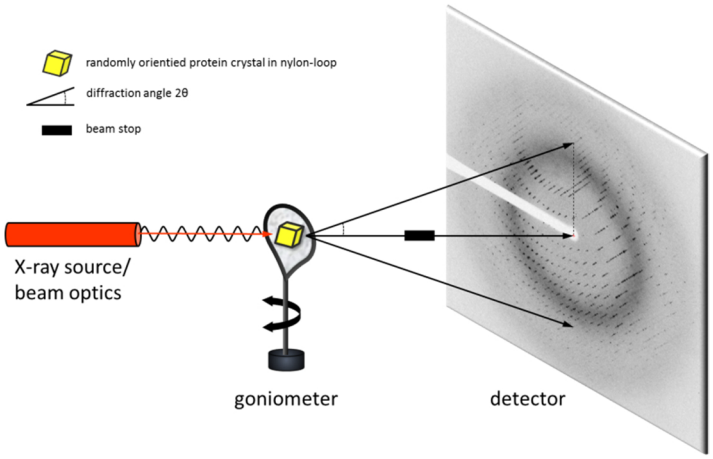

Figure 7: Experimental setup of a macromolecular X-ray diffraction experiment.
A cryo-protected protein crystal harvested from the crystallization drop using a nylon-loop is mounted on a multi-angle goniometer in front of an X-ray source. While the crystal is constantly rotated, the X-ray source generates the incident X-ray beam, which is partially diffracted by the crystal. The reflections are recorded as diffraction images on a detector. As the intensity of the undiffracted incident beam is very high, a beam stop prevents damage of the detector.

The principle of X-ray diffraction is the interaction of an electromagnetic wave with regularly arranged matter, *e.g*. a protein crystal that is built up by small identical unit cells in a periodic arrangement. Within these unit cells, the protein atoms are located in a three-dimensional lattice that is defined by the vectors a, b, c and the angles between these vectors α, β, γ. The atom positions within this lattice (relative to an origin) are described with the coordinates x, y, z (Figure 8 left panel). When X-rays hit a protein crystal, the electromagnetic waves interact with the electrons of the individual, periodically arranged atoms, inducing their oscillation. Consequently, this leads to emission of electromagnetic waves of the same frequency (elastic scattering), but with phase differences compared to the incoming wave. As electrons move within discrete orbitals (the electron cloud), only electrons in the right position r can interact with the waves. This can be described as a probability distribution (electron density ρ(r)) and the amplitude of the scattered wave depends on this density. Moreover, depending on the distance between the atoms, the emitted waves will display constructive or destructive interference and only in the former case diffraction can be observed. Constructive interference however will only occur in certain angles as it is described by the Bragg's law (equation 6):

$$\lambda = 2d_{hkl} \cdot sin\theta \quad \textbf{(6)}$$

with

n positive integer
λ wavelength of incident electromagnetic wave
d_{hkl} path difference between hypothetical lattice planes with the Miller indices *hkl*
θ diffraction angle

In this equation, diffraction is regarded as a reflection from sets of hypothetical parallel planes rather than from single periodically arranged atoms or their electrons (Figure 8 top right panel). The lattice planes divide the crystal in a periodic way and each set of planes can be described by three vectors **h**, **k**, **l**, the so-called Miller indices, and their interplanar spacing $d_{\mathbf{hkl}}$. Diffraction occurs if the path difference between these planes is a multiple positive integer of the wavelength. This leads to two deductions: First, as λ is known and the diffraction angle can be measured, the distance d_{hkl} between the lattice planes can be calculated. Second, this relation limits the minimum distance between the planes and hence the maximum resolution to d_{min} = ½ λ. However, as chemical bond lengths are in the range of 1 to 2 Å even in-house X-ray sources with $Cu_{K\alpha}$-radiation of a wavelength of 1.54 Å are sufficient for structure determination. Modern synchrotrons, in addition to their higher brilliance compared to in-house sources, even have tunable wavelength, usually optimized around 1.0 Å, and thus allow better theoretical resolution limits.

So far, all theoretical considerations were made in real space, however in order to fully understand a diffraction pattern one has to comprehend another theoretical construction, the reciprocal space. The reciprocal space is inversely proportional to the real space, *i.e.* $d^*_{\mathbf{hkl}} = 1/d_{\mathbf{hkl}}$. In the reciprocal space, the Bragg's law can be illustrated with the mathematical construction of a three-dimensional sphere centered on the crystal with radius r = 1/λ, the so-called Ewald's sphere (Figure 8 bottom right panel). The origin of the reciprocal lattice is positioned at the intersection of the sphere and the exiting direct X-ray beam. In this construction, for each reciprocal lattice point laying on the surface of the sphere (highlighted as red dots in Figure 8 bottom right panel), the Bragg's law is true and constructive interference occurs, appearing as a reflection on a detector. In other words, the diffraction pattern is a projection of the three-dimensional reciprocal lattice and the position of the reflections is related to the diffraction angle θ. Each reflection can be described in relation to the Miller indices *hkl* of the reciprocal lattice planes. The central

reflection (h, k, l) = (0, 0, 0) is the origin, but it can never be measured since it is masked by the incoming X-ray beam.

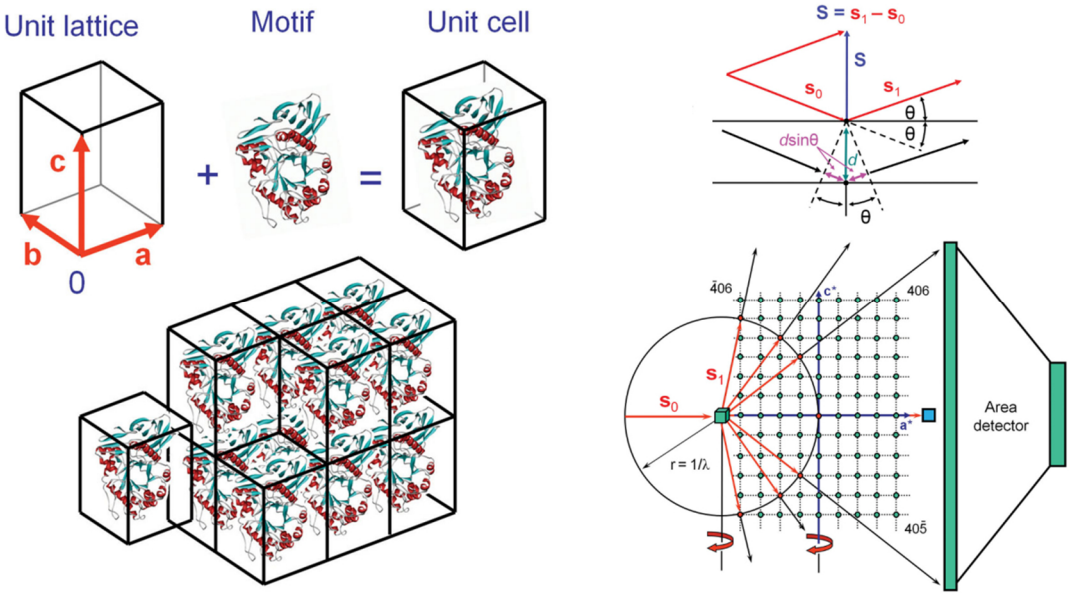

Figure 8: The crystal organization and principles of X-ray diffraction.
Left panel: The unit cell, which is translationally stacked to build the crystal, is a combination of a unit lattice that is defined by its three vectors a, b, c and their associated angles α, β, γ, and a motif. **Top right panel**: Graphical representation of the diffraction of X-rays as defined by the Bragg's law. X-ray diffraction is represented as reflection on a set of hypothetical planes in a crystal. The path difference between scattered waves is equal to 2d·sinθ, which must equal a multiple integer of the wavelength λ for maximum constructive interference. **Bottom right panel:** Visualization of the Bragg's law in reciprocal space using the Ewald construction. The conditions for constructive interference (**red** arrows) are met, when reciprocal lattice points are located on the Ewald's sphere of radius 1/λ that is centered on the crystal. During data collection, the crystal is rotated, thus other lattice points will cross the Ewald's sphere and produce reflections on the detector. Figure adapted and reproduced with permission from Biomolecular Crystallography by Bernhard Rupp, © 2009-2014 Garland Science/Taylor & Francis LLC.

In a diffraction experiment, the crystal is usually rotated within the beam, which translates in satisfying the Bragg's law for other reciprocal lattice points when they cross the Ewald's sphere. A dataset represents a total rotation of the crystal from 100 to several 100 degrees, which are split into frames, typically of 0.1 to 1 degree rotation.

3.1.4.3. Data processing and structure determination

The desired information from a macromolecular X-ray crystallography experiment is the location of the protein atoms/electrons within the crystal (real space). In order to reconstitute this electron density ρ(r) from the diffraction pattern, first the position and then the intensity of all reflections have to be determined.

Having a diffraction dataset at hand, the first step of data processing consists in so-called indexing, which aims at determining the unit cell parameters as well as the space group

of the crystal. The space group defines the internal symmetry of a crystal lattice and describes the reconstruction of the unit cell starting from its smallest element, the asymmetric unit, by employing rotational and/or translational symmetry operators. In three-dimensional space, 14 crystal lattices, the so-called Bravais lattices exist. These are obtained by combining one of the seven crystal systems (triclinic, monoclinic, orthorhombic, tetragonal, hexagonal, trigonal, and cubic) with one of the centering types, which identify the locations of the lattice points in the unit cell (Figure 9). In the most simple case, the lattice points correspond to the corners of the unit cell and this centering is called primitive (P). Other centering types such as face (F) or body (I) centered also exist. Although, there are 230 space groups possible, in macromolecular crystallography, due to the chiral character of biomolecules, only 65 space groups are observed.

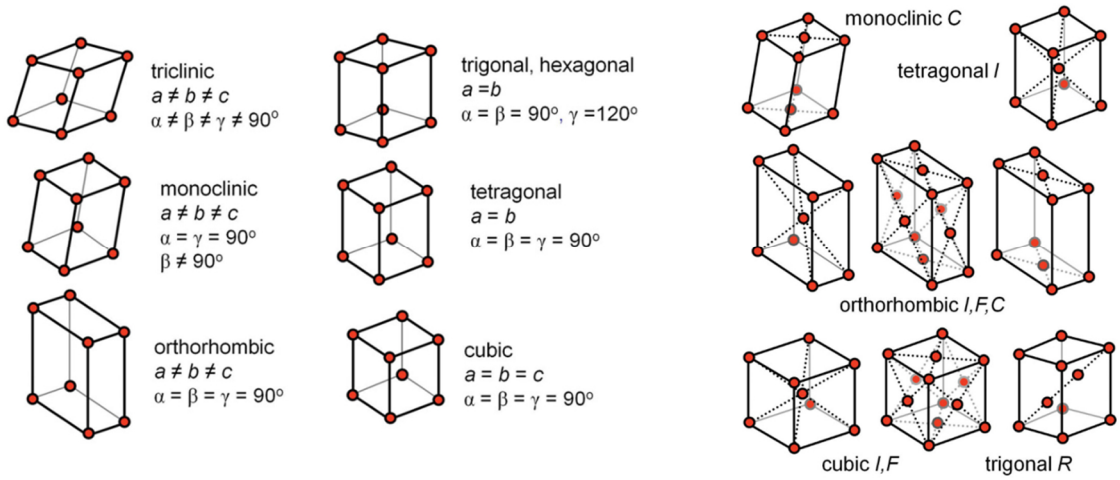

Figure 9: Crystal systems and the corresponding Bravais lattices.
Left panel: The six primitive crystal systems with their characteristic unit cell parameters**. Right panel:** Symmetry groups with non-primitive centering types, which, together with the six primitive unit cells, complete the 14 Bravais lattices. Figure adapted and reproduced with permission from Biomolecular Crystallography by Bernhard Rupp, © 2009-2014 Garland Science/Taylor & Francis LLC.

For indexing, the relative positions of the reflections in a reduced set of the diffraction data as well as experimental parameters such as crystal-to-detector distance, wavelength, and position of the incident beam are used to obtain the unit cell parameters, to define the orientation of the crystal and to propose possible space groups. This will allow the attribution of the Miller indices *hkl* for each reflection and, more importantly, to predict the position of every reflection in the dataset.

With this knowledge, data processing software will be able to proceed with the second step, data integration. In brief, the software defines a zone at the location of a predicted

reflection, in which the intensity of this reflection is measured relative to the background. Given the internal symmetry, a reflection will be measured multiple times in different orientations of the crystal in the beam.

Finally, the last step of data processing constitutes the reduction of the dataset to obtain one intensity value (with its error) for each reflection. Since the intensity of a reflection does not only depend on the content of the unit cell, but also on the morphology of the crystal or the intensity of the beam, which can vary over time, a so-called scaling procedure is applied to obtain an "averaged" value of the intensities.

However, the task to reconstruct the electron density of the molecule(s) composing the crystal from these intensities remains. To this end, one has to consider that every scatterer in a unit cell influences the intensity of each recorded reflection, *i.e.* each atom contributes to every reflection. Hence, the scattering function $\mathbf{F_S}$ of a crystal is the sum of individual atomic scattering factors (equation 7):

$$\boldsymbol{F_S} = \sum_{j=1}^{atoms} f_{s,j}^{0} \cdot e^{2\pi i \boldsymbol{S} \boldsymbol{r}_j} \qquad \textbf{(7)}$$

with

$\mathbf{F_S}$	scattering function
$f_{s,j}^{0}$	wavelength independent atomic scattering factor of the atom j
S	general scattering vector
$\mathbf{r}_j$	position vector of the atom j

In reciprocal space, equation 7 can be rearranged as a function of the index vector **h** to the so-called complex structure factor $\mathbf{F_h}$ (equation 8):

$$\boldsymbol{F_h} = \sum_{j=1}^{atoms} f_{s,j}^{0} \cdot e^{2\pi i \boldsymbol{h} \boldsymbol{x}_j} \qquad \textbf{(8)}$$

with

$\mathbf{F_h}$	the complex structure factor, *i.e.* a vector representing the diffracted X-rays in a given direction **h**
$f_{s,j}^{0}$	wavelength independent atomic scattering factor of the atom j
h	reciprocal lattice vector giving the direction of scattering as **hkl**
$\mathbf{x}_j$	position of the atom j in fractional coordinates xyz

This complex structure factor is the Fourier transform (FT) of the electron density ρ(**x**). In order to describe the content of the whole unit cell, the electron density is integrated over its complete volume (V), *i.e.* at every position x, y, and z, while the scattering vectors in every direction of the reciprocal space (**h**, **k**, and **l**) are considered (equation 9):

$$\rho(xyz) = \frac{1}{V}\sum_{\boldsymbol{h}}\sum_{\boldsymbol{k}}\sum_{\boldsymbol{l}} \boldsymbol{F_{hkl}} \cdot e^{-2\pi i(\boldsymbol{h}x+\boldsymbol{k}y+\boldsymbol{l}z)} \quad \textbf{(9)}$$

with

ρ(xyz) electron density at grid point xyz
V volume of the unit cell
$\mathbf{F_{hkl}}$ the complex structure factor in direction **hkl**

Using the Euler relation $\boldsymbol{F_{hkl}} = F_{hkl} \cdot e^{i\alpha_{hkl}}$, which separates the complex structure factor $\mathbf{F_{hkl}}$ into an explicit amplitude term F_{hkl} and a phase angle term α_{hkl}, equation 9 can be rewritten into its final form (equation 10):

$$\rho(xyz) = \frac{1}{V}\sum_{\boldsymbol{h}}\sum_{\boldsymbol{k}}\sum_{\boldsymbol{l}} F_{hkl} \cdot e^{i\alpha_{hkl}} \cdot e^{-2\pi i(\boldsymbol{h}x+\boldsymbol{k}y+\boldsymbol{l}z)} \quad \textbf{(10)}$$

Under this form, the density summation explicitly includes both, the structure factor amplitude F_{hkl} and its associated phase α_{hkl}. While the former can be determined from the measured intensities I_{hkl}, as these are proportional to the structure factor amplitude ($I = |F_h|^2$), the phases, which carry most of the structural information, are lost during the physical process of diffraction data collection. This gives rise to the crystallographic phase problem.

A variety of methods has been developed to obtain the phase information. Nowadays, the most commonly used one is the so-called molecular replacement (MR). Since it is assumed that proteins with at least 30 % sequence identity share similar folds, the structure of a known protein can be used as initial phasing model. To obtain an initial approximation of the phase, it is necessary to position the model in the unit cell of the unknown structure. This is achieved in two consecutive steps. The first aims at orienting the model in the unit cell through rotation to find then its exact position using a translational search. Once the model is positioned, it is indeed possible to derive the phase information that, combined with the intensities of the unknown structure, is necessary to calculate initial electron density maps.

Although the number of structures available for MR is constantly increasing, this method is not always successful. In such cases, experimental phasing is employed. This typically involves introduction of heavy atoms or markers in the crystal either by derivatization of the protein during expression with *e.g*. selenomethionine or by co-crystallization or soaking with heavy metals, such as mercury, lead or gold. The process of phasing will thus

be simplified to the resolution of the "simpler" structure of the heavy atom(s), or so-called substructure. One method is the isomorphous replacement (SIR/MIR = single/multiple isomorphous replacement). Since structure factors contain contributions from every atom of the unit cell, it is conceptually possible to decompose a heavy atom derivative crystal (PA) as the sum of the protein atoms (P) and of the heavy atom(s) (A), *i.e.* $\mathbf{F_{PA}} = \mathbf{F_P} + \mathbf{F_A}$ (Figure 10A).

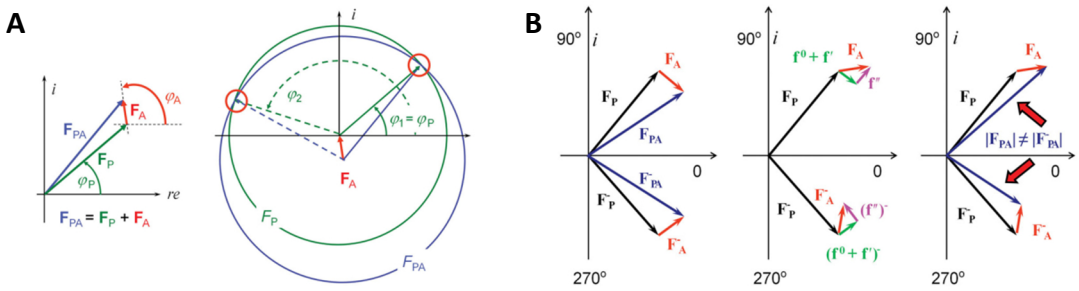

Figure 10: Basic principles of experimental phasing.
A Graphical solution of the phasing equations. The left panel shows how the complex structure factors for protein (**F_P**), derivative (**F_{PA}**) and heavy atom (**F_A**) are related for a reflection *hkl*. Intensity measurements only reveal the magnitude of the structure factors for the derivative F_{PA} and the native F_P, but from the difference data, the position(s) of the heavy atom(s) can be determined. Therefore, the entire complex structure factor for the heavy atom **F_A** is known, and the two possible solutions (○) for the protein phase angle can be determined for each reflection by the graphical procedure shown on the right panel. However, only one phase angle (φ) will be correct, the other one not. **B** Breakdown of the Friedel's law through anomalous scattering. The vector **F_P** represents the partial sum of all non-anomalous contributions and the remaining vectors are the contributions from the anomalously scattering atom, **F_A**. The real and imaginary components of **F_A** are indicated in **green** ($f^0 + f'$) and **magenta** (f'') respectively. When the indices *hkl* are inverted to *–h-k-l* as indicated by the "minus" superscripts, normal and anomalous scattering contributions become mirrored across the real and imaginary axis respectively. Consequently, in presence of anomalous scattering contributions, Friedel's law (*i.e.* $\mathbf{F_{hkl}} = \mathbf{F_{-h-k-l}}$) breaks down and the structure factor amplitude, and thus the intensities of Friedel pairs become different. Figure adapted and reproduced with permission from Biomolecular Crystallography by Bernhard Rupp, © 2009-2014 Garland Science/Taylor & Francis LLC.

By comparing the intensities obtained from a native crystal to the ones obtained from an isomorphous heavy metal derivative, it is possible to extract merely the contribution of the heavy atom(s). From this information, phasing programs will try to solve the heavy atom substructure, which consists in finding its location (or sites) in the asymmetric unit. It is achieved by using Patterson and/or direct methods. When the substructure is known, it is possible to derive phase information, which will be used for producing initial electron density maps. SIR/MIR methods can be applied with X-rays of any wavelength, however, one of the limitations is the necessity for isomorphism between the two crystals, *i.e.* both native and derivative crystals must belong to the same space group and their unit cell parameters not differ by more than a few percent.

The other experimental phasing method is called SAD/MAD, which stands for single or multiple wavelength anomalous dispersion. It uses a particular phenomenon of "heavy" atoms, which absorb X-rays at a certain wavelength characteristic for the element (absorption edge) and reemit X-rays with a phase difference, thus influencing the intensity and phase of the diffracted beam. Indeed, at a wavelength corresponding to the absorption edge of the heavy atom, the atomic scattering factor (f^0) will be composed of two additional components, f' and f", the dispersive and anomalous scattering factors dependent of the wavelength (Figure 10B). The dispersive contribution leads to a difference in the intensities measured at different wavelength. The anomalous component is imaginary and as such has a different phase than the normal and dispersive contributions. Consequently, within a diffraction dataset collected at the characteristic absorption edge, the so-called Friedel's law owing to which $\mathbf{F_{hkl}}$ and $\mathbf{F_{-h-k-l}}$ have equal amplitudes but opposite phases is no longer valid. Various strategies can then be used and combined to obtain initial phase information. One is based on the comparison of the diffraction data (intensities) collected at different wavelength (MAD methods), the other on the comparison of the intensities of Friedel reflection pairs measured at the absorption edge of the heavy atom (SAD). Once again, the goal of the phasing program is to solve the substructure of the heavy atom that will provide an approximation of the phases for calculating initial electron density maps. These methods require access to X-ray sources with tunable wavelength such as synchrotron facilities. However, all information can be obtained from a single crystal and thus isomorphism is no longer limiting. Strategies, which combine both isomorphous replacement and anomalous scattering approaches (SIRAS/MIRAS) are also possible.

At this step, further techniques aim at improving the initial phases and are commonly termed density modification. One of the most powerful is called solvent flattening and is based on the fact that protein crystals are in average composed of 50 % of disordered solvent and, as such, large regions of the asymmetric unit have no electron density. The density modification program will identify these "empty" regions and proceed with the "flattening" by optimizing the phase so that $\rho(\mathbf{x})$ is equal to zero in these regions. In addition, the asymmetric unit of most protein crystals contains more than one copy of the macromolecule. These molecules are related to each other by so-called non-

crystallographic symmetry and it is possible to use this information to modify the phase and significantly improve the quality of the initial electron density map.

3.1.4.4. Model building, refinement and validation

Once an electron density map of an unknown structure is obtained, it has to be interpreted in terms of the atomic positions giving rise to this density. To this aim, an initial structural model is placed and subsequently fitted into in the electron density. For each atom at least four different characteristic parameters will be refined, the three positional coordinates (x, y, z) and its temperature factors (B-factors). The latter accounts for the displacement of an atom from its mean position that can be caused by thermal vibrations or other dynamic effects. It can also arise from static disorder, *i.e*. the fact that each atom occupies slightly different positions in different unit cells that are averaged.

Both, automated and manual model building take advantage of prior knowledge of the correct protein sequence and of fundamental geometrical properties of the building blocks including the length of a chemical bond, the angle between these bonds, as well as non-bonded interatomic distances or van der Waals radii. Furthermore, the planarity of the peptide bond and its stereo-chemical restraints in secondary structure elements like α-helices or β-strands are taken into account.

In practice, the electron density is traced by building consecutive amino acids into the map. Depending on the resolution, different levels of molecular details are visible. At low resolution (~4 Å) only the peptide backbone, *i.e.* an array of amino acids without characteristic side chains can be assembled. With increasing resolution, these individual amino acid side chains can be identified. Potentially even their different rotameric conformations can be built and the corresponding occupancies attributed.

As mentioned earlier in this section (paragraph 3.1.4.1. and 3.1.4.3.), a protein crystal contains large solvent channels. Typically, the solvent within these channels is disordered and thus not visible in the structure. However, water molecules or individual components of the crystallization solution, which directly interact with protein residues, *e.g*. via hydrogen bonds, are ordered and hence their corresponding electron density can be interpreted. Model building is an iterative step and, after several of these manual adjustments of the structural model, it is refined against the experimental data using a so-called maximum-likelihood target function, an algorithm implemented in typical

refinement software packages. In contrast to model building, global restrained refinement is carried out in the reciprocal space. The theoretical structure factor F_{calc} of the model is calculated and compared to the experimental structure factor F_{obs} of the data. Structure refinement aims at minimizing the difference between these structure factors by optimizing the model, *i.e.* the atomic positions and B-factors of each atom with regard to chemical plausibility (empirical chemical bond geometries). The process of refinement is monitored through the evolution of the so-called R-factor R_{work} (equation 11) that represents the correlation between the model and the experimental data (electron density).

$$R_{work} = \sum_{hkl} |F_{obs} - kF_{calc}| \Big/ \sum_{khl} F_{obs} \qquad \textbf{(11)}$$

$$R_{free} = \sum_{hkl \in free} |F_{obs} - kF_{calc}| \Big/ \sum_{khl \in free} F_{obs} \qquad \textbf{(12)}$$

with

R_{work} R-factor assessing the correlation between model and electron density
F_{obs} experimental structure factor
kF_{calc} calculated structure factor of the model with the weighting factor k
R_{free} R-factor calculated with 5 % of the reflections excluded from refinement

In order to avoid overfitting of the data, a second R-factor, the R_{free}, was introduced (equation 12). This R-factor weighs the model against approximately 5 % of the data excluded from the refinement and thus is unbiased.

Model refinement is considered as completed when each R-factor converges to a minimum value and the gap between both R-factors does not exceed ~5 %.

Different criteria exist to evaluate the quality of a model. Naturally, chemical properties of the molecule such as bond lengths and angles have to be within a certain minimal range from empirical values. Furthermore, within secondary structure elements, the peptide bond adopts certain characteristic conformations described by the angles φ, ψ and ω. Due to the partial double-bond character of the peptide bond, ω is typically 180 °. The statistical distributions of the two other torsion angles in protein structures are visualized in the Ramachandran plot (Figure 11) that clusters secondary structure elements in favored or allowed regions depending on the relative conformations of the dihedral peptide angles φ and ψ.

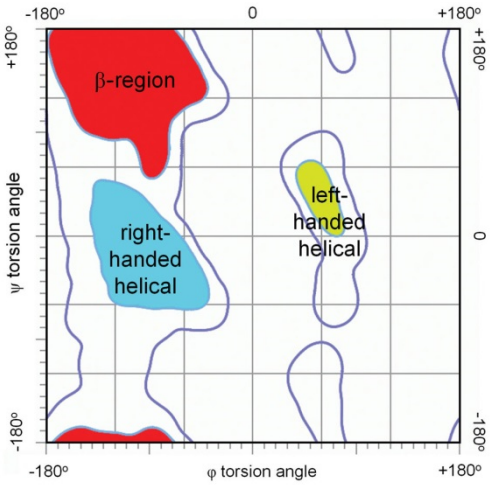

Figure 11: Statistical distribution of the peptide torsion angles of protein structures in the Ramachandran plot. For each protein secondary structure element, the values of the backbone torsion angles φ and ψ cluster in characteristic zones of the Ramachandran plot. The colored zones represent favored backbone conformations, the extended areas around, additionally allowed ones. Figure adapted and reproduced with permission from Biomolecular Crystallography by Bernhard Rupp, © 2009-2014 Garland Science/Taylor & Francis LLC.

3.2. Experimental Section

3.2.1. General materials

All chemicals, biochemicals and enzymes (except Tobacco etch virus (TEV) protease) used in this study were purchased in the highest purity available (*p.a.*, *pro analysis*) from the companies AppliChem GmbH (Darmstadt, Germany), Becton Dickinson GmbH. (BD; Heidelberg, Germany), Bio-Rad Laboratories GmbH (Munich, Germany), Eurofins Scientific GmbH (Hamburg, Germany), Merck KGaA (Darmstadt, Germany), New England Biolabs GmbH (Frankfurt/Main, Germany), Peqlab (Erlangen, Germany), QIAGEN GmbH (Hilden, Germany), Carl Roth GmbH + Co. KG (Karlsruhe, Germany), SERVA Electrophoresis GmbH (Heidelberg, Germany), ThermoFischer Scientific Inc. (Waltham, Massachusetts, USA) and Sigma-Aldrich Chemie GmbH (Munich, Germany) unless otherwise noted.
Crystallization screens were purchased from Molecular Dimensions (Newmarket, Suffolk, UK), QIAGEN, and Hampton Research (Aliso Viejo, California, USA).

3.2.1.1. Oligonucleotides, plasmids and microorganisms

For mechanistic studies of the isomerase PhzF a variety of active site variants were generated using a modified site-directed mutagenesis protocol (*q.v.* 3.2.2.3.). A detailed list of the oligonucleotides utilized for introduction of specific mutations can be found in Table 1.

Table 1: Overview of oligonucleotides used for site-directed mutagenesis.*

oligo name	sequence 5' → 3'	length (bp)	T_M (°C)	variant
*phzF*_D208E_fw	GCA TAC GGC GTT GTA GAG **GAA** GCG GCC ACA GGC TCC	36	77.4	PhzF D208E and PhzF E45D/D208E
*phzF*_D208E_rv	GGA GCC TGT GGC CGC **TTC** CTC TAC AAC GCC GTA TGC	36	77.4	PhzF D208E and PhzF E45D/D208E
*phzF*_H74D_fw	GAA CTG CCT TTT GCC GGG **GAC** CCG TTG CTG GGT ACA GCC	39	78.9	PhzF H74D
*phzF*_H74D_rv	GGC TGT ACC CAG CAA CGG **GTC** CCC GGC AAA AGG CAG TTC	39	78.9	PhzF H74D
*phzF*_H74N_fw	GAA CTG CCT TTT GCC GGG **AAT** CCG TTG CTG GGT ACA GCC	39	76.8	PhzF H74N
*phzF*_H74N_rv	GGC TGT ACC CAG CAA CGG **ATT** CCC GGC AAA AGG CAG TTC	39	76.8	PhzF H74N
*phzF*_S213A for	GAG GAT GCA GCC ACA GGC **GCA** GCC GCA GGA CCA TTG	36	78.6	PhzF S213A
*phzF*_S213A rev	CAA TGG TCC TGC GGC **TGC** GCC TGT GGC TGC ATC CTC	36	78.6	PhzF S213A
*phzF*_Y4A_fw	GGC AGC CAT ATG CAC AAC **GCC** GTC ATT ATC GAC GCC	36	75.2	PhzF Y4A
*phzF*_Y4A_rv	GGC GTC GAT AAT GAC **GGC** GTT GTG CAT ATG GCT GCC	36	75.2	PhzF Y4A

*All oligonucleotides were designed using the program OligoCalc (Kibbe, 2007) and purchased from Eurofins Scientific GmbH. In general, underlined base triplets indicate an introduced mutation. Additional bold letters represent the specific mutation denoted in the name of the oligonucleotide while all other mutations are silent. The gray highlighted triplets indicate non-gene specific bases that belong to the expression plasmid.

Expression plasmids resulting from site-directed mutagenesis as well all other expression constructs used in this study are listed in Table 2.

Table 2: Overview of all plasmid constructs used in this study.*

plasmid	source	application
pET15b_*phzF* (WT)	Mavrodi *et al*. 2008	biochemical assay, ITC, crystallization
pET15b_*phzF* D208A	MPI Dortmund	biochemical assay
pET15b_*phzF* D208E	this study	biochemical assay, crystallization
pET15b_*phzF* D208T	MPI Dortmund	biochemical assay
pET15b_*phzF* E45A	MPI Dortmund	biochemical assay, crystallization
pET15b_*phzF* E45D	Lips, 2012	biochemical assay, crystallization
pET15b_*phzF* E45Q	MPI Dortmund	biochemical assay, ITC, crystallization
pET15b_*phzF* E45D/D208E	this study	biochemical assay, crystallization
pET15b_*phzF* H74A	MPI Dortmund	biochemical assay, crystallization
pET15b_phzF H74D	this study	biochemical assay
pET15b_*phzF* H74L	Lips, 2012	biochemical assay
pET15b_*phzF* H74N	this study	biochemical assay
pET15b_*phzF* N42A	Gazdag, MPI Dortmund	biochemical assay
pET15b_*phzF* S213A	this study	biochemical assay
pET15b_*phzF* Y4A	this study	biochemical assay
pET19TEV_*BgluphzF*	Pfaff, MPI Dortmund	biochemical assay, crystallization
pET19TEV_*BgluphzF*Δ123	Pfaff, MPI Dortmund	biochemical assay, crystallization
pET15b_*Bcphz*(A)/B	Ahuja *et al*. 2008	biochemical assay, ITC, CD, crystallization
pET15b_*phzA*	Ahuja *et al*. 2008	Biochemical assay, ITC, CD, crystallization
pET15b_*phzB*	Ahuja *et al*. 2004	biochemical assay, MST, CD
pET19TEV_*phzAB*	Weikart, 2006	biochemical assay, MST, CD, crystallization

*All plasmids were utilized for protein production and for further applications as depicted in the table. The produced protein constructs carry an N-terminal hexahistidine-tag with either thrombin or TEV-cleavage site. MPI = Max Planck Institute

For amplification of expression plasmids or heterologous gene expression, different *E. coli* strains were used. Their specifications are shown in Table 3.

In cellulo compound screening of potential PhzB-inhibitors was carried out in two different *Pseudomonas aeruginosa* strains, PAO1 and PA14 (Table 3).

Table 3: Overview of the microorganisms used in this study.*

bacterial strain	genotype	antibiotic resistance
E. coli DH5α (Invitrogen)	*fhuA2* Δ(*lacZ)U169 phoA glnV44 Φ80'* Δ(lacZ)M15 *gyrA96 recA1 relA1 endA1 thi-1 hsdR17*	-
E. coli GC5 (Gene Choice)	*fhuA2 Δ(argF-lacZ)U169 phoA glnV44 Φ80' Δ(lacZ)M15 gyrA96 recA1 relA1 endA1 thi-1 hsdR17*	-
E. coli TOP10 (Invitrogen)	*F–* mcr*A Δ(*mrr-hsd*RMS*-mcr*BC) Φ80*lac*ZΔM15 Δ*lac*X74* rec*A1* ara*D139 Δ(*ara leu*) 7697* gal*U* gal*K* rps*L (StrR)* end*A1* nup*G*	streptomycin
E. coli XL1-blue (Stratagene)	*F´ proAB lacIqZΔM15 Tn10 Tet^r/ recA1 endA1 gyrA96 thi-1 hsdR17 supE44 relA1 lac*	tetracycline
E. coli Rosetta1 (Novagen)	*F$^-$ ompT hsdS$_B$(r_B^- m_B^-) gal dcm pRARE (Cam^R)*	chloramphenicol
E. coli Rosetta1 (DE3) *pLysS* (Novagen)	*F- ompT hsdSB(rB- mB-) gal dcm (DE3) pLysSRARE (CamR)*	chloramphenicol
E. coli Rosetta2 (Novagen)	*F$^-$ ompT hsdS$_B$(r_B^- m_B^-) gal dcm pRARE2 (Cam^R)*	chloramphenicol
E. coli Rosetta2 (DE3) *pLysS* (Novagen)	*F$^-$ ompT hsdS$_B$(r_B^- m_B^-) gal dcm (DE3) pLysSRARE2 (Cam^R)*	chloramphenicol
P. aeruginosa PAO1 (Häußler, HZI Braunschweig)	-	-
P. aeruginosa PA14 (Häußler, HZI Braunschweig)	-	-

*HZI = Helmholtz-Zentrum für Infektionsforschung (Helmholtz Centre for Infection Research).

3.2.1.2. Media, buffers and stock solutions

For media preparation distilled and deionized water (ddH_2O) was used and the media additionally autoclaved. All other buffers and stock solutions were prepared using ultrapure Milli-Q® ddH_2O and filter sterilized. Buffers used for protein purification and ITC experiments were degassed. Antibiotics were used at final concentrations of 100 µg mL^{-1} and 34 µg mL^{-1} for ampicillin (aqueous solution) and chloramphenicol (ethanolic solution) respectively.

A. Media:

- LB-medium: 10 g L^{-1} tryptone, 5 g L^{-1} yeast extract, 10 g L^{-1} NaCl
- 1.5 % (w/v) LB-agar: 10 g L^{-1} tryptone, 5 g L^{-1} yeast extract, 10 g L^{-1} NaCl, 15 g L^{-1} agar
- TB-medium: 12 g L^{-1} tryptone, 24 g L^{-1} yeast extract, 0.4 % (w/v) glycerol, 170 mM KH_2PO_4, 720 mM K_2HPO_4

- PPGAS-medium: 20 mM NH_4Cl, 20 mM KCl, 120 mM TRIS/HCl pH 7.2, 1.6 mM $MgSO_4$, 1 % (w/v) tryptone, 0.5 % (w/v) glucose
- M63-medium: 15 mM $(NH_4)_2SO_4$, 100 mM KH_2PO_4 pH 7.0, 1.8 µM $FeSO_4$ x $7H_2O$, 1 mM $MgSO_4$, 0.2 % (w/v) glucose, 0.1 % (w/v) casamino acids

B. Buffer:

PhzF-variants

- buffer A: 50 mM NaH_2PO_4/Na_2HPO_4 pH 7.5, 300 mM NaCl, 10 % (v/v) glycerol
- buffer B: 50 mM NaH_2PO_4/Na_2HPO_4 pH 7.5, 300 mM NaCl, 10 % (v/v) glycerol, 500 mM imidazole
- dialysis buffer A1: 50 mM NaH_2PO_4/Na_2HPO_4 pH 7.5, 10 % (v/v) glycerol
- dialysis buffer A2: 20 mM TRIS/HCl pH 7.5, 150 mM NaCl, 10 % (v/v) glycerol
- size-exclusion buffer: equivalent to dialysis buffer A1 for enzymatic assays or dialysis buffer A2 for crystallization experiments

PhzB-orthologues

- buffer A: 150 mM NaH_2PO_4/Na_2HPO_4 pH 8.0, 300 mM NaCl
- buffer B: 150 mM NaH_2PO_4/Na_2HPO_4 pH 8.0, 300 mM NaCl, 500 mM imidazole
- dialysis/size-exclusion buffer: 20 mM TRIS/HCl pH 8.0, 150 mM NaCl

HeteroPhzAB

- buffer A: 50 mM NaH_2PO_4/Na_2HPO_4 pH 8.0, 300 mM NaCl
- buffer B: 50 mM NaH_2PO_4/Na_2HPO_4 pH 8.0, 300 mM NaCl, 500 mM imidazole
- dialysis buffer A: 50 mM TRIS/HCl pH 8.0, 150 mM NaCl, (5 mM β-mercaptoethanol)

- dialysis buffer B: 50 mM TRIS/HCl pH 8.0, 150 mM NaCl, 500 mM imidazole
- size-exclusion buffer: 20 mM TRIS/HCl pH 8.0, 150 mM NaCl

Buffer used for enzymatic assays or other specific applications are described in the corresponding paragraph of each chapter.

C. Other solutions

SDS-PAGE

- 4x stacking gel buffer: 0.5 M TRIS/HCl pH 6.8, 0.4 % (w/v) SDS
- stacking gel: 1x stacking gel buffer, 5 % (w/v) acrylamide (from 30 % (w/v) stock solution: 37.5:1), 0.1 % (w/v) APS, 0.001 % (v/v) TEMED
- 4x resolving gel buffer: 1.5 M TRIS/HCl pH 8.8, 0.4 % (w/v) SDS
- resolving gel (16 %): 1x resolving gel buffer, 16 % (w/v) acrylamide (from 30 % (w/v) stock solution: 37.5:1), 200 µL 10 % APS, 0.001 % (v/v) TEMED
- 5x SDS-PAGE sample buffer: 50 mM TRIS/HCl pH 6.8, 500 mM β-mercapto-ethanol, 50 % (v/v) glycerol, 10 % (w/v) SDS, 0.05 % (w/v) bromophenol blue
- running buffer: 25 mM TRIS/HCl, 200 mM glycine, 0.1 % (w/v) SDS
- staining solution: 0.2 % (w/v) Coomassie Brilliant Blue G-250, 30 % (v/v) methanol, 10 % (w/v) glacial acetic acid
- destaining solution: 20 % (v/v) methanol, 10 % (v/v) glacial acetic acid

3.2.2. General molecular biology methods

3.2.2.1. Cloning and generation of expression plasmids

As listed in section 3.2.1.2., most of the plasmid constructs used in this study were generated beforehand either by Dimitri Mavrodi (Mavrodi *et al*., 2003) or other PhD students in the group of Prof. Dr. Wulf Blankenfeldt. A few additional variants of PhzF were generated using a modified site-directed mutagenesis protocol.

3.2.2.2. Extraction of plasmid DNA

For any genetic manipulation, amplified expression plasmids need to be extracted from cloning strains such as *E. coli* DH5α. After harvesting cells from an overnight bacterial cell culture in LB-medium, the plasmid preparation is carried out using standardized protocols (including alkaline/detergent-based cell lysis and alcoholic DNA precipitation) as provided together with the application specific material from the manufacturer. Typically, either the E.Z.N.A.® Plasmid Mini Kit I from OMEGA bio-tek (Norcross, Georgia, USA) or the QIAGEN Plasmid Mini Kit were used for this purpose. After incubation with 50 µL elution buffer over a period of 20 minutes at room temperature, the extracted and purified plasmid DNA is eluted via centrifugation at 13000 rpm in a benchtop centrifuge. Determination of the concentration of the purified plasmid is done photometrically at A_{260} using a NanoDrop™ 2000 spectrophotometer (ThermoFischer Scientific Inc.) under the assumption that one absorbance unit equals 50 µg mL^{-1} double-stranded DNA.

3.2.2.3. Site-directed mutagenesis

The introduction of local specific changes to a DNA sequence can be achieved via so-called site-directed mutagenesis. Starting from short and specific oligonucleotides, which contain the desired mutation but otherwise perfectly align with the template DNA strand, the polymerase chain reaction (PCR) can be initiated and the new target DNA amplified. In this study a modified Quick change® II site-directed mutagenesis protocol (Stratagene) that is based on the "ligation during amplification"-method was used. A typical setup using the KAPAHifi™ DNA polymerase (Kapa Biosystems Ltd., London, UK) is shown in Table 4.

Table 4: Composition of a typical setup for site-directed mutagenesis.

reagent	volume (µL)	final concentration
template DNA	1.00	~2-4 ng $µL^{-1}$
oligonucleotide primer (sense strand)	0.75	300 nM
oligonucleotide primer (antisense strand)	0.75	300 nM
dNTPs	1.00	200 µM
buffer	5.00	1x
ddH_2O	to 25 µL	-
KAPAHifi™ DNA polymerase	0.75	0.03 u $µL^{-1}$

A corresponding PCR-protocol for site-directed mutagenesis is depicted in Table 5.

Table 5: Modified Quick change® II site-directed mutagenesis PCR-protocol.

step		temperature T (°C)	time t (s)
initial denaturation		95	120
denaturation	**30 x**	98	20
annealing		*58*	60
elongation		72	270 (30s/kB)
final elongation		72	300
storage		8	∞

During the PCR the oligonucleotide primer are extended leading to generation of a hybrid DNA double strand consisting of one template and one target strand. Since the methylated template DNA does not contain the introduced mutation, it has to be digested. To this aim 1 µL of the restriction endonuclease DpnI, which specifically recognizes and digests methylated DNA, is added to the PCR mix and the sample incubated for 1 h at 37 °C. After heat deactivation of the enzyme, the whole sample is transformed into chemically competent *E. coli* cells.

3.2.2.4. Transformation of plasmid DNA in chemically competent E. coli

Chemically competent *E. coli* cells used for transformation and amplification of plasmid DNA or protein production were prepared either by Norbert Grillenbeck (University of Bayreuth; calcium (Ca^{2+})-competent cells) or by Claudia Hanko (Helmholtz Centre for Infection Research, HZI; rubidium (Rb^{+})-competent cells) using standardized protocols.

For plasmid transformation 50 µL of the chemically competent cells are augmented with 5-10 µL of (purified) plasmid DNA and incubated for 30 min on ice. Subsequently, the whole sample is heat-shock-treated for 40 s at 42 °C and immediately thereafter placed on ice for 2 min. The cells are resuspended in 1 mL LB-medium and incubated for 1 h at 37 °C and 140 rpm. Finally, 100 µL of the cell suspension are plated on LB-agar plates containing the respective antibiotics for selection.

3.2.2.5. Heterologous gene expression and protein production in E. coli

Expression plasmids for protein production are transformed in *E. coli* expression cell lines such as *E. coli* Rosetta2 (DE3) *pLysS* and plated on LB-agar plates with the corresponding antibiotics. For heterologous gene expression, a LB-pre-culture supplemented with the corresponding antibiotics is inoculated with a single colony of the expression cell line and incubated overnight at 37 °C and 140 rpm.

The next day, 4 - 8 L medium complemented with the respective antibiotics are inoculated

with about 10 mL L^{-1} of the pre-culture to yield a starting OD_{600} of 0.05. The cultures are incubated at 37 °C and 140 rpm and their OD_{600} followed in regular time intervals using a photometer blanked against pure medium. As soon as the cells reach an OD_{600} of 0.6 - 0.8, addition of IPTG to a final concentration of 0.5 mM induces gene expression. Afterwards, incubation of the cultures is continued for another 20 h at 140 rpm, but at a reduced temperature of 20 °C.

3.2.3. General protein biochemical methods

Unless explicitly stated otherwise, protein production and purification followed standard procedures and thus was very similar for all phenazine biosynthesis proteins. Claudia Hanko, Vanessa Hering, and Ute Widow (HZI) assisted in protein production of some of the used Phz-proteins. PhzF and PhzFΔ123 from *Burkholderia glumae* BGR-1 were produced and purified by Christiane Pfaff (MPI Dortmund). In the following paragraphs, a standard protein purification is described in more detail.

3.2.3.1. Cell lysis

After heterologous gene expression, the cells are harvested by centrifugation for 20 min at 4 °C and 6000 rpm. The resulting pellets are resuspended in the respective buffer A supplemented with lysozyme, DNaseI, and $MgSO_4$ to final concentrations of 200 µg mL^{-1}, 1 µg mL^{-1}, and 5 mM respectively. As protease inhibitor either PMSF to a final concentration of 1 mM or one tablet cOmplete™ Mini, EDTA-free protease inhibitor cocktail (Roche Deutschland Holding GmbH, Grenzach-Wyhlen) are added. The cell suspension is stirred for 45 min on ice, before complete cell lysis is achieved by sonication. Insoluble cell debris is removed by centrifugation for 45 min at 4 °C and 16000 rpm and the supernatant filtered through a 0.45 µM syringe filter.

3.2.3.2. Immobilized metal ion affinity chromatography

All produced proteins contain an N-terminal hexahistidine-tag that can be used for immobilized metal ion affinity chromatography by interaction of the imidazole groups of the histidine with immobilized divalent cations such as nickel Ni(II).

For protein purification a HisTrap™ HP-column (column volume (CV) = 5 mL; GE Healthcare, Munich) charged with 100 mM $NiSO_4$ is used. An ÄKTA™prime plus or

ÄKTA^{TM}purifier FPLC-system (GE Healthcare, Munich) is equipped with the column and both are primed with 3 CV buffer A. Then, the cleared protein-containing supernatant is applied using a constant flow-rate of 3 mL min^{-1} and automatically collecting the flow through in fractions of 7 mL. The progress of the purification is monitored by recording the change in absorbance at a wavelength of 280 nm. Afterwards, the column is washed using 2 % buffer B (equivalent to 10 mM imidazole) keeping flow-rate and fraction size constant. Elution of specifically bound protein is done by applying a stepwise gradient of 10, 20, 50, and 100 % buffer B (equivalent to 50, 100, 250, and 500 mM imidazole respectively) each over 5 CV. During elution, the flow-rate is reduced to 2 mL min^{-1} and fractions of 3 mL are collected. Protein containing fractions, as identified by an increased absorbance signal A_{280} are analyzed by SDS-PAGE.

3.2.3.3. Dialysis and protein digest

Collected fractions from the affinity chromatography step comprising the target protein are combined in a flexible dialysis tube with 3 kDa MWCO and dialyzed under continuous stirring against dialysis buffer A at 4 °C overnight to remove the residual imidazole. In order to ensure sufficient buffer exchange, 50 times excess volume of dialysis buffer is used.

If the protein construct contains a protease recognition site for cleavage of the affinity tag, typically a TEV-site, the dialysis buffer A is additionally supplemented with 5 mM β-mercaptoethanol as reducing agent and the protease added in 1:20-molar ratio regarding the target protein. After proteolysis, the tag-free protein is again subjected to a "reverse" Ni(II) ion affinity chromatography as described in paragraph 3.2.3.2. to separate the target protein (in the flow-through) from the affinity tag and other residual contaminants.

3.2.3.4. Preparative size-exclusion chromatography

Many applications, especially protein crystallization requires a homogenous protein sample of high purity. To this aim, all proteins after dialysis or reverse affinity chromatography are subjected to a final size-exclusion chromatography step. First, proteins are loaded on a HiLoad^{TM} 26/600 Superdex™75 prep grade column (CV = 320 mL) equilibrated against size exclusion buffer and connected to an ÄKTA^{TM}purifier FPLC-system. Then, the column is isochratically developed in size exclusion buffer applying a

constant flow-rate of 2 mL min^{-1} to elute the protein separated in different oligomeric species and from residual protein contaminations. Fractions of 2 mL are collected and the protein samples analyzed using SDS-PAGE. Fractions containing pure and homogenous protein are pooled and concentrated via ultrafiltration using spin-concentrators (MWCO = 10 kDa). The concentration of the protein sample is determined photometrically at A_{280} using a NanoDrop™ 2000 spectrophotometer and the specific molar extinction coefficient of the protein construct, as well as its molecular weight. Aliquots of the pure protein are snap-frozen in liquid nitrogen and stored at -80 °C until further usage.

CHAPTER I:
Investigations of the isomerization reaction catalyzed by the phenazine biosynthesis enzyme PhzF

4. The isomerase PhzF

As described in detail in the introduction (*cf*. paragraph 1.3.1.), previous structural and functional studies (Mavrodi *et al*., 2003; Blankenfeldt *et al*., 2004; Parsons *et al*., 2004a) identified the phenazine biosynthesis enzyme PhzF to be an isomerase converting *trans*-2*S*,3*S*-dihydro-3-hydroxyanthranilic acid (DHHA) into the highly reactive ketamine 6-amino-5-oxo-2-cyclohexene-1-carboxylic acid (AOCHC). The reaction is proposed to proceed via a two-step mechanism: an isomerization, which requires the suprafacial movement of a non-acidic proton from position C3 to C1 along the conjugated π-system of the cyclohexadiene ring, and a subsequent keto-enol tautomerization of the intermediate 6-amino-5-hydroxy-2,4-cyclohexadiene-1-carboxylic acid (AHCDC) to the final reaction product. Since ^{1}H-NMR spectra revealed full recycling of the non-acidic proton upon rearrangement, potential reaction pathways ensuring conservation of this proton were hypothesized and their energy profiles analyzed using quantum chemistry/molecular mechanics (QC/MM) calculations. Moreover, enzyme kinetics using two different substrate isotopologues as well as biophysical and crystallographic experiments were carried out to gain deeper insights into PhzF catalysis and find evidence for either a stepwise base-initiated reaction via an anionic intermediate or for a concerted mechanism, potentially following a pericyclic, so-called [1,5]-prototropic shift reaction, which has not yet been described in enzyme catalysis.

4.1. Specific Methods & Materials

The investigation of the catalytic mechanism of PhzF was a collaborative project. Mario Leypold from the group of Prof. Dr. Rolf Breinbauer at the Graz University of Technology synthesized and analyzed specific, enantiopure substrates, substrate analogs, and potential inhibitors and performed ^{1}H-NMR experiments probing hydrogen/deuterium migration. Martin Culka from the Group of Prof. Dr. Matthias Ullmann at the University of Bayreuth carried out quantum chemistry/molecular mechanics (QC/MM) calculations to

analyze the different energy profiles of potential reaction pathways. Although some of their results are discussed in context of this work, materials and methods for these specific experiments are not elaborated in further detail.

4.1.1. Protein production

PhzF from *Pseudomonas fluorescens* 2-79 used in this study was produced after a modified protocol as described in Mavrodi *et al.* (2003). In brief, mutations were introduced using a modified Quick change® II site-directed mutagenesis protocol (Stratagene, see also paragraph 3.2.2.3.). Overexpression of the wild type protein (UniProt-entry: Q51792 (PHZF_PSEFL)) and different active site variants was carried out using the pET15b expression vector (Novagen) in *E. coli* Rosetta (DE3) *pLysS* (Novagen) in luria bertani-medium at 20 °C o/n after induction with 0.5 mM Isopropyl β-D-1-thiogalactopyranoside (IPTG) at an OD_{600} of 0.6. Purification of the N-terminal hexahistidine-tagged proteins followed standard procedures (as described in paragraph 3.2.3.), including immobilized Ni(II) affinity chromatography and a final size-exclusion chromatography step in standard assay (50 mM Na_2HPO_4/NaH_2PO_4 pH 7.5) or crystallization buffer (20 mM TRIS/HCl pH 7.5, 150 mM NaCl) supplemented with 10 % (v/v) glycerol. Purified proteins were concentrated, snap-frozen in liquid nitrogen, and stored at -80 °C until further usage.

PhzF from *Burkholderia glumae* BGR-1 (UniProt-entry: C5AHF3 (C5AHF3_BURGB)) was used from flash frozen aliquots produced and purified by Christiane Pfaff from the Max Planck Institute of Molecular Physiology in Dortmund, Germany

4.1.2. Photometric assay

Enzyme kinetic studies of the isomerase PhzF were carried out in a continuous assay following substrate depletion at 275 nm using an Infinite® M200 microplate reader (Tecan Group Ltd.). Unless explicitly stated otherwise, a standard assay mixture contained 40 nM PhzF dimer and substrate up to a final concentration of 1 mM in 50 mM sodium phosphate buffer at pH 7.5 supplemented with 1 % (v/v) dimethyl sulfoxide (DMSO). All reactions were carried out in a final volume of 100 µL in UV-Star® 96-Well microplates (Greiner Bio-One) at 25 or 42 °C. The reaction was initiated by the addition of 50 µL enzyme solution to an equal volume of each substrate dilution and data were acquired in 30 s intervals

over a time course of 20 minutes. For background signal correction a reaction mixture lacking substrate was used. Reaction rates were determined from the slopes of the linear phase of each curve using a path length of 0.278 cm and an extinction coefficient of 6500 M^{-1} cm^{-1}. This extinction coefficient at 275 nm, the absorption maximum of the substrate *trans*-2*S*,3*S*-dihydro-3-hydroxyanthranilic acid (DHHA), was determined experimentally from standard curves of both isotopologues in standard assay and crystallization buffer. Each standard curve was measured in triplicate (Figure A1). Kinetic parameters were obtained by fitting the averaged data from three independent measurements to the Michaelis-Menten model using GraFit 5 (Erithacus Software Ltd.). In order to obtain measurable rates for the deuterium labeled, heavy substrate isotopologue 2*S*,3*S*-(3-^{2}H)-DHHA (d-DHHA) or racemic *O*-ethylated DHHA (*O*-Et-DHHA), a synthetic substrate analog, the enzyme concentration was increased to 200 and 1000 nM respectively.

4.1.3. Isothermal titration calorimetry

Calorimetric titrations of substrate analogs to PhzF variants were carried out at 25 °C using a MicroCal™ VP-ITC System (GE Healthcare, now Malvern Instruments) with 10 µcal s^{-1} reference power in high feedback mode. The sample cell was filled with either wild type PhzF or the inactive variant E45Q diluted to 50 or 100 µM final concentration in crystallization buffer. After an initial delay of 120 s, the proteins were titrated with 450 µM or 1 mM of different ligands prepared either from aqueous or DMSO stock solutions. The ligands were injected at a rate of 0.5 µL s^{-1} and a stirring speed of 307 rpm with 240 s intervals between individual injections. The data were analyzed and plotted using the programs NITPIC (Keller *et al.,* 2012; Scheuermann and Brautigam, 2015), SEDPHAT (Houtman *et al*., 2007; Zhao *et al.,* 2015) and GUSSI (Brautigam, 2015; and for review Brautigam *et al.*, 2016).

4.1.4. Crystallization and structure determination

Co-crystallization experiments of wild type protein or variant E45Q, each at 10 mg mL^{-1} pre-incubated with 10 mM ligand, were carried out via sitting-drop vapor diffusion method at room temperature in 96-well INTELLI-PLATES® (ARI). For identification of new crystallization conditions either the commercial JCSG+ and the Cryos screening suites

(QIAGEN) or a random layer screen around the published conditions (0.1 M tri-sodium citrate pH 4.4-5.0 or pH 5.6; 0.2 M ammonium acetate or sulfate; 8-12 or 24-30 % (w/v) polyethylene glycol 4000; Mavrodi *et al.*, 2003; Blankenfeldt *et al.*, 2004) were used. Drops consisted of 200 nL protein solution and 200 nL precipitant. Initial crystals for the complex of PhzF E45Q with racemic *O*-ethylated DHHA were obtained after 12 hours from a reservoir comprising 0.085 M sodium acetate at pH 4.6, 0.17 M ammonium acetate, 25.5 % (w/v) polyethylene glycol 4000 and 15 % (v/v) glycerol. First crystals for the putative complex of PhzF WT and the substrate analog/inhibitor H_2-DHHA, were also obtained within 12 h from a reservoir composed of 0.1 M tri-sodium citrate pH 5.6, 0.0556 M tri-lithium citrate, 23.3 % (w/v) polyethylene glycol 3350 and 17.8 % (v/v) polyethylene glycol 400.

Diamond-shaped crystals for the complex of variant E45Q with *O*-Et-DHHA of a maximum size of 30*30*25 µm, which grew within a week, were mounted on a nylon loop and flash frozen in liquid nitrogen. The same procedure was followed for crystals of wild type PhzF, crystallized in the presence of 2,3,4,5-tetrahydro-3-hydroxy anthranilic acid (H_2-DHHA) with dimensions of 130*130*125 µm. Diffraction data were collected at 100 K at beamline MX BL14.1, BESSY II at the Helmholtz Centre Berlin (complex with *O*-Et-DHHA) or at beamline X06DA (PXIII) at the Swiss Light Source (SLS) of the Paul Scherrer Institute (putative complex with H_2-DHHA). Data reduction was carried out with XDS (Kabsch, 2010) followed by AIMLESS (Evans and Murshudov, 2013) of the CCP4 package (Winn *et al.*, 2011). Refinement and model building were achieved by alternating rounds of manual adjustment in COOT (Emsley *et al.*, 2010) and maximum-likelihood refinement by phenix.refine (Afonine *et al.*, 2012) of the PHENIX software suite (Adams *et al.*, 2010). Ligand restraints for *O*-ethylated DHHA were generated using the program phenix.elbow (Moriarty *et al.*, 2009) of the latter software suite. With respect to the apparent resolution of 1.7 Å of the complex with *O*-Et-DHHA structural flexibility was modelled using TLS (Translation/Libration/Screw) refinement (Schomaker and Trueblood, 1968). Eight TLS groups were identified by the program phenix.find_tls_groups, implemented in phenix.refine. In the last step of refinement, heteroatoms like waters and ligands were attributed to their nearest TLS group using a script developed in the group (Reichelt and Blankenfeldt, unpublished). Due to near atomic resolution of 1.18 Å of the wild type

dataset, anisotropic B-Factors were considered for all atoms of the protein except hydrogens. Waters were also excluded from anisotropic B-factor refinement. Final structure validation was done with MolProbity (Chen *et al.*, 2010). Diffraction data and coordinates have been deposited to the Protein Data Bank (Berman *et al.,* 2000; PDB entry 5IWE for the complex with *O*-Et-DHHA). Full data collection and refinement statistics are shown in Table 14 (and Table A5 in the appendix for the high-resolution structure).

4.2. Results & Discussion

4.2.1. Development of the photometric assay

Studies of the isomerization mechanism of PhzF required the development of a new activity assay. This assay should allow not only direct and continuous monitoring of the reaction, but also be adaptable to a semi-high-throughput setup. Many obstacles had to be overcome during assay development, since finding an UV-observable signal for the product failed. Eventually, following depletion of the substrate using its maximum absorption at 275 nm was the method of choice.

Originally setup in a conventional UV-Vis spectrometer equipped with a cuvette holder, the assay platform was adapted to a 96-well plate format in order to facilitate rapid semi-high-throughput measurements. A major disadvantage of the plate format was the concentration range of the substrate limited by the path length, *i.e.* the liquid level in the microplate. Accordingly, only substrate concentrations up to a final concentration of 1 mM were applicable for the experiments. Nevertheless, this range was sufficient to obtain reproducible kinetic parameters. Interference of intrinsic protein absorption at the chosen wavelength of 275 nm seemed not to be an issue, since the typical protein concentrations in the assay mixture were in the nM or low µM-range. Thus, their contribution to the absorption signal was negligible. Moreover, all data were background corrected.

The general assay setup was chosen such that the decrease in absorption followed a linear gradient over the whole time course of the experiment as shown in Figure 12A.

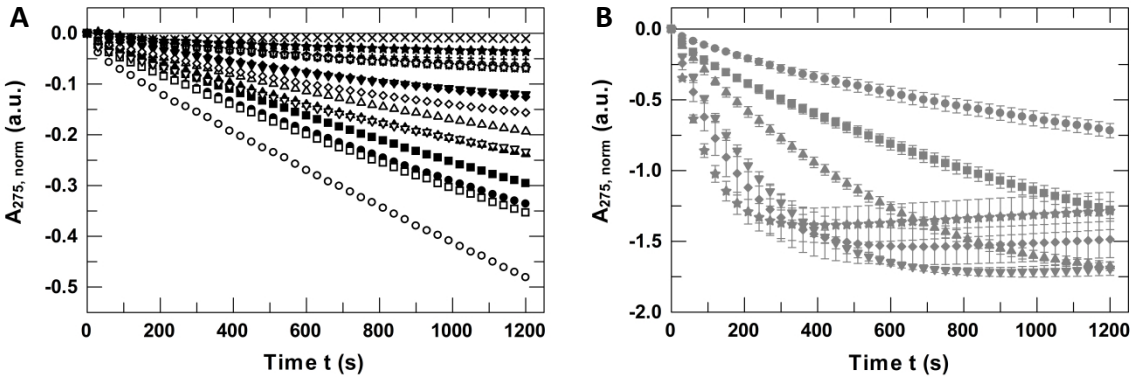

Figure 12: Typical kinetic data for the reaction of PhzF from *P. fluorescens* 2-79 with its natural substrate DHHA.
A Time traces of the reaction using 40 nM PhzF dimer at different substrate concentrations ranging from × = 0 mM to ○ = 1 mM DHHA. **B** Time traces of the conversion of 1 mM substrate using various concentrations of dimeric PhzF (● = 40 nM, ■ = 100 nM, ▲ = 200 nM, ▼ = 400 nM, ◆ = 600 nM, and ★ = 1 µM). The plotted curves in **B** are averaged data of three independent measurements. All data were obtained in standard assay buffer at 25 °C and normalized to zero.

Linearity was observed for most measurements, although for some of them, especially at higher substrate concentrations, fluctuations within the first 30 s to 3 min occurred. This might be a sign of simple experimental errors or indicate pre-steady state processes. Yet, when probing the latter hypothesis by following conversion of the natural substrate using increasing PhzF concentrations in the standard assay buffer (50 mM sodium phosphate pH 7.5), no significant burst phase could be detected (Figure 12B).

4.2.2. General buffer effects

Many experiments addressed the question whether the nature of the buffer has an influence on the enzymatic activity. This was especially interesting since it was known from previously published structures (Blankenfeldt *et al.*, 2004; Parsons *et al.*, 2004a), that buffer ions such as sulfate or phosphate can bind to the active site of the enzyme (Figure 13).

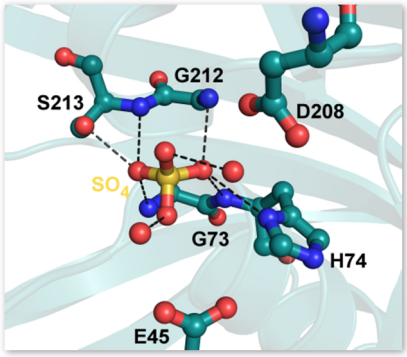

Figure 13: Active site of PhzF (*P. fl* 2-79) with bound sulfate ion.
Close-up on the active site of PhzF (PDB entry 1U1V; Blankenfeldt *et al.*, 2004) in its open conformation. The sulfate ion and active site residues are shown as balls and sticks with the hydrogen-bonding network to the sulfate ion being highlighted as dashes (- - -).

In contrast to what was expected from these crystal structures, the kinetic parameters for the substrate DHHA obtained in sodium phosphate buffer, namely a k_{cat} of 3.23 s^{-1} and a k_{cat}/K_M of 6251 M^{-1} s^{-1}, turned out to be in good agreement with the turnover number calculated with QC/MM methods of approximately 3 s^{-1}. As such, sodium phosphate

appears to be an appropriate buffer substance for further mechanistic studies.

In addition, when varying the phosphate concentration from 10 to 500 mM, no significant influence on k_{cat} could be detected (Table 6 and Table A1 in appendix A1). Nonetheless, a small increase of K_M is observed when the ionic strength of the buffer was raised (Table 6 and Figure A2). Consequently, the overall catalytic efficiency decreased with increasing phosphate concentrations, suggesting a weak competitive effect of phosphate ions with a calculated K_I of 488 mM (using a competitive inhibition model in GraFit 5). However, under standard assay conditions using 50 mM phosphate, a concentration ten times below the K_I, this inhibitory effect can be neglected.

Table 6: Enzyme kinetic parameters for PhzF (*P. fl* 2-79) catalyzed DHHA conversion in presence of increasing phosphate concentrations.*

sodium phosphate pH 7.5	k_{cat} (s^{-1})	K_M (µM)	k_{cat}/K_M ($M^{-1}s^{-1}$)
10 mM	3.06 ± 0.12	574 ± 40	5332 ± 426
20 mM	2.58 ± 0.36	313 ± 61	8245 ± 1983
50 mM	2.55 ± 0.12	623 ± 42	4096 ± 337
100 mM	3.61 ± 0.22	779 ± 60	4637 ± 455
200 mM	2.62 ± 0.07	715 ± 27	3667 ± 172
500 mM	2.87 ± 0.09	866 ± 41	3315 ± 189

* The obtained values are averaged data of three independent measurements fitted to a Michaelis-Menten model. All data were obtained in the respective buffer at 25 °C, normalized to zero, and background corrected.

In a similar way, the effect of sulfate on PhzF activity was tested using up to 100 mM Na_2SO_4 as an additive to the standard assay buffer (50 mM sodium phosphate pH 7.5). Considering this series independently, increasing sulfate concentrations seem to have a positive influence on the turnover rate of the PhzF reaction, but no significant effect on K_M (Table 7). When taking k_{cat}/K_M of the sulfate series in account, the acceleration of substrate turnover with increasing sulfate concentrations is even more distinct and thus showing an inverse behavior compared to phosphate.

The increase in the overall catalytic efficiency in presence of sodium sulfate can be explained with the Hofmeister effect of the SO_4^{2-}-anion (Hofmeister, 1888 and for review Kunz *et al.*, 2004). SO_4^{2-} is classified as a kosmotropic anion, *i.e.* a highly hydrated anion that increases protein surface hydrophobicity and therefore, at least to some extent, protein stability. In addition, the Na^+-counter ion, as a chaotropic cation, is also known to stabilize proteins (Zhao, 2016). Altogether, sodium sulfate might have a beneficial effect on protein stability and therefore enzymatic activity. However, from structural data it is known that sulfate binds to the active site of PhzF - at least under crystallization

conditions, *i.e.* 0.2 M ammonium sulfate – as such an inhibitory effect of this ion was anticipated. Yet, the tested concentrations of sodium sulfate were in the lower mM-range and therefore enzyme stabilizing effects of the SO_4^{2-}-ion might have outbalanced its inhibitory effects, which most likely would become visible only at higher sulfate concentrations.

Table 7: Enzyme kinetic parameters for PhzF (*P. fl* 2-79) catalyzed DHHA isomerization in presence of increasing sulfate concentrations.*

Na_2SO_4	k_{cat} (s^{-1})	K_M (μM)	k_{cat}/K_M ($M^{-1}s^{-1}$)
0 mM	1.99 ± 0.09	506 ± 39	3923 ± 351
1 mM	3.12 ± 0.42	765 ± 120	4078 ± 840
10 mM	2.76 ± 0.06	443 ± 18	6240 ± 281
100 mM	4.00 ± 0.15	565 ± 36	7086 ± 530

* The obtained values are averaged data of three independent measurements fitted to a Michaelis-Menten model. All data were obtained in 50 mM sodium phosphate pH 7.5 at 25 °C supplemented with the depicted sulfate concentrations, normalized to zero, and background corrected.

After all, an explanation for the influence of buffer ions on enzymatic activity according to the Hofmeister series would also account for sodium phosphate (kosmotrop → PO_4^{3-} > SO_4^{2-} > HPO_4^{2-} → chaotrop). However, the differing observations for these two ions, namely a slight activating effect of sulfate and a weak inhibitory effect of phosphate, might be due to their specific affinities to the enzymes active site, which in turn might depend on their protonation states. At pH 7.5, the value of the standard assay buffer, the sulfate anion is completely deprotonated, *i.e.* it carries two negative charges, while phosphate is in equilibrium between hydrogen phosphate and dihydrogen phosphate, which carry two and only one negative charge respectively.

In general, the active site of PhzF is perfectly shaped to accommodate one negatively charged group, which is stabilized by the positive helix dipoles of two central α-helices (α2 and α6). Hence, the discrimination between phosphate and sulfate has to be provided by other active site residues. Although the two obvious candidates would be E45 and D208, with both amino acids theoretically bearing a negatively charged side chain at pH 7.5, analysis of the sulfate bound structure (Figure 13, PDB entry 1U1V, Blankenfeldt *et al.*, 2004) reveals that both residues mediate only indirect interactions to the sulfate ion via water molecules. Thus, the only other residue being able to discriminate between phosphate and sulfate would be H74, whose imidazole side chain was determined to be in its neutral N_ε-protonated form by QC/MM calculations. Indeed in this form, the

unprotonated N_δ-atom can only be a hydrogen bond acceptor and consequently would preferentially bind phosphate over sulfate.

In comparison, substrate turnover in the standard crystallization buffer (20 mM TRIS/HCl pH 7.5, 150 mM NaCl, 10 % (v/v) glycerol) is much slower with a k_{cat} of only 1.61 s^{-1} and a k_{cat}/K_M of 3454 M^{-1} s^{-1} (Table 8 and Figure 14). Since this buffer, in contrast to the standard assay buffer, contained not only additional salt, *i.e.* 150 mM sodium chloride, but also 10 % (v/v) glycerol, it was necessary to investigate whether this finding derived from enhanced viscosity or other salt or glycerol associated effects. Accordingly, a 50 mM TRIS/HCl buffer at pH 7.5 without salt or glycerol, but of similar concentration as phosphate in the standard assay buffer, was used. Using this buffer, the turnover rate is accelerated to the level of the phosphate buffer (k_{cat} = 3.26 s^{-1}), but, with a K_M-value of 1176 µM, almost twice as high as the one obtained for the crystallization buffer. In consequence, the overall catalytic efficiency (k_{cat}/K_M) is unaltered compared to the latter buffer.

Table 8: Enzyme kinetic parameters for the isomerization of DHHA by PhzF (*P. fl* 2-79) in different buffer systems.*

	k_{cat} (s^{-1})	K_M (µM)	k_{cat}/K_M ($M^{-1}s^{-1}$)
sodium phosphate	3.23 ± 0.19	517 ± 57	6251 ± 773
TRIS w/ salt and glycerol	1.61 ± 0.06	466 ± 27	3454 ± 241
TRIS w/o salt or glycerol	3.26 ± 0.40	1176 ± 168	2768 ± 518

* The obtained values are averaged data of three independent measurements fitted to a Michaelis-Menten model. All data were obtained in the respective buffer at 25 °C, normalized to zero, and background corrected.

These results also indicate that the enhanced buffer viscosity in presence of 10 % (v/v) glycerol potentially has an impact on PhzF catalysis. In a more viscous solution, free diffusion of ligand and enzyme is reduced and therefore formation of a productive enzyme-substrate complex is impeded. This leads to a decrease in the substrate turnover rate and hence less overall catalytic efficiency. In addition, the presence of 150 mM sodium chloride leading to an increased ionic strength possibly interfered with DHHA isomerization by altering the electronic state of the active site, in particular that of E45 whose protonation state is essential for catalysis. Yet, to confirm these hypotheses, an additional series of experiments with different glycerol and/or sodium chloride concentrations would be required.

Besides the unfavorable effects on PhzF catalysis caused by enhanced viscosity or increased ionic strength, also an effect of TRIS as a buffer substance was observed.

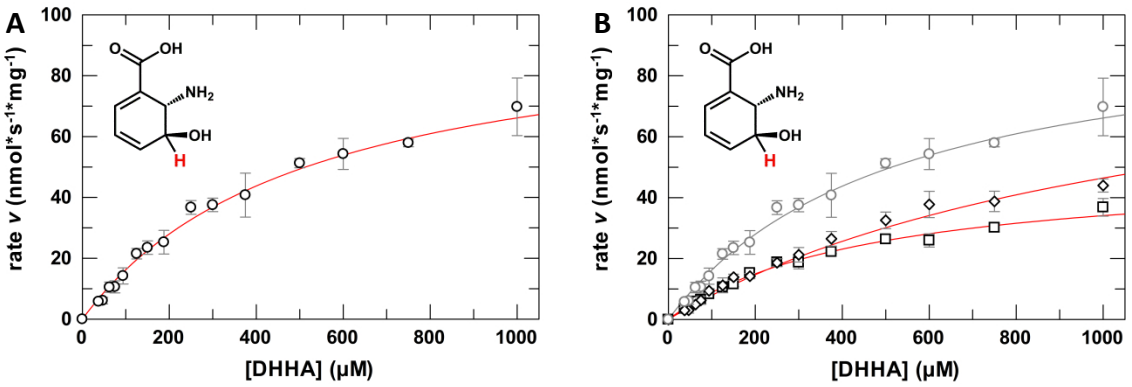

Figure 14: Enzyme kinetics of the isomerization of DHHA by PhzF (*P. fl* 2-79) in different buffer systems.
The turnover of the natural substrate DHHA was followed via substrate depletion over time at 275 nm. Kinetic plots (rate *v* as a function of substrate concentration) of the reaction in **A** 50 mM sodium phosphate buffer pH 7.5 (○; ○ for comparison in plot B) and **B** crystallization buffer (20 mM TRIS/HCl pH 7.5, 150 mM sodium chloride, 10 % (v/v) glycerol, □) or 50 mM TRIS/HCl pH 7.5 (◇) are shown. After normalization to zero and background correction, averaged data from three independent measurements were fitted to a Michaelis-Menten model (—) using GraFit 5. All data were obtained at 25 °C. Inset: Structural formula of the substrate DHHA, with the migrating proton (**H**) highlighted.

Despite similar substrate turnover rates in TRIS (without salt or glycerol) or phosphate buffer, the apparent affinity in presence of TRIS is doubled. The finding might be explained by the reactivity of the primary amine of this buffer substance. As mentioned earlier, the isomerization product AOCHC is a highly reactive ketamine, which can react with primary amines to form so-called Schiff bases. Accordingly, an unfavored side reaction with the buffer could occur (Figure A3A in appendix A1) and the resulting imine could bind to PhzF's active site as shown in Figure A3B. Since it was possible to model the Schiff base in the active site of PhzF in such a way that proper hydrogen bonds could be established and no clashes were observed, it can be hypothesized that a TRIS-based buffer could lead to product-like inhibition. However, further mechanistic studies are required to understand this observation completely.

In summary, the kinetic data show that TRIS buffer seems to be less suitable for studies of PhzF than phosphate, despite the weak competitive inhibition of the phosphate ion.

4.2.3. pH-dependency

Another aspect of PhzF catalysis, its pH-dependency, has been evaluated as well. Originally, a buffer consisting of a mixture of boric acid (200 mM), citric acid (50 mM) and tertiary sodium phosphate (100 mM), as described by Carmody (Carmody, 1961), was used. This unusual, yet phosphate-based buffer offers a broad buffer range from pH 2 - 12, however only a range between pH 4 – 10 proved to be suitable for PhzF stability as the protein otherwise precipitated immediately. Furthermore, when following the reaction in

this buffer, only pH 6.0, 7.0, and 8.0 yielded analyzable, yet noisy data (data not shown). A potential explanation could be the high ionic strength of this complex buffer, which contains a mixture of three different salts. In addition, all three substances could potentially bind to PhzF's active site, depending on their respective protonation states and thus drastically influence PhzF catalysis.

In order to obtain more reliable data, the standard sodium phosphate buffer was used within a narrow pH-range from 6.5 to 8.0 in steps of 0.25 pH-units. The kinetic parameters from these experiments are summarized in Table A3 in the appendix A1 and depicted in Figure 15A. At first glance lower pH-values (except pH 6.5) with k_{cat} values of ~5 s^{-1} seem to be more favorable for catalysis. However, the associated Michaelis constants are higher the lower the pH. The decrease in apparent substrate affinity might correlate with the protonation states of the buffer ions and consequently their affinity to the active site of PhzF leading to weak competitive inhibition (*cf*. paragraph 4.2.2.). On that account, the overall catalytic efficiency k_{cat}/K_M (Figure 15B) was considered to determine a pH-optimum for PhzF catalysis in phosphate buffer, whereupon pH 7.5 and 7.75 gave the highest numbers with k_{cat}/K_M values of 5329 $M^{-1}\,s^{-1}$ and 5407 $M^{-1}\,s^{-1}$ respectively.

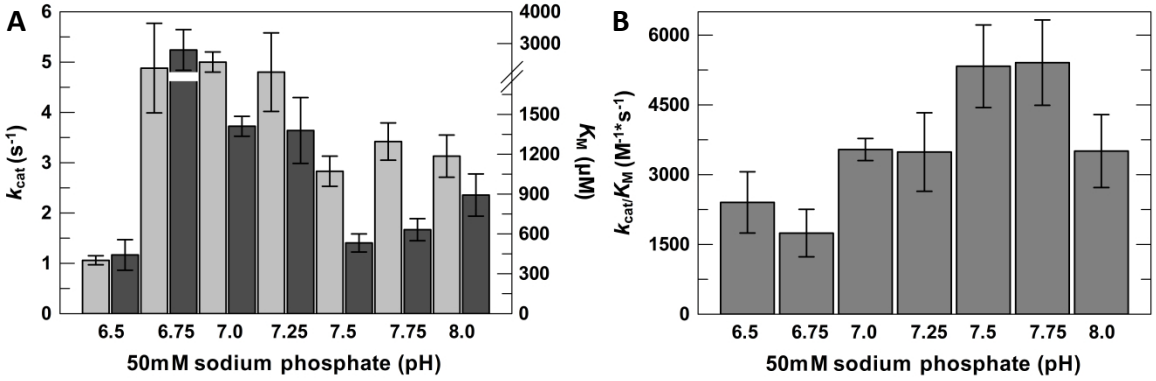

Figure 15: pH-dependency of PhzF-catalyzed DHHA isomerization in 50 mM sodium phosphate buffer.
A The turnover number k_{cat} (; left y-axis) and the Michaelis-constant K_M (; right y-axis), as well as **B** k_{cat}/K_M ( ) were plotted against different pH-values ranging from pH 6.5 to 8.0 in steps of 0.25 pH-units. The plotted values were derived by fitting normalized, background corrected, and averaged data of three independent measurements to a Michaelis-Menten model using GraFit 5. All data were obtained at 25 °C.

A broader pH-range was also screened using a TRIS-like buffer, *i.e.* Bis-TRIS propane (BTP). A first screen covered the whole pH-range of BTP from pH 6.5 to 9.5 in 0.5 pH-units (data not shown). From this series, it became evident, that pH-values above 7.5 are not applicable as they gave noisy and inaccurate data. Consequently, a narrower pH-range from 6.5 to 7.5 in steps of 0.1 pH-units was used for further analysis. However, the data

obtained in this buffer were also inconclusive and thus are not discussed in further detail, but can be found in the appendix A1 (Figure A4 and Table A3).

4.2.4. Turnover of a C3-deuterated substrate – probing kinetic isotope effects

The aim of this study was the identification of the rate-limiting step of catalysis and hence the determination of the fundamental reaction pathway that PhzF employs to convert DHHA into AOCHC. As the reaction is supposed to proceed via a hydrogen transfer, a way to address these questions is to probe primary kinetic isotope effects (KIEs). In theory, the primary kinetic isotope effect of a C-H bond cleavage in solution can be predicted with a semi-classical model to a value of ~7 at room temperature (300 K, Melander and Saunders, 1987). At this temperature the difference of the reaction rates predominantly depends on the differing zero point energies (ZPE) of hydrogen *versus* deuterium. In enzymatic reactions, this intrinsic primary KIE can be masked by the rates of additional, non-rate-limiting catalytic steps. Consequently, the apparent (observed) KIE includes contributions of all steps of catalysis and thus often appears smaller (Allemann and Scrutton, 2009).

The studies of KIEs for PhzF catalysis required synthesis of an enantiomerically pure substrate isotopologue, 2*S*,3*S*-(3-^{2}H)-DHHA (d-DHHA, Mario Leypold). As expected, enzymatic turnover of this heavy substrate isotopologue in sodium phosphate buffer was significantly decreased in comparison with the natural substrate DHHA (0.34 s^{-1} and 3.23 s^{-1} for d-DHHA and DHHA respectively; Table 9 and Figure 16).

Table 9: Enzyme kinetic parameters for the conversion of the light (DHHA) and heavy (d-DHHA) substrate isotopologues by the isomerase PhzF (*P. fl* 2-79) in different buffer systems.*

		k_{cat} (s^{-1})	K_M (µM)	k_{cat}/K_M ($M^{-1}s^{-1}$)	KIE_{app} (k_{cat})	KIE_{app} (k_{cat}/K_M)
sodium phosphate	DHHA	3.23 ± 0.19	517 ± 57	6251 ± 773	9.5 ± 0.6	5.7 ± 0.8
	d-DHHA	0.34 ± 0.01	311 ± 14	1099 ± 58		
TRIS w/ salt and glycerol	DHHA	1.61 ± 0.06	466 ± 27	3454 ± 241	5.4 ± 0.3	3.2 ± 0.3
	d-DHHA	0.30 ± 0.01	271 ± 14	1095 ± 65		
TRIS w/o salt or glycerol	DHHA	3.26 ± 0.40	1176 ± 168	2768 ± 518	8.4 ± 1.1	2.9 ± 0.6
	d-DHHA	0.39 ± 0.01	400 ± 23	963 ± 65		
D_2O : sodium phosphate (9:1)	DHHA	5.69 ± 0.41	937 ± 109	6068 ± 834	12.8 ± 1.1	4.8 ± 0.8
	d-DHHA	0.45 ± 0.02	349 ± 25	1275 ± 108		

* The obtained values are averaged data of three independent measurements fitted to a Michaelis-Menten model. All data were obtained in the respective buffer at 25 °C, normalized to zero, and background corrected.

In other words, substitution of the proton at position C3 (the predicted position for initial deprotonation) with a heavier deuterium gives rise to a large primary deuterium kinetic isotope effect (k_H/k_D) on k_{cat}.

With regard to the theoretical assumptions described above, an apparent KIE of 9.5 on k_{cat} indicates an even higher intrinsic KIE for the proton abstraction from C3. This observation cannot be explained with the differing ZPEs of the substrates alone and additional quantum mechanical contributions such as altered bending frequencies or torsional stiffness of the breaking bond, possibly even hydrogen tunneling through the energy barrier might be involved in the deprotonation step.

In addition, QC/MM calculations that were employed to simulate energy profiles for PhzF catalysis (Martin Culka) also predict that the first deprotonation is the rate-limiting step of the whole catalytic cycle, but, in contrast to the experimental data, these calculations give intrinsic KIEs of 4.76 and 5.69 after Wigner (Wigner, 1932) or 7.36 after Bell (Bell, 1980) tunneling correction. The cause of this large discrepancy between apparent and calculated KIEs is not evident, however it cannot be ruled out that despite the high observed KIE (9.5 on k_{cat}) the associated intrinsic one is not significantly larger and thus might not differ as much from the calculated KIEs. Nevertheless, similar tendencies for apparent KIEs, however less pronounced, are also observed when comparable measurements were carried out in different TRIS buffers (Table 9).

Since the exact reaction mechanism of PhzF catalysis was unknown, a potential involvement of solvent molecules was investigated as well. To study so-called solvent kinetic isotope effects (SIEs), the kinetic parameters of substrate turnover in a light and heavy solvent, here buffer or a buffer mixture comprised of D_2O/ 50 mM sodium phosphate pH 7.5 in a 9:1-ratio, were compared (Figure 16).

Again, when comparing the data for both isotopologues in the D_2O-buffer mixture, a large apparent primary KIE of $k_H/k_D = 12.6$ on k_{cat} is detected (Table 9). Although this finding might be a result of slightly differing pH-values of the two buffers (D_2O *vs.* H_2O), it could as well support the hypothesis that indeed quantum tunneling contributes to PhzF catalysis. Another peculiarity is the increased turnover rate of 5.69 s^{-1} for DHHA in 90 % D_2O that gives rise to an inverse solvent kinetic isotope effect of 0.57 ± 0.05 on k_{cat}.

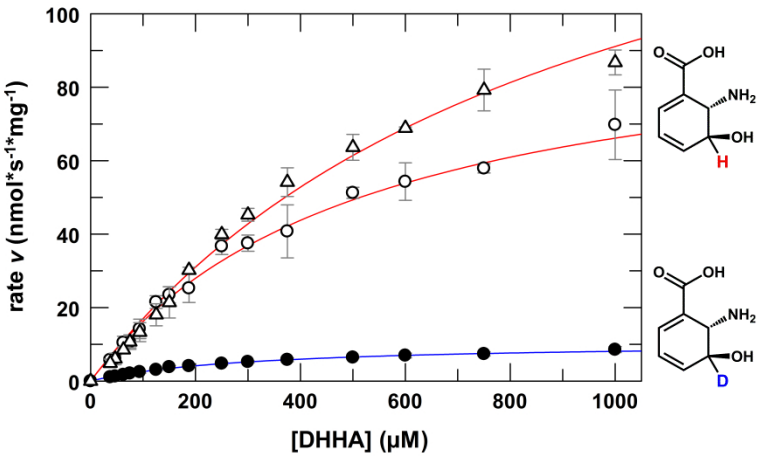

Figure 16: Enzyme kinetics for the conversion of light and heavy substrate isotopologues by the isomerase PhzF (*P. fl* 2-79).
Kinetic plots (rate *v* as a function of substrate concentration) showing the turnover of the natural, light substrate DHHA (○) and of the heavy isotopologue d-DHHA (●) in 50 mM sodium phosphate buffer pH 7.5, as well as turnover of DHHA in D_2O/50 mM sodium phosphate pH 7.5 (9:1) (△). The reaction was followed via substrate depletion over time at 275 nm. After normalization to zero and background correction, averaged data from three independent measurements were fitted to a Michaelis-Menten model (— for DHHA and — for d-DHHA) using GraFit 5. All data were obtained at 25 °C. Adjacent: Structural formula of the substrates DHHA and d-DHHA, with the migrating proton (H) or deuterium (D) highlighted respectively.

However, as the obtained value for k_{cat}/K_M of 6068 M^{-1} s^{-1} is in a similar range as for the standard assay buffer and thus correlates to a SIE of 1.03 ± 0.19 (close to unity), the exchange of solvent did not show any effect on the overall catalytic efficiency. Moreover, the deuterated substrate was affected in a different way, *i.e.* the reaction exhibits a weaker inverse SIE of 0.77 ± 0.04 regarding k_{cat}, but in addition also a weak inverse SIE on k_{cat}/K_M with a value of 0.86 ± 0.09. Since reproduction of these solvent effects by QC/MM calculations failed, a connection between the experimental results and one of the proposed mechanisms cannot be made. Several explanations for an (inverse) SIE have been put forward previously, *e.g.* enhanced or altered solvent viscosity (Karsten *et al.*, 1995) or the impact on the pre-equilibrium protonation (H/D-exchange) to "a site involved in catalysis which prefers deuterium over protium" (Scheuring and Schramm, 1997), but the available data on PhzF catalysis do not allow a conclusive statement about the source of the observed inverse SIEs.

4.2.5. A two domain PhzF orthologue from *Burkholderia glumae* BGR-1

As mentioned in the introduction, the phenazine biosynthesis protein PhzF is a highly conserved enzyme among phenazine producing bacterial strains. To address whether different PhzF orthologues exhibit different reactivity, the enzyme from *Burkholderia*

glumae BGR-1 (*Bglu*PhzF) was tested for DHHA conversion. One peculiarity of this enzyme is the predicted two-domain architecture, which was verified from its crystal structure (Sung *et al.,* unpublished). In addition to an isomerase domain, which adopts the typical DapF-fold and can be found in all PhzF orthologues, *Bglu*PhzF features a ~ 120-amino acid-long N-terminal extension forming a domain with yet unknown function. Structural comparison revealed that this domain bears resemblance to a ferredoxin-like α+β-fold similar to YdhR (sequence identity 28 % over 39 residues according to BLAST; structural similarity 75 % over 97 residues according to PDBe fold), a yet biochemically uncharacterized protein from *E. coli* (PDB entries 1WD6 and 2HIQ). Furthermore, the domain also exhibits a structural relationship to the co-factor independent monooxygenase SnoaB from *Streptomyces nogalater* (PDB entry 3KG0; Grocholski *et al.*, 2010) with a sequence identity of 27 % (52 residues) and a structural identity of 57 % (97 residues).

Upon following substrate depletion of DHHA with two variants of PhzF from *B. glumae* BGR-1, full length *Bglu*PhzF and the isolated isomerase domain *Bglu*PhzFΔ123 (amino acids 124-402), the first observation was that the obtained kinetic parameters for substrate turnover and catalytic efficiency and hence the observed KIEs for full length PhzF are in a similar range as the data obtained for the enzyme from *P. fl* 2-79 (Table 10 and Figure 17).

Table 10: Enzyme kinetic parameters for the conversion of the light and heavy DHHA isotopologue by a PhzF-orthologue from *Burkholderia glumae* BGR-1.*

		k_{cat} (s^{-1})	K_M (μM)	k_{cat}/K_M ($M^{-1}s^{-1}$)	KIE_{app} (k_{cat})	KIE_{app} (k_{cat}/K_M)
full length	DHHA	5.93 ± 1.00	848 ± 156	6994 ± 1742	12.4 ± 2.1	5.7 ± 1.4
	d-DHHA	0.48 ± 0.01	388 ± 17	1236 ± 65		
Δ123	DHHA	0.23 ± 0.01	61 ± 8	3738 ± 525	3.7 ± 0.2	4.8 ± 0.7
	d-DHHA	0.06 ± 0.00	79 ± 5	786 ±56		

* The obtained values are averaged data of three independent measurements fitted according to a Michaelis-Menten model. All data were obtained in 50 mM sodium phosphate pH 7.5 at 25 °C, normalized to zero, and background corrected.

Moreover, the apparent KIE on k_{cat} for the PhzF-orthologue from *B. glu* BGR-1 yields a value of 12.4, which supports the previously made hypothesis of a tunneling contribution to PhzF catalysis (*q.v.* paragraph 4.2.4).

In contrast, the isolated domain (*Bglu*PhzΔ123) shows reduced enzymatic activity in comparison to the full-length enzyme. More precisely, DHHA isomerization with

k_{cat} = 0.23 s^{-1} is 25-fold decreased, while turnover of the heavy isotopologue is slowed down only 8-fold (k_{cat} = 0.06 s^{-1}, Table 10 and Figure 17).

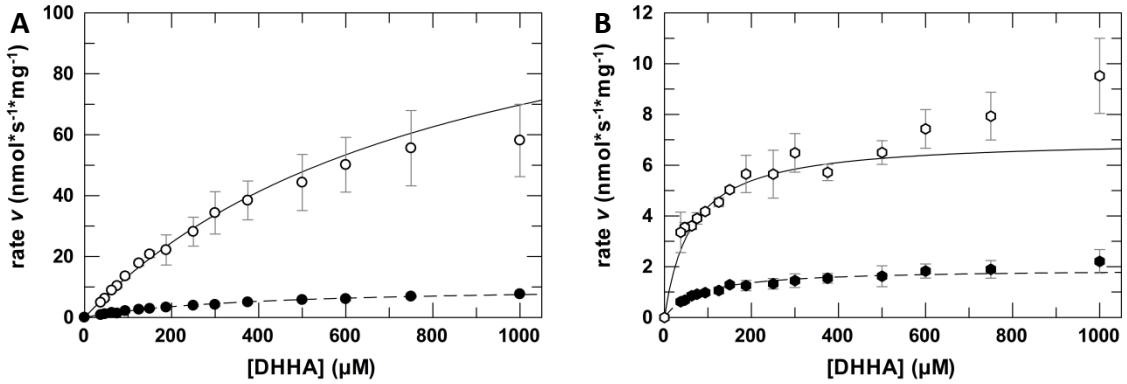

Figure 17: Enzyme kinetics for the conversion of light and heavy substrate isotopologues by a PhzF-orthologue from *Burkholderia glumae* BGR-1.
Kinetic plots (rate *v* as a function of substrate concentration) showing the turnover of the natural, light substrate DHHA (○ and ○) and of the heavy isotopologue d-DHHA (● and ●) in 50 mM sodium phosphate buffer pH 7.5 at 25 °C. Plot **A** represents the data obtained for the full length protein, while **B** shows the kinetic plots for the N-terminal truncated variant Δ123 (isolated isomerase domain). The reaction was followed via substrate depletion over time at 275 nm. After normalization to zero and background correction, averaged data from three independent measurements were fitted to a Michaelis-Menten model (— for DHHA and - - for d-DHHA) using GraFit 5.

An explanation for these results might be decreased protein stability due to the missing N-terminal domain in *Bglu*PhzΔ123. Furthermore, since the function of the N-terminal domain is unknown, it cannot entirely be ruled out that it plays a direct role in catalysis. At this point however, no conclusive hypothesis for enzymatic function can be established, especially as some of the gathered data for the N-terminally truncated domain show unexpected characteristics, *e.g.* an approximately 5-10-fold smaller K_M-value compared to the full-length enzyme, and thus have to be considered with caution. With regard to the current understanding of PhzF catalysis, no definite or convincing conclusion can be drawn from this data. Nevertheless, upon potential future uncovering of the presently unknown role of the N-terminal domain, additional information could contribute to this understanding.

4.2.6. Temperature dependency – Evidence for cooperativity?

4.2.6.1 Temperature dependency of apparent reaction rates and KIEs

Typically, when enzyme kinetic experiments are carried out at elevated temperatures, an accelerated substrate turnover is observed. This phenomenon can be explained by the Arrhenius-equation (Arrhenius, 1889; equation 13), which, at a defined temperature (*T),*

links a thermal energy barrier (activation energy E_A) and atomic motion (A) of a (bio)chemical process to its apparent reaction rate (k):

$$k = A \cdot e^{\frac{-E_A}{R \cdot T}} \quad \textbf{(13)}$$

Although an elevated temperature has no direct effect on the activation energy (E_A) of an enzymatic reaction, the temperature factor (T) in the exponential term of the Arrhenius-equation drastically affects the reaction rate, with the exponential function getting larger with higher temperatures. Additionally, the Arrhenius pre-exponential factor A, which is a product of the number of collisions Z and the proper orientation of the colliding molecules P ($A = Z \cdot P$) also depends on the temperature in form of decreased solvent viscosity and consequently enhanced protein/ligand diffusion.

Similar to individual reaction rates, kinetic isotope effects exhibit also a temperature dependency that can be described by the Arrhenius-equation (Arrhenius, 1889; Allemann and Scrutton, 2009; equation 14):

$$KIE = \frac{k_L}{k_H} = \frac{A_L}{A_H} \cdot e^{\frac{\Delta E_{A(H-L)}}{R \cdot T}} \quad \textbf{(14)}$$

The largest contribution to a KIE comes from the difference in activation energies for the light (L) and heavy (H) substrate isotopologue. In turn, the magnitude of the activation energy E_A for a specific reaction mainly depends on the different zero point energies (ZPE) of the reactants in the ground (GS) and transition state (TS) (Kohen and Klinman, 1999). Based on Heisenberg's uncertainty principle, protium (^{1}H), being a smaller particle, has a less defined location and therefore a higher ZPE than deuterium (^{2}H = D) (Heisenberg, 1927; Kohen and Klinman, 1999). This statement holds true for both, the ground as well as the transition state. However, in case of (bio)chemical reactions no atom alone, but rather the chemical bond, which is cleaved or formed during catalysis, accounts for different ZPEs of reactants. In the ground state, bond stretching (C-H or C-D) has a large impact on ZPE, but as the respective bond will be partially broken in the transition state, the influence on the ZPE will be smaller. In other words, the difference of ZPEs for light and heavy substrates is larger in the ground state than in the transition state and hence differing activation energies for two substrate isotopologues can be observed. Although, this relationship does not directly explain the temperature dependent reaction rates of

two isotopologues and their resulting kinetic isotope effect, an Arrhenius plot as shown in Figure 18 can promote a better understanding of this correlation.

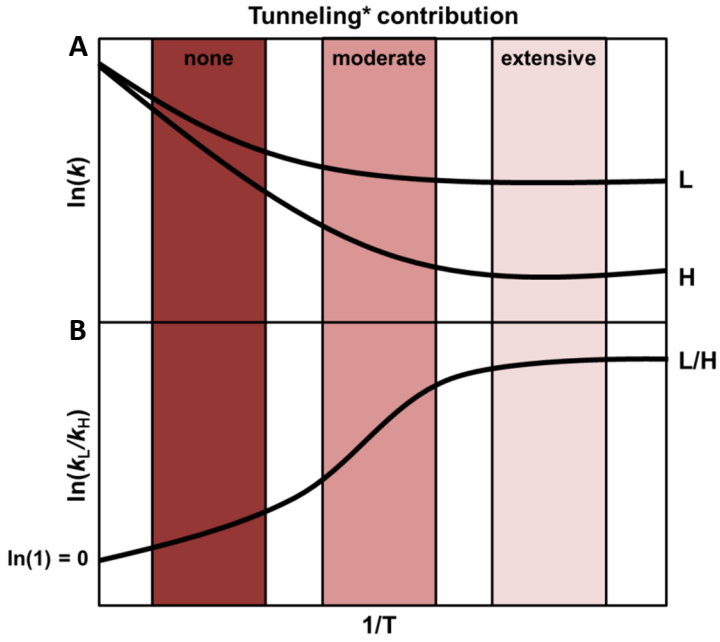

Figure 18: Theoretical, tunneling corrected Arrhenius plots for the temperature dependency of different isotopes in hydrogen transfer reactions.
Logarithmic plots for **A** the reaction rates of light (L) and heavy (H) isotopes as a function of temperature (1/T) and **B** the temperature-dependent proportionality of their kinetic isotope effects. The three highlighted areas are colored corresponding to the temperature range (low, medium, high) and illustrate the contribution of quantum tunneling to the observed reaction rates and KIEs. *Quantum tunneling itself is considered as temperature-independent. Figure adapted from Alleman and Scrutton 2009 (Chapter 7 p. 173).

The plot depicts that with increasing temperature (darker red) the reaction rates *k* for two isotopes increase until (at infinite temperature) they are uniform. It is also evident that at lower temperatures the rate difference for light (L) and heavy (H) isotopes is larger than at higher temperatures. Hence, their kinetic isotope effect ($\ln (k_L/k_H)$) is close to zero at elevated temperatures, but large at low temperatures. A reason for this varying temperature dependency is not only the different activation energy for two substrate isotopologues, but also the influence of so-called quantum tunneling on the reaction rate. In principle, tunneling can be observed for all atoms, however, hydrogen transfer reactions were found to be especially affected by this quantum effect. Again, according to Heisenberg's uncertainty principle, a particle exhibits an uncertainty in its position not only in the ground or transition state but also all along the reaction coordinate. This uncertainty might be estimated from the de Broglie wavelength of the particle (Broglie, 1970; Kohen and Klinman, 1999). At a certain position along the energy landscape (close to the transition state), the wavelength of the particle will be larger than the width of the

E_A barrier and thus it can cross/tunnel the barrier leading to product formation. Since the probability of tunneling correlates with the de Broglie wavelength of the particle, which in turn depends on its mass, protium (^1H), having a broader wavelength than deuterium (^2H), can tunnel easier than its heavier isotope. Hence, the influence of tunneling on reaction rates will be larger on lighter isotopes. This quantum effect explains why KIEs tend to be larger when tunneling strongly contributes to the reaction rate. Furthermore, the plots in Figure 18 show that the contribution of tunneling to a reaction is reduced with increasing temperatures, as under these conditions excess energy is available, hence, thermal activation is sufficient for turnover and tunneling can be disregarded. This means that at low temperatures, tunneling (strongly) contributes to the reaction rate of the light substrate, but less to the turnover rate of the heavy one and hence the KIE is high. With increasing temperatures this contribution diminishes, the two rates converge and consequently the KIE decreases.
It should be mentioned that the model described so far is simplified, as it considers only rigid E_A barriers. In some cases, *e.g.* when a high energy barrier correlates with a high tunneling rate, but shows no temperature dependency, besides its height also the barrier width and especially fluctuations in the barrier dimensions have to be considered.

In terms of PhzF catalysis, this means that a way to gain deeper insights into mechanistic details is to probe the temperature dependency of the observed kinetic isotope effects. As described before (*q.v.* paragraph 4.2.3.), the turnover of the light substrate isotopologue (DHHA) at 25 °C is faster than the one for the heavy isotopologue (d-DHHA) and hence the corresponding KIE is high (9.5 on k_{cat}). If indeed tunneling (strongly) contributes to the reaction rate (as already suggested in paragraph 4.2.3.), with increasing temperatures, this contribution should diminish, the two rates converge and consequently the KIE decrease.

In order to confirm this hypothesis, enzyme kinetic experiments using both light and heavy substrate isotopologue were carried out at 42 °C in two different buffer systems, the standard assay buffer as well as a buffer containing 90 % D_2O (Figure 19). As anticipated, substrate turnover by PhzF is accelerated at higher temperature. In case of the natural, light substrate DHHA a 1.5-fold increase of the apparent rate (k_{cat} = 5.15 s^{-1}) is observed at 42 °C in phosphate buffer (Table 11).

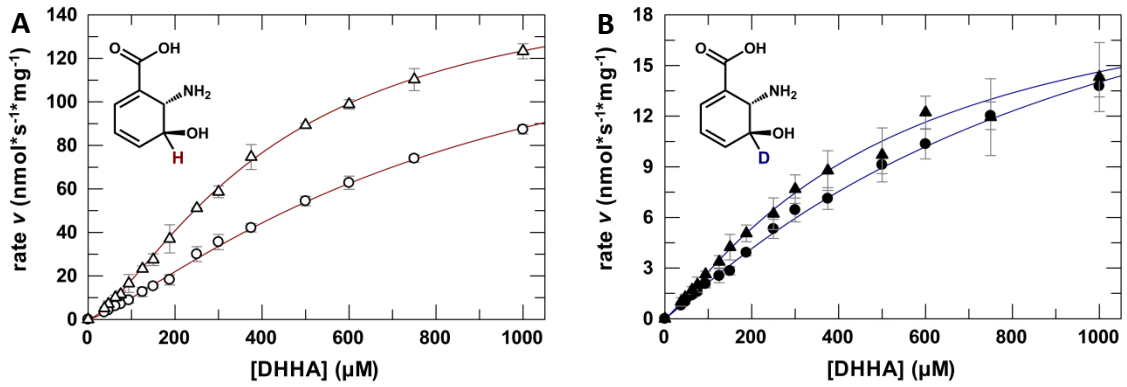

Figure 19: Enzyme kinetics for the isomerization of DHHA and d-DHHA by PhzF (*P. fl* 2-79) at 42 °C.
Kinetic plots (rate *v* as a function of substrate concentration) showing the turnover of **A** the light substrate DHHA and **B** the heavy isotopologue d-DHHA in 50 mM sodium phosphate buffer pH 7.5 (○ = DHHA; ● = d-DHHA) as well as in D_2O/50 mM sodium phosphate pH 7.5 (9:1) (△ = DHHA; ▲ = d-DHHA) at 42 °C. The reaction was followed via substrate depletion over time at 275 nm. After normalization to zero and background correction, averaged data from three independent measurements were fitted according to the Hill-equation (— for DHHA and — for d-DHHA) using GraFit 5. Inset: Structural formula of the substrates DHHA and d-DHHA, with the migrating proton (**H**) or deuterium (**D**) highlighted respectively.

Turnover of the heavy substrate isotopologue d-DHHA (k_{cat} = 0.93 s^{-1}) is even raised 2.5-fold compared to the reaction followed at 25 °C. In turn, a decreased magnitude of the apparent primary KIEs is detected, thus indicating a tunneling contribution in PhzF catalysis. This is further supported by the data obtained in the buffer containing 90 % D_2O which also yielded a smaller KIE than obtained at lower temperature (KIE (k_{cat}) = 7.5 at 42 °C *vs.* 12.8 at 25 °C, Table 9 and Table 11).

Table 11: Enzyme kinetic parameters for the conversion of both substrate isotopologues by the isomerase PhzF (*P. fl* 2-79) in different buffer systems at 42 °C.*

		k_{cat} (s^{-1})	$K_{1/2}$ (µM)	Hill-coefficient *n*	KIE_{app} (k_{cat})
sodium phosphate	DHHA	5.15 ± 0.32	852 ± 80	1.27 ± 0.03	5.5 ± 0.6
	d-DHHA	0.93 ± 0.09	1057 ± 161	1.07 ± 0.02	
D_2O : sodium phosphate (9:1)	DHHA	5.15 ± 0.09	424 ± 10	1.43 ± 0.02	7.5 ± 0.6
	d-DHHA	0.69 ± 0.05	514 ± 66	1.16 ± 0.04	

* The obtained values are averaged data of three independent measurements fitted according to the Hill-equation. All data were obtained in the respective buffer at 42 °C, normalized to zero, and background corrected.

In addition, when comparing the two buffer systems at 42 °C, the two rates for DHHA isomerization converge to a similar value and hence the corresponding solvent kinetic isotope effect (SIE) is completely abolished as it can be expected with increasing temperatures (data not shown). In case of the heavy substrate (d-DHHA), however, the SIE becomes inverted, *i.e.* a positive effect. As previously discussed in paragraph 4.2.3., the origin of the SIE for PhzF catalysis is still unclear, but, at least in case of d-DHHA the different tendencies (inverse SIE at 25 °C and normal SIE at 42 °C) might arise from the fact that the measured activities are much lower than for DHHA and thus lead to larger

uncertainties. Furthermore, the data obtained data at 42 °C displayed sigmoidal curves and hence were fitted using the Hill-equation (for details see below). Thus, they are not fully comparable to the data obtained at 25 °C (fitted to a Michaelis-Menten model) and hence the aforementioned interpretation of their temperature dependency should be considered with caution, especially regarding the absolute values.

4.2.6.2. Sigmoidal curves indicate cooperativity in PhzF catalysis

Another observation was made when kinetic data for the two DHHA isotopologues were recorded at 42 °C. The obtained plots (rate *v* as a function of substrate concentration) show a slightly sigmoidal curvature and as such are not fittable with the Michaelis-Menten-equation. In fact, sigmoidal kinetic plots were also observed under other conditions, *e.g.* in a buffer consisting of 50 mM HEPES pH 7.5 (data not shown) or when different active site variants of PhzF were tested for substrate conversion (see paragraph 4.2.9.).

Since a sigmoidal curve is indicative of cooperative substrate binding, the data were fitted according to the Hill-equation to evaluate the degree of cooperativity (Table 11). In all four tested cases, positive cooperativity is observed. However, with Hill-coefficients around a value of $n = 1$, turnover of the deuterated substrates seems to be less influenced by cooperativity. Although there is no universal explanation for this small positive cooperativity observed under some conditions, it might be explained with regard to previously obtained structural data of PhzF (Blankenfeldt *et al*., 2004).

From these structures, it is known that, upon substrate binding, PhzF adopts a closed conformation, whereupon not only the active site cleft of one monomer closes, but also the enclosed surface at the dimer interface increases when the two closed monomers rotate and tilt towards each other (see also Figure 23). This structural feature might indeed hint towards cooperativity such as closing of the active site of one monomer could influence substrate affinity and/or catalytic efficiency of the other monomer. Cooperativity could be mediated via the contacting surface residues such as R244 and E40* which are forming a salt bridge, or via Y4, which is involved in hydrogen bonding with its counterpart from the second monomer. Indeed, the structurally related diaminopimelate epimerase (DAP) was - despite previous reports (Cirilli *et al*., 1998; Lloyd *et al*., 2004) - not only found to be a dimer in solution, but Perugini and co-workers also

discovered that its enzymatic activity strongly depends on dimerization, as a monomeric variant with Y268 (Y4 in PhzF) mutated to an alanine, was completely inactive (Hor *et al.*, 2013). As described in a subsequent paragraph, when a similar mutation (Y4A) is introduced into PhzF, no protein expression could be observed. Although this observation does not prove that cooperativity plays a role in PhzF catalysis, it at least emphasizes the importance of dimerization for PhzF in terms of stability and enzymatic activity.

4.2.7. Substrate spectrum and specificity

4.2.7.1. Finding new substrates for PhzF

Supposed to serve as mechanistic probes, substrate analogs such as 2*S*,3*S*-dihydro-3-hydroxysalicylic acid (DHHS) or *O*-alkylated derivatives of DHHA, namely 2,3-dihydro-3-methoxy- or 2,3-dihydro-3-ethoxy anthranilic acid (*O*-Me-DHHA and *O*-Et-DHHA respectively) were tested for enzymatic conversion by PhzF (Figure 20).

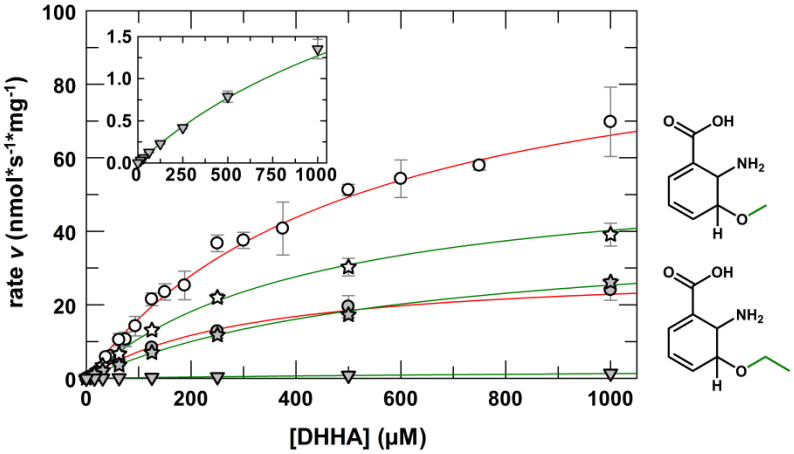

Figure 20: Enzyme kinetics for the isomerization of DHHA and two *O*-alkylated substrate analogs by PhzF (*P. fl* 2-79). The turnover of DHHA (○), racemic DHHA (●), *trans*-2*S*,3*S*-*O*-methylated DHHA (*O*-Me-DHHA, ✿), racemic *O*-Me-DHHA (✿), and racemic *O*-ethylated DHHA (*O*-Et-DHHA, ▽) was followed via substrate depletion over time at 275 nm in 50 mM sodium phosphate buffer pH 7.5 at 25 °C. Kinetic plots (rate *v* as a function of substrate concentration) of normalized, background corrected, and averaged data from three independent measurements were fitted to a Michaelis-Menten model (— for DHHA and — for *O*-alkylated derivatives) using GraFit 5. Inset: Zoom on the kinetic plot of *O*-Et-DHHA (labelling as described before). Adjacent: Structural formula of the two O-alkylated substrates *O*-Me-DHHA (top) and *O*-Et-DHHA (bottom), with the alkyl-group shown with green dashes (—).

Among these molecules the derivative bearing a simple hydroxyl group (DHHA) is the best substrate for PhzF, whereas the methoxy-modification leads to a slower turnover with a k_{cat} of 1.86 s^{-1} (K_M = 437 µM) and 1.33 s^{-1} (K_M = 622 µM) for enantiopure and racemic *O*-Me-DHHA respectively. For the ethoxy-derivative, detectable conversion (k_{cat} = 0.12 s^{-1}

and K_M = 1842 µM) is only seen when the enzyme concentration is increased to 1 µM (Table 12). For DHHS no conversion could be detected at all.

Table 12: Enzyme kinetic parameters for the turnover of different native and synthetic substrate analogs by the isomerase PhzF (*P. fl* 2-79).*

	k_{cat} (s^{-1})	K_M (µM)	k_{cat}/K_M ($M^{-1}s^{-1}$)
racemic DHHA	0.97 ± 0.06	314 ± 24	3088 ± 299
trans-2*S*,3*S*-*O*-Me -DHHA	1.86 ± 0.13	437 ± 47	4268 ± 545
racemic *O*-Me-DHHA	1.33 ± 0.08	622 ± 56	2134 ± 231
racemic *O*-Et-DHHA	0.12 ± 0.02	1842 ± 355	63 ± 17

* The obtained values are averaged data of three independent measurements fitted to a Michaelis-Menten model. All data were obtained in 50 mM sodium phosphate pH 7.5 at 25 °C, normalized to zero, and background corrected.

^{1}H-NMR experiments confirmed these findings and showed that derivatives with an even larger alkoxy-substituent at C3, such as *O*-n-propylated DHHA (*O*-*n*Pr-DHHA), are not converted by PhzF at all (Mario Leypold). Furthermore, these measurements revealed that the *O*-alkylated compounds cannot undergo tautomerization to form the final ketamine, but rather eliminate ammonia to yield aromatic products (Scheme 9).

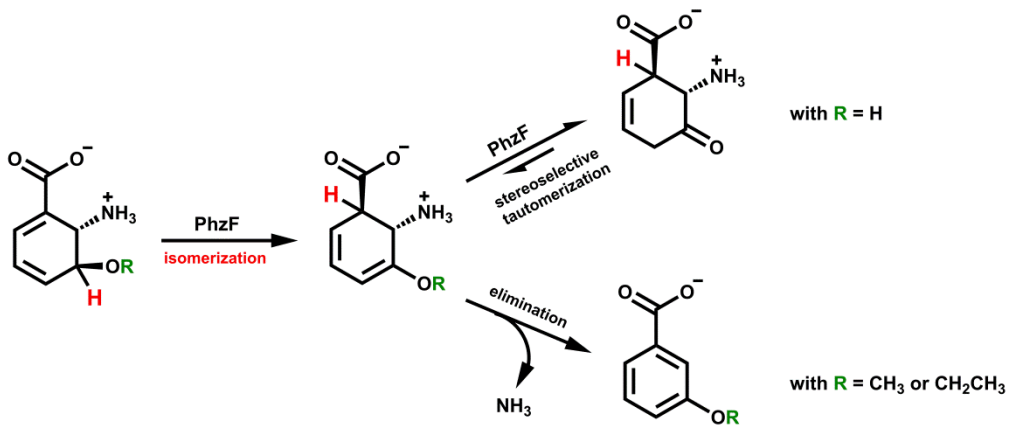

Scheme 9: Potential pathway for the PhzF (*P. fl* 2-79)-catalyzed isomerization of different *O*-alkylated DHHA derivatives and their modification dependent product formation.
It can be assumed that, independent of the substituent (**R**), the first step of catalysis constitutes the [1,5]-hydrogen shift (**H**) to the intermediate AHCDC or to its *O*-alkylated derivatives. The simple 3-hydroxy-AHCDC undergoes PhzF catalyzed stereoselective tautomerization to the ensuing ketamine AOCHC. Intermediates with larger alkyl-substituents (**R**) cannot undergo this tautomerization, but probably eliminate ammonia instead to yield the aromatic 3-methoxy- or 3-ethoxy-benzoeic acid respectively.

A comparison of the kinetic parameters obtained for the enantiopure compounds or their corresponding racemic mixture (50:50) reveals that substrate turnover rates are lower with racemic mixtures. This effect is more pronounced for DHHA with k_{cat}–values of 3.23 s^{-1} and 0.97 s^{-1} for the enantiopure compound and the racemic mixture respectively, but can also be observed for the methoxy-derivative (Table 12). A similar tendency is also observed for k_{cat}/K_M, *i.e.* the catalytic efficiency decreases not only with increasing size of

the alkyl-substituent (k_{cat}/K_M: DHHA > *O*-Me-DHHA > *O*-Et-DHHA), but is also negatively affected by the presence of the other substrate enantiomorph (2*R*,3*R*) in the racemic mixtures.

From calculations and the published structure (PDB entry 1U1X; Blankenfeldt *et al*., 2004), which indicate a unique stereochemistry of the reaction, it is anticipated that the 2*R*,3*R*-enantiomer of DHHA (*trans*-2*R*,3*R*-dihydro-3-hydroxyanthranilc acid = *ent*-DHHA) and consequently all *O*-alkylated derivatives (*ent*-*O*-Me-DHHA and *ent*-*O*-Et-DHHA) with similar chirality cannot be converted by PhzF (*P. fl* 2-79). In order to confirm this hypothesis, conversion of DHHA, d-DHHA and their respective enantiomers was tested under standard assay conditions but with a 12.5-fold higher PhzF concentration (500 nM) to increase the probability of detecting measurable signal for conversion of the 2*R*,3*R*-enantiomers. As shown in Figure 21, under the tested conditions no turnover of *ent*-DHHA or *ent*-d-DHHA was detected, whereas a fast decay of the UV-Vis signal of DHHA and d-DHHA was observed.

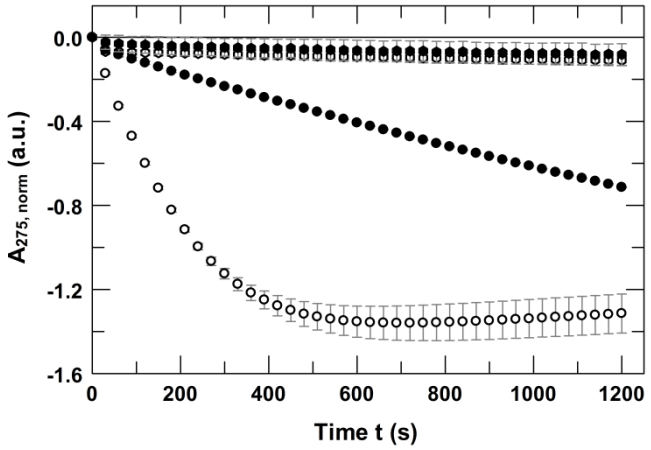

Figure 21: Time traces for the conversion of different substrate enantiomorphs by the isomerase PhzF from *P. fluorescens* 2-79.
The conversion of DHHA (○), *ent*-DHHA (○), d-DHHA (●), and *ent*-d-DHHA (●), each 1 mM, using 500 nM dimeric PhzF was followed for 1200 s and the normalized absorbance signal was plotted as a function of time (t). All data were obtained in standard assay buffer at 25 °C, normalized to zero, and background corrected.

Although the data in Figure 21 show that the 2*R*,3*R*-enantiomers are not converted by PhzF, it cannot be excluded that these substrate analogs still bind to the active site of the enzyme and thereby act as competitive inhibitors. In order to confirm this hypothesis, binding measurements of *ent*-DHHA and other substrates, substrate analogs, or potential inhibitors to wild type PhzF or an inactive E45Q variant were carried out using isothermal titration calorimetry (ITC). However, no binding of either of the two DHHA-enantiomers

(DHHA or *ent*-DHHA) is observed under the tested conditions (Figure 22A and Figure A5A). In a similar way, no binding to wild type PhzF is observed for DHHS and the two enantiomers of the potential inhibitor 2,3,4,5-tetrahydro-3-hydroxy anthranilic acid (H_2-DHHA; Figure A5B-D). Since these results were not anticipated, additional ITC experiments with a known PhzF binder, 3-hydroxy anthranilic acid (3OHAA; Blankenfeldt *et al., 2004)*, and anthranilic acid (AA) were performed. Indeed, binding in the µM range could be observed for both compounds (Figure 22 and Figures A6 - A8 in appendix A1).

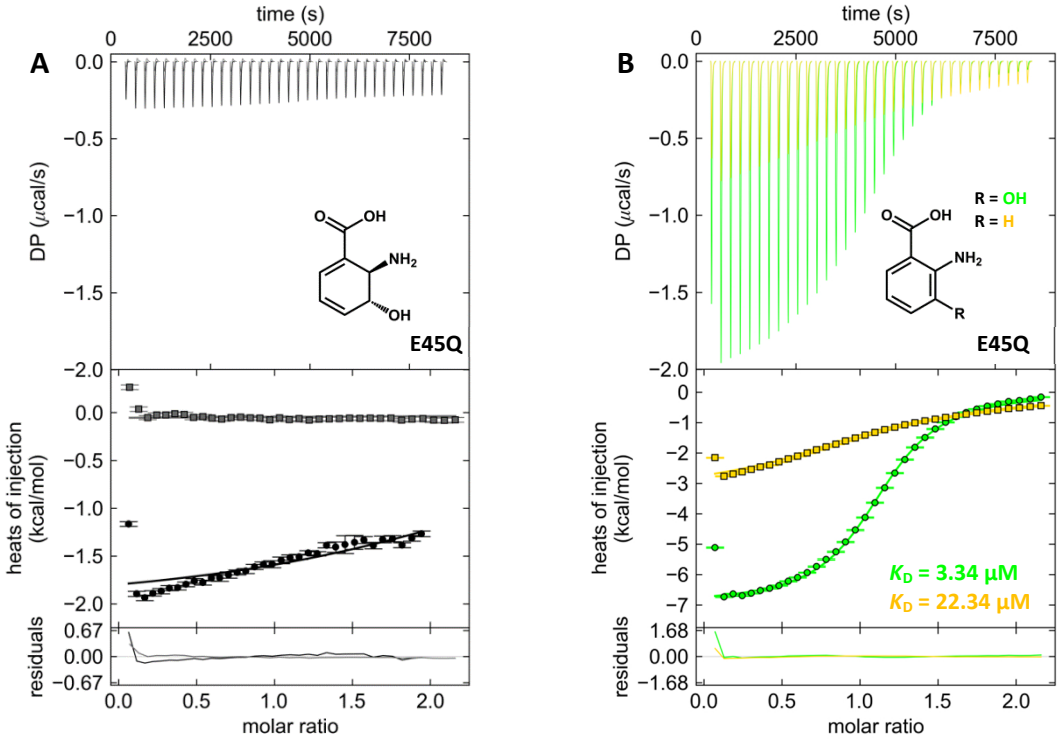

Figure 22: ITC profiles for affinity titrations of different DHHA-substrate analogs against PhzF E45Q.
The individual plots show the generated heat per injection at different time points (upper panel), the fitted binding curves for individual titration experiments (middle panel), and the quality of the fit (lower panel). **A** Titration of the 2*R*,3*R*-substrate enantiomorph *ent*-DHHA (■ = 1 mM and ● = 450 µM) to PhzF E45Q (■ = 100 µM and ● = 50 µM). For both experiments, no binding event could be observed. **B** Titration of each 1 mM of 3-hydroxy anthranilic acid (3OHAA, ●) and anthranilic acid (AA, ■) to 100 µM PhzF E45Q. Binding of 3OHAA and AA to PhzF E45Q was exothermic, with 1:1 stoichiometry and occurred with K_D values of 3.34 µM and 22.34 µM, respectively. All data were analyzed and fitted using the programs NITPIC (Keller *et al.*, 2012; Scheuermann and Brautigam, 2015) and SEDPHAT (Houtman *et al.*, 2007; Zhao *et al.*, 2015) and plotted using the program GUSSI (Brautigam, 2015).

In addition, the binding parameters and affinity constants obtained by ITC (Table 13) for 3OHAA are in good agreement with the published values, obtained from fluorescence spectroscopy measurements (K_D (WT) = 1.4 µM; K_D (E45Q) = 4.0 µM; Blankenfeldt *et al.*, 2004). In comparison to 3OHAA, a decreased affinity of AA towards PhzF is observed. As known from PhzF wild type structures in complex with DHHA or 3OHAA (PDB entries 1U1X and 1U1W respectively), the C3-hydroxy group of the ligands is involved in hydrogen

bonding to a conserved active site water molecule (~2.7 Å). Furthermore two additional, however weak hydrogen bonds (~3.4 Å) between the hydroxy group and two important active site residues, E45 and D208, stabilize the residues in the active site. Anthranilic acid in contrast to 3OHAA is lacking this hydroxy group and in consequence, its affinity is decreased.

Table 13: Thermodynamic binding parameters for ITC affinity titrations of 3OHAA and AA to wild type PhzF and variant E45Q.*

Ligand	PhzF variant	K_D (µM)	ΔG (kcal mol^{-1})	ΔH (kcal mol^{-1})	-T*ΔS (kcal mol^{-1})	*N*	c
3OHAA	WT	0.99 ± 0.01	-8.19 ± 0.01	-8.55 ± 0.17	0.36 ± 0.18	1.0 ± 0.02	50.1 ± 1.09
		1.07 ± 0.21	-8.16 ± 0.12	-6.34 ± 0.48	-1.82 ± 0.55	0.93 ± 0.04	43.3 ± 8.75
	E45Q	4.01 ± 1.22	-7.39 ± 0.17	-8.39 ± 0.80	1.00 ± 0.96	0.87 ± 0.04	10.89 ± 3.34
		2.26 ± 0.07	-7.70 ± 0.02	-5.89 ± 0.19	-1.82 ± 0.20	1.07 ± 0.02	23.77 ± 0.83
	†E45Q 100µM	3.34	-7.47	-7.83	0.36	1.15	34.32
AA	WT	14.10 ± 0.46	-6.62 ± 0.02	-6.07 ± 0.40	-0.55 ± 0.42	0.84 ± 0.02	2.99 ± 0.12
	E45Q	26.34 ± 2.42	-6.25 ± 0.06	-3.99 ± 0.26	-2.26 ± 0.31	0.89 ± 0.02	1.69 ± 0.16
	†E45Q 100µM	22.34	-6.35	-3.90	-2.45	1.06	4.76

* All ITC experiments were carried out at 25 °C in 20 mM TRIS/HCl pH 7.5, 150 mM NaCl, 10 % (v/v) glycerol. 450 µM of the respective compound were titrated to 50 µM PhzF. The data are averaged from at least two independent measurements. † In contrast to the afore described experimental setup, 1 mM of the respective compound were titrated to 100 µM PhzF E45Q. The presented data derive from a single titration experiment.

The binding data for these two aromatic anthranilic acid derivatives indicate not only that the tested proteins were in fact stable and active, but also hint towards very week binding (K_D >> 100 µM) of the other tested substrates or inhibitors, such as DHHA, *ent*-DHHA, or H_2-DHHA. Attempts to obtain binding constants for these ligands by other methods, such as microscale thermophoresis (MST) remained unsuccessful, since labeling of the protein proved difficult and in consequence, no reliable data could be obtained from these experiments.

Despite lacking affinity parameters for many of the tested substrates or substrate analogs, soaking experiments and co-crystallization trials of wild type protein or different active site variants of PhzF with various ligands were carried out. Although crystals could easily be grown and even yielded structures at very high resolution of up to 1.18 Å (Figure A9 and Table A5), in most cases the electron density maps did not provide any clear evidence for a bound ligand. Yet finally, one new complex structure of PhzF could be obtained (Figure 23 and Table 14). Surprisingly, this structure of the inactive PhzF variant E45Q co-crystallized with racemic *O*-Et-DHHA was found in the open conformation (RMSD = 0.128 over 1826 atoms to PDB entry 1U1V (open) *vs*. RMSD = 0.736 over 1546 atoms to PDB

entry 1U1X (closed), Figure 23A), which was so far only observed in the absence of a specific ligand (Blankenfeldt *et al.*, 2004). In addition, instead of the productive DHHA-enantiomer (2*S*,3*S*), the non-convertible enantiomorph *ent*-*O*-Et-DHHA was bound to the active site (Figure 23B and C).

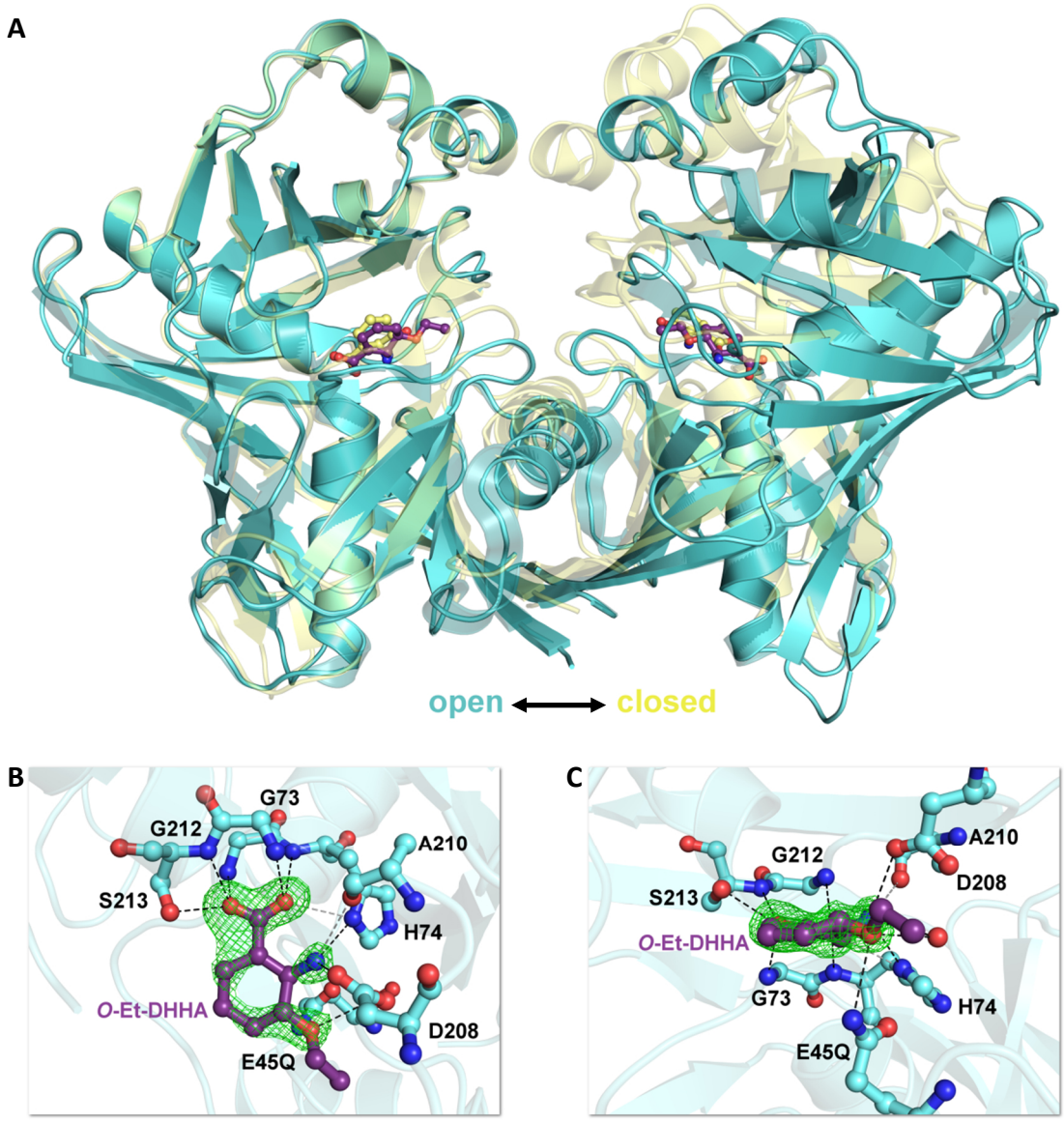

Figure 23: Crystal structure of PhzF variant E45Q (*P. fl* 2-79) in complex with *ent*-*O*-Et-DHHA.
A Overall topology of the biological, dimeric assembly of the complex shown in an open conformation (aquamarine). The ligand *O*-Et-DHHA is shown in dark purple. For comparison: Overlay with a closed conformation structure of PhzF WT in complex with the natural substrate DHHA shown in palegoldenrod (PDB entry 1U1X, Blankenfeldt *et al.*, 2004). The ligands in both structures are highlighted as balls and sticks. **B** and **C** Close-up on the active site of the complex with *O*-Et-DHHA from front (**B**) and side view (**C**). The active site residues as well as the ligand are shown as balls and sticks. Additionally the ligand is depicted in its Fourier difference density (mF_o-DF_c) omit map contoured at 3σ in green. Its hydrogen-bonding network formed by strong (- - -; < 3.2 Å) or weaker (· · ·; ≥ 3.2 Å) interactions is highlighted.

Upon careful inspection of the new crystal structure, it becomes evident that, in comparison to previously obtained complex structures of the closed conformation, *e.g.*

with bound DHHA (PDB entry 1U1X; Blankenfeldt *et al.*, 2004), the hydrogen-bonding pattern in the active site is slightly altered. The ligand *ent*-*O*-Et-DHHA is stabilized by twelve hydrogen bonds - ten strong and two weaker ones (≥ 3.2 Å) - with seven active site residues and one highly coordinated water molecule (water 142). The carboxyl moiety of the ligand is tightly bound to the active site, with one oxygen stabilized by hydrogen bonds to the γ-hydroxyl of S213 and the backbone amide of the same serine as well as the one of G73. Stabilization of the other oxygen of the carboxylate is facilitated via a hydrogen-bonding network comprising of two strong hydrogen bonds to the backbone amides of G212 and H74 and additionally via a weak bond to the N_{δ}-moiety of H74. The C2-amino group of *ent*-*O*-Et-DHHA is stabilized by three strong and one weak (≥ 3.2 Å) hydrogen bonds. Similar to the previously published DHHA-complex (Blankenfeldt *et al.*, 2004) H74 and D208 are involved in binding of this moiety, but in addition a tightly bound water molecule (water 142) coordinates the group. Moreover, a fourth, weaker hydrogen bond between the ligand and the main chain carbonyl of A210 can be found. In contrast, the "catalytic" residue Q45 (E45 in the complex with DHHA) is no longer in hydrogen-bonding distance to the amino-moiety. The coordination of the C3-alkoxy group is drastically altered, too. The tightly bound water 142 as well as the amide group of Q45 coordinate the bridging oxygen of the alkoxy-group, whereas binding to D208 is no longer observed. An overlay of the two complex structures, with *ent*-*O*-Et-DHHA or DHHA, reveals that the ethyl-moiety of the former complex occupies the position of the conserved water in the active site of the latter complex (data not shown).

Altogether, these findings indicate that the crystal structure with *ent*-*O*-Et-DHHA represents a non-productive complex. It might be possible that with *O*-ethylated DHHA bound, the protein cannot adopt the closed conformation of a productive complex. The open and therefore less stable conformation however might explain why turnover of the ethoxy-derivative is much slower and less efficient than turnover of the native substrate DHHA. Yet, since the obtained structure constitutes a complex of an inactive PhzF variant with a non-convertible substrate enantiomer, it cannot entirely be ruled out that PhzF might adopt a different productive conformation for complexes with convertible substrates bearing a bigger alkoxy-substituent at position C3. In any case, the structure

showed that indeed the 2*R*,3*R*-substrate enantiomers can bind to the active site of the enzyme, even though with weak affinity.

Table 14: Data collection and refinement statistics for PhzF (*P. fl* 2-79) in complex with *O*-ethylated DHHA

	Complex with *O*-ethylated DHHA
Data collection[1]	
Beamline[†]	MX BL14.1, BESSY II
Wavelength (Å)	0.91841
Resolution range (Å)	77.87 – 1.71 (1.74 – 1. 71)
Space group	$P3_221$
unit cell dimensions	
a, b, c (Å)	56.03, 56.03, 155.74
α, β, γ (°)	90, 90, 120
Mosaicity (°)[‡]	0.07
Measured reflections	164740 (7396)
Unique reflections	31593 (1662)
Multiplicity	5.2 (4.5)
Mean *I*/σ(*I*)	8.9 (1.9)
$CC_{1/2}$*	0.995 (0.573)
Completeness (%)	99.9 (99.9)
R_{meas}[§]	13.8 (86.2)
$R_{p.i.m.}$[¶]	6.0 (40.8)
Refinement	
Resolution range (Å)	46.33 – 1.71 (1.76 – 1.71)
R_{cryst} (%)	14.92 (23.78)
R_{free} (%)	17.34 (27.20)
No. of non H-atoms	
Protein	2170
Ligand / Ion	47
Water	242
Average B-factors (Å²)	
Protein	16.3
Ligand / Ion	34.9
Water	33.8
R.m.s deviations	
Bond lengths (Å)	0.007
Bond angles (°)	0.945
Ramachandran plot (%)	
Favored regions	98.6
Outliers	0
MolProbity score [#]	1.21

Values in parentheses are for the highest resolution shell -

[1] The dataset was collected from a single crystal.

[†] BESSY II: Berlin Electron Storage Ring Society for Synchrotron Radiation, Helmholtz Centre Berlin, Berlin, Germany.

[‡] Mosaicity values reported by *XDS* (Kabsch, 2010).

* $CC_{1/2}$ is the correlation coefficient between two random half datasets (Karplus and Diederichs, 2012)

[§] $R_{meas} = \sum_{hkl}\{N(hkl)/[N(hkl)-1]\}^{1/2}\sum_i|I_i(hkl)-\langle I(hkl)\rangle|\,/\,\sum_{hkl}\sum_i I_i\,(hkl)$, where *N(hkl* is the number of observations of the reflection with index *hkl* and $I_i(hkl)$ is the intensity of its *i*th observation (Diederichs and Karplus, 1997);

[¶] $R_{p.i.m.} = \sum_{hkl}\{1/[N(hkl)-1]\}^{1/2}\sum_i|I_i(hkl)-\langle I(hkl)\rangle|/\sum_{hkl}\sum_i I_i(hkl)$ (Weiss, 2001)

[#] As reported by *MolProbity* (http://molprobity.biochem.duke.edu/ (Chen *et al*., 2010)

4.2.7.2. Potential PhzF-inhibitors

In the course of investigations of PhzF's enzymatic activity also two enantiomers of the substrate analog 2,3,4,5-tetrahydro-3-hydroxy anthranilic acid (H_2-DHHA; Figure 24) were analyzed for conversion.

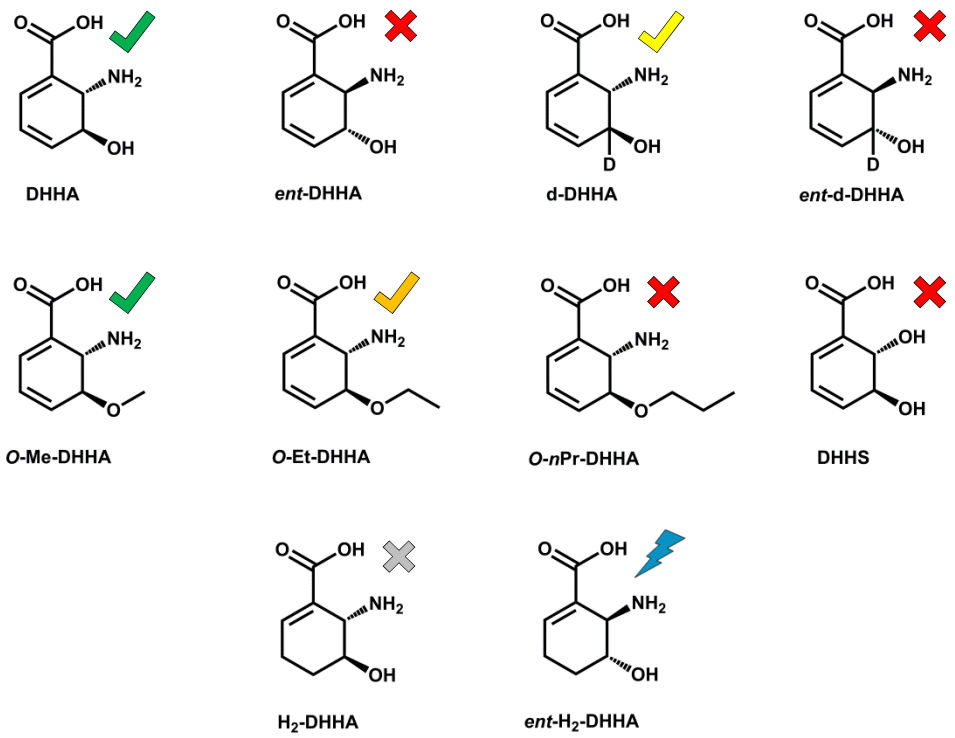

Figure 24: Overview of different PhzF substrates, substrate analogs, and inhibitors.
The symbols illustrate the interaction of the respective compound with PhzF. The small check marks (✔) indicate whether these compounds are substrates for PhzF, with the colors specifying the velocity of the turnover (fast, slow, very slow). The red and gray crosses (✖) symbolize that these compounds cannot be converted by PhzF (*P. fl* 2-79) with H_2-DHHA (🗵) also being no inhibitor for PhzF catalysis. The blue lightning (🗲) specifies that this compound is a competitive inhibitor.

However, attempts to monitor H_2-DHHA depletion directly under standard assay conditions failed, as the compound does not show any absorption at 275 nm. Since also binding measurements and crystallization experiments (Figure A9 and Table A5) remained unsuccessful, the inhibitory potency of H_2-DHHA on substrate conversion was evaluated. It was anticipated that, regardless of its own conversion, the high structural similarity of this compound to the substrate DHHA would qualify it as a potential competitive inhibitor. However, for the 2*S*,3*S*-enantiomer of H_2-DHHA no inhibition of DHHA-isomerization is observed, independently of the substrate concentration used (Figure 25). Though surprising, these data also show that H_2-DHHA is no substrate for PhzF, since otherwise it would compete with the native substrate for conversion.

In contrast, when the other H_2-DHHA enantiomer (*ent*-H_2-DHHA) is titrated against high (1 mM) or lower (125 µM) DHHA concentrations a decrease in substrate turnover is observed. As estimated from the data shown in Figure 25, IC_{50}-values for this compound are in the high µM-range, *i.e.* between 150 and 550 µM. In addition, these data confirm

that indeed, although not detectable with calorimetric experiments, *ent*-H2-DHHA can bind to PhzF, albeit with low affinity.

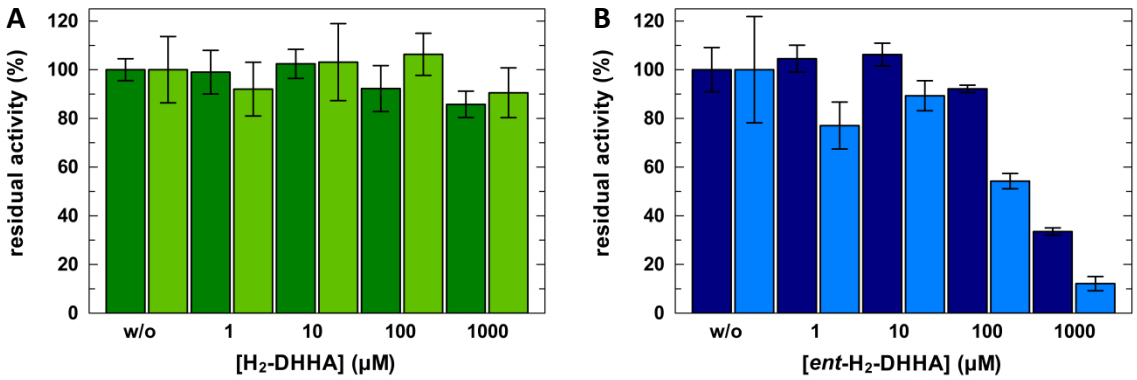

Figure 25: Inhibition of PhzF catalyzed DHHA isomerization by two enantiomorphs of the substrate analog H_2-DHHA. Residual activity of DHHA turnover as a function of inhibitor concentrations is plotted in **A** for the dose-response of H_2-DHHA (,) and **B** for the enantiomorph *ent*-H_2-DHHA (,). Increasing inhibitor concentrations were titrated in presence of 1 mM (dark **green**/**blue**) or 125 µM (light green/blue) DHHA respectively. PhzF was used at a concentration of 40 nM (dimer) in all assays. All data were obtained in standard assay buffer consisting of 50 mM sodium phosphate pH 7.5 at 25 °C, normalized to zero, background corrected, and averaged from three independent measurements.

Altogether, these findings suggest that *ent*-H_2-DHHA and similar substrate analogs might be starting points for PhzF inhibitor development.

4.2.8. Exploring the active site of PhzF with generated enzyme variants

For biochemical characterization of PhzF's isomerization mechanism various active site variants of the protein from *Pseudomonas fluorescens* 2-79 were either generated in context of this work or already available from a previous study (Blankenfeldt *et al.*, 2004), such as the active site variants (E45Q/A, D208A/T and H74A) or a dimer interface variant (N42A). Mutagenesis was based on preliminary knowledge of the reactivity of the already available mutants. As described in Blankenfeldt *et al.* (2004) mutation of the catalytic residue E45 to alanine (E45A) or glutamine (E45Q) completely abolished enzymatic activity without impairing substrate binding. Indeed, when following the conversion of racemic DHHA using 500 nM final concentration of each variant, no conversion of this substrate could be observed (data not shown). Assuming that the carboxyl group of E45 plays an important role in catalysis and thus mutations to alanine or glutamine eventually lead to a complete loss of activity, two additional strategies were employed. One attempt was a so-called chemical rescue with sodium acetate or sodium formate (10 and 50 mM) as additives to the assay solution containing E45A. Both anions were supposed to mimic

the carboxyl moiety of E45 and thus restore, at least partially, catalytic activity. However, when incubating variant E45A with either of the two salts, no turnover of DHHA is observed, *i.e.* chemical rescue failed (data not shown). In order to test whether a protonation susceptible side chain alone is sufficient for catalysis or if spatial factors play an important role as well, the variant E45D was generated, which still bears a carboxyl group similar to the wild type enzyme, but with a shorter side chain. Likewise, D208, from previous analysis of the variants D208A/T known to be involved in substrate binding, was mutated to a glutamate (D208E). In addition, a double variant, carrying both mutations (E45D/D208E) was generated. When tested for substrate conversion, none of these five PhzF variants (E45D, D208A/T/E and E45D/D208E) showed enzymatic activity (data not shown). These results confirm the importance of a specific environment in the active site for PhzF catalysis and demonstrate that even "small" changes like a mutation of E45 to a glutamine or aspartate can cause complete depletion of enzymatic activity.

In a way, the double variant E45D/D208E represents an inversion of the active site, hence this variant was not only tested for activity on the racemic mixture, but also on both substrate enantiomorphs (DHHA and *ent*-DHHA), though with similar results as observed for the racemic mixture, *i.e.* no conversion (data not shown).

Besides E45 and D208, there are two other important active site residues, S213 and H74. From crystal structures (Blankenfeldt *et al.*, 2004 and this work) it is evident that the serine, together with the positive helix dipoles of the two central α-helices α2 and α6, is mainly involved in positioning and binding of the carboxyl group of the substrate. A mutation to alanine (S213A) would presumably impair substrate binding and hence lead to complete loss of activity. The predominant role of H74 is to provide a hydrogen-bonding network for the substrate. Surprisingly, previously obtained biochemical data (Blankenfeldt *et al.*, 2004) showed that replacement of this histidine with an alanine (H74A) does not abolish enzymatic activity entirely but decreases it fourfold. Indeed, when conversion of the racemic substrate by H74A was investigated, turnover of DHHA could be confirmed, albeit with a k_{cat} of $0.07 \pm 0.01\ s^{-1}$ ($k_{cat}/K_M = 245 \pm 63\ M^{-1}\ s^{-1}$) corresponding to a 15-fold decrease compared to wild type PhzF. This discrepancy might be due to the use of the racemic mixture rather than pure DHHA in the assay. However, an additional experiment with variant H74A and enantiopure DHHA yielded an even larger

difference in enzymatic activity compared to wild type PhzF (data not shown). Despite the order of magnitude, analysis of the structure of H74A in the open form (PDB entry 1XUB, Blankenfeldt *et al*., 2004) can explain why substrate turnover was observed after all. In this structure, the space that is occupied by the imidazole ring of H74 in wild type PhzF was filled with water molecules instead. These water molecules replace the N_δ-atom of the imidazole moiety as hydrogen bond acceptor and hence secure necessary formation of a hydrogen-bonding network for the substrate. In order to address the role of H74 further, three additional variants, H74L, H74N, and H74D were generated and tested for activity on racemic DHHA. H74L did not show any activity in the assay most likely due to the large, yet hydrophobic sidechain of this amino acid. It occupies a similar spatial envelope as the imidazole ring of the histidine and thus prevents water molecules from binding. Introduction of an asparagine at position 74, which carries a polar, but uncharged sidechain of similar size to leucine aimed at restoring the hydrogen-bonding network. Indeed, when testing this variant in the assay, conversion of the racemic substrate is observed, however even slower than for variant H74A (Table 15).

Table 15: Enzyme kinetic parameters for the turnover of racemic DHHA by different PhzF variants.*

PhzF variant	k_{cat} (s^{-1})	K_M (µM)	k_{cat}/K_M ($M^{-1}s^{-1}$)	$K_{1/2}$ (µM)	Hill-coefficient *n*
WT	1.01 ± 0.03	-	-	610 ± 28	1.64 ± 0.04
N42A	0.18 ± 0.01	558 ± 68	328 ± 44	-	-
	0.15 ± 0.00	-	-	352 ± 20	1.19 ± 0.03
H74N	0.02 ± 0.00	31 ± 2	558 ± 34	-	
	0.02 ± 0.00	-		35 ± 4	0.78 ± 0.11
H74A	0.07 ± 0.01	284 ± 63	246 ± 63	-	

* The obtained values are averaged data of three independent measurements fitted either to a Michaelis-Menten model or to the Hill-equation as indicated. All data were obtained in 50 mM sodium phosphate pH 7.5 at 25 °C, normalized to zero, and background corrected.

Finally, when an aspartate (H74D) instead of the asparagine is introduced at this position, substrate turnover is completely abolished. Although a polar, potentially negatively charged sidechain, as in case of aspartate could stabilize the positively charged amino group of the substrate, an exchange of the basic amino acid histidine with an acidic aspartate, drastically alters the overall active site protonation and charge distribution, which was found to be crucial for PhzF catalysis in QC/MM calculations.

In a recent publication the enzymatic activity of the structurally related bacterial diaminopimelate epimerase (DAP) was analyzed (Hor *et al.*, 2013). The authors were specifically interested in the interconnection of dimerization and enzymatic activity and

indeed found that dimer formation is essential for DAP mediated catalysis. In order to address whether a similar behavior could be observed for PhzF, two variants with mutations at the dimer interface (N42A and Y4A; Figure A10 in appendix A1) were tested for enzymatic activity. Variant Y4A is equivalent to the reported mutant of DAP (Y268A), *i.e.* the amino acid is located at a similar position and thus mediates a similar interaction. However, overexpression of the Y4A variant of PhzF remained unsuccessful and hence might indicate that this residue is essential for dimerization and protein stability.

Residue N42 is located at the dimer interface of PhzF, adjacent to the entrance of the active site cleft (Figure A10). Consequently, a mutation at this position was not only expected to impair dimerization but potentially also substrate binding. Contrary to these expectations, variant N42A remains catalytically active, although at a 10-fold decreased rate compared to the wild type enzyme. This finding might support the hypothesis that N42 is only involved in "guiding" the substrate to the active site and not actively participating in its turnover. Accordingly, substitution with a smaller, apolar residue such as alanine would weaken the potentially important interaction and lead to decelerated substrate turnover.

In course of these experiments, the kinetic plots of two out of the three active PhzF variants as well as the wild type enzyme exhibited a sigmoidal curve (Figure 26). Therefore, the experimental data for wild type PhzF, variant N42A and H74N were fitted to the Hill-equation (Table 15). Kinetic data for H74A could not be fitted with this equation and hence were analyzed with a Michaelis-Menten model. For better comparison of their enzyme kinetic parameters, the other two active variants (N42A and H74N) were additionally fitted to the latter model. Only the data of the wild type enzyme could not be interpreted with the Michaelis-Menten model, at least not in this experimental context. Because of this inconsistency, the data should be considered with caution. However, the phenomenon of sigmoidal kinetic plots was already observed during other kinetic experiments, *e.g.* when the temperature dependency of DHHA isomerization was studied (paragraph 4.2.6.), and might indicate cooperative substrate binding to PhzF.

Overall, the results of the mutagenesis studies illustrate that the catalytic site of PhzF is a very sensitive environment not even permitting small changes in terms of protein engineering.

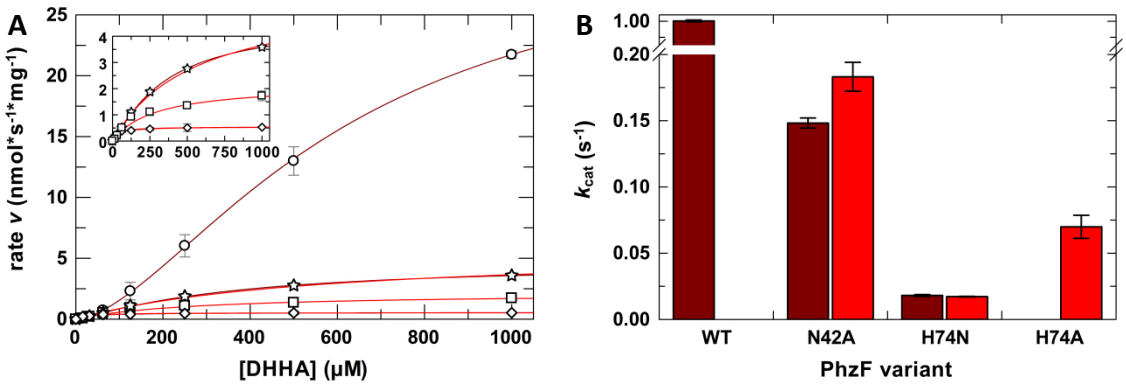

Figure 26: Enzyme kinetic plots for the isomerization of racemic DHHA by active PhzF variants.
A Kinetic plots (rate *v* as a function of substrate concentration) showing the turnover of racemic DHHA in 50 mM sodium phosphate buffer pH 7.5 at 25 °C catalyzed by either 500 nM dimeric PhzF WT (○), N42A (✩), H74A (□) or H74N (◇). The reaction was followed via substrate depletion over time at 275 nm. After normalization to zero and background correction, averaged data from three independent measurements were fitted according to a Michaelis-Menten model (—) or to the Hill-equation (—) using GraFit 5. Inset: Close-up on the kinetic plots for variants N42A and H74A/N. **B** Obtained k_{cat}-values from the plots in A either derived from a Michaelis-Menten (■) or Hill-Fit (■) using GraFit 5.

4.2.9. *In silico* studies to elucidate the reaction mechanism of PhzF

As mentioned in the beginning of this chapter, analysis of the different potential reaction mechanisms for PhzF catalysis was conducted in collaboration with two other groups from the University of Bayreuth and the Graz University of Technology. The theoretical QC/MM calculations carried out by Martin Culka (University of Bayreuth) are particularly important for the understanding of the catalytic mechanism. Hence, the results will be presented in this paragraph.

Initial ^{1}H-NMR experiments by Mario Leypold (Graz University of Technology) revealed that PhzF catalysis features several characteristics of a sigmatropic reaction, as reported for other enzymes, such as chorismate mutases (Burschowsky *et al.*, 2014) or the isochorismate pyruvate lyase PchB from *Pseudomonas aeruginosa* (DeClue *et al.*, 2005). First, when DHHA isomerization is followed in D_2O, no incorporation of a deuterium at position C1 is observed indicating no exchange of the transferred proton with the solvent as would be expected for acid/base-catalyzed reactions. Instead, after transfer to position C1, the signal originating from the proton at position C3 is retained and hence indicates a concerted mechanism. In a similar way, when conversion of the selectively mono-deuterated substrate d-DHHA was followed in aqueous solution, the characteristic absence of an NMR-signal for the deuterium at position C3 was preserved at position C1 after catalysis. Second, the shifted proton at position C3 was found to be non-acidic (estimated pKa = 21.3 after binding to PhzF's active site). Third, the NMR-data revealed

that, upon tautomerization, incorporation of a solvent proton/deuterium at position C4 leads to *R*-configuration of the new stereogenic center. Although these observations are required for validation of a sigmatropic reaction, alone they are not sufficient. Thus, after initial determination of the active site protonation, which identified the substrate to be present in its zwitterionic form with protonated amine and deprotonated carboxylate, and surprisingly suggests that the crucial catalytic residue E45 is protonated (pKa = 9) at the onset of catalysis, QC/MM calculations for different reaction trajectories were carried out (Scheme 10 and Scheme 11).

To begin with, an intramolecularly concerted transfer via [1,5]-sigmatropic shift (Scheme 10IA) was modelled starting from either protonated, as suggested by the theoretical active site titrations, or deprotonated E45. In both cases the energy barrier for proton abstraction at C3 was found to be 32.5 kcal mol^{-1} (even higher under consideration that E45 has to be deprotonated prior to catalysis) and as such too high to be plausible in terms of enzyme catalysis. Consequently, a direct, intramolecularly concerted mechanism for PhzF catalysis is unlikely. Secondly, another concerted mechanism involving protonated E45 was analyzed (Scheme 10IB). In this case, when simultaneous transfer of a proton from E45 to C1 and abstraction of the non-acidic proton at position C3 was investigated, a high E_A barrier of 27.2 kcal mol^{-1} was determined. This high energy barrier renders this mechanism implausible. The third mechanism, a stepwise acid/base-catalysis, including consecutive abstraction of the C3-proton, leading to an anionic intermediate, and stereoselective protonation at C1, led to an E_A barrier of 13-14 kcal mol^{-1} (after refinement, including initial deprotonation of E45 and ZPE correction, 16 kcal mol^{-1}; Scheme 10IC). Hence, a mechanism, in which E45 acts as proton shuttle seems to be the most likely for the first step of PhzF catalysis, although the necessary initial deprotonation of E45 still remains questionable.

The next step in catalysis is supposed to be a tautomerization of the enol intermediate 6-amino-5-hydroxy-2,4-cyclohexadiene-1-carboxylic acid (AHCDC). Again, NMR-experiments showed that protonation at position C4 of AHCDC is stereospecific, suggesting an enzyme assisted/catalyzed mechanism. This is also supported by the fact that the energy barrier for a spontaneous tautomerization was calculated to be 14.2 kcal mol^{-1}, making an uncatalyzed step unlikely.

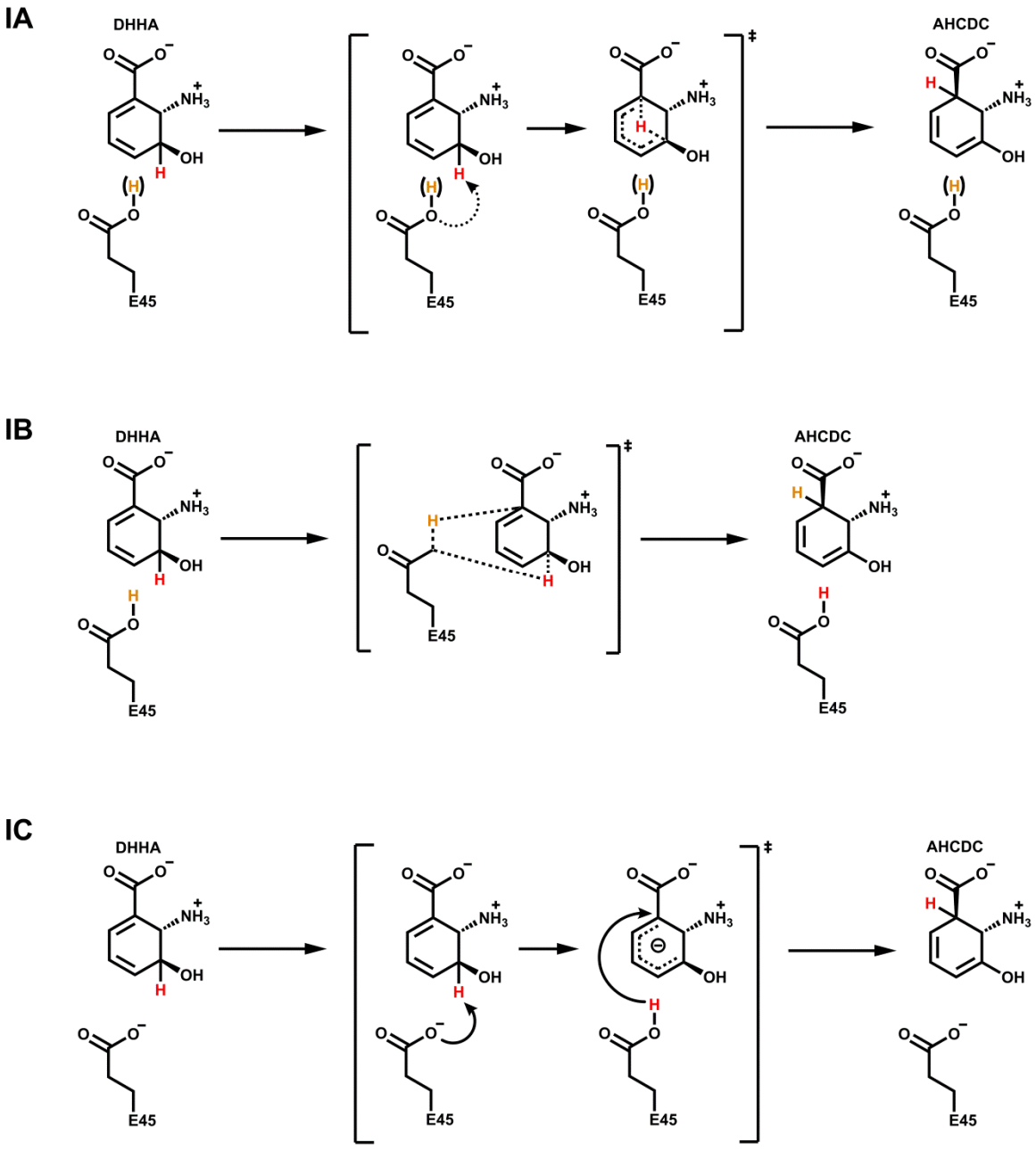

Scheme 10: Hypothetical reaction schemes for the first step of PhzF catalysis, namely DHHA isomerization to the reaction intermediate AHCDC.
Three different reaction pathways were analyzed by QC/MM calculations. **IA** represents a concerted mechanism via a pericyclic [1,5]-prototropic shift with the conserved (de)protonated active site residue E45 only having a stabilizing function. **IB** shows a concerted mechanism involving protonated E45, which donates a proton to the C1-carbon of the substrate and simultaneously abstracts a proton from position C3. **IC** depicts a stepwise mechanism via an anionic intermediate. The deprotonated E45 acts as catalytic base abstracting the proton from the substrate carbon at position C3. After reorientation E45 protonates the substrate at position C1 yielding the reaction intermediate AHCDC. The migrating, non-acid proton from position C3 (**H**) as well as the proton of E45 (**H**) are highlighted. Figure adapted from Diederich *et al.*, 2017.

The active site of PhzF comprises only two suitable reactants in close distance to the reacting groups of the substrate, the carboxylate of E45 and a conserved water molecule, both able to perform the required steps for tautomerization of AHCDC, *i.e.* first deprotonation of the 3-hydroxy group and then protonation at position C4.

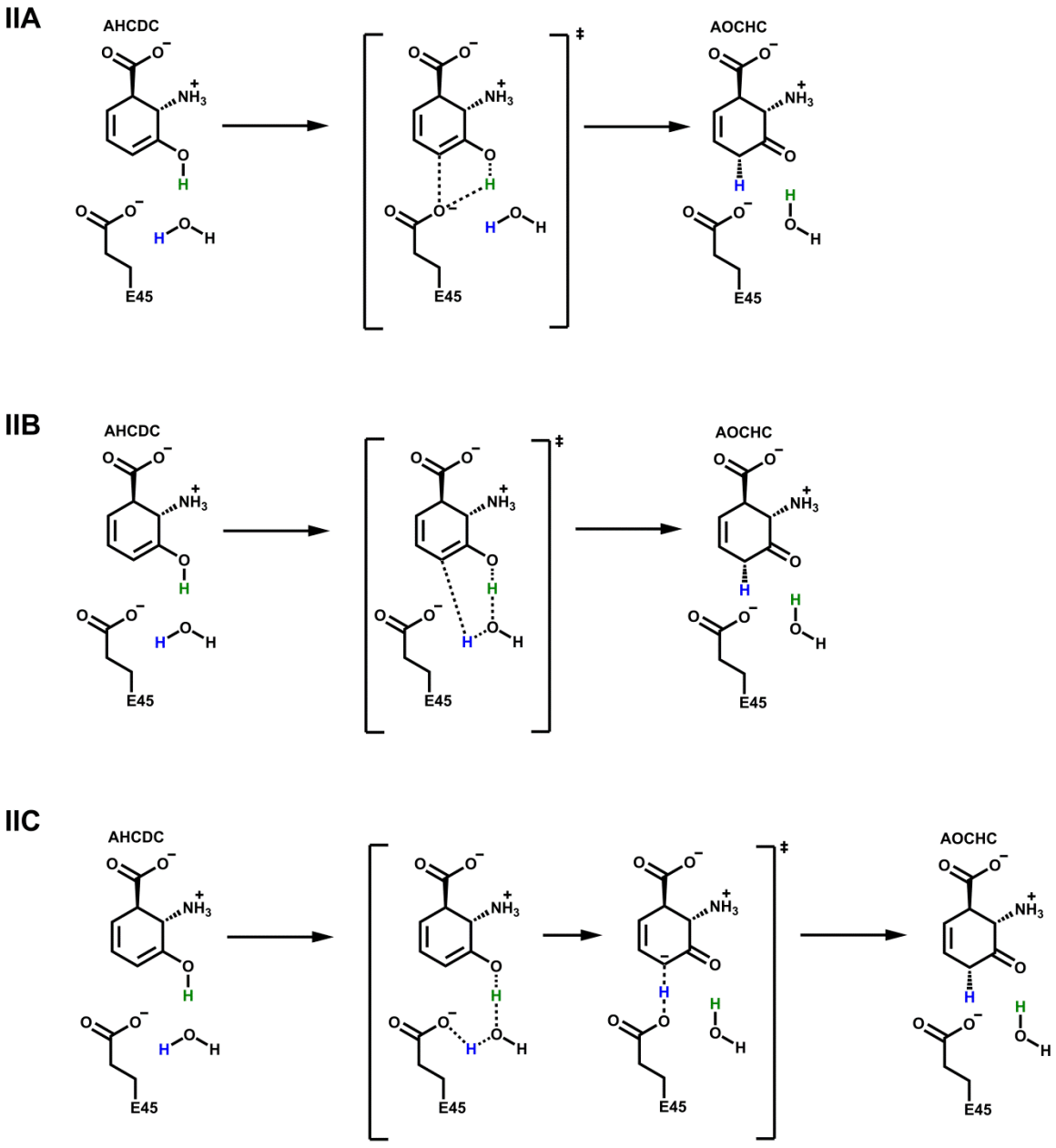

Scheme 11: Hypothetical reaction mechanisms for the second step of PhzF catalysis - stereoselective keto-enol tautomerization of the intermediate AHCDC to the ketamine product AOCHC.
Three different reaction pathways were analyzed by QC/MM calculations. **IIA** shows a stepwise mechanism with the conserved active site residue E45 abstracting a proton from the intermediate's 3-hydroxy group and retransferring it to position C4. **IIB** shows a similar mechanism, but here the conserved active site water molecule acts as an acid/base catalyst. **IIC** depicts a stepwise mechanism where first the water molecule abstracts a proton from the 3-hydroxy group of AHCDC, then transfers another proton to E45, which in finally protonates position C4 yielding the reaction product AOCHC. The migrating proton of the 3-hydroxy group of AHCDC's (**H**) as well as from the conserved water molecule (**H**) are highlighted. Figure adapted from Diederich *et al.*, 2017.

Hence, the first potential mechanism involves E45. To accomplish proton abstraction from the 3-hydroxy group, the residue has to rotate back to its original position at the onset of catalysis. Then a stepwise deprotonation of the hydroxy group and subsequent protonation at C4 could yield the ketamine AOCHC (Scheme 11IIA). However, QC/MM-calculations found the barrier for this reaction to be in a similar range than the

uncatalyzed reaction, therefore rendering this hypothesis improbable. The same holds true for a reaction pathway solely involving the conserved water molecule either via a concerted or stepwise deprotonation/protonation mechanism (Scheme 11IIB). This leaves only one other potential mechanism, involving both the conserved active site water and the catalytic residue E45 (Scheme 11IIC). QC/MM calculations established that, after back rotation, residue E45 repositions the conserved water molecule thus establishing a new hydrogen-bonding network that allows deprotonation of the 3-hydroxy group by the water molecule. The latter, in turn, transfers a proton to E45, which protonates the ligand at position C4 and yields the final reaction product AOCHC. This pathway is in good agreement with stereospecific pro-*R*-protonation of the C4-carbon as found by NOE (nuclear overhauser enhancement)-experiments and furthermore was found to be energetically most likely (E_A = 9.2 kcal mol^{-1}).

In summary, the *in silico*-studies suggest that PhzF first employs acid/base catalysis involving the conserved catalytic residues E45 as proton shuttle to facilitate DHHA isomerization and then catalyzes stereoselective tautomerization of the reaction intermediate via a water-E45 relay.

4.3. Conclusion

This chapter focused on the isomerase PhzF, which functions as a key-enzyme within the phenazine biosynthesis pathway by converting *trans*-2*S*,3*S*-dihydro-3-hydroxyanthranilic acid (DHHA) into the highly reactive amino ketone 6-amino-5-oxo-2-cyclohexene-1-carboxylic acid (AOCHC), the direct precursor for formation of the characteristic phenazine heterocycle.

Previous data (Blankenfeldt *et al.*, 2004) suggested that the enzyme employs a two step mechanism for DHHA isomerization: first, a [1,5]-hydrogen shift of a non-acidic proton along the cyclohexadiene ring-system and second, stereoselective tautomerization of the reaction intermediate to a ketamine product. However, the detailed mechanism of PhzF catalysis remained unclear. Therefore, different potential reaction pathways for both steps were hypothesized.

The isomerization, for instance, might proceed either via a rare pericyclic reaction, which follows a concerted sigmatropic rearrangement of the proton from position C3 to position

C1, or PhzF might employ classic acid/base catalysis with the conserved active site residue E45 serving as proton shuttle. The subsequent tautomerization appears to be stereoselective, hence the question is whether this reaction is also facilitated by PhzF, *e.g.* via E45 or possibly by a conserved water molecule found in the active site.

In a collaborative approach, comprised of QC/MM calculations (Martin Culka, University of Bayreuth), NMR-experiments (Mario Leypold, Graz University of Technology) as well as enzyme kinetic and X-ray crystallographic methods, the mechanistic details of PhzF catalysis were investigated.

Primarily based on the computational calculations, a mechanism, in which PhzF first promotes DHHA isomerization by employing acid/base catalysis involving the conserved catalytic residues E45 as proton shuttle and subsequently catalyzes stereoselective tautomerization of the reaction intermediate via a water-E45 relay was proposed (Scheme 12).

In order to support the theoretical studies, an enzymatic assay was specifically developed and allowed determination of a turnover rate k_{cat} of 3.23 s^{-1} for DHHA isomerization. Furthermore, the calculations revealed that the isomerization step, with an energy barrier of 16 kcal mol^{-1}, compared to E_A = 9.2 kcal mol^{-1} for the tautomerization step, is rate limiting for PhzF catalysis and therefore should be susceptible for isotopic substitutions of the migrating proton by deuterium. NMR experiments and enzyme kinetics confirmed this theory, as the reaction rate was found to be decreased drastically when turnover of a C3-mono-deuterated substrate isotopologue (d-DHHA) was analyzed.

These results also account for a large primary kinetic isotope effect of 9.5 on k_{cat}. The value is in the same order of magnitude as the one obtained from the *in silico* studies, although it has to be mentioned, that calculated intrinsic KIEs cannot directly be compared to the observed, apparent KIE. The latter involves contributions of all catalytic steps and not only of the rate-limiting one and hence the apparent KIE often appears smaller than the intrinsic one. Nevertheless, the dimension of the calculated/observed KIE hints towards tunneling contribution in PhzF catalysis.

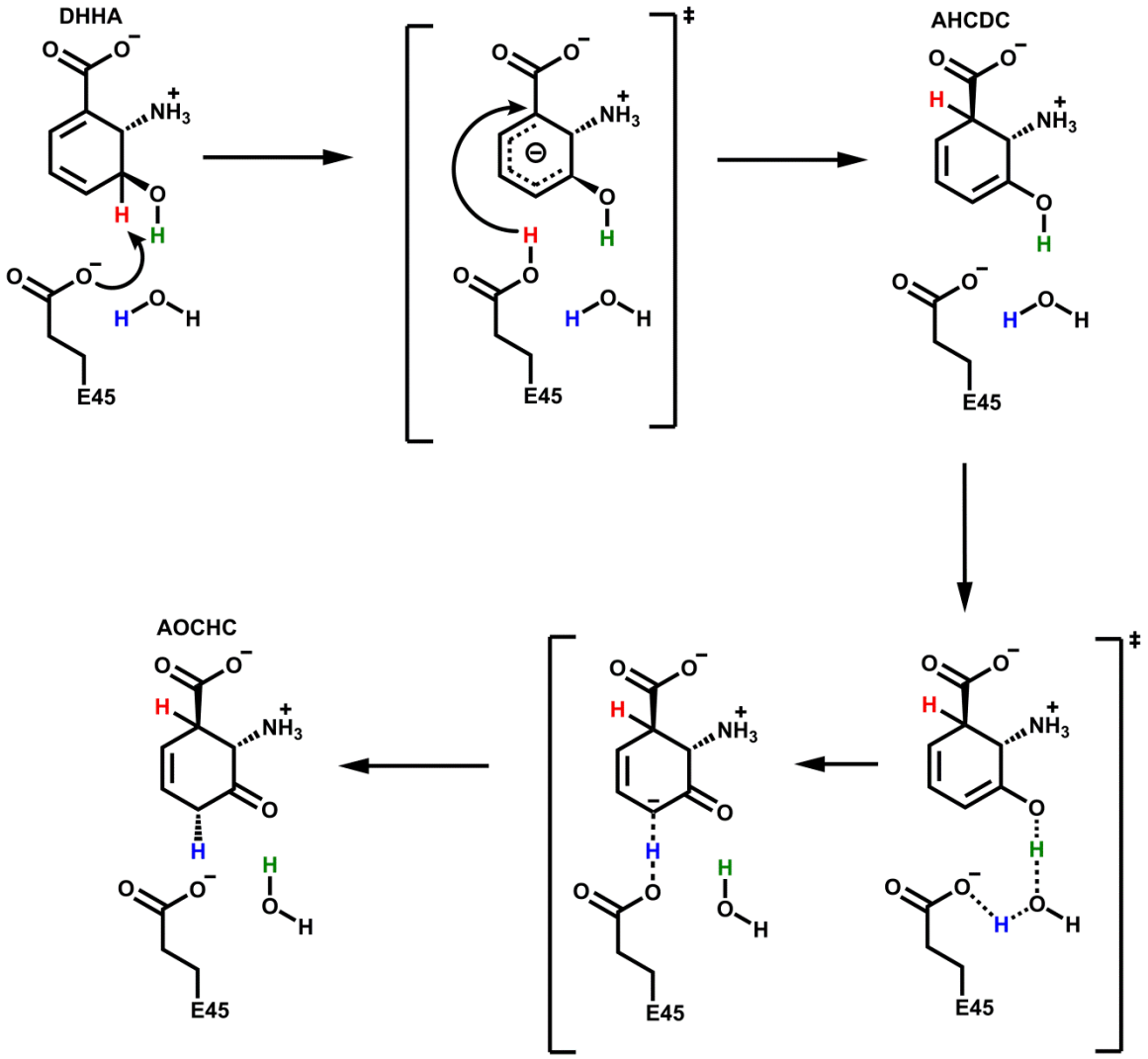

Scheme 12: Overall reaction mechanism for PhzF catalyzed DHHA isomerization and subsequent keto-enol tautomerization to the highly reactive ketamine AOCHC.
Zwitterionic DHHA is converted into AOCHC via a two-step mechanism: an initial base-catalyzed proton abstraction from position C3 (**H**) leads to formation of an anionic intermediate, which, after protonation, yields the reaction intermediate AHCDC. In the next step, this intermediate undergoes enzyme-catalyzed keto-enol tautomerization facilitated via an E45-water relay (**H** and **H**) to yield the final reaction product AOCHC. Figure adapted from Diederich *et al*., 2017.

Beside these fundamental investigations, which were carried out in order to affirm the results of the QC/MM calculations, a variety of additional experiments were performed to explore PhzF catalysis further. pH- and temperature dependency measurements, for instance, revealed that PhzF has a rather narrow pH-optimum around pH 7.5, but remains active even at temperatures above 40 °C. This is particularly interesting, since the focus of this study was on the protein from the soil bacterium *Pseudomonas fluorescens* 2-79 which has a temperature optimum at 28 °C. The data obtained at elevated temperatures additionally support the hypothesis that tunneling is involved in PhzF catalysis and suggest that cooperative effects could play a role in substrate binding and turnover. This

hypothesis is further supported as other active variants from mutagenesis studies also showed tendency to cooperativity. The substrate spectrum of PhzF was analyzed as well. Surprisingly, it was found that in addition to DHHA and its heavy isotopologue d-DHHA, PhzF is able to convert alkoxy-derivatives bearing a short alkyl-moiety at the 3-hydroxy group. For one of these alkoxy-derivatives, *O*-Et-DHHA, even a crystal structure in complex with the 2*R*,3*R*-enantiomorph could be obtained. Albeit PhzF can convert these short alkoxy-derivatives, the substrate spectrum of the enzyme seems to be narrow as a variety of other substrate analogs were not converted by PhzF. Yet, one of the tested compounds, *ent*-H_2-DHHA, was identified as a potential PhzF-inhibitor. This molecule shows resemblance to the substrate. As such, substrate or product analogs might be developed into potent selective PhzF-inhibitors.

All in all, the obtained data show that PhzF not only has a narrow pH-optimum and seems to be very sensitive to electronic alterations, *e.g.* by increasing ionic strength, but also that its active site promotes DHHA isomerization in a way that even "small" manipulations can lead to complete abolishment of catalytic activity. Together with the observed, narrow substrate spectrum, this finding points out that PhzF has evolved into a unique enzyme, perfectly adapted for the isomerization reaction of DHHA, which is crucial for phenazine biosynthesis.

CHAPTER II:
Biochemical and biophysical characterization of PhzAB heterodimerization and its relevance for phenazine biosynthesis

5. PhzAB heterodimerization

Previous investigations revealed that, subsequent to PhzF catalysis, the next step of the phenazine biosynthesis pathway consists in the formation of the characteristic tricyclic "core" (Ahuja *et al.*, 2004 and 2008). This step, which requires the symmetrical head-to-tail double condensation of two identical, highly reactive ketamine precursor molecules, known as AOCHC, can proceed spontaneously *in vitro.* However, it was found to be catalyzed and thereby accelerated by the homodimeric enzyme PhzB *in vivo* (*q.v.* paragraph 1.3.2. and 5.2.1.). Beyond that, it was also discovered that among phenazine producing species, pseudomonads carry a second copy of the *phzB* gene, termed *phzA*, directly upstream in their highly conserved biosynthesis operon (*phz*-operon, Scheme 13).

Scheme 13: Gene organization of the "core" phenazine biosynthesis cluster *phzABCDEFG* as found in the *phz*-operons from different *Pseudomonas spp.*
The gene products of *phzA* and *phzB* (highlighted in darker blue) share a sequence identity of 69 % on the protein level and exhibit a high structural similarity. It is hypothesized that they might have arisen from ancient gene duplication.

This enzyme was however found to be inactive in the condensation reaction, due to two active site mutations of the catalytic residues H73 and S77 to leucine. Nevertheless, the high sequence identity of 69 % between PhzA and PhzB as well as their structural similarity, which was uncovered from crystal structures of the two enzymes from *P. fluorescens* 2-79 (Ahuja, 2007), led to the hypothesis that both enzymes are not only found as homodimers, but could form heterodimers as well. Indeed, when co-expressing both genes, a heterodimeric protein could be isolated (Weikart, 2006) and its crystal structure solved. This raised questions on the physiological relevance of heterodimerization, *i.e.* whether a distinct advantage exists for phenazine biosynthesis when heterodimers rather than homodimers are formed, although the PhzA copy of the

protein was found to be inactive.

A variety of crystal structures of the enzymes from *P. fluorescens* 2-79 and in particular *B. cepacia* R18194 in complex with different substrate and product analogs helped to understand the catalytic mechanism of PhzB, yet so far no basic enzymatic activity assay for determination of the kinetic reaction parameters was at hand. During this study, a new activity assay was developed and subsequently employed to measure and compare enzymatic activities of the different homo- and heterodimers. Furthermore, dimer stability and affinity towards previously identified PhzB ligands was evaluated using different biophysical methods.

5.1. Specific Methods & Materials

This study of the dimerization behavior of PhzAA, PhzBB and PhzAB from *P. fluorescens* 2-79 is based on biochemical and X-ray crystallographic results from a number of previous bachelor, master and PhD theses within the group, mainly the work from Nadine Weikart, Sascha Fuchs, Ekta Ahuja, Arthur Porfetye, Christian Feiler and Yvonne Nerbl (Weikart, 2006; Fuchs, 2006; Ahuja, 2007; Porfetye, 2009; Feiler, 2010; Nerbl, 2012). Furthermore, collaborators from the USA, Dimitri Mavrodi and Linda Thomashow, were investigating the abundance of PhzA/B homo-and heterodimers *in vivo* using RT-qPCR. Their results as well as the data from the other previous studies, especially the structural data including different apo and complex structures for PhzA, PhzB, and PhzAB from *P. fl* 2-79, will also be discussed in context of this work.

5.1.1. Protein production

The homodimeric protein PhzAA from *Pseudomonas fluorescens* 2-79 (UniProt-entry: Q51787 (PHZA_PSEFL)) was overexpressed from a pET15b expression vector (Novagen) in *E. coli* Rosetta2 (DE3) *pLysS* (Novagen) as described previously (Ahuja *et al.*, 2004). The cells were grown in terrific broth medium at 20 °C o/n after induction with 0.5 mM isopropyl β-D-1-thiogalactopyranoside (IPTG) at an OD_{600} of 0.6. Purification of the N-terminal hexahistidine-tagged protein followed standard procedures (as described in section 3 paragraph 3.2.3.), including stepwise immobilized Ni(II) affinity chromatography and a final size-exclusion chromatography step in 20 mM TRIS/HCl pH 8.0, 150 mM NaCl. Overexpression and purification of PhzBB from *P. fluorescens* 2-79 (UniProt-entry: Q51788

(PHZB_PSEFL)) as well as of Phz(A)/B from *Burkholderia cepacia* R18194 (UniProt-entry: Q396C9 (Q396C9_BURL3)) followed the same procedures. Purified proteins were concentrated, snap-frozen in liquid nitrogen and stored at -80 °C until further usage.

Heterodimeric PhzAB from *P. fluorescens* 2-79 was expressed and purified following methods similar to the ones described in Weikart (2006). In brief, the genes, *phzA* and *phzB*, encoding for the two proteins from *P. fl* 2-79 were cloned as a bicistronic gene construct *phzAB* into a modified pET19 expression system (Novagen). Co-expression of the two proteins, of which only PhzA carries an N-terminal hexahistidine-tag, was carried out in *E. coli* Rosetta2 (DE3) *pLysS* (Novagen) in TB-medium at 20 °C o/n after induction with 0.5 mM IPTG at an OD_{600} of 0.6. Protein purification followed a stepwise protocol; the initial immobilized Ni(II) affinity chromatography with a linear gradient to 250 mM imidazole resulted in the separation of two peaks, corresponding to PhzAB heterodimer and PhzAA homodimer. Pooled fractions containing PhzAB heterodimer were either directly applied to a HiLoad™ 26/600 Superdex™ 75 prep grade column for final size-exclusion chromatography in 20 mM TRIS/HCl pH 8.0, 150 mM NaCl or subjected to removal of the affinity tag by addition of tobacco etch virus (TEV) protease. After dialysis, a second Ni(II) affinity chromatography was performed in order to separate the TEV protease from the digested target protein. Cleaved protein-containing fractions were pooled and subjected to size-exclusion chromatography in 20 mM TRIS/HCl pH 8.0, 150 mM NaCl. Cleaved and uncleaved proteins, termed HeteroPhzABcut and HeteroPhzAB respectively, were concentrated, snap-frozen in liquid nitrogen and stored at -80 °C until further usage.

5.1.2. Coupled photometric assay

Kinetic parameters for different PhzB para- and orthologues (all carrying an N-terminal hexahistidine-tag) were determined using a continuous photometric coupled enzyme assay in an Infinite® M200 microplate reader (Tecan Group Ltd.). In order to ensure that the coupled enzyme is not rate-limiting, control experiments with different concentrations of PhzF were carried out prior to all quantitative activity assays. If not explicitly stated otherwise, standard solutions contained 1 µM of the dimeric enzyme of interest (PhzA, PhzB, PhzAB, or *Bc*Phz(A)/B), 1 µM (dimer) of the coupled enzyme PhzF

(from different species), and the substrate DHHA up to a final concentration of 1 mM in 50 mM sodium phosphate buffer at pH 7.5 supplemented with 2 % (v/v) dimethyl sulfoxide (DMSO). All reactions were carried out in a final volume of 150 µL in UV-Star® 96-Well microplates (Greiner Bio-One) at 25 °C. The enzymatic reaction was initiated by the addition of 75 µL of the pre-mixed enzyme solution to an equal volume of each substrate dilution and data were acquired in 40 s intervals over a 20 minutes time course. Increasing absorption of a metastable tricyclic phenazine intermediate, formed by oxidative decarboxylation downstream of the PhzB catalyzed condensation reaction, was followed at 330 nm. For background signal correction a reaction mixture lacking substrate was used. The background of the uncatalyzed auto condensation was evaluated using reaction mixtures lacking PhzB para- or orthologues. Reaction rates were determined from the slopes of the linear phase of each curve using a path length of 0.417 cm and an extinction coefficient of 2880 M^{-1} cm^{-1}. This extinction coefficient at 330 nm was estimated from experimental data. Indeed, when following the kinetics of the reaction of PhzBB and HeteroPhzAB in presence of various substrate concentrations over 20 min, a plateau of the absorbance signal could systematically be observed indicating complete conversion of the substrate. Therefore, the maximal ΔA_{330} was plotted against the theoretical product concentration achievable given the starting substrate concentration and stoichiometry of the reaction ([S]/2). The data were fitted by linear regression yielding the aforementioned extinction coefficient.

Kinetic parameters were obtained by fitting the averaged data from three independent measurements to the Hill-equation using GraFit 5 (Erithacus Software Ltd.).

5.1.3. Circular dichroism spectroscopy

Far ultraviolet (UV) spectra for all PhzB para- and orthologues, diluted to a final concentration corresponding to 1 mM amide bond, were recorded in standard assay buffer (50 mM sodium phosphate pH 7.5) at 10 °C in a JASCO J-815 spectropolarimeter in 1 mm quartz cuvettes (Hellma analytics). Spectral data were collected in the range from 260 to 190 nm in steps of 1 nm at 50 nm min^{-1} scanning speed and 8 s digital integration time (D.I.T.). Signal-to-noise correction was achieved by recording ten spectra per sample. For background/solvent correction, a buffer spectrum was recorded using the same experimental setup and the identical quartz cuvette.

Protein stability was addressed by recording melting/unfolding curves in the temperature range from 10 to 60 °C with 0.4 °C min^{-1} sampling rate at 212 and 222 nm; the bandwidth was 1 nm and the D.I.T. 16 s. For comparison of the data from different para- and orthologues, the measured molar ellipticity (Θ) in mdeg was converted to the mean residue ellipticity $[\Theta]_{MRW}$ in deg cm^2 $dmol^{-1}$ (equation 15):

$$[\Theta]_{MRW} = \frac{\Theta}{c \times d \times N_{aa} \times 10} \quad \textbf{(15)}$$

with

c	protein concentration in M
d	path length in cm
N_{aa}	number of amino acids per protein

Melting temperatures (T_M) in Kelvin were obtained by fitting the mean residue ellipticity data to a two state model using equation 16 in GraFit 5 (Erithacus Software Ltd.):

$$y(T) = \frac{y_N^0 + m_N \times [T] + (y_U^0 + m_U \times [T]) \times e^{\left(\frac{\Delta H_D}{R} \times \left(\frac{1}{T} - \frac{1}{T_M}\right) - \frac{\Delta C_p}{R} \times \left(1 - \frac{T_M}{T} + ln\frac{T_M}{T}\right)\right)}}{1 + e^{\left(\frac{\Delta H_D}{R} \times \left(\frac{1}{T} - \frac{1}{T_M}\right) - \frac{\Delta C_p}{R} \times \left(1 - \frac{T_M}{T} + ln\frac{T_M}{T}\right)\right)}} \quad \textbf{(16)}$$

where

y(T)	temperature dependent obtained value, here $[\Theta]_{MRW}$ in deg cm^2 $dmol^{-1}$
y_N^0	theoretical measure for native protein at 0 K
y_U^0	theoretical measure for denatured protein at 0 K
m_N	baseline slope for the native state (K^{-1})
m_U	baseline slope for the unfolded/denatured state (K^{-1})
ΔH_D	van't Hoff enthalpy for the unfolding transition (kJ mol^{-1})
ΔC_P	change in molar heat capacity (J mol^{-1} K^{-1}), here empirically set to 6000 J mol^{-1} K^{-1}
R	gas constant for an ideal gas (kJ mol^{-1} K^{-1})
T	measured temperature in K
T_M	melting temperature

5.1.4. Microscale thermophoresis

Affinity parameters for binding of phenazistatin A, a previously reported synthetic ligand and potential inhibitor for *Bc*Phz(A)/B (Mentel *et al*., 2009a), to different N-terminally hexahistidine-tagged PhzB paralogues were determined using microscale thermophoresis (Wienken *et al*., 2010) with the protein intrinsic tryptophan fluorescence as molecular probe. Starting from either 160 µM (titration against PhzBB) or 4 mM (titration against HeteroPhzAB or PhzAA) phenazistatin A, a serial 1:1-dilution of the ligand in 20 mM TRIS/HCl pH 8.0, 150 mM NaCl, supplemented with 2 % (v/v) dimethyl sulfoxide (DMSO) was prepared. For titration series, 10 µL of each 2 µM protein stock solution (PhzBB, PhzAA or HeteroPhzAB) in the aforementioned buffer were mixed with 10 µL of each

dilution sample, yielding final protein concentrations of 1 µM and ligand concentrations starting from 80 µM or 2 mM in buffer containing 1 % (v/v) DMSO. The measurement was carried out at 25 °C in standard treated, zero background capillaries in a Monolith NT.LabelFree instrument (NanoTemper technologies) with 25 % LED power. After an initial delay of 5 s, the laser at 20 % MST power was switched on for 30 s. Back diffusion was recorded with a final laser-off time of 5 s. Binding parameters were obtained by fitting normalized, averaged data from three independent measurements to equation 17 using GraFit 5 (Erithacus Software Ltd.):

$$[L]_{bound} = \frac{[L]_{free} \times C_B}{K_D + [L]_{free}} + background \qquad \textbf{(17)}$$

with

$[L]_{bound}$ fraction of bound ligand
$[L]_{free}$ fraction of free ligand
C_B binding capacity/amplitude
K_D dissociation constant

5.1.5. Crystallization and structure determination

Crystallization experiments of heterodimeric PhzAB (HeteroPhzABcut) at 17 mg mL^{-1} were carried out via sitting-drop vapor diffusion method at room temperature in 96-well INTELLI-PLATES® (ARI) using the commercial JCSG CoreI-IV screening suites (QIAGEN). Drops consisted of 200 nL protein solution and 200 nL precipitant. Initial crystals grew within a week from a reservoir comprising 0.09 M HEPES pH 7.5, 1.26 M tri-sodium citrate and 10 % (v/v) glycerol. After further crystal growth for two additional weeks, crystals of a maximum size of 130*65*50 µm were soaked with 10 mM phenazistatin A (stock: 100 mM in DMSO) in mother liquor supplemented with 25 % (v/v) glycerol for 2 h or o/n at room temperature.

For other soaking experiments, crystals of native *Bc*Phz(A)/B were regularly obtained at 12 °C from a grid screen around the previously published condition (0.1 M Bis-TRIS pH 6.1 – 6.7, 0.2 M ammonium acetate, 16 – 20 % (w/v) PEG 3350; Ahuja *et al*., 2008). Hanging drops, comprised of 1 µL protein solution (15 mg mL^{-1}) and 1 µL precipitant solution were equilibrated against 500 µL reservoir. Crystals of an average dimension of 120*120*100 µm, which appeared within a few days, were soaked in mother liquor supplemented with 25 % (v/v) glycerol and different concentrations (5, 10, 20, and 50 mM from aqueous stocks) of the two substrate analogs 3-oxo- or 2-amino-

cyclohexanecarboxlic acid (3OCHCA/2ACHCA) at 12 °C overnight.

Soaked crystals were mounted on a nylon loop and flash frozen in liquid nitrogen. Diffraction data were collected at 100 K at beamline MX BL14.1, BESSY II at the Helmholtz Centre Berlin (HeteroPhzAB in complex with phenazistatin A) or at beamline X06DA (PXIII) at the Swiss Light Source (SLS) of the Paul Scherrer Institute (*Bc*Phz(A)/B complexes). Data reduction, structure refinement, and model building were carried out as described in paragraph 4.1.4. Ligand restraints where either downloaded from the Protein Data Bank (Berman *et al.*, 2000), as in case of phenazistatin A and 3OCHCA (Ligand-IDs: AOD and 3OC) or generated from SMILES-strings (2ACHCA) using the program phenix.elbow (Moriarty *et al.*, 2009) of the PHENIX software suite (Adams *et al.*, 2010). Structural flexibility was modelled using TLS refinement (Schomaker and Trueblood, 1968). In the last step of refinement, heteroatoms like waters and the ligand were attributed to the nearest TLS group using a script developed in the group (Reichelt and Blankenfeldt, unpublished). Final structure validation was done with MolProbity (Chen *et al.*, 2010). Full data collection and refinement statistics are shown in Table A7 and A8 as well as Table 20.

5.2. Results & Discussion

5.2.1. Design of a coupled enzymatic assay

In order to evaluate whether the heterodimerization of PhzA and PhzB is significant or even beneficial for substrate turnover - and hence for overall phenazine biosynthesis - a coupled enzymatic assay was established. This photometric assay constitutes a further adaptation of the activity assay previously developed for PhzF, the preceding enzyme in phenazine biosynthesis (*q.v.* chapter I). Multiple obstacles had to be overcome in the course of its development. Firstly, the reaction substrate AOCHC is a highly reactive amino ketone that could potentially react unspecifically with other primary amines such as the N_{ζ}-atom of lysine. Hence, this instable molecule had to be generated *in situ* by using a coupled assay with the enzyme PhzF. Yet, even if unwanted side reactions with other primary amines could be limited by this method, auto condensation of two of these ketamine molecules, also leading to the reaction product hexahydro-phenazine-1,6-dicarboxylic acid (HHPDC/HHPDC*), represented a perpetual problem that could not be

avoided. Consequently, this background reaction (Figure 27) had to be accounted for in every measurement.

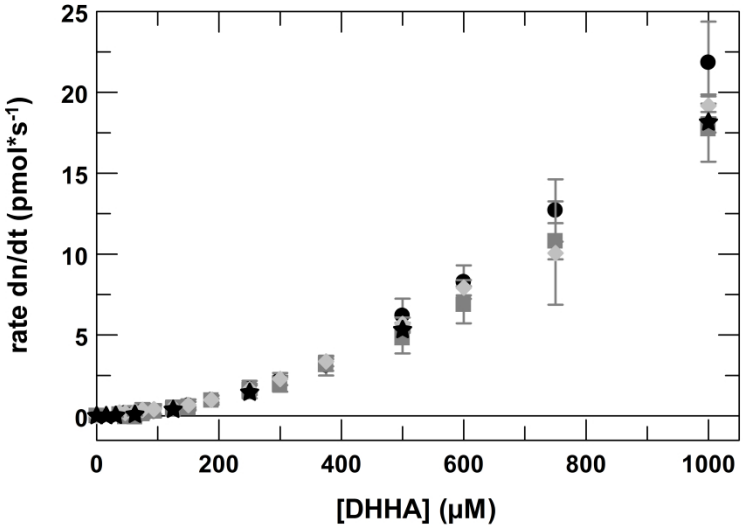

Figure 27: Auto condensation reaction of the highly reactive ketamine AOCHC.
Substrate auto condensation, in dependency of the coupled enzyme (● = 1 µM *Pfl*PhzF, ■ = 1 µM *Bglu*PhzFfull, ◆ = 1 µM *Bglu*PhzFΔ123, ★ = 2 µM *Pfl*PhzF), was followed at 330 nm by monitoring the formation of an oxidatively decarboxylated product downstream of the condensation reaction in 50 mM sodium phosphate buffer at 25 °C. The production rate dn/dt is plotted against the concentration of DHHA, the substrate of the coupled enzyme PhzF. The plotted curves are averaged data of three independent measurements. All data were normalized to zero.

As illustrated in the plots in Figure 27, no difference could be observed in the AOCHC condensation rate, independent of the coupled enzyme used in the assay, *i.e.* PhzF from *P. fluorescens* 2-79 or both variants (full length and Δ123) of PhzF from *Burkholderia glumae* BGR-1. Even when increasing the concentration of one of these enzymes to 2 µM no increase in the auto condensation rate could be detected. This shows that all coupled enzymes are producing enough AOCHC not to be rate limiting for the auto condensation, which appears to be at its maximum rate under these conditions. This simplified background correction, as per substrate concentration a constant value could be subtracted from the PhzB-catalyzed reaction.

The third complication of this assay setup was that HHPDC, the direct reaction product of the PhzB catalyzed AOCHC condensation, not only undergoes rearrangement to HHPDC*, but is also susceptible to oxidative decarboxylation in presence of molecular oxygen (Scheme 14).

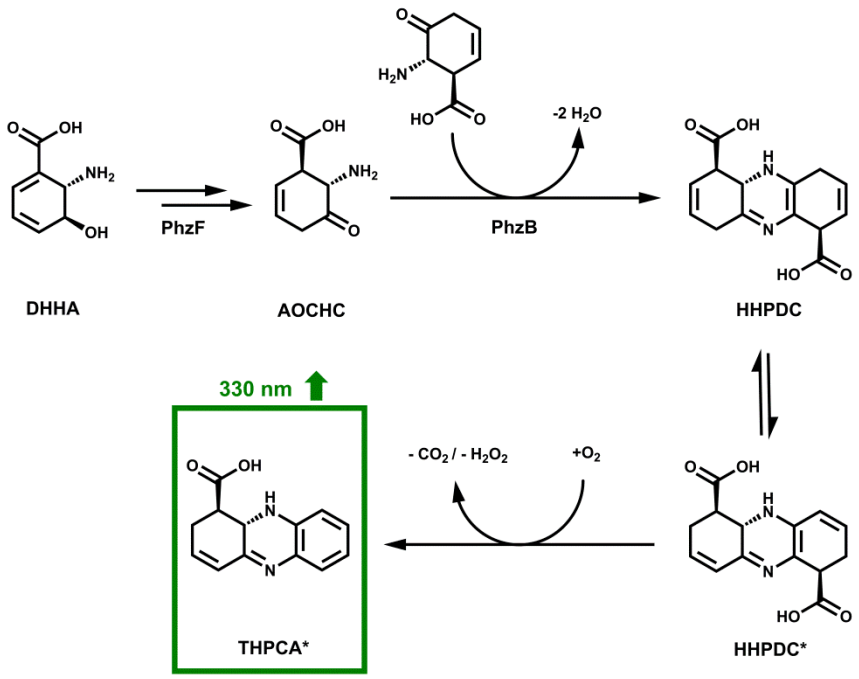

Scheme 14: Reaction pathway within the coupled enzymatic assay employed for kinetic characterization of PhzB-para- and orthologues.
The continuous assay was designed in a way that PhzF as a coupled enzyme is generating the PhzB substrate AOCHC *in situ* from DHHA to avoid unfavored side reactions of this reactive molecule. AOCHC is then further converted by PhzB to initially form the direct condensation product HHPDC, which subsequently undergoes rearrangement, potentially also facilitated by PhzB, yielding HHPDC*. This rearrangement is assumed to prevent back hydrolysis of the direct reaction product HHPDC. The secondary reaction product of PhzB, HHPDC*, is susceptible to oxidative decarboxylation and hence under the assay conditions THPCA* is formed. Formation of this metastable intermediate is followed at 330 nm.

This phenomenon rendered direct monitoring of the reaction product impossible. Instead formation of the metastable intermediate after oxidative decarboxylation, tetrahydro-phenazine-1-carboxylic acid (THPCA*), was followed at 330 nm. To minimize the potential influence of this enzyme-independent reaction on observed reaction rates, buffers and other assay solutions were not degassed and assay plates, used without lid, were shaken prior to each readout cycle to ensure availability of sufficient oxygen.

Moreover, not only the experimental setup proved to be challenging, also data evaluation led to complications, since the proposed mechanism does not follow classical Michaelis-Menten kinetics. Instead, it rather resembles a special case of a bisubstrate reaction where both substrates are identical. Consequently, none of the substrates could be applied in excess what would simplify data evaluation, as in such a case the Michaelis-Menten equation could be used as approximation and the data fitted accordingly. Alternatively, another model to analyze PhzB catalysis is an ordered sequential bi-uni

mechanism as described in equation 18 or - with regard to the special case where the first and second substrate are identical, *i.e.* A = B - as shown in equation 19:

$$v = \frac{v_{max}}{\frac{K_a}{[A]} + \frac{K_{ia} \times K_b}{[A] \times [B]} + \frac{K_b}{[B]} + 1} \quad \textbf{(18)}$$

$$v = \frac{v_{max}}{\frac{K_{a1}}{[A]} + \frac{K_{ia} \times K_{a2}}{[A]^2} + \frac{K_{a2}}{[A]} + 1} \quad \textbf{(19)}$$

with

v_{max}	maximal turnover velocity
K_a	equilibrium constant for binding of the first substrate A (M) ≡ K_{a1}
[A]	concentration of the first substrate (M)
K_{ia}	inhibitory constant of the first substrate A on binding of the second one B (M)
K_b	equilibrium constant for binding of the second substrate B (M) ≡ K_{a2}
[B]	concentration of the second substrate (M)

It is important to note that, although both substrates are identical, the respective equilibrium constants K_{a1} and K_{a2} (termed K_a and K_b in equation 18) are not the same, since the affinity constant for the "second" substrate K_{a2} is dependent on binding of the "first" substrate.

Despite the fact that this derived equation could easily be implemented in the program used for data analysis (GraFit 5, Erithacus Ltd.), fitting of the obtained kinetic data failed. Derivation of equation 19 leads to a binomial function of the type (ax^2+bx+c), thus no simple linearization is possible and consequently no initial fitting estimates can be provided. However, as the obtained kinetic plots exhibited a slight sigmoidal progression curve, data fitting was carried out using the Hill-equation assuming cooperativity within an enzyme dimer might influence catalysis. Indeed, the curvature of the fit aligns well with the actual data points. Thus, the Hill-equation was used as approximation for further data analysis

5.2.2. Catalytic activity of different PhzB para- and orthologues

Having developed a suitable activity assay, determination of enzyme kinetic parameters for Phz(A)/B from *B. cepacia* R18194, the homodimers PhzAA and PhzBB from *P. fl* 2-79 as well as for the corresponding heterodimer PhzAB was carried out.

As anticipated from previous studies (Ahuja *et al.*, 2004; Fuchs, 2006; Ahuja, 2007) the PhzAA homodimer, which carries a variety of deleterious mutations compared to the

PhzBB homodimer (for details see the sequence alignment in Figure A11) showed no detectable activity in the assay (Figure 28).

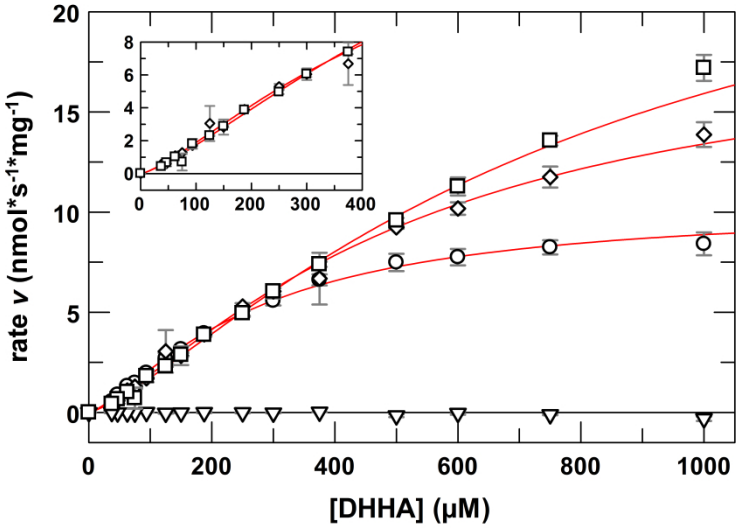

Figure 28: Enzyme kinetics for AOCHC condensation catalyzed by different PhzB para- and orthologues.
Kinetic plots (rate *v* as a function of substrate concentration) showing the turnover of DHHA, the substrate of the preceding coupled enzyme PhzF monitored by following the increase in absorption at 330 nm of a spontaneously forming downstream intermediate of the condensation reaction in 50 mM sodium phosphate buffer pH 7.5. PhzF generates the PhzB substrate AOCHC *in situ*, which in turn is converted either by *Bc*Phz(A)/B (○), homodimeric PhzBB (□), or heterodimeric PhzAB (◇) from *P. fl* 2-79. Homodimeric PhzAA (▽) shows no catalytic activity for the condensation reaction. After normalization to zero and solvent/background correction, averaged data from three independent measurements were fitted according to the Hill-equation (—) using GraFit 5. All data were obtained at 25 °C. **Inset**: Close-up on the kinetic plots of the PhzBB and PhzAB catalyzed reaction for low substrate concentrations up to 375 µM. Both dimers show similar turnover rates under these conditions.

Indeed, when indirectly following product formation at 330 nm by monitoring the downstream intermediate of the condensation reaction, THPCA*, the level of this intermediate was similar to the uncatalyzed auto condensation (Figure A12A and B). Hence, it could be confirmed that PhzAA is catalytically inactive.

In contrast to PhzAA, all other tested PhzB para- and orthologues showed catalytic activity in the enzymatic assay, but substrate turnover occurred at different rates (Figure 28 and Table 16). Comparing the maximum turnover rate v_{max} of these active enzymes revealed that *Bc*Phz(A)/B is the slowest enzyme among the three, with a maximum velocity of 10.3 nmol s^{-1} mg^{-1} and accordingly a turnover rate of 0.22 s^{-1}. However, the apparent affinity of this enzyme for its substrate ($K_{½}$ = 266 µM) is the highest in comparison to the other tested orthologues and hence the overall "catalytic efficiency", with a value of 835 µM, is comparable to the one of the "faster" enzyme *Pfl*PhzBB ($K_{½}$ = 797 µM). In fact, solely considering the maximum velocity, the homodimeric enzyme PhzBB was found to

be the fastest of the tested enzymes with a value of 27.8 nmol s^{-1} mg^{-1} for v_{max}, while the maximum velocity for PhzAB heterodimer was only 19.0 nmol s^{-1} mg^{-1} (Table 16).

Table 16: Enzyme kinetic parameters for AOCHC condensation catalyzed by different PhzB para- and orthologues.*

	v_{max} (nmol s^{-1} mg^{-1})	k_{cat} (s^{-1})	$K_{½}$ (µM)	$k_{cat}/K_{½}$ (M^{-1} s^{-1})	Hill-coefficient
***Bc*Phz(A)/B**	10.3 ± 0.3	0.22 ± 0.01	266 ± 12	835 ± 46	1.37 ± 0.02
HeteroPhzAB	19.0 ± 0.9	0.75 ± 0.03	522 ± 35	1444 ± 117	1.34 ± 0.03
PhzBB	27.8 ± 2.3	0.58 ± 0.05	797 ± 83	731 ± 98	1.30 ± 0.02

* The obtained values are averaged data of three independent measurements fitted to the Hill-equation. All data were obtained in 50 mM sodium phosphate buffer pH 7.5 at 25 °C, normalized to zero, and solvent/background corrected.

Yet, when carefully analyzing the enzyme kinetic plots, it becomes evident that at lower substrate concentrations, *i.e.* up to 250 µM, all three studied enzymes exhibit comparable substrate turnover rates. In fact, for the homo- and heterodimer of the same species this tendency can even be observed up to a substrate concentration of 375 µM (Figure 28 inset). This shows that, especially under substrate limitation, PhzAB heterodimers are as active as PhzBB homodimers. This trend is even more pronounced when, instead of comparing the maximum velocity, k_{cat} is taken in account. Since k_{cat} is a measure for catalytic activity per active site, the number of active sites per dimer has to be accounted for when analyzing the differences in enzymatic activity. PhzBB homodimers possess two active sites whereas PhzAB heterodimers feature only one. Consequently, the k_{cat}-value for PhzBB is found to be only 0.58 s^{-1} compared to 0.75 s^{-1} for the heterodimer. Furthermore when taking the catalytic efficiency $k_{cat}/K_{½}$ into account, PhzAB heterodimers are found to be twice as efficient as PhzBB homodimers with $k_{cat}/K_{½}$-values of 1444 M^{-1} s^{-1} and 731 M^{-1} s^{-1} respectively. The pronounced difference originates from the fact that the apparent substrate affinity ($K_{½}$) is higher in PhzAB heterodimers than in active homodimers. This finding is particularly important at low substrate concentrations and can be explained by the peculiarity of the condensation reaction, *i.e.* that for generation of one molecule of HHPDC (or HHPDC*), two AOCHC molecules have to bind to the same active pocket of PhzB (Scheme 15 top). Indeed, a crystal structure of the enzyme from *B. cepacia* in complex with the substrate analog 3-oxo-cyclohexanecarboxylic acid (3OCHCA; PDB entry 3DLZ; Ahuja *et al.*, 2008) revealed that two substrate molecules bind to each subunit and additionally suggested that one molecule binds tighter to the active site than the other (Scheme 15 bottom).

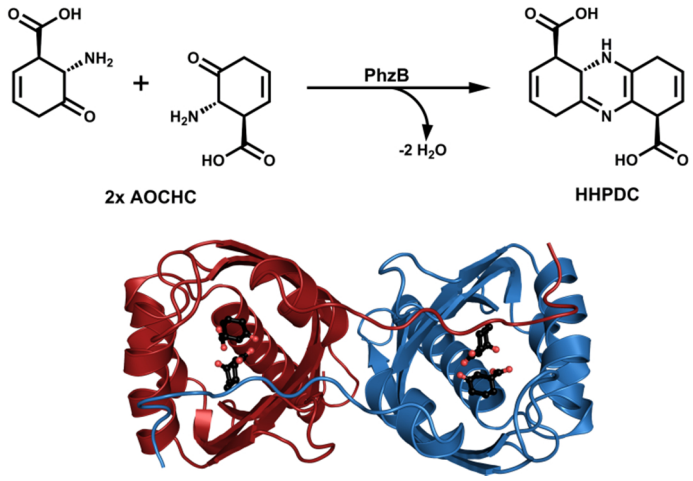

Scheme 15: PhzB-catalyzed double-condensation of the ketamine AOCHC.
Top: Schematic representation of the PhzB- catalyzed condensation reaction. Two molecules of AOCHC undergo head-to-tail condensation to yield the tricyclic HHPDC and two water molecules. **Bottom:** Structure of *Bc*Phz(A)/B in complex with the substrate analog 3OCHCA as cartoon representation (PDB entry 3DLZ; Ahuja *et al.*, 2008). Each monomer of the homodimer, shown in **firebrick** and **skyblue**, binds two molecules of 3OCHCA, depicted as balls and sticks in **black**, in its active site.

In order to gain deeper insight into the different substrate binding modes, a series of soaking experiments of *Bc*Phz(A)/B apo crystals with increasing concentrations (5, 10, 20, and 50 mM) of either 3OCHCA or another substrate analog, 2-aminocyclohexane-carboxylic acid (2ACHCA) were carried out.

As expected, Fourier-difference density (mF_o-DF_c) omit maps of the crystals soaked with 50 mM 3OCHCA clearly show that the ligand is more tightly bound to the first binding site, which is closer to the interior of the protein. In fact, this tendency is more distinct the less compound was soaked, *i.e*. the occupancy for the ligand in the four binding sites decreases with decreasing ligand concentration (Figure 29A - D). At the same time, the average temperature factors of the ligand increase with reduced occupancy (Table A6 in appendix A2); the same holds true for crystal structures in complex with 2ACHCA (Figure A13). Although, it cannot be excluded that - in particular in crystals soaked with low ligand concentrations (5 mM) - acetate from the crystallization solution is occupying the second binding site rather than the substrate analog 3OCHCA (or 2ACHCA), for comparison of the soaking experiments with different concentrations, the ligand was built in all potential binding sites and its occupancy as well as its temperature factors (B-factors) refined. Furthermore, feature enhanced maps (FEM; Afonine *et al.*, 2015) for the low concentration (5 mM) crystal structure give additional evidence that indeed the ligand and not acetate is at least partially occupying the second binding site (data not shown).

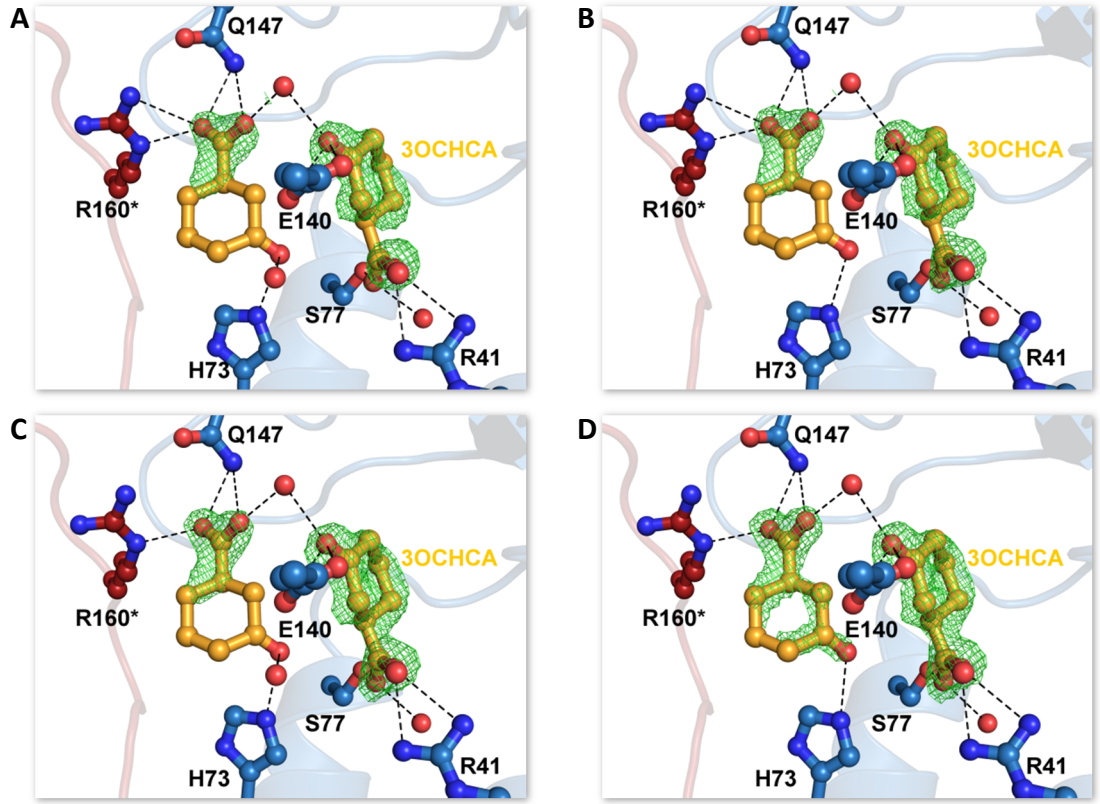

Figure 29: Crystal structures of *Bc*Phz(A)/B in complex with the substrate analog 3OCHCA after soaking with increasing concentrations.
Close-ups on the active site (chain B) of different *Bc*Phz(A)/B complex structures each with two molecules of the substrate analog **3OCHCA** bound to the active site. The structures were obtained after soaking of apo crystals with increasing concentrations of the analog overnight (**A** = 5 mM, **B** = 10 mM, **C** = 20 mM and **D** = 50 mM). The ligands as well as the coordinating active site residues are shown as ball and stick representation (* indicates that this residue is belonging to the second protein chain). The ligands are additionally depicted in their Fourier difference density (mF_o-DF_c) omit map contoured at 3σ in green. Hydrogen bonds (- - -) and coordinating water (red balls) are highlighted as well.

Altogether, the results of these soaking experiments confirm that each subunit of an active PhzBB homodimer has one high- and one low affinity binding site. This means that for catalysis at first all high affinity binding sites (one in each monomer) will be loaded before substrate molecules will occupy the second binding site and generate a productive complex. As shown in detail in paragraph 5.2.4, the PhzA subunit of the heterodimer is not only catalytically inactive but, in addition, shows no or only very low affinity towards the tested ligand. Accordingly, a heterodimer is assumed to have only one catalytic center with a high- and low-affinity binding site. This also means that as soon as the high-affinity binding site is occupied the second molecule can bind to the low-affinity binding site to form a productive complex and lead to product formation. Hence, a lower effective substrate concentration is needed. This explains why PhzAB heterodimers are found to be more effective than homodimers *in vitro.* It also suggests an important role of the heterodimer *in vivo*, where phenazine biosynthesis is a coupled process, *i.e.* the substrate

of PhzB is produced in dependence of the catalytic activity of the preceding enzymes and possibly does not reach the higher effective concentration needed for PhzBB-catalyzed condensation.

In order to investigate whether further factors influence PhzB catalysis and to assess the accuracy of the previously obtained catalytic parameters, additional enzymatic assays were performed (Figure 30). For this second set of experiments, the catalytic efficiency of 1 and 2 µM of each active dimer (*Bc*Phz(A)/B, PhzBB, and PhzAB) was compared.

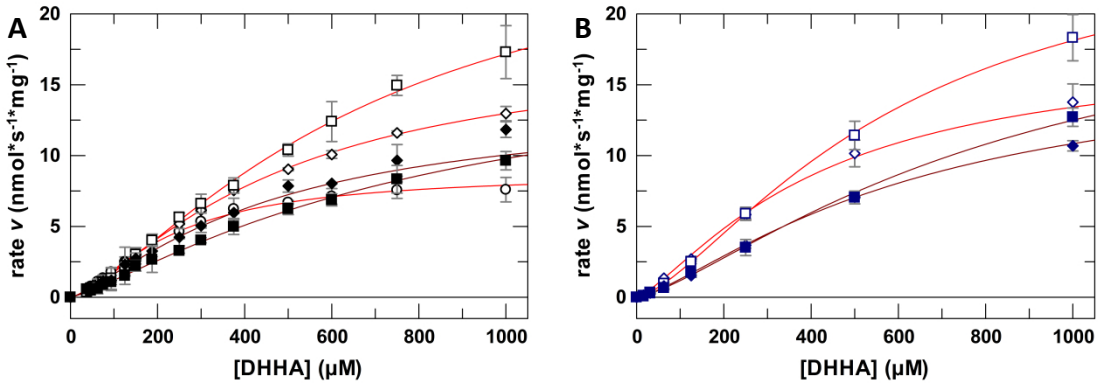

Figure 30: Enzyme kinetics for AOCHC condensation catalyzed by 1 or 2 µM of different PhzB para- and orthologues. Kinetic plots (rate *v* as a function of substrate concentration DHHA = AOCHC) showing substrate turnover by following the increase in absorption at 330 nm of a spontaneously forming downstream intermediate of the condensation reaction. **A** 1 µM and **B** 2 µM of PhzF were added to generate the PhzB substrate AOCHC *in situ*, which in turn is converted by 1 µM *Bc*Phz(A)/B (○), 1 (□, □) or 2 µM (■, ■) homodimeric PhzBB and 1 (◇, ◇) or 2 µM (◆, ◆) heterodimeric PhzAB from *P. fl* 2-79. After normalization to zero and solvent/background correction, averaged data from three independent measurements were fitted according to the Hill-equation (— and —) using GraFit 5. All data were obtained in 50 mM sodium phosphate buffer pH 7.5 at 25 °C.

The kinetic parameters for 1 µM active PhzB para- and orthologues are in very good agreement with the parameters reported before (Table 16) and attest of the good experimental reproducibility (Table 17).

Table 17: Enzyme kinetic parameters for the repeated analysis of AOCHC condensation catalyzed by different PhzB para- and orthologues at final enzyme concentrations of 1 and 2 µM.*

	v_{max} (nmol s^{-1} mg^{-1})	k_{cat} (s^{-1})	$K_{½}$ (µM)	$k_{cat}/K_{½}$ (M^{-1} s^{-1})	Hill-coefficient
1 µM *Bc*Phz(A)/B	8.8 ± 0.2	0.19 ± 0.00	230 ± 9	822 ± 35	1.50 ± 0.03
1 µM HeteroPhzAB	17.7 ± 0.5	0.70 ± 0.02	476 ± 19	1470± 70	1.36 ± 0.02
1 µM PhzBB	27.4 ± 2.4	0.57 ± 0.05	688 ± 80	836 ± 122	1.38 ± 0.04
2 µM HeteroPhzAB	13.6 ± 0.9	0.54 ± 0.04	451 ± 50	1190 ± 154	1.31 ± 0.05
2 µM PhzBB	17.5 ± 3.2	0.37 ± 0.07	824 ± 210	445 ± 140	1.24 ± 0.06

* The obtained values are averaged data of three independent measurements fitted to the Hill-equation. All data were obtained in 50 mM sodium phosphate buffer pH 7.5 at 25 °C, normalized to zero, and solvent/background corrected.

However, using 2 µM of PhzAB heterodimer or PhzBB homodimer leads to an unexpected drastic decrease of the substrate turnover when compared to the setup using 1 µM of the respective dimer. At the same time, the magnitude of the equilibrium constant $K_{½}$ was not

exceptionally affected, however, its accuracy declined remarkably by a factor of two to three. A reduced turnover rate can be observed over the whole concentration range and thus might hint towards limited substrate availability or insufficient subsequent oxidative decarboxylation (Figure 30A).

In order to assess the potentially limiting substrate availability and to exclude that the coupled enzyme is rate-limiting, additional coupled enzyme kinetic experiments with two concentrations of each PhzB dimer were performed in presence of 2 µM PhzF (Figure 30B). The results are comparable to the ones obtained in presence of 1 µM coupled enzyme and hence strongly suggest that *in situ* AOCHC production by PhzF is not rate-limiting (Table 18).

Table 18: Enzyme kinetic parameters for PhzA/B catalyzed AOCHC condensation in presence of increased final concentration of the coupled enzyme PhzF.*

2 µM PhzF	v_{max} (nmol s^{-1} mg^{-1})	k_{cat} (s^{-1})	$K_{½}$ (µM)	$k_{cat}/K_{½}$ (M^{-1} s^{-1})	Hill-coefficient
1 µM HeteroPhzAB	17.6 ± 4.3	0.70 ± 0.17	415 ± 145	1679 ± 717	1.32 ± 0.12
2 µM HeteroPhzAB	16.6 ± 1.3	0.66 ± 0.05	628 ± 68	1047± 140	1.35 ± 0.05
1 µM PhzBB	26.6 ± 0.9	0.56 ± 0.02	593 ± 25	940 ± 51	1.46 ± 0.02
2 µM PhzBB	22.5 ± 4.1	0.47 ± 0.09	846 ± 214	557 ± 174	1.36 ± 0.07

* The obtained values are averaged data of three independent measurements fitted to the Hill-equation. All data were obtained in 50 mM sodium phosphate buffer pH 7.5 at 25 °C, normalized to zero, and solvent/background corrected.

Thus, evidence suggests that in fact oxygen availability is the main obstacle in these experiments. Although, the experimental setup was created in such way that oxygen availability was maximized, it cannot be excluded that under the aforementioned conditions it is not sufficient for a rapid oxidative decarboxylation. Consequently, the intermediate HHPDC* would accumulate and could undergo unspecific side reactions diverging from the route leading to the assay probe THPCA*. As such, the obtained data for 2 µM of the dimers should be considered with caution.

5.2.3. Stability of the different PhzA/B dimers

Although the enzyme kinetic data on their own strongly support the hypothesis that PhzAB heterodimers are the prevalent form *in vivo*, it is important to analyze if heterodimers are stable and do not spontaneously dissociate into PhzAA and PhzBB homodimers. In order to address this question, enzymatic assays were carried out whereupon, additionally to 1 and 2 µM of HeteroPhzAB, also mixtures of PhzAA and PhzBB homodimers were tested for catalytic activity. Mixtures of a 1:1 ratio of the two native

homodimers were prepared in such a way that 1 and 2 µM PhzAB heterodimers would be present in the assay solution if dimerization is dynamic.

As seen in Figure 31, under the tested assay conditions no dynamic homo- and heterodimerization can be observed, as in this case the kinetic curves for native PhzAB heterodimers and mixed dimers, reconstituted from native homodimers, should be similar.

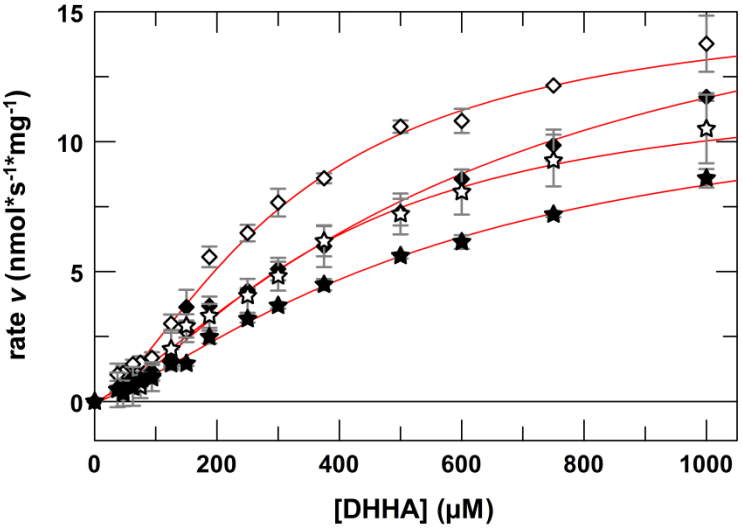

Figure 31: Kinetic plots of the enzyme catalyzed condensation of AOCHC for evaluation of dimerization dynamics in PhzA/B homo- and heterodimers.
In presence of 1 µM PhzF as coupled enzyme, PhzB catalyzed substrate turnover was followed via the increase in absorption at 330 nm of the downstream intermediate THPCA*. Kinetic plots (rate *v* as a function of substrate concentration DHHA = AOCHC) of the reaction catalyzed by 1 (◇) or 2 µM (◆) heterodimeric PhzAB from *P. fl* 2-79 or by 1:1-mixtures of homodimeric PhzAA and PhzBB, theoretically yielding heterodimer concentrations similar to the native heterodimer (✿ = 1 µM; ★ = 2 µM), are presented. All date were normalized to zero and the solvent/background subtracted. Averaged data from three independent measurements were fitted according to the Hill-equation (—) using GraFit 5. All data were obtained in 50 mM sodium phosphate buffer pH 7.5 at 25 °C.

Instead, substrate turnover for the mixture shows a remarkable decrease in comparison to the one corresponding to the heterodimer (Table 19).

Table 19: Kinetic parameters for AOCHC condensation catalyzed by native PhzAB heterodimers or 1:1 mixtures of the respective, native homodimers.*

	v_{max} (nmol s^{-1} mg^{-1})	$K_{½}$ (µM)	Hill-coefficient
1 µM HeteroPhzAB	15.4 ± 0.7	317 ± 26	1.52 ± 0.10
2 µM HeteroPhzAB	18.5 ± 1.7	653 ± 103	1.26 ± 0.08
1 µM PhzAA:PhzBB (1:1)	12.2 ± 1.3	374 ± 57	1.55 ± 0.14
2 µM PhzAA:PhzBB (1:1)	12.3 ± 1.0	572 ± 68	1.34 ± 0.04

* The obtained values are averaged data of three independent measurements fitted to the Hill-equation. All data were obtained in 50 mM sodium phosphate buffer pH 7.5 at 25 °C, normalized to zero, and solvent/background corrected.

This observation can logically be explained by the fact that within the enzyme mixtures, the actual concentration of the active homodimer PhzBB is only half the one of the theoretically reconstituted heterodimer, *i.e.* 0.5 or 1 µM respectively. As the remaining

PhzAA homodimer was found to be inactive, the turnover rate is reduced.

In addition, doubling of the enzyme concentration again led to a decrease in catalytic efficiency, *i.e.* substrate turnover is less efficient when 2 µM heterodimer or 2 µM of the mixture (accordingly 1 µM PhzBB) are used in the assay. Although attempts to address this observation were made before (*q.v.* paragraph 5.2.2.), it is especially surprising for the 2 µM mixture. This mixture comprises 1 µM PhzBB homodimer and as such should yield similar progression curves as 1 µM heterodimer (*cf.* Figure 28). As with doubled enzyme concentration, also larger values of the equilibrium constant $K_{½}$ were obtained for both the heterodimer and the mixture, a possible explanation could be that PhzA subunits bind the substrate (or other intermediates and products of the reaction), too, thus reduce the levels of free substrate and hence interfere with the condensation reaction. Yet, this behavior was not observed in experiments using PhzAB dimers before (*cf.* paragraph 5.2.2.) and binding data as well as a crystal structure (see paragraph 5.2.4.) do not support this mechanism.

Although the kinetic data alone implicate that heterodimers - once formed - are stable, dimer stability was additionally addressed by recording melting curves using CD spectroscopy. As verified by standard CD spectra that were recorded prior to the unfolding experiment, all four PhzB para- and orthologues, *Bc*Phz(A)/B, PhzBB, PhzAA and HeteroPhzAB, are correctly folded (Figure 32).

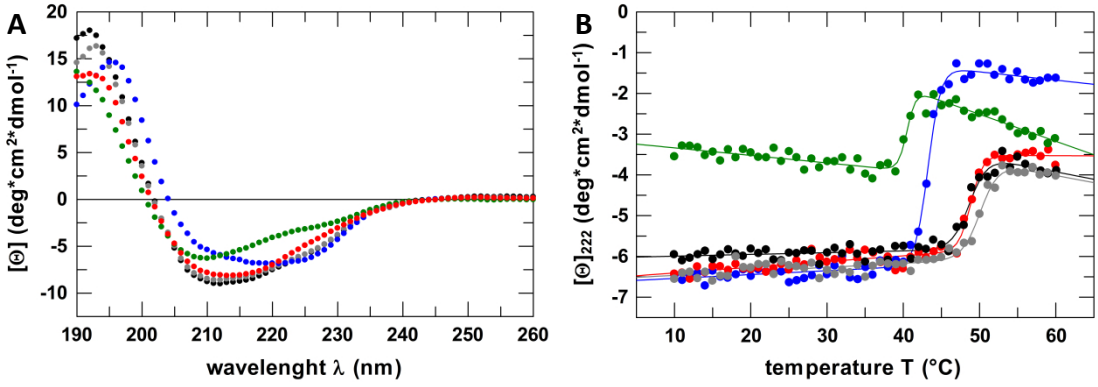

Figure 32: Structural integrity and thermal stability of different PhzB para- and orthologues.
A Far-UV CD spectra of *Bc*Phz(A)/B (●), HeteroPhzAB w/ (●) and w/o N-terminal hexahistidine-tag (●), PhzBB (●) and PhzAA (●) dimers obtained at 10 °C in 50 mM sodium phosphate pH 7.5. **B** Melting curves of the PhzB para- and orthologues (colors according to plot **A**) recorded within a temperature range from 10 to 60 °C using the CD signal at 222 nm. The signal was converted to mean residue ellipticity [Θ]MRW and plotted against the temperature T (°C).

Furthermore, the spectral data in Figure 32A show no major difference between a hexahistidine-tagged and tag-free HeteroPhzAB dimer, hence it appears that the N-

terminal His_6-tag does not significantly affect dimer stability. Likewise, the spectra show that the organization of secondary structure elements of PhzAB heterodimers and PhzBB homodimers is very similar. Both enzymes resemble a typical mixed α-β-type. This observation is in good agreement with previously obtained crystal structures (Ahuja *et al*., 2004; Ahuja, 2007; Porfetye, 2009).

Based on these findings, melting curves were determined at two different wavelengths, 222 and 212 nm as shown in Figure 32B and Figure A14 (appendix A2) respectively. The calculated melting temperatures revealed that the enzyme from *B. cepacia* R18194, with an average melting temperature of 43.8 °C, is less stable than the similar homodimer from *P. fluorescens* 2-79 (T_M (Ø) = 48.6 °C), while the heterodimer of the latter species shows no significant difference in thermal stability (T_M (Ø) = 48.8 °C). The PhzAA homodimer is found to be less stable enzyme, with an average melting temperature of 40.4 °C. This 8 K lower stability suggests that PhzAA homodimers are unlikely to be found *in vivo*. Since heterodimers appear as stable as active homodimers, this result provides additional evidence that in fact heterodimers could be the predominant dimerization form in *P. fluorescens* 2-79 *in vivo*.

5.2.4. One or two? – A closer look at active site(s) of PhzAB heterodimers

In order to verify the assumption that the A subunit of PhzAB is not only catalytically inactive, but cannot bind substrate molecules either, binding experiments of PhzAA and PhzBB homodimers as well as of PhzAB heterodimers were carried out. Originally, isothermal titration calorimetry (ITC) was chosen for this purpose. However, initial experiments yielding no interpretable binding information revealed that the aforementioned enzymes are not compatible with this method. This unusual behavior was also reported previously (Porfetye, 2009) and presumably is an intrinsic property of these enzymes. Instead, affinity parameters for a known PhzB ligand (phenazistatin A) were determined for either of the dimers from *P. fluorescens* 2-79 using microscale thermophoresis (MST). As the dissociation constant for its complex with phenazistatin A was known from previous ITC experiments, the homodimeric enzyme from *B. cep* R18194 was supposed to serve as internal reference, however it proved to be incompatible with the MST setup. Hence, only the three dimers of interest were analyzed using this method.

Figure 33 shows that, among the tested paralogues, the active homodimer PhzBB has the highest affinity towards phenazistatin A (K_D = 1.47 µM).

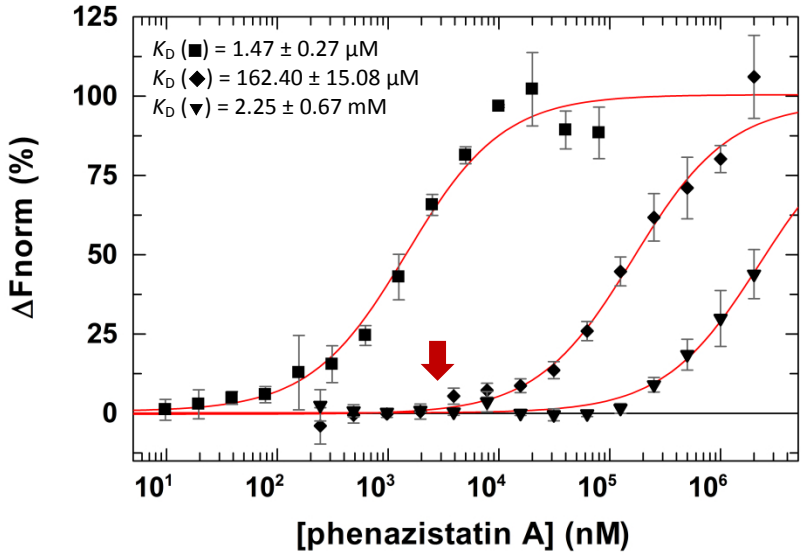

Figure 33: Affinity titrations of phenazistatin A to different PhzB paralogues from *P. fluorescens* 2-79.
Microscale thermophoresis measurements of 80 µM PhzBB (■) and each 2 mM PhzAA (▼) and PhzAB (◆) incubated with the indicated concentrations of Phenazistatin A were carried out in 20 mM TRIS/HCl pH 7.5, 150 mM at 25 °C. The protein intrinsic tryptophan fluorescence was used as molecular probe. All data were normalized and the averaged values from three independent measurements fitted according to a two-state-model (—) using GraFit 5.

Since MST measurements for the known phenazistatin A binding protein *Bc*Phz(A)/B failed, this value cannot be compared to the known affinity of 64 nM, however it suggests that binding of phenazistatin A to PhzBB is less strong than binding to the enzyme from the *Burkholderia* species. This is also in good agreement with the kinetic data (*q.v.* paragraph 5.2.2.), which showed that the enzyme from *B. cep* R18194 has a three-fold higher apparent affinity for its substrate than the enzyme from *P. fl* 2-79 (approximately 250 and 800 µM respectively).

The K_D of phenazistatin A for the inactive PhzAA was found to be ≥ 2 mM (2.25 mM) and thus more than three orders of magnitude higher than for the corresponding active paralogue PhzBB. This indicates that, besides lacking catalytic activity, binding of substrates to the PhzAA homodimer might be drastically impaired as well. Finally, the K_D for the PhzAB heterodimer is 162 µM. Although this value is also two orders of magnitude higher than the one for the PhzBB homodimer, it can be explained by the fact that this observed K_D represents an average K_D of the high affinity binding site in the active B-subunit and the very weak-affinity binding site in the inactive A-subunit. Indeed, the plot in Figure 33 for the PhzAB heterodimer shows a small double transition curve with a step

~1-2µM (arrow), but this is mostly "masked" by the weak binding event of the ligand to the A-subunit.

In addition, biochemical activity assays and IC_{50} determinations with the potential inhibitor phenazistatin A were carried out. Although, these results will only be presented in the next chapter (chapter III), it can already be stated, that they are in good agreement with the binding data.

In order to analyze binding of phenazistatin A to the PhzAB heterodimer further, co-crystallization experiments with HeteroPhzABcut were carried out. The structure of the complex could be solved at 1.53 Å resolution using molecular replacement with the previously obtained apo structure (Blankenfeldt *et al.*, unpublished) as a search model (Figure 34 and Table 20).

The heterodimer crystallized in space group P1 with two heterodimers in the asymmetric unit. These two heterodimers are related by non-crystallographic two-fold symmetry (Figure 34A). After soaking with 10 mM of the ligand for 2 h, positive difference electron density (mF_o-DF_c), which is exclusively observed in the active site of B-subunits of the heterodimer, was attributed to the presence of phenazistatin A (Figure 34B and C). Moreover, since the diffraction data were collected at a wavelength corresponding to the K-edge of bromine, the anomalous signal, again only found in the B-subunits of the protein, allowed unambiguous positioning of the Br-atom of phenazistatin A (Figure 34D). Analysis of the binding site reveals that the ligand is bound in a very similar way as reported previously for the *Burkholderia* enzyme (PDB entry: 3JUM; Mentel *et al.*, 2009), *i.e.* mainly via its carboxylic acid moieties. The carboxylic acid group attached to the aromatic ring of the ligand is coordinated by Q144, as well as R160*, the C-terminal arginine from the A-subunit, and a water molecule, which in turn is stabilized via hydrogen bond to Y117 and E137. This glutamate further accepts a hydrogen bond from the bridging amino group of phenazistatin A. The second carboxylate of the ligand is primarily stabilized via a salt bridge to the guanidine moiety of R38. Further hydrogen bonds stabilizing this group are involving the hydroxyl-group of S74 and two additional water molecules.

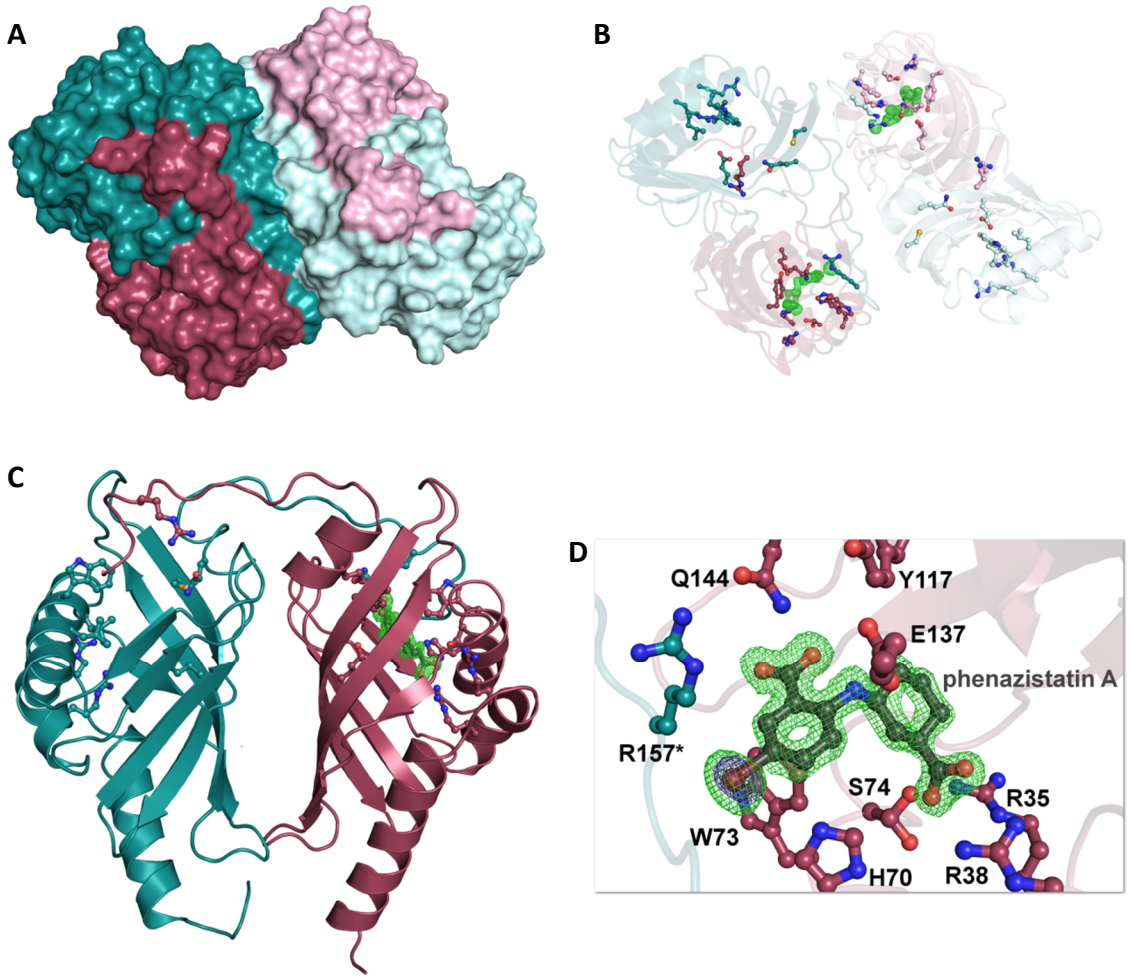

Figure 34: Crystal structure of the PhzAB heterodimer from *P. fluorescens* 2-79 in complex with the potential inhibitor phenazistatin A.
A Surface representation of two PhzAB heterodimers as found in the asymmetric unit of the crystal. The A-subunits are colored in **deepteal** and **palecyan** respectively, while the B-subunits are shown in **raspberry** and **lightpink**. **B** The two PhzAB heterodimers of the asymmetric unit are shown as cartoon representation with the active site residues of all subunits highlighted as balls and sticks (colors as described previously). Additionally, the ligands Fourier difference density (mF_o-DF_c) omit map contoured at 3σ is shown in **green**. **C** Overall view of a PhzAB heterodimer and **D** close-up on the active site of the B-subunit with the ligand highlighted as balls and sticks in **dark gray** and the anomalous map for the bromine atom countered at 8σ shown in **purpleblue**. The protein is again shown as cartoon and the active site residues as balls and sticks colored in a similar way as described before.

Analysis of the active site pocket using the program KVFinder (Oliveira *et al.*, 2014) revealed that the pocket in the B-subunit of the heterodimer has a volume of ~500 Å³ and as such is 60 Å³ smaller than the one in *Bc*Phz(A)/B. Interestingly the pocket in the inactive A-subunit is way larger with a volume of 765 Å³. This difference is mainly due to a substitution of tyrosine 117 to cysteine in PhzA and the displacement of the C-terminus leading to an opening of the pocket (Figure A15 in appendix A2). Consequently, less hydrogen bonds for stabilization of the ligand can be established and thus no binding of phenazistatin A to the A-subunit can be observed.

Table 20: Data collection and refinement statistics for HeteroPhzABcut (*P. fl* 2-79) in complex with phenazistatin A.‡

	Complex with phenazistatin A
Data collection[1]	
Beamline†	MX BL14.1, BESSY II
Wavelength (Å)	0.91841
Resolution range (Å)	49.63 – 1.53 (1.56 – 1.53)
Space group	P1
unit cell dimensions	
a, b, c (Å)	46.03, 55.61, 65.45
α, β, γ (°)	72.00, 70.73, 65.65
Mosaicity (°)‡	0.20
Measured reflections	156883 (7859)
Unique reflections	79502 (3896)
Multiplicity	2.0 (2.0)
Mean I/σ(I)	9.8 (2.0)
$CC_{1/2}$*	0.996 (0.567)
Completeness (%)	96.4 (95.1)
R_{meas}§	8.1 (62.8)
$R_{p.i.m.}$¶	5.5 (42.6)
Refinement	
Resolution range (Å)	49.63– 1.53 (1.55 – 1.53)
R_{cryst} (%)	18.00 (28.12)
R_{free} (%)	20.26 (30.90)
No. of non H-atoms	
Protein	5083
Ligand / Ion	40
Water	602
Average B-factors (Å²)	
Protein	17.6
Ligand / Ion	13.3
Water	30.3
R.m.s deviations	
Bond lengths (Å)	0.009
Bond angles (°)	0.902
Ramachandran plot (%)	
Favored regions	98.9
Outliers	0
MolProbity score #	1.14

‡Values in parentheses are for the highest resolution shell -

[1] The dataset was collected from a single crystal.

† BESSY II: Berlin Electron Storage Ring Society for Synchrotron Radiation, Helmholtz Centre Berlin, Berlin, Germany.

‡ Mosaicity values reported by *XDS* (Kabsch, 2010).

* $CC_{1/2}$ is the correlation coefficient between two random half datasets (Karplus and Diederichs, 2012)

§ $R_{meas} = \sum_{hkl}\{N(hkl)/[N(hkl)-1]\}^{1/2}\sum_i|I_i(hkl)-\langle I(hkl)\rangle|\,/\sum_{hkl}\sum_i I_i\,(hkl)$, where *N(hkl* is the number of observations of the reflection with index *hkl* and $I_i(hkl)$ is the intensity of its *i*th observation (Diederichs and Karplus, 1997);

¶ $R_{p.i.m.} = \sum_{hkl}\{1/[N(hkl)-1]\}^{1/2}\sum_i|I_i(hkl)-\langle I(hkl)\rangle|/\sum_{hkl}\sum_i I_i(hkl)$ (Weiss, 2001)

As reported by *MolProbity* (http://molprobity.biochem.duke.edu/ (Chen *et al*., 2010)

Overall, the binding data as well as the new crystal structure support the hypothesis that PhzAB heterodimers indeed have only one active site, which provides them with an advantage over PhzBB homodimers especially under substrate limitations. At the same time, since PhzAB heterodimers feature only one active site (B-subunit) that binds substrates or other ligands such as the inhibitor phenazistatin A a lower effective concentration of this inhibitor will be needed to suppress Phz(A)/B activity (see also paragraph 6.2.2.).

5.2.5. Addressing a potential protein-protein interaction between the two subsequent enzymes of phenazine biosynthesis, PhzF and PhzB

Several steps of phenazine biosynthesis involve instable intermediates. One of these is the product of the isomerase PhzF, AOCHC. This highly reactive amino ketone undergoes not only PhzB-catalyzed or uncatalyzed condensation to the tricyclic phenazine precursor HHPDC, but is also expected to unspecifically react with other free primary amines. In order to reduce or even circumvent these unfavored side reactions, nature might have developed different strategies such as the formation of protein-protein complexes between the two consecutive enzymes PhzF and PhzB to facilitate direct transfer of the instable intermediate between the two active sites without releasing it to the environment.

In order to probe whether PhzF and PhzB and/or the respective dimers form protein-protein complexes, a variety of experiments such as affinity titrations via ITC, analytical size-exclusion chromatography (SEC) or dynamic light scattering (DLS) were carried out. However, none of these studies yielded any evidence for the presence of such complexes *in vitro* (data not shown). Yet, it might be possible that these multiprotein complexes form only transiently and in presence of the intermediate AOCHC. To test this hypothesis, enzymatic assays were carried out whereupon PhzF – as the coupled enzyme - and PhzB-orthologues from two different species, namely *P. fluorescens* and *Burkholderia spp.*, were alternatively combined and the mixtures' catalytic efficiencies, regarding formation of the tricyclic phenazine precursor HHPDC (and accordingly THPCA*), compared (Table 21 and Figure 35). It is assumed that enzymatic turnover of AOCHC is only accelerated if a favorable interaction between the two enzymes of the same species is established. In that case AOCHC would be directly transferred from one active site (PhzF) to the next one (PhzB) instead of being released in the environment. The results of experiments with PhzF from *P. fluorescens* 2-79 in combination with both PhzB orthologues were already discussed in a previous paragraph (paragraph 5.2.2.). Yet for better comparison, they are also shown in Figure 35 together with the data obtained when using PhzF from *B. glumae* BGR-1 as coupled enzyme.

Table 21: Enzyme kinetic parameters for AOCHC condensation catalyzed by two different PhzB orthologues in dependency of the origin of species of the coupled enzyme PhzF.*

		k_{cat} (s^{-1})	$K_{½}$ (µM)	$k_{cat}/K_{½}$ (M^{-1} s^{-1})	Hill-coefficient
***Pfl*PhzF**	*Bc*Phz(A)/B	0.22 ± 0.01	266 ± 12	835 ± 46	1.37 ± 0.02
	PhzBB	0.58 ± 0.05	797 ± 83	731 ± 98	1.30 ± 0.02
***Bglu*PhzF**	*Bc*Phz(A)/B	0.18 ± 0.01	231 ± 15	792 ± 59	1.54 ± 0.08
	PhzBB	0.62 ± 0.08	907 ± 168	687 ± 155	1.24 ± 0.05
***Bglu*PhzFΔ123**	*Bc*Phz(A)/B	0.19 ± 0.01	233 ± 14	832 ± 63	1.73 ± 0.07
	PhzBB	0.44 ± 0.04	593 ± 74	751 ± 120	1.39 ± 0.04

* The obtained values are averaged data of three independent measurements fitted to the Hill-equation. All data were obtained in 50 mM sodium phosphate buffer pH 7.5 at 25 °C, normalized to zero, and solvent/background corrected.

Furthermore, not only full length *Bglu*PhzF was used in these studies, but also the isolated isomerase domain *Bglu*PhzΔ123 (for details see chapter I, paragraph 4.2.5.). The idea behind the usage of these two variants was to figure out whether the additional non-isomerase domain of the enzyme from the *Burkholderia* species plays a specific role in a potential protein-protein interaction or influences PhzB catalysis by other means.

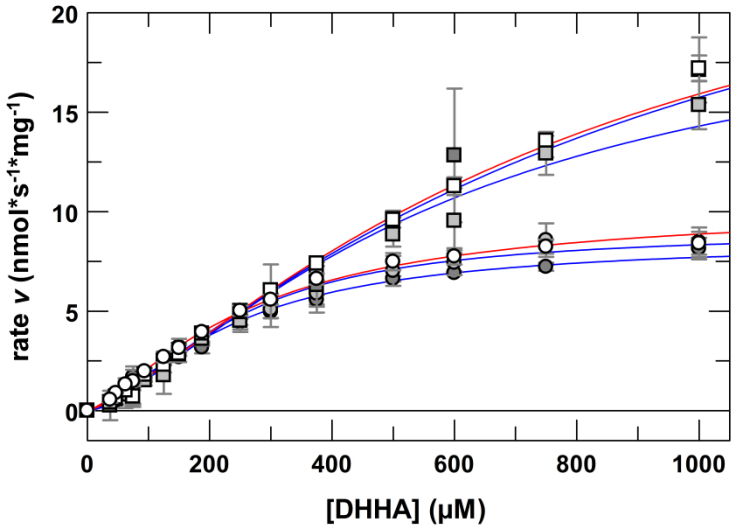

Figure 35: Kinetic plots of the enzyme catalyzed condensation of AOCHC by two PhzB orthologues in dependency of the origin of species of the coupled enzyme PhzF.
Following the increase in absorption at 330 nm of the downstream intermediate THPCA*, PhzB catalyzed substrate turnover is visualized in kinetic plots (rate *v* as a function of substrate concentration DHHA = AOCHC). The PhzB substrate AOCHC is generated *in situ* by 1 µM of the coupled enzyme PhzF, either from *P. fluorescens* 2-79 (○; □) or *B. glumae* BGR-1 (●; ■ = full length protein; ○; □ = isolated isomerase domain) and in turn converted by 1 µM *Bc*Phz(A)/B (circles) or 1 µM (squares) homodimeric *Pfl*PhzBB. The data were normalized to zero and solvent/background corrected. Averaged data from three independent measurements were fitted according to the Hill-equation (— = *Pfl*PhzF and — = *Bglu*PhzF) using GraFit 5. All data were obtained in 50 mM sodium phosphate buffer pH 7.5 at 25 °C.

However, as shown in Figure 35 and Table 21, no matter which PhzF/PhzB protein-protein combination was tested, no significant difference in the enzyme kinetic parameters could be observed, all values were within the range of their standard deviation.

Hence, also the kinetic data cannot positively confirm that PhzF and PhzB form a multiprotein complex in order to optimize phenazine biosynthesis. Yet, since all previously

described data were only obtained with isolated enzymes *in vitro*, it cannot fully be excluded that complex formation might occur *in vivo* - potentially even assisted by an additional interaction partner - and thereby assist in efficient phenazine production.

5.3. Conclusion

Based on the previously identified catalytic mechanism of PhzB (Ahuja *et al.*, 2008) and the description of its role in phenazine biosynthesis a coupled enzymatic assay was developed to further characterize this enzyme. Not only kinetic parameters regarding the head-to-tail double condensation of the ketamine substrates should be studied, but also in particular the occurrence of different dimeric enzyme species in pseudomonads, one group of phenazine producing bacteria. Indeed, it was found that *Pseudomonas spp.* carry a second copy of the *phzB*-gene called *phzA* in their genome. Previous data as well as experiments undertaken in this study showed that this copy is catalytically inactive in the condensation reaction. In addition, quantitative real-time PCR experiments from collaborators (Dimitri Mavrodi and Linda Thomashow, unpublished) revealed that, at least in *Pseudomonas fluorescens 2-79*, only one transcript of the *phz*-operon can be found. This suggests simultaneous translation of the resulting full length mRNA, leading to similar protein levels in the cell. This raised the question about the biological role of PhzA, especially in *P. fluorescens*, as it seems energetically unfavorable that nature spends metabolic resources for production of an inactive "enzyme". However, from a closer look at the two gene products, it becomes clear that the resulting proteins share a high sequence similarity of almost 70 % and as such, it is not surprising that they also exhibit a high structural similarity (Ahuja, 2007). This peculiarity in mind and knowing that all other enzymes of the "core" phenazine biosynthesis pathway are active dimers, it was hypothesized that PhzA and PhzB form PhzAB heterodimers.

Indeed, after heterologous co-expression of both genes simultaneously in *E. coli*, a PhzAB heterodimer could be isolated (Weikart, 2006) and even crystallized (Blankenfeldt *et al.,* unpublished). Yet, a more detailed biochemical and biophysical characterization of this heterodimer was lacking, especially regarding its enzymatic activity in comparison to PhzBB homodimers. To this aim, a new activity assay was developed and used for enzyme kinetic experiments. These experiments resulted in the finding that in fact PhzAB heterodimers are, regarding their turnover rate, more active (higher k_{cat}-value), but also

overall more efficient in catalysis (larger $k_{cat}/K_{½}$-values) than PhzBB homodimers, especially at low substrate concentrations (Figure 36).

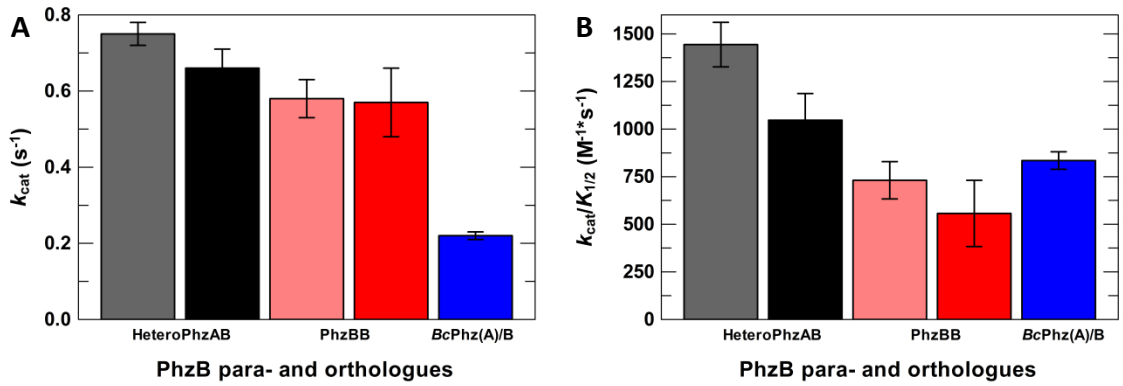

Figure 36: Direct comparison of the key kinetic parameters k_{cat} and $k_{cat}/K_{½}$ for different PhzB para- and orthologues. **A** Comparison of the catalytic turnover rate (k_{cat}) for heterodimeric PhzAB (= 1 µM; = 2 µM), homodimeric PhzBB (= 1 µM; = 2 µM) and *Bc*Phz(A)/B (= 1 µM). **B** Overall catalytic efficiency $k_{cat}/K_{½}$ compared for different PhzB para- and orthologues. (color scheme as described in **A**). The data were normalized to zero and solvent/background corrected. Averaged data from three independent measurements were fitted according to the Hill-equation using GraFit 5. All data were obtained in 50 mM sodium phosphate buffer pH 7.5 at 25 °C.

Together with the observation that the heterodimer is as stable as the PhzBB homodimer and both show an increased stability of 8 °C in comparison to the inactive homodimer PhzAA, these data strongly support the hypothesis that PhzAB heterodimers might be the prevalent form *in vivo*. However, it cannot fully be excluded that also PhzBB homodimers are present under physiological conditions or that pseudomonads can switch between production of homo- and heterodimers. Since the homodimers carry two active sites each baring two substrate-binding sites, the maximal catalytic velocity (v_{max}) that can be reached is higher. This might especially be important at higher substrate levels as the substrate AOCHC is highly reactive and thus unfavored side reactions, which might be harmful to the phenazine producer itself, could be minimized.

In addition to the kinetic characterization of PhzB para- and orthologues, binding studies and crystallographic experiments were carried out. The purpose of these experiments was mainly the characterization of the interaction between a previously identified synthetic Phz(A)/B ligand, called phenazistatin A, and the homodimeric proteins PhzAA and PhzBB or the PhzAB heterodimer. In line with previously made mechanistic assumptions, the absence of a ligand in the inactive A-subunit of the heterodimer crystal structure confirmed that specific ligands can only bind to active B-subunits. This study also revealed

phenazistatin A as a promising starting point for further inhibition studies (as discussed in detail in the next chapter), since it binds very tightly to PhzBB homodimers (K_D ~1.5 µM).

Furthermore, it is not yet fully understood how phenazine-producing organisms ensure efficient condensation of the highly reactive amino ketone substrate while limiting its potentially harmful side reactions. A proposed mechanism of a direct interaction between the two subsequent enzymes in the biosynthesis pathway, PhzF and PhzB, could not be detected so far, although it cannot be ruled out that additional partners are involved *in vivo*. This hypothesis and the actual *in vivo* abundance of homo- and heterodimers have to be evaluated further, for example using additional techniques such as proteomics.

CHAPTER III:
Triggering self-intoxication – Development of synthetic PhzB product analogs into inhibitors of phenazine biosynthesis

6. PhzB-inhibitors

Phenazines, such as the blue pigment pyocyanin produced by the human pathogen *Pseudomonas aeruginosa*, are important virulence factors in nosocomial infections. Hence, their biosynthesis is a potential drug target to fight infectious diseases caused by phenazine producing pathogens. Phenazine biosynthesis is characterized by five enzyme-catalyzed steps leading from chorismate to formation of two core phenazines, dihydro-phenazine-1-carboxylic acid (DHPCA) or dihydro-phenazine-1,6-dicarboxylic acid (DHPDC) (*cf*. paragraph 1.2.2.). One step catalyzed by the small dimeric protein PhzB (*q.v*. chapter II) involves the symmetrical head-to-tail double condensation of two identical ketamine precursor molecules. For mechanistic studies of this reaction, a variety of substrate and product analogs were synthesized. Specifically, two classes of these analogs, termed "mavericks" and "phenazistatins", turned out to bind the enzymes from *B. cepacia* and *P. fluorescens* tightly, *i.e.* in low µM- or even nM-range. Despite having some preliminary binding data (Mentel, 2008), no information was available for these ligands regarding their inhibitory potency *in vitro* or *in cellulo*.

In order to conduct a comprehensive structure-activity-relationship study, a new library composed of approximately 80 compounds was synthesized and about ⅓ of these ligands were analyzed in binding assays using isothermal titration calorimetry (ITC). In addition, the binding mode of several ligands to the active site of Phz(A)/B from *B. cep* R18194 was revealed by X-ray crystallography. The inhibitory potency of the complete library was also evaluated using a newly developed enzyme inhibition assay allowing rapid screening of this large number of compounds.

A selection of the most promising compounds together with bioisosteres and prodrug esters was analyzed regarding their efficacy for reduction of pyocyanin levels in *Pseudomonas aeruginosa* cultures.

6.1. Specific Methods & Materials

The investigation of potential PhzB-inhibitors is based on previous data, in particular the work from Matthias Mentel (Mentel, 2008; Mentel *et al.*, 2009a and 2009b). Some experiments were carried out in collaboration with other groups: Florian Gräf, a PhD student in the group of Prof. Dr. Claus-Michael Lehr from the Helmholtz Institute for Pharmaceutical Research Saarland, evaluated membrane permeability of some of the identified inhibitors. The *in cellulo* compound screening was carried out in collaboration with the group of Prof. Dr. Rolf Hartmann of the same institute based on an assay developed by Dr. Christine Maurer and with special assistance by Antonio Martins.
Finally, the work from Jakob Pletz from the group of Prof. Dr. Rolf Breinbauer at the Graz University of Technology deserves a special mentioning as he synthesized the majority of the compounds tested in the course of this study.
Parts of their data and results will be presented within the framework of this thesis without discussing their employed experimental techniques.

6.1.1. Protein production

The dimeric enzymes, *Bc*Phz(A)/B, PhzBB and HeteroPhzAB were produced as described in the previous chapter (paragraph 5.1.1.). The coupled enzyme PhzF was expressed as presented in paragraph 4.1.1 in chapter I.

6.1.2. Isothermal titration calorimetry

Affinity titrations were carried out at 25 °C using a MicroCal™ VP-ITC System (GE Healthcare, now Malvern Instruments). In all experimental setups, the sample cell contained *Bc*Phz(A)/B at a final concentration of 100 µM (active site) in 20 mM TRIS/HCl pH 8.0, 150 mM NaCl. After an initial delay of 60 s, the protein was titrated with 2 mM ligand prepared either from aqueous (10 mM in 200 mM TRIS/HCl pH 9.0) or from DMSO (200 mM) stock solutions. If residual DMSO (up to 1 % (v/v)) was present in the syringe, the same amount was added to the sample cell to ensure buffer homogeneity. Using 10 µcal s^{-1} reference power in high feedback mode, the ligands were injected at a rate of 0.5 µL s^{-1} and a stirring speed of 307 rpm with 240 s gaps between individual injections. The data were analyzed and plotted using the programs NITPIC (Keller *et al*., 2012;

Scheuermann and Brautigam, 2015), SEDPHAT (Houtman *et al*., 2007; Zhao *et al*., 2015), and GUSSI (Brautigam, 2015; and for review Brautigam *et al*., 2016).

6.1.3. Crystallization and structure determination

All soaking experiments were carried out using crystals of native *Bc*Phz(A)/B which could regularly be obtained at 12 °C from a grid screen of 0.1 M Bis-TRIS pH 6.1 – 6.7, 0.2 M ammonium acetate, 16 – 20 % (w/v) PEG 3350 (Ahuja *et al*., 2008) as described in paragraph 4.1.5. Crystals were soaked overnight in mother liquor supplemented with 25 % (v/v) glycerol and 10 mM of the respective compound at 12 °C. Co-crystallization attempts with 10 or 40 mM compound WB086 (stock solution: 500 mM in pure DMSO) were carried out in a grid screen with 0.1 M Bis-TRIS pH 6.6 – 7.0, 0.2 M ammonium acetate, 18 – 28 % (w/v) PEG 3350 (Mentel *et al.*, 2009a). Cryo protection of these crystals was achieved similarly to the soaks.

Crystals were mounted on nylon loops and flash frozen in liquid nitrogen. Diffraction data were collected at 100 K at beamline MX BL14.1, BESSY II at the Helmholtz Centre Berlin, at beamline X06DA (PXIII) at the Swiss Light Source (SLS) of the Paul Scherrer Institute, at the European Synchrotron Radiation Facility (ESRF), Grenoble or at beamline P11, PETRA-III at DESY (Deutsches Elektronen-Synchrotron), Hamburg. Data reduction, structure refinement, and model building were carried out as described in paragraph 4.1.4. Ligand restraints where generated from SMILES-strings using the program phenix.elbow (Moriarty *et al.*, 2009) of the PHENIX software suite (Adams *et al.*, 2010). Structural flexibility was modelled using TLS refinement (Schomaker and Trueblood, 1968). In the last step of refinement, heteroatoms like waters and the ligand were attributed to the nearest TLS group using a script developed in the group (Reichelt and Blankenfeldt, unpublished). Final structure validation was done with MolProbity (Chen *et al.*, 2010). Full data collection and refinement statistics are shown in Tables A11-A16 in the appendix.

6.1.4. *In vitro* inhibition assay

In order to evaluate the inhibitory effect of different compounds on PhzB catalysis, the previously described coupled photometric condensation assay (*q.v.* paragraph 5.1.2.) was adapted. In brief, standard solutions containing both 1 µM (dimer) of the coupled enzyme

PhzF and the target *Bc*Phz(A)/B) were used for dose-response experiments. A serial ten times dilution (from aqueous or DMSO stock solutions) of the respective compound, *i.e.* 100, 10, 1, and 0.1 µM, was tested in presence of either 125 µM or 1 mM DHHA. All experiments were carried out in UV-Star® 96-Well microplates (Greiner Bio-One) at 25 °C in an Infinite® M200 microplate reader (Tecan Group Ltd.). A final reaction volume of 150 µL in 50 mM sodium phosphate buffer at pH 7.5 supplemented with 2 % (v/v) DMSO was obtained by addition of 75 µL pre-mixed enzyme solution to an equal volume of each substrate/inhibitor dilution. The increasing absorption of the metastable tricyclic phenazine intermediate THPCA*was monitored at 330 nm over a 20 minutes time course and in 40 s intervals. As reference, a reaction mixture lacking inhibitor was used. The background of the uncatalyzed auto condensation was evaluated with reaction mixtures lacking *Bc*Phz(A)/B and the potential inhibitor. Reaction rates were determined from the slopes of the linear phase of each curve after normalization to zero. After background correction, the residual enzyme activity was calculated in relation to the inhibitor free sample. All samples were analyzed in triplicate.

6.1.5. *In cellulo* pyocyanin assay

In cellulo, the influence of the inhibitors on pyocyanin production was analyzed according to a previously described protocol (Klein *et al*., 2012, Essar *et al.*, 1990). In brief, cultures of *Pseudomonas aeruginosa* PA14 or PAO1 in PPGAS- (20 mM NH_4Cl, 20 mM KCl; 120 mM TRIS/HCl pH 7.2, 1.6 mM $MgSO_4$, 1 % (w/v) tryptone, 0.5 % (w/v) glucose) or M63-medium (15 mM $(NH_4)_2SO4$, 100 mM KH_2PO_4 pH 7.0, 1.8 µM $FeSO_4$ x $7H_2O$, 1 mM $MgSO_4$, 0.2 % (w/v) glucose, 0.1 % (w/v) casamino acids) were grown in presence of 100 µM of each inhibitor. CELLSTAR® 24-well plates (Greiner Bio-One) were filled with 1.5 mL bacterial culture (OD_{600} = 0.02) per well. 10 mM inhibitor solution (in pure DMSO) was added to the cultures to yield a final concentration of 100 µM inhibitor in 1 % (v/v) DMSO, for control experiments, pure DMSO was added. Culture plates were sealed with an air-permeable membrane and incubated at 37 °C, 200 rpm, and ~75 % humidity for 16 h. After that, the OD_{600} of the samples was determined. For pyocyanin quantification, 900 µL of each culture were extracted with 900 µL chloroform and the phases separated by centrifugation at 14 000 rpm for 15 min. 800 µL of the organic phase were taken off, mixed with 250 µL of 0.2 M HCl and centrifuged at 14 000 rpm for 15 min. 80 µL of the

aqueous phase were transferred to Nunc U96 MicroWell™-plates and the OD_{520} measured using a FLUOstar Omega (BMG Labtech) or an Infinite® M200 (Tecan Group Ltd.) microplate reader. For each sample, cultivation and extraction were performed in triplicates. Percent inhibition was calculated in relation to the DMSO control after growth correction.

6.2. Results & Discussion

6.2.1. Binding behavior of PhzB product analogs

In order to optimize ligand efficiency, new potential PhzB-inhibitors were synthesized following a rational design approach (Jakob Pletz) and analyzed regarding their affinity towards Phz(A)/B from *B. cepacia* R18194. As a proof of concept, the already determined dissociation constant for the pure *S*,*R*-isomer (WB001) of a compound called phenazistatin A, was confirmed by ITC experiments (K_D = 63.7 ± 10.7 nM compared to 51 nM as determined by Matthias Mentel).

Having successfully repeated this titration experiment, binding affinities of overall 30 different newly synthesized compounds were investigated. Differing in the derivatization of the characteristic anthranilic acid either by an *N*-piperidinyl- or *N*-carboxycycloalkyl-moiety, these compounds can be divided in two sub-groups, which are termed "mavericks" and "phenazistatins" respectively (Figure 37). "Phenazistatins" with affinities in the low µM- or even nM-range (Figure 38, Table 22 and Table A9 in appendix A3) appeared to be generally more potent binders than "mavericks" with K_D-values of approximately 10 - 20 µM (see below).

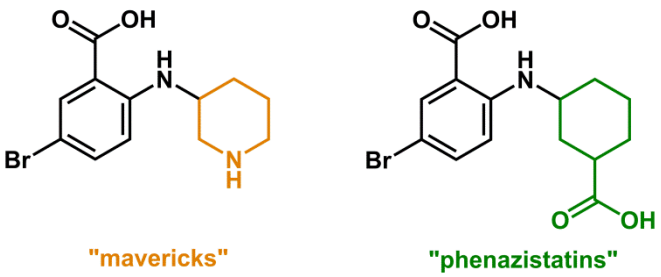

Figure 37: Schematic representation of the two sub-groups of anthranilic acid derived PhzB ligands.
The figure shows the chemical formula of 5-bromo-2-(piperidin-3-ylamino)benzoic acid (WB078), a representative of the *N*-piperidinyl anthranilic acid derivatives called **"mavericks"**, and 5-bromo-2-((3-carboxycyclohexyl)amino)benzoic acid (*rac*-WB001), a member of the *N*-carboxycycloalkyl anthranilic acid derivatives called **"phenazistatins"**. The characteristic moiety allowing differentiation of these two groups is highlighted.

Five compounds (WB019, WB020, WB035, WB067, and WB071) showed either no affinity towards *Bc*Phz(A)/B or accurate data evaluation failed (*q.v.* Figure A17C and D, Figure A19A and D and Figure A20B in the appendix A3). Three compounds, termed WB025, WB047, and WB073 yielded unusual binding curves (Figure A18A, Figure A19B, and Figure A20C). Nevertheless, either parts of these curves, as in case of WB047 or WB073, or the whole data range, in case of WB025, have been fitted for K_D-estimation and comparison to related compounds. Furthermore, three "phenazistatin" compounds, WB011, WB077, and WB082, yielded clear double transition curves in ITC experiments (Figure 38B and Figures A22-A24). This behavior could already be observed for racemic phenazistatin A (Mentel, 2008) and hints towards differing affinities of the enantiomers. With the exception of WB001, all tested compounds are racemic mixtures of the *cis* (*S*,*R* and *R*,*S*)- or *trans* (*S*,*S* and *R*,*R*)-isomers; as such, the obtained dissociation constant represents rather a "mixed" affinity than a specific one. For comparison with titration series where no or only a weak second transition at the onset or at the end of the binding curve is observed, all double transition data were fitted as one transition curve as shown in Figure 38B. This method however, might lead to underestimation of the actual K_D (*q.v.* Table A6). Nevertheless, a detailed evaluation for individual transitions can be found in the appendix in Table A10 and Figures A17-A19. In these cases, all curves from individual titration experiments were fitted at once and the confidence level of the fit evaluated for the full range of the curve as well as single transitions.

As described by Fokkens and Klebe (2006) the shape of the titration curve allows an estimation of the difference in binding affinity of the strong and weak binding enantiomer. The authors suggested that a clear double transition, as observed especially for WB011 and WB077, indicates a 50 to 200-fold difference in binding affinity with the first transition representing a "mixed" association/dissociation event of both enantiomers and the second rather the affinity of the stronger binding enantiomer. Similarly to phenazistatin A, analysis of the double transition curves of WB011, WB077, and WB082, resulted in comparable affinity parameters for the weak binding enantiomers (approximately 1 – 2 µM; Table A10). Hence, with the expected 50 to 200-fold higher affinity of the *S*,*R*-enantiomer, these values should be comparable to phenazistatin A.

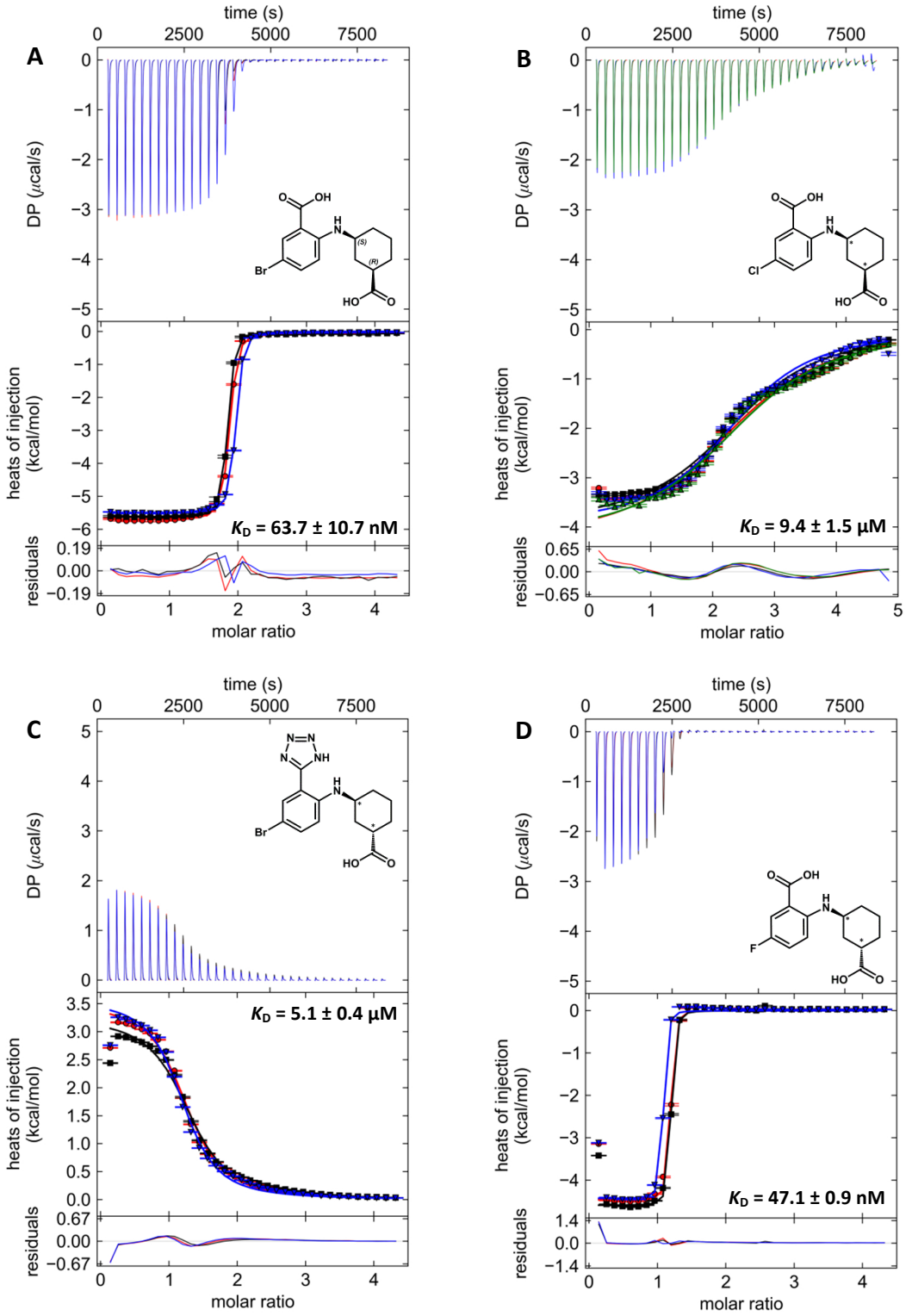

Figure 38: ITC profiles for affinity titrations of different "phenazistatin"-type substrate analogs against *Bc*Phz(A)/B. The individual plots show the generated heat per injection at different time points (upper panel), the fitted binding curves for individual titration experiments (middle panel), and the quality of the fit (lower panel). All profiles represent titrations of 2 mM of the respective analog to 100 µM *Bc*Phz(A)/B. Binding is exothermic for three of the represented compounds: **A** WB001 (phenazistatin A), **B** WB011, and **D** WB070; and endothermic for WB024 (**C**). Stoichiometries are ranging from approximately 1:1 (**D**) up to 2.5:1 (**B**) and binding affinities were determined to 63.7 ± 10.7 nM (**A**), approx. 9.4 ± 1.5 µM (**B**), 5.1 ± 0.4 µM (**C**) and 47.1 ± 0.9 nM (**D**). The symbols ●, ■ and ▼ (and ▲) represent individual experiments All data were analyzed and fitted using the programs NITPIC (Keller *et al.*, 2012; Scheuermann and Brautigam, 2015) and SEDPHAT (Houtman *et al.*, 2007; Zhao *et al.*, 2015) and plotted using the program GUSSI (Brautigam, 2015).

This finding was unexpected especially in case of WB077, which bears a much larger substitution (phenylethyl-) at position five of the anthranilic acid moiety than *e.g*. WB001 (Br-), WB011 (Cl-) or WB082 (H-). Yet, binding of WB077 could also be confirmed by a crystal structure of the complex with *Bc*Phz(A)/B (Figure 41D, see below).

Table21 shows an overview of well binding compounds of the "phenazistatins" (a more detailed overview can be found in Table A9 in the appendix A3).

Table 22: Thermodynamic binding parameters for ITC affinity titrations of various newly synthesized product analogs of the "phenazistatin" sub-group to *Bc*Phz(A)/B.[#]

Ligand	K_D (µM)	ΔG (kcal mol^{-1})	ΔH (kcal mol^{-1})	-T*ΔS (kcal mol^{-1})	*N*	c
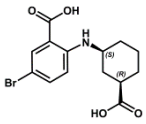 **WB001**	6.4 ± 1.1 • 10^{-2}	-9.8 ± 0.1	-10.3 ± 0.2	0.5 ± 0.2	1.8 ± 0.1	1610.6 ± 242.7
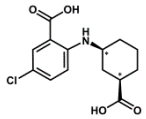 **WB011[‡]**	9.4 ± 1.5	-6.9 ± 0.1	-10.2 ± 0.5	3.4 ± 0.6	2.4 ± 0.0	10.9 ± 1.8
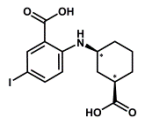 **WB012**	5.8 ± 0.2	-7.1 ± 0.0	-9.4 ± 0.2	2.3 ± 0.2	2.8 ± 0.0	17.3 ± 0.7
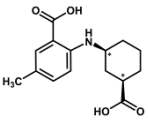 **WB013**	1.7 ± 0.2	-7.9 ± 0.1	-8.7 ± 0.4	0.8 ± 0.4	1.9 ± 0.0	58.4 ± 5.8
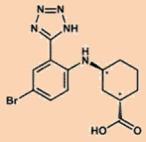 **WB024**	5.1 ± 0.4	-7.2 ± 0.0	4.3 ± 0.1	-11.5 ± 0.1	1.3 ± 0.0	19.7 ± 1.5
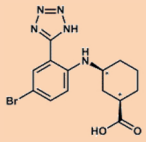 **WB025**	4.0 ± 0.6 • 10^{-1}	-8.7 ± 0.1	1.3 ± 0.0	-10.0 ± 0.1	1.0 ± 0.0	255.8 ± 39.0
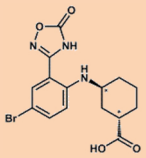 **WB026**	13.0 ± 0.1	-6.7 ± 0.0	5.0 ± 0.0	-11.7 ± 0.0	1.9 ± 0.2	7.7 ± 0.1

Ligand	K_D (µM)	ΔG (kcal mol^{-1})	ΔH (kcal mol^{-1})	-T*ΔS (kcal mol^{-1})	*N*	c
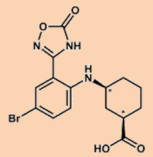 **WB027**	16.9 ± 1.8	-6.5 ± 0.1	3.3 ± 0.2	-9.8 ± 0.3	2.4 ± 0.1	6.0 ± 0.7
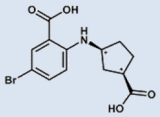 **WB047**	4.7 ± 0.3 • 10^{-1}	-8.6 ± 0.0	-1.3 ± 0.0	-7.3 ± 0.1	3.0 ± 0.1	212.2 ± 14.1
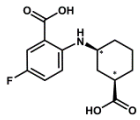 **WB069**	1.0 ± 0.2	-8.2 ± 0.1	-10.8 ± 0.4	2.6 ± 0.3	1.3 ± 0.0	103.7 ± 16.2
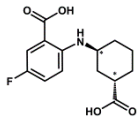 **WB070**	4.7 ± 0.1 • 10^{-2}	-10.0 ± 0.0	-5.0 ± 0.3	-5.0 ± 0.3	1.1 ± 0.1	2126.1 ± 41.9
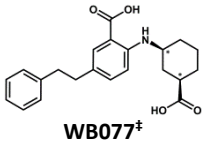 **WB077**‡	5.6 ±0.4	-7.2 ± 0.0	-8.0 ± 0.4	0.9 ± 0.4	1.7 ± 0.0	17.9 ±1.2
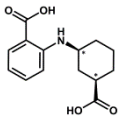 **WB082**	3.6 ± 0.4	-7.4 ± 0.1	-8.4 ± 0.3	1.0 ± 0.3	1.3 ± 0.1	28.5 ± 3.4
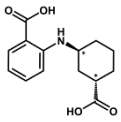 **WB083**	1.2 ± 0.3 • 10^{-1}	-9.4 ± 0.1	-3.2 ± 0.0	-6.3 ± 0.1	1.2 ± 0.0	855.8 ± 176.9
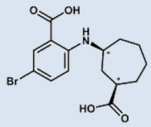 **WB084**	4.5 ± 0.3 • 10^{-1}	-8.7 ± 0.0	-7.3 ± 0.1	-1.3 ± 0.1	0.9 ± 0.0	222.3 ± 16.0

[#] All ITC experiments were carried out at 25 °C in 20 mM TRIS/HCl pH 8.0, 150 mM NaCl (if necessary supplemented with up to 1 % DMSO). 2 mM of the respective compound were titrated to 100 µM *Bc*Phz(A)/B. The data are averaged from at least two independent measurements. [‡] The given values arise from fitting of the complete binding curve similar to other compounds. Highlighted are compounds with *trans*-configuration in **green**, endothermic binders with shaded areas in light orange and compounds with different ring sizes of the cycloalkane moiety with shaded areas in lightblue.

Besides phenazistatin A (WB001) and WB011, compounds bearing another halogen at the position of the bromine/chlorine group, such as fluorine (WB069) or iodine (WB012) seem to show a similar affinity towards *Bc*Phz(A)/B with K_D-values of 1.0 µM and 5.8 µM respectively. Although no double transition curve was observed for these compounds, it seems that ligands bearing a smaller halogenic group tend to bind slightly tighter to the

enzyme. However, the individual thermodynamic parameters ΔG, ΔH and –T*ΔS, obtained from these calorimetric titrations (Figure 39) as well as structural (see below) and biochemical assay data (*q.v.* paragraph 6.2.2) show no significant difference in binding and/or inhibitory potency of these different halogenated compounds or any other substitution at the same position.

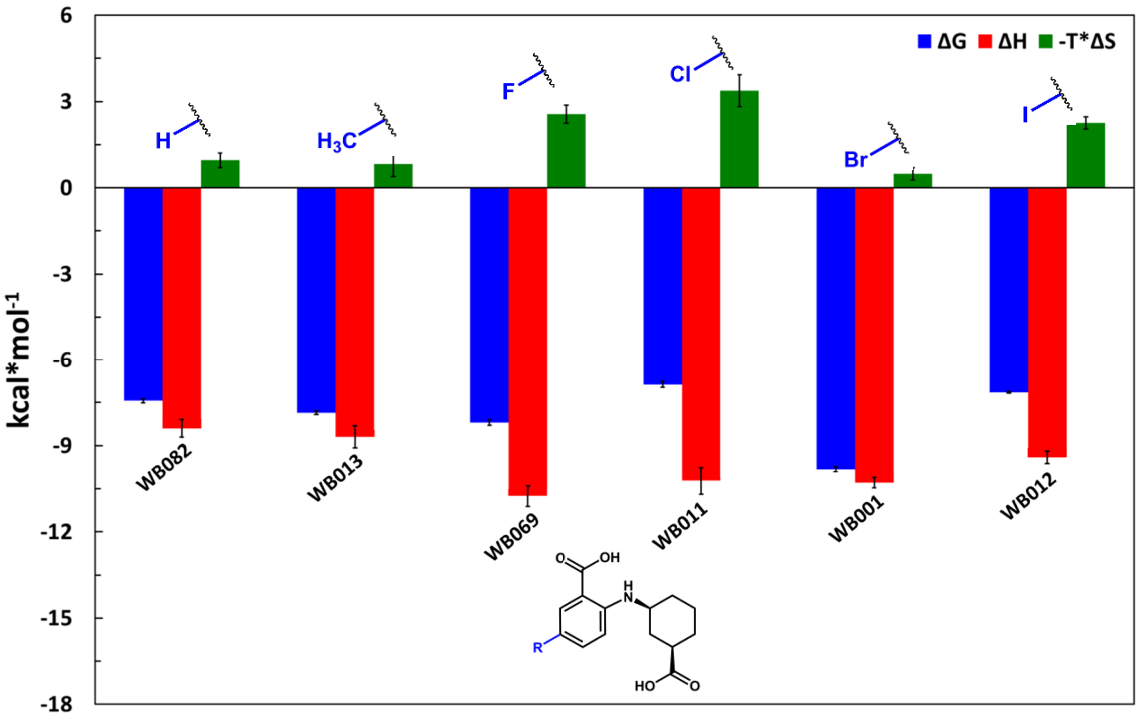

Figure 39: ITC data analysis of characteristic thermodynamic parameters for different "phenazistatin" derivatives. Plotted are the values for the Gibb's free energy ΔG ( ), which in turn is the sum of the enthalpy ΔH ( ) and the entropy, expressed as –T*ΔS ( ), in kcal*mol^{-1}. All derivatives share a common chemical core as depicted by the inset in the lower area of the graph. Their individual groups are highlighted in **blue** above the respective data columns.

In general, a strong enthalpic (ΔH) contribution to ligand binding can be explained with regard to the structural data. All crystal structures of *Bc*Phz(A)/B in complex with different "phenazistatins" show the formation of up to eleven hydrogen bonds, ranging from 2.6 to 3.2 Å, stabilizing the ligand via its carboxylic acid moieties and the bridging amine as shown in Figure 41 (Figures A31 and A32 in appendix A3). Even a crystal structure of *Bc*Phz(A)/B in complex with WB077 (Figure 41D), a ligand bearing a large phenylethyl-substitution at position five, shows a very similar hydrogen-bonding pattern as for WB001 (PDB entry 3JUM; Mentel *et al.*, 2009a). However, the characteristic phenylethyl-group induces a 100-degree rotation of H73 and simultaneously a displacement of two coordinating water molecules in comparison to the published complex. In turn, the new position of H73 is stabilized by two new hydrogen bonds to the backbone carbonyls of K69

and P164. Together these data explain why WB077, despite its large substitution, binds to *Bc*Phz(A)/B with similar affinity as observed for smaller "phenazistatins".

A positive value for the entropic factor (–T*ΔS) indicates unfavorable conformational changes upon ligand binding. However, in comparison to the apo structure (PDB entry 3B4O; Ahuja *et al*., 2008) only minor conformational differences can be observed and this does not seem to affect ligand binding as much as the enthalpic contribution.

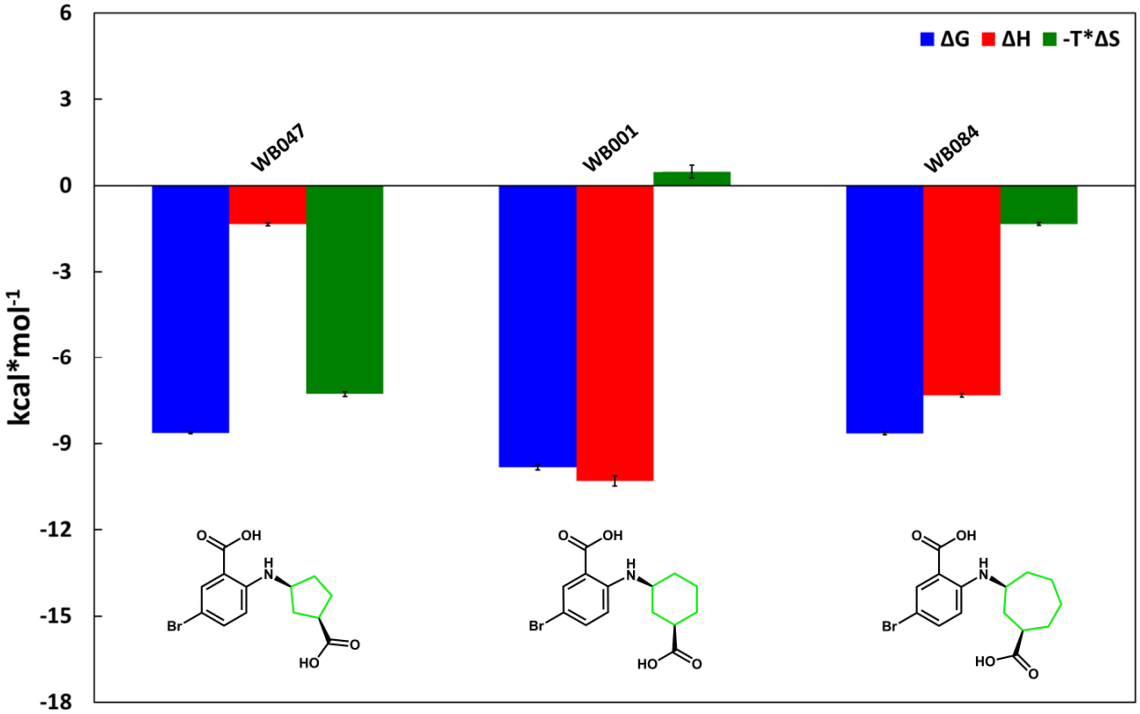

Figure 40: ITC data analysis of characteristic thermodynamic parameters for different cycloalkane derivatives of phenazistatin A.

Plotted are the values for the Gibb's free energy ΔG ( ), which is the sum of the enthalpy ΔH ( ) and the entropy, expressed as –T*ΔS ( ), in kcal*mol^{-1}. All derivatives share a common bromo-anthranilic acid moiety with different carboxycycloalkyl moieties attached via the amino group, shown as insets in the lower area of the graph. Their individual, characteristic rings are highlighted in green.

Besides the series of modifications at position five of the anthranilic acid moiety, the influence of the ligand's *N*-carboxycycloalkyl moiety was also analyzed. To this aim, Jakob Pletz synthesized a cyclopentane- (WB047) and cycloheptane-derivative (WB084) of phenazistatin A. Although WB047 produced an unusual titration curve (see before) and its K_D should be considered with caution, both ligands were found to bind with a comparable affinity of approximately 450 nM (Table 22). Further analysis of the individual thermodynamic parameters (Figure 40) indicates that binding is entropically driven, which indicates formation of favorable hydrogen bonds as well as stabilizing hydrophobic interactions. At first sight, the structural data (Figure 41) suggest no difference compared

to phenazistatin A, regarding space requirements or the hydrogen-bonding network of these ligands.

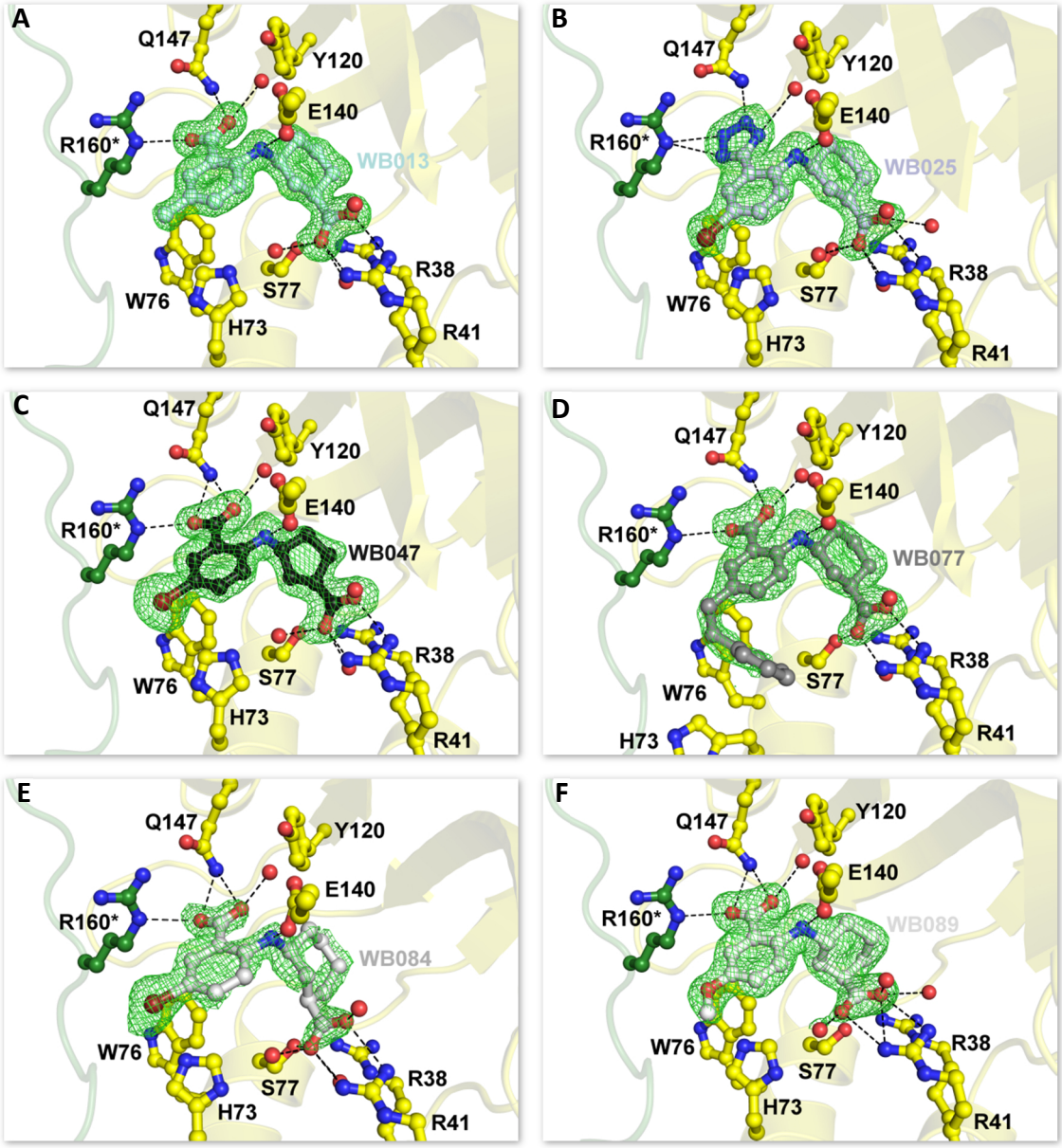

Figure 41: Crystal structures of *Bc*Phz(A)/B in complex with different synthetic "phenazistatin" derivatives.
Close-ups on the active site (chain A or B) of different *Bc*Phz(A)/B complex structures with potential PhzB-inhibitors of the "phenazistatin"-class after soaking with 10 mM of the respective ligand overnight. The ligands are highlighted as balls and sticks in different colors and depicted in their Fourier difference density (mF_o-DF_c) omit map contoured at 3σ in green: **A** *cis*-methyl-phenazistatin (WB013), **B** *cis*-tetrazole-phenazistatin (WB025), **C** *cis*-penta-phenazistatin (WB047), **D** *cis*-phenylethyl-phenazistatin (WB077), **E** *cis*-hepta-phenazistatin (WB084), and **F**: *trans*-methoxy-phenazistatin (WB089). The protein is shown as cartoon and the coordinating active site residues as balls and sticks colored in yellow and forest (for residues belonging to the second chain, depicted with *). Hydrogen bonds (- - -) and coordinating water (red balls) are highlighted as well.

WB047 and WB084, similarly to the reference structure (PDB entry: 3JUM, Mentel *et al.*, 2009a), were observed in their *cis*-*S*,*R*-configuration. Yet, upon a closer look, the electron difference density for WB084 is ambiguous. Seemingly, the *trans*-isomer in *S*,*S*-

configuration could be bound to the active site as well. In fact, it is known from crystal structures of *Bc*Phz(A)/B in complex with different *trans*-isomers (Figure 41F and Figures A31 and A32 in the appendix), that the enzyme can bind these isomers as well. However, these ligands bind in the *trans*-*R*,*R*-configuration. It is possible that the ring-size directs binding of one or the other isomer, yet, from currently available data, no conclusive hypothesis for the preferentially bound configuration of WB084 can be made.

In general, affinity titrations suggest slightly tighter binding to *Bc*Phz(A)/B for the *trans*-stereoisomers than for the respective *cis*-isomers, *e.g. cis*-fluoro-phenazistatin (WB069) binds with a K_D of 1.0 µM, while the K_D for *trans*-fluoro-phenazistatin (WB070) is 47 nM. The thermodynamic parameters (Figure 42) indicate that binding of the *cis*-isomer is enthalpically driven, while binding of the *trans*-isomers seems to have a larger entropic contribution.

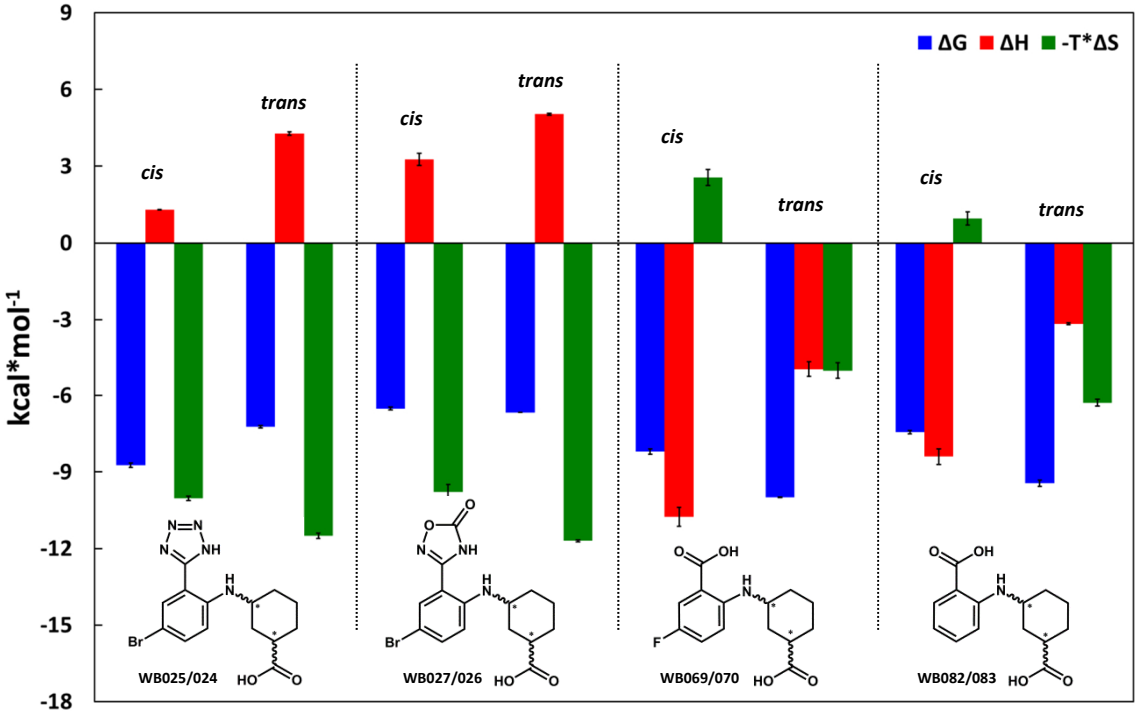

Figure 42: Characteristic thermodynamic parameters for different *cis*- and *trans*-isomers of "phenazistatin" derivatives as derived from ITC experiments.
Plotted are the values for the Gibb's free energy ΔG ( ), which in turn is the sum of the enthalpy ΔH ( ) and the entropy, expressed as –T*ΔS ( ), in kcal*mol^{-1}. All derivatives share a common chemical core as depicted by the insets in lower area of the graph. Bioisosteres of phenazistatin A with tetrazole- or oxadiazolone modification are depicted on the left.

Yet, crystal structures of different *cis*-/*trans*-isomer pairs do not allow a distinct explanation for this observation, as the spatial requirements as well as the hydrogen-bonding patterns are very similar for both stereoisomers.

Future drug application requires good bioavailability of the administered compound and thus the most potent inhibitors have to be tested *in vivo* eventually. Anticipating permeability issues for compounds bearing free carboxylic acids and aiming to improve drug uptake without loss of inhibitory potency, some bioisosteres of phenazistatin A were synthesized (Jakob Pletz). Two of these derivatives with the aromatic carboxylic acid replaced either by a tetrazole-(WB024 and WB025) or by an oxadiazolone-group (WB026 and WB027), were analyzed with ITC and crystallographic methods. Based on previous binding and structural data, which revealed that the carboxylic acid moiety is a central node in the hydrogen-bonding network of the ligand, it was expected that binding of these ligands should drastically be impaired. Yet, when analyzing the respective racemic *cis*- and *trans*-isomers, binding in the µM-range could be observed for all four ligands (Table 22). The tetrazole-derivatives with K_D-values in the low µM- and nM-range show tighter binding to *Bc*Phz(A)/B than the oxadiazolone-derivatives (K_D-values of 13.0 and 16.9 µM for the *trans*- (WB026) and *cis*-isomer (WB027) respectively). Furthermore, for the first time endothermic binding (Figure 38C and Figure 42), which probably indicates major conformational changes of *Bc*Phz(A)/B, was observed. Indeed, crystal structures in complex with WB024 (*trans*-tetrazole-phenazistatin), WB025 (*cis*-tetrazole-phenazistatin, Figure 41B) or WB026 (*trans*-oxadiazolone-phenazistatin) reveal that, for these larger compounds, the C-terminus, which acts as flexible lid to shield the active site, is less well defined and thus flexible. For *cis*-oxadiazolone-phenazistatin (WB027) two crystal structures could be obtained as well, however in both structures residual difference electron density did not allow a clear attribution to this ligand. This might indicate weak binding of WB027 in multiple conformations, which is supported by the binding data. The hydrogen-bonding network for the other three ligands of this class is however very similar to other "phenazistatin"-derivatives. Together, these structures explain why binding of these bioisosteres to *Bc*Phz(A)/B is still possible yet with lower affinity.

As mentioned in the beginning of this paragraph also a second class of PhzB-binders, the "mavericks", were characterized biophysically. Eight members of this class were tested regarding their binding affinity towards *Bc*Phz(A)/B (Table 23), yet for two, WB019 and WB020 no reliable binding data could be obtained. Nevertheless, a crystal structure of *Bc*Phz(A)/B in complex with WB019 verified binding of this compound to the enzyme,

though the structure revealed that the ligand adopts a different conformation than other members of this compound class (Figure 43A).

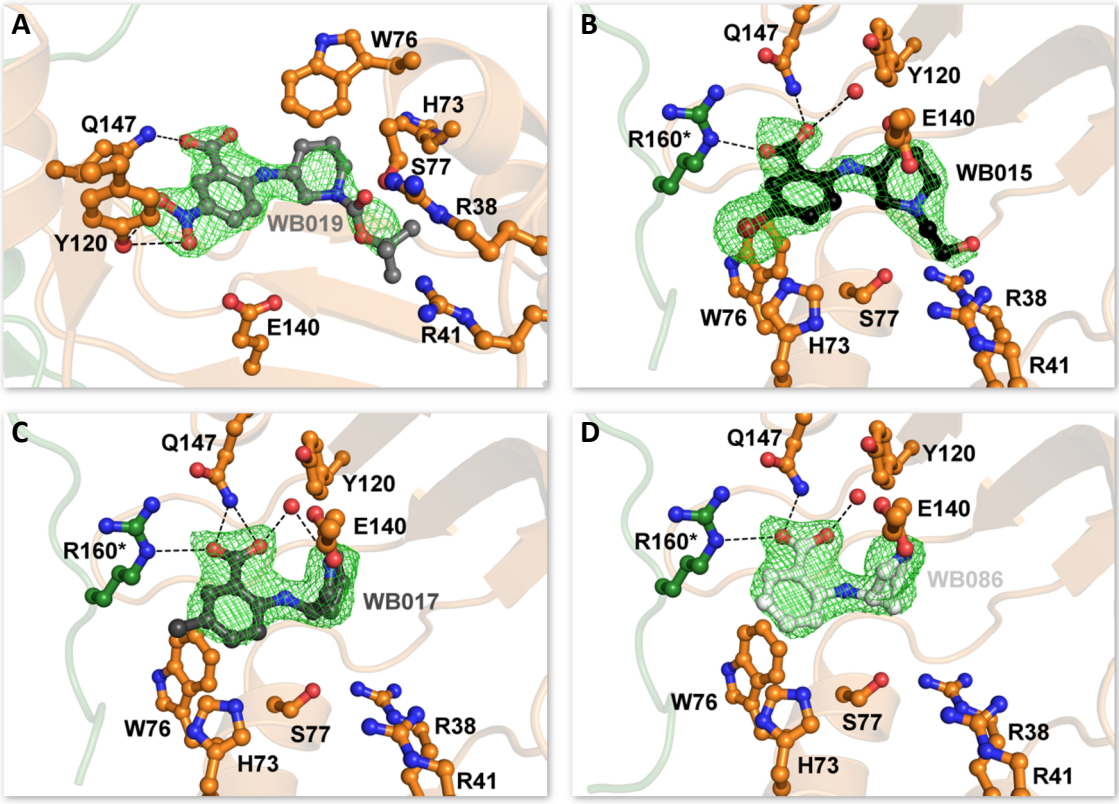

Figure 43: Crystal structures of *Bc*Phz(A)/B in complex with different synthetic "maverick" derivatives.
Close-ups on the active site (chain A or B) of different *Bc*Phz(A)/B complex structures with potential inhibitors of the "maverick"-class after soaking with 10 mM of the respective ligand overnight or, in case of **D** WB086, co-crystallization with 40 mM. The ligands are highlighted as balls and sticks in different colors and depicted in their Fourier difference density (mF_o-DF_c) omit map contoured at 3σ in green: **A** *rac*-nitroBoc-maverick (WB019), **B** *rac*-hydroxyethyl-maverick (WB015), **C** *rac*-methyl-maverick (WB017), and **D** *rac*-H-maverick (WB086). The protein is shown as cartoon and the coordinating active site residues as balls and sticks colored in **orange** and **forest** (for residues belonging to the second chain, depicted with *). Hydrogen bonds (- - -) and coordinating water (red balls) are highlighted as well.

The aromatic carboxylic group of WB019 is coordinated via a hydrogen bond to Q147, as observed for other PhzB binding compounds such as WB017 (Figure 43C). Yet, coordination of this group by a water molecule or residue R160* from the second protein chain is no longer observed, instead the ligand is stabilized via its nitro group at position five and two hydrogen bonds to Y120. As no further stabilization of this ligand can be seen, this weak hydrogen-bonding network might indicate low affinity for the enzyme and hence explain why no reliable binding affinity could be determined using ITC. Furthermore, when superimposing ligand WB019 on other ligands of the same class, *e.g.* WB017, it becomes evident, that the *tert*-butyloxycarbonyl-(Boc) protecting group at the piperidin-ring impairs binding of this compound in a similar orientation than related ones, as it would induce clashes with the side chains of W86 and R41 (data not shown).

Table 23: Thermodynamic binding parameters for ITC affinity titrations of synthetic substrate analogs of the "maverick" class to *Bc*Phz(A)/B.[#]

Ligand	K_D (µM)	ΔG (kcal mol^{-1})	ΔH (kcal mol^{-1})	-T*ΔS (kcal mol^{-1})	*N*	c
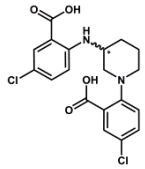 **WB014**	27.7 ± 0.7	-6.2 ± 0.0	8.1 ± 0.2	-14.3 ± 0.2	1.8 ± 0.0	3.6 ± 0.1
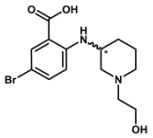 **WB015**	2.4 ± 0.5	-7.7 ± 0.1	-6.7 ± 0.9	-1.0 ± 1.0	4.2 ± 0.5	43.1 ± 8.0
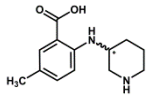 **WB017**	11.3 ± 0.1	-6.7 ± 0.0	-10.8 ± 0.1	4.0 ± 0.1	2.6 ± 0.1	8.8 ± 0.1
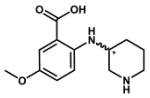 **WB018**	36.4 ± 9.4	-6.1 ± 0.1	-9.5 ± 0.6	3.5 ± 0.8	3.7 ± 0.9	2.9 ± 0.7
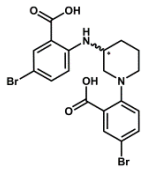 **WB085**	6.1 ± 0.2	-7.1 ± 0.0	4.7 ± 0.1	-11.9 ± 0.1	1.7 ± 0.1	16.5 ± 0.5
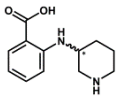 **WB086**	22.9 ± 0.5	-6.3 ± 0.0	-8.9 ± 0.1	2.6 ± 0.2	3.3 ± 0.1	4.4 ± 0.1

[#] All ITC experiments were carried out at 25 °C in 20 mM TRIS/HCl pH 8.0, 150 mM NaCl (if necessary supplemented with up to 1 % DMSO). 2 mM of the respective compound were titrated to 100 µM *Bc*Phz(A)/B. The data are averaged from at least two independent measurements.

In contrast to this unexpected binding behavior of WB019, other ligands, such as WB017 or WB086 bind to the enzyme‘s active site in a similar way (Figure 43C and D) as seen for a complex structure of *Bc*Phz(A)/B and the so-called *S*-Br-maverick (PDB entry 3JUP; Mentel *et al*., 2009a). These ligands are stabilized via three to four hydrogen bonds coordinating the aromatic carboxylic acid group and partially via an additional hydrogen bond to the nitrogen of the piperidinyl moiety.

As seen for WB019, the reduced hydrogen-bonding network could explain the general weaker affinity of this compound class, *e.g.* 11.3 ± 0.1 µM for WB017 (Table 23 and Figure 45). Previous investigations of the binding behavior of the "mavericks" also revealed that the active site of PhzB can bind the two enantiomers of a racemic mixture

simultaneously (Figure 44A; PDB entry 3JUN, Mentel *et al.*, 2009a). Based on these data, "maverick" derivatives that represent a fusion of two single "mavericks" into one were synthesized (Figure 44). Two of these fused ligands, carrying either two chlorine (WB014) or two bromine groups (WB086) as characteristic modification (Figure 44B), were analyzed regarding their binding behavior towards *Bc*Phz(A)/B.

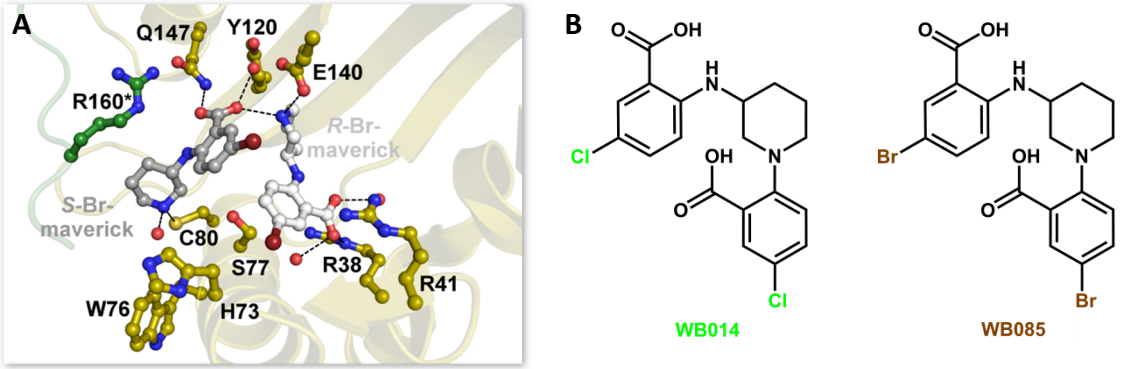

Figure 44: Schematic representation of the ligand development of fused "maverick" derivatives.
A Close-up on the active site (chain B) of *Bc*Phz(A)/B crystallized in a simultaneous complex with racemic Br-maverick after soaking with 4 mM of the mixture overnight. The two ligand-stereoisomers are highlighted as balls and sticks. The protein is shown as cartoon and the coordinating active site residues as balls and sticks colored in olive and forest (for residues belonging to the second chain, depicted with *). Hydrogen bonds (- - -) and coordinating water (red balls) are highlighted as well. **B** The figure shows the chemical formula of two fused "maverick"-derivatives, WB014 and WB085. The characteristic moiety allowing differentiation of these two ligands is highlighted.

As shown in Figure 45, WB086 exhibits endothermic binding to *Bc*Phz(A)/B. A Similar behavior could also be observed for WB014 (Figure A16D). In both cases, also an altered binding stoichiometry can be observed. While the calorimetric data suggest that small "mavericks" bind in a 3:1 or even 4:1-ratio, the larger coupled "mavericks" appears to bind only in a 2:1-stoichiometry that is consistent with the fact that they consist of the fusion of two smaller units. However, X-ray crystallographic experiments could not confirm these stoichiometries, since neither multiple binding of smaller ligands could be observed, nor unambiguous structural data for larger Mavericks such as WB014 or WB085 were obtained. Different datasets for a putative complex of *Bc*Phz(A)/B and WB014 were collected, but the residual positive electron density present in the active site did not allow unequivocal building of the ligand.

Despite missing crystal structures for WB014 or WB085, endothermic binding of these ligands might be explained by comparing the complex of *Bc*Phz(A)/B and racemic-Br-maverick (PDB entry 3JUN, Mentel *et al.*, 2009a) to the complex with phenazistatin A (PDB entry 3JUM, Mentel *et al.*, 2009a) or the apo structure (PDB entry 3B4O, Ahuja *et al.*,

2008). In case of the racemic complex, H73 and W76 are displaced from their original position in the active site and the C-terminus of both chains is disordered. Together these data reveal conformational changes, similarly to what could be expected when the larger, fused ligands bind to the enzyme.

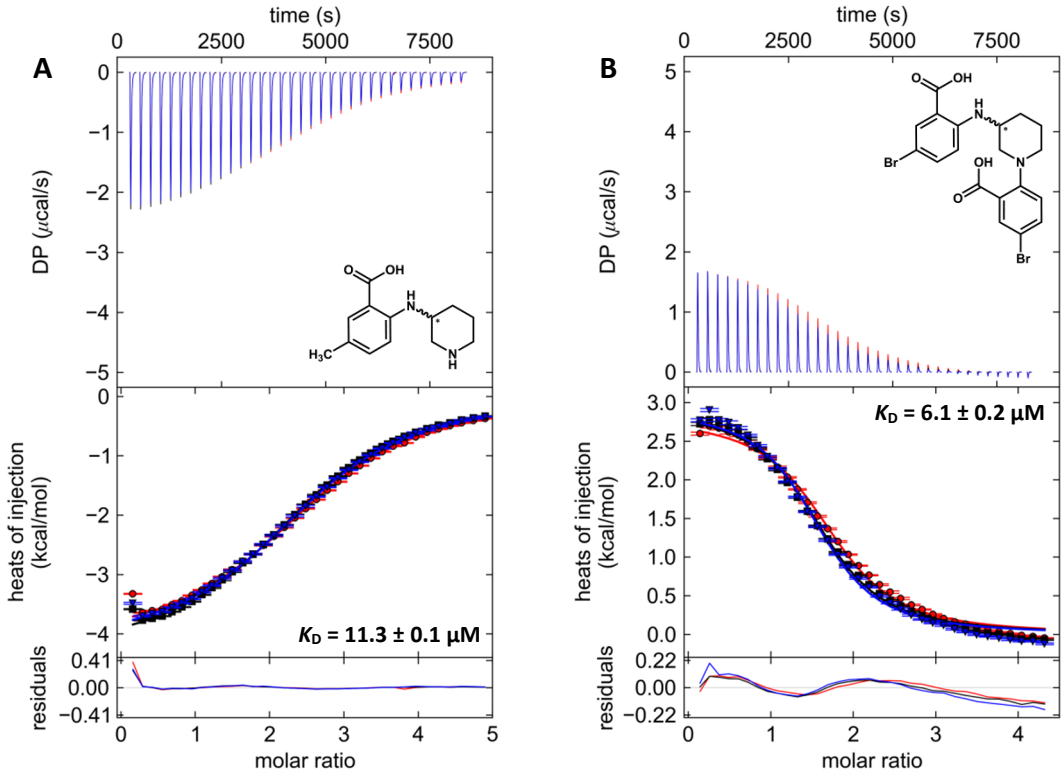

Figure 45: ITC profiles for affinity titrations of two different ligands of the "maverick"-class against *Bc*Phz(A)/B. The individual plots show the generated heat per injection at different time points (upper panel), the fitted binding curves for individual titration experiments (middle panel), and the quality of the fit (lower panel). All profiles represent titrations of 2 mM of the respective analog to 100 µM *Bc*Phz(A)/B. Binding is exothermic for **A** WB017 with a K_D of 11.3 ± 0.1 µM and endothermic for **B** WB085 (K_D = 6.1 ± 0.2 µM). Stoichiometries are approx. 2.6:1 for WB017 and 1.7:1 for WB085. The symbols ●, ■ and ▼ represent individual experiments All data were analyzed and fitted using the programs NITPIC (Keller *et al.*, 2012; Scheuermann and Brautigam, 2015) and SEDPHAT (Houtman *et al.*, 2007; Zhao *et al.*, 2015) and plotted using the program GUSSI (Brautigam, 2015).

In summary, new potent PhzB ligands were identified and characterized using calorimetric and structural methods. The experiments revealed that the *N*-piperidinyl-anthranilic acid-derived "mavericks" are weaker binding ligands. In addition, fusion of two small "mavericks" into a larger one alters the binding properties, leading to endothermic binding behavior. In contrast, "phenazistatins" with affinities up to the nM-range are strong binding ligands. As mainly their two carboxylic acid groups facilitate binding, even large substitutions at other positions of the aromatic ring do not drastically alter affinity. Yet, even bioisosteres with tetrazole- or oxadiazolone groups replacing one of the

carboxylates exhibit µM-affinities. Furthermore, *cis*- as well as *trans*-stereoisomers were found to bind to the enzyme from *B. cepacia*.

6.2.2. *In vitro* inhibition of PhzB catalysis by synthetic product analogs

The *in vitro* inhibitory potency of synthetic ligands against PhzB catalysis was addressed utilizing the enzymatic assay previously described (*q.v.* chapter II). When using 1 mM DHHA and up to 100 µM compound, no or only a very weak inhibitory effect against *Bc*Phz(A)/B could be detected for the tested *N*-piperidinyl anthranilic acid derivatives ("mavericks"; Scheme 16).

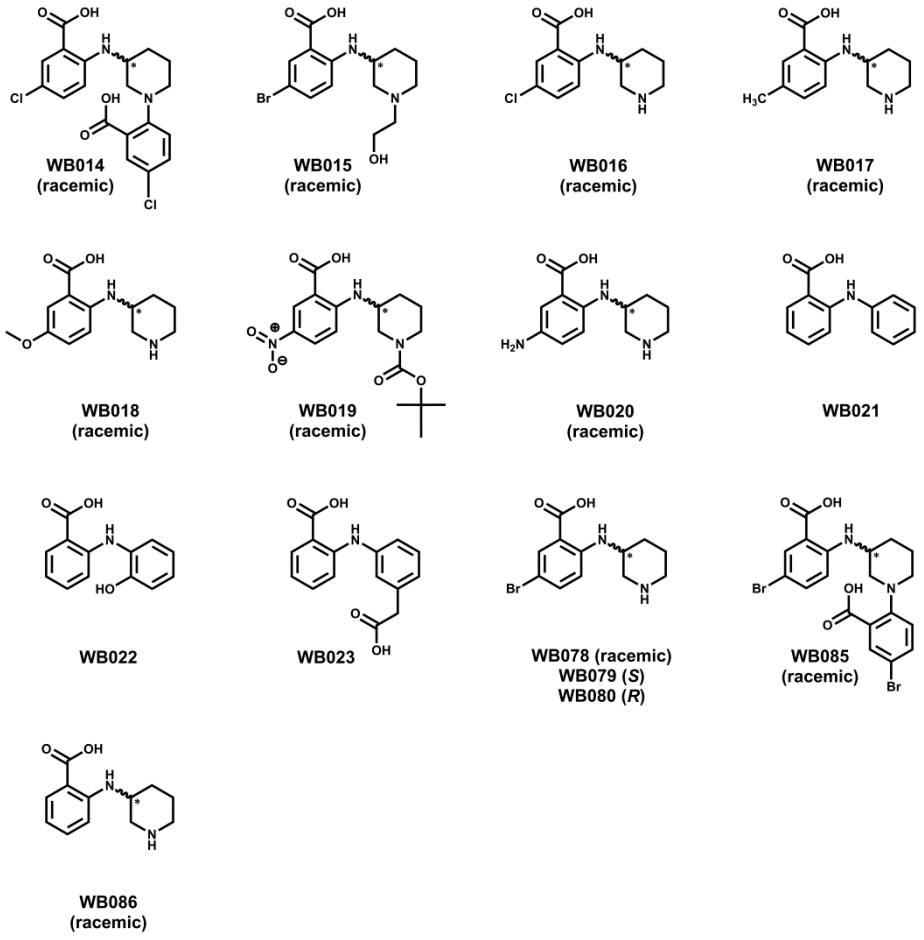

Scheme 16: Chemical structures of all *N*-piperidinyl ("mavericks") and *N*-phenyl anthranilic acid derivatives.
Schematic overview over all "maverick"- and *N*-phenyl anthranilic acid derivatives tested for *in vitro* PhzB-inhibition. Except WB021-WB023, all ligands are shown without absolute stereochemistry, indicating racemic mixtures.

The only significant inhibitory effect was observed for WB085 (60 % residual activity at 100 µM, Figure 46). Even when reducing the substrate concentration to 125 µM, no significant increase in enzyme inhibition could be detected. Most "mavericks" show approximately 10 to 50 % inhibition (80 % for WB085), but only at their highest tested

concentration, *i.e*. 100 µM (Figure A25). As expected from the complex structures (see before), the increase in potency when less substrate is used confirms that these compounds act as (weak) competitive inhibitors. This weak inhibitory effect indeed correlates with the reduced hydrogen-bonding network observed in the crystal structures and with the weak affinities determined by ITC. In comparison to the substrate/product of the reaction, "maverick" compounds lack a second carboxylic acid moiety which is found to be highly coordinated in these complex structures (Ahuja *et al*., 2008).

The three *N*-phenyl anthranilic acid derivatives (WB021 – WB023; Mentel, 2008), show similar tendencies (Figure 46 and Figure A25).

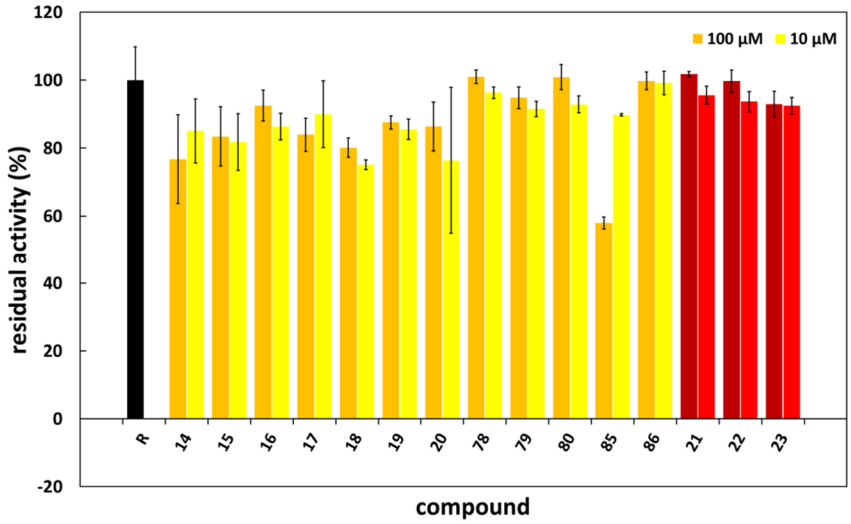

Figure 46: Residual enzymatic activity of *Bc*Phz(A)/B in presence of *N*-piperidinyl or *N*-phenyl anthranilic acid-derived inhibitors

The plot shows the residual enzymatic activity of Phz(A)/B from *B. cepacia* in presence of 1 mM DHHA and either 10 (light colors) or 100 µM (dark colors) inhibitor compared to the uninhibited reaction (R). The numbers represent the individual compound, *e.g*. 14 = WB014. *Bc*Phz(A)/B and the coupled enzyme PhzF were used at 1 mM (dimer) final concentration in all assays. The data, obtained in 50 mM sodium phosphate buffer pH 7.5, supplemented with 2 % (v/v) DMSO, at 25 °C, were normalized to zero, corrected, and averaged from three independent measurements.

In contrast, the majority of *N*-carboxycycloalkyl anthranilic acid derivatives ("phenazistatins", Scheme 17) are very potent inhibitors (Figure 47). Compared to an inhibitor-free reference, the residual activities in presence of most derivatives are less than 20 %, even when only 10 µM inhibitor was used. In presence of 1 mM substrate IC_{50}-values can be estimated to be in the low µM-range (for details see below and Figure A26A - C in the appendix).

The inhibitory potency is even more pronounced when less substrate (125 µM) is used (data not shown) and supports the competitive mode of inhibition, which was suggested by the binding modes observed in crystal structures (see before). However, some

"phenazistatins", such as WB035 or WB067, show no inhibition at high substrate concentrations and only 50 % inhibition at lower ones (for WB067/WB068), indicating IC_{50}–values above 100 µM. These results are consistent with the fact that no ligand binding could be observed for these two compounds neither by ITC experiments nor by crystal structures.

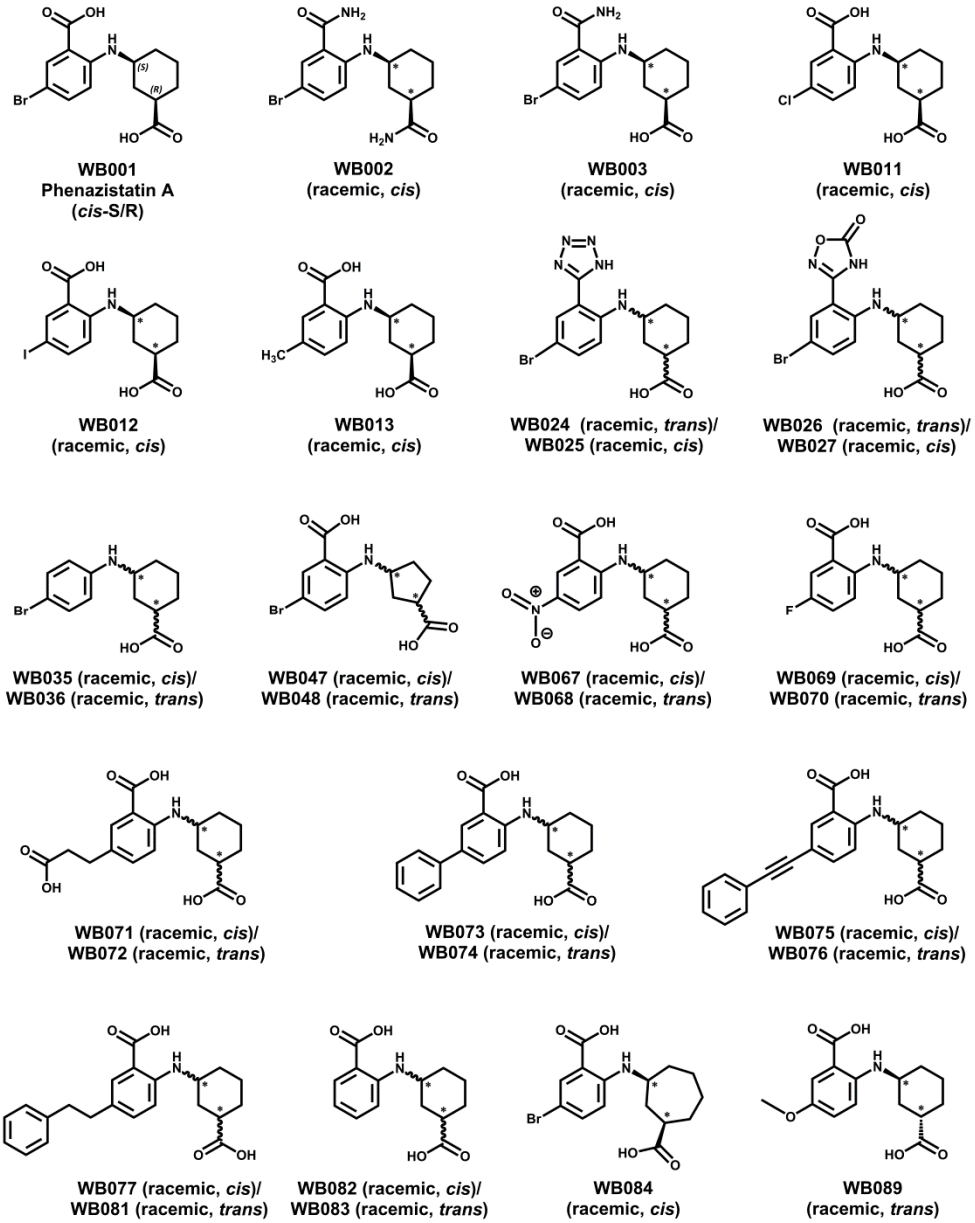

Scheme 17: Chemical structures of *N*-carboxycycloalkyl anthranilic acid-derived compounds ("phenazistatins"). Schematic overview over all "phenazistatin" derivatives tested for *in vitro* PhzB-inhibition. Except WB001, all ligands are shown without absolute configuration, as these compounds were only available as racemic mixtures of *cis*- and/or *trans*-isomers.

For some other compounds, such as carboxyethyl-phenazistatin (WB071/WB072), phenyl-phenazistatin (WB073/WB074) or phenylethynyl-phenazistatin (WB075/WB076), distinct differences between their *cis*- and *trans*-isomers could be observed (Figure 47).

In fact, assay data for these three diastereoisomers systematically reveal more efficient enzyme inhibition by ligands in *cis*-configuration. The IC_{50} of the two latter *cis*-isomers can be estimated below 10 µM (at 1 mM substrate). Under similar conditions, WB071 exhibits an IC_{50} of approx. 100 µM, while the corresponding *trans*-isomer (WB072) shows no inhibition (Figure 47). This finding is again in agreement with results from ITC experiments, whereupon no binding for WB071 could be observed (*q.v.* paragraph 6.2.1.).

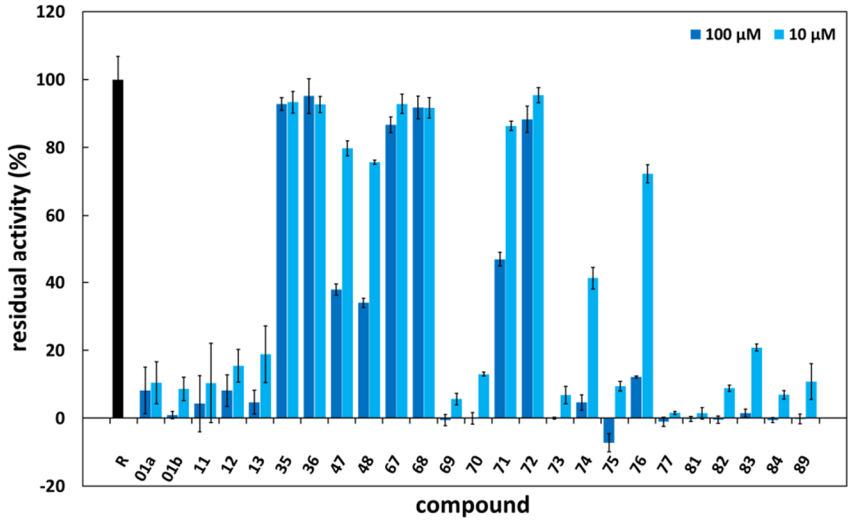

Figure 47: Residual enzymatic activity of *Bc*Phz(A)/B in presence of *N*-carboxycycloalkyl anthranilic acid-derived inhibitors ("phenazistatins").
The residual enzymatic activity of *Bc*Phz(A)/B in presence of 1 mM DHHA and either 10 (light colors) or 100 µM (dark colors) inhibitor is compared to the uninhibited reaction (R). The numbers represent the individual compounds, *e.g.* 11 = WB011. *Bc*Phz(A)/B and the coupled enzyme PhzF were used at 1 mM (dimer) final concentration. After normalization to zero and background correction, the data from three independent measurements in 50 mM sodium phosphate pH 7.5 buffer, supplemented with 2 % (v/v) DMSO, at 25 °C were averaged. The experiments for WB001 were repeated and individual triplicates are depicted as 01a and 01b.

Penta-phenazistatin (WB047/WB048) represents another peculiarity among the tested compounds. Despite similar activity of both racemic mixtures against *Bc*Phz(A)/B, the overall efficiency of these derivatives, with IC_{50}-values of approximately 100 µM (in presence of 1 mM substrate), is almost 100-fold reduced compared to similar compounds, such as WB001 or WB084. While comparison of the corresponding complex structures does not provide any rational explanation for differing behavior among "phenazistatin" derivatives, ITC data for WB047 revealed unusual biphasic binding curves, potentially indicating different/multiple binding modes.

As anticipated from affinity titrations (*q.v.* paragraph 6.2.1.), tetrazole- and oxadiazolone-phenazistatins also show inhibitory effects on PhzB catalysis (Figure 48). However, the oxadiazolones (WB026/WB027), with estimated IC_{50}-values of approximately 100 µM (at 1 mM substrate), are 10-fold less potent than the tetrazoles, which is in agreement with their respective binding affinities (see before). Yet, as seen for WB028, the inhibitory potency is drastically reduced when other groups such as tetrazoles or methyl ester replace both carboxylic acid moieties of the "phenazistatins" (Figure 48). In general, prodrugs or other bioisosteres (Scheme A1) with methyl esters, pivaloyloxymethyl esters (WB087/WB088), phosphoryl moieties (WB063), or methylsulfonylamide groups (WB090) show no inhibition in the *in vitro* assay (Figure A27), even when the substrate concentration is reduced to 125 µM (data not shown).

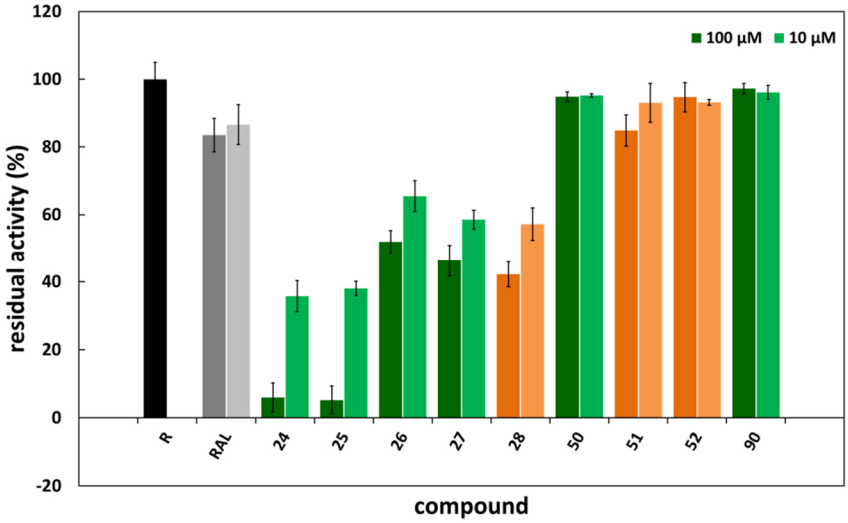

Figure 48: Residual enzymatic activity of *Bc*Phz(A)/B in presence of different potential bioisosteric inhibitors.
The residual enzymatic activity of *Bc*Phz(A)/B in presence of 1 mM DHHA and either 10 (light colors) or 100 µM (dark colors) inhibitor is compared to the uninhibited reaction (R). The numbers represent the individual compounds, *e.g.* 24 = WB024. Green colors indicate simple tetrazole- or oxadiazolone derivatives, while orange represents compounds bearing at least one ester modification. A previously reported PhzB-inhibitor, raloxifene (RAL; Ho Sui *et al.*, 2012) was tested as well. *Bc*Phz(A)/B and the coupled enzyme PhzF were used at 1 mM (dimer) final concentration. After normalization to zero and background correction the data from three independent measurements in 50 mM sodium phosphate buffer pH 7.5, supplemented with 2 % (v/v) DMSO, at 25 °C were averaged.

Besides "maverick" and "phenazistatin" derivatives, the inhibitory potency of another previously described inhibitor of PhzB, raloxifene (Ho Sui *et al.*, 2012), was tested. In the frame of their drug repurposing study, the authors showed that the selective estrogen receptor modulator raloxifene (RAL) leads to a dose-dependent reduction of pyocyanin levels in *Pseudomonas aeruginosa* which they attributed to the inhibition of PhzB2 (Ho Sui *et al.*, 2012). Indeed, although it was not possible to determine affinity data for raloxifene,

binding of this compound to PhzB (here Phz(A)/B from *B. cepacia* R18194) could be confirmed by crystal structures (Figure 49).

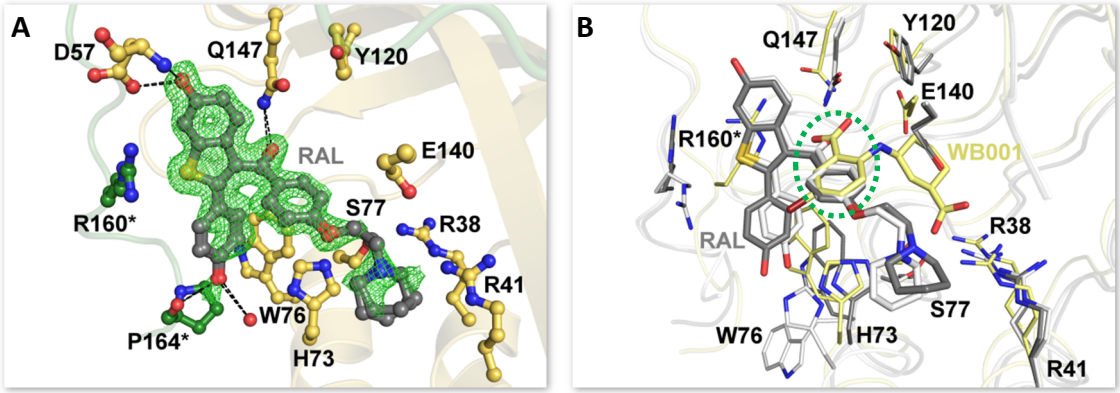

Figure 49: Crystal structures of *Bc*Phz(A)/B in complex with raloxifene.
A Close-up on the active site of *Bc*Phz(A)/B (chain B) co-crystallized with 5 mM raloxifene (RAL). The ligand, in gray, is highlighted as balls and sticks and depicted in its Fourier difference density (mF_o-DF_c) omit map contoured at 3σ (green). The protein is shown as cartoon and the coordinating active site residues as balls and sticks colored in gold and forest (for residues belonging to the second chain, depicted with *). Hydrogen bonds (- - -) and coordinating water (red balls) are highlighted as well. **B** Structural comparison of the raloxifene (RAL) complexes obtained either by co-crystallization with 5 mM (gray) or overnight soaking with 10 mM (white) compound, with the phenazistatin A complex (WB001, PDB entry 3JUM, Mentel *et al.*, 2009a). The superposition reveals a conserved benzaldehyde moiety as common structural feature between both inhibitors (⋮), which can be considered as pharmacophore.

The crystallographic data reveal that raloxifene binds directly to the active site and suggest a competitive mode of inhibition similar to the other studied compounds. This is further supported by assay data which showed improved inhibitory potency for raloxifene at lower substrate concentrations (estimated $IC_{50} \approx 100$ µM at 125 µM DHHA *vs*. no detectable inhibition at 1 mM DHHA; Figure 48). In comparison to complex structures with other inhibitors, such as WB001 (PDB entry 3JUM, Mentel *et al.*, 2009a), binding of raloxifene induces a displacement of the C-terminal arm and, more generally, a distortion/opening of the active site presumably in adaptation to the bulky ligand (Figure 49B). Five to six hydrogen bonds are also formed between RAL and active site residues or conserved waters (Figure 49A). Interestingly, the central benzaldehyde moiety of the ligand binds in a similar position as the anthranilic acid group of "phenazistatin" or "maverick" derivatives and thus marks this central moiety as a conserved pharmacophore (Figure 49B).

Since "phenazistatins" turned out to be very potent inhibitors of the enzyme from *B. cepacia*, phenazistatin A (WB001) and the bioisostere WB024 were also tested against the dimeric enzymes PhzBB and HeteroPhzAB from *P. fluorescens* 2-79 (Figure 50).

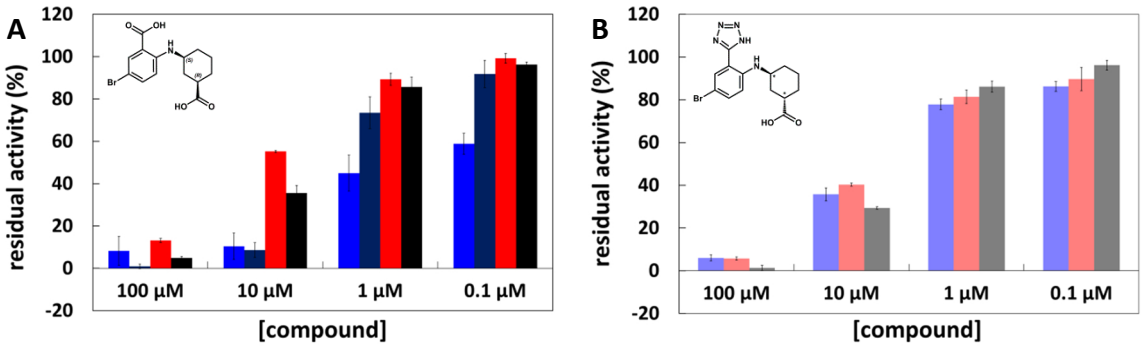

Figure 50: Residual enzymatic activity of different PhzB para- and orthologues in dependency of phenazistatin A (WB001) and WB024.

The residual enzymatic activity of *Bc*Phz(A)/B (and), PhzBB ( ) and HeteroPhzAB ( ) in presence of 1 mM DHHA and increasing phenazistatin A (WB001) (**A**) or WB024 (**B**) concentrations (0.1, 1, 10, and 100 µM) is represented. PhzB para- and orthologues as well as the coupled enzyme PhzF were used at 1 mM (dimer) final concentration. After normalization to zero and background correction the data from three independent measurements in 50 mM sodium phosphate pH 7.5, supplemented with 2 % (v/v) DMSO, at 25 °C were averaged. The insets show the chemical formulas of the ligands.

As expected from the high structural similarity and sequence identity, dose-response curves for both ligands against the PhzB orthologues display inhibition tendencies similar to the one observed for *Bc*Phz(A)/B. All enzymes show approximately 60 % inhibition at 10 µM WB024 and 1 mM substrate (Figure 50B). Since small differences can be observed between the three PhzB para- and orthologues in response to WB001 (Figure 50A), a more rigorous IC_{50}-determination was carried out (WB001; Figure 51).

These experiments yielded IC_{50}-values of 1.9 ± 0.1 µM, 13.9 ± 1.2 µM and 6.9 ± 1.1 µM for *Bc*Phz(A)/B, PhzBB and HeteroPhzAB respectively. As such, phenazistatin A is most efficient against the enzyme from *B. cepacia*. This is in good agreement with affinity titrations (*q.v.* paragraph 6.2.1), as the K_D for this complex was found to be 64 nM while the affinity of phenazistatin A to PhzBB was determined to 1.5 µM (see chapter II). The differing inhibitory potency of WB001 against PhzBB and HeteroPhzAB can also be explained in context of the previously presented kinetic studies (*q.v.* chapter II). The heterodimer is comprised of one active PhzB subunit and an inactive PhzA subunit. Structural as well as binding data verified that the inhibitor shows no or only weak affinity to the inactive PhzA subunit. As such, less inhibitor is needed to reach the half-maximal inhibitory concentration for the heterodimer than is needed for the homodimer (6.9 *vs.* 13.9 µM). Under physiological conditions where the heterodimer might be the prevalent form, this should lead to an increased inhibitory potency of phenazistatin A.

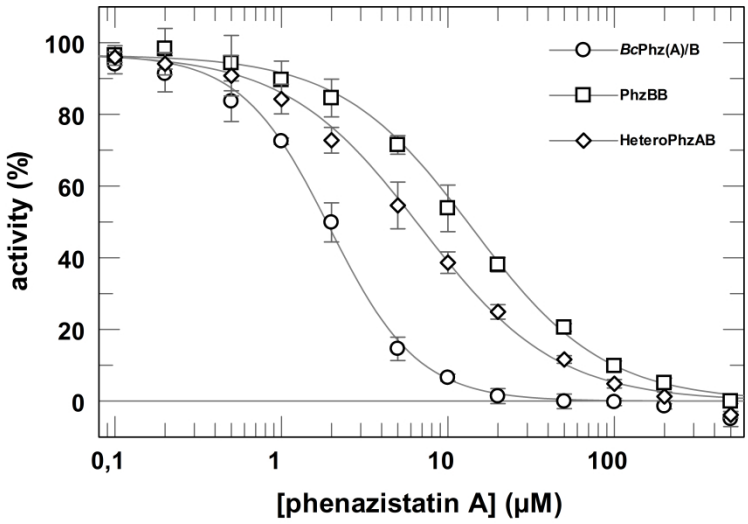

Figure 51: IC_{50}-determination of phenazistatin A towards different PhzB para- and orthologues.
Concentration dependent inhibition of *Bc*Phz(A)/B (○), PhzBB (□), and HeteroPhzAB (◇) by phenazistatin A (WB001). PhzB para- and orthologues as well as the coupled enzyme PhzF were used at 1 mM (dimer) final concentration. After normalization to zero and background correction, data from three independent measurements in 50 mM sodium phosphate pH 7.5, supplemented with 2 % (v/v) DMSO, at 25 °C were averaged and fitted using GraFit5 (Erithacus Software Ltd.).

As a potential universal PhzB-inhibitor in pseudomonads, the inhibitory potency of raloxifene was also tested against PhzBB and HeteroPhzAB (Figure 52). In contrast to the two "phenazistatins", at 1 mM substrate, PhzB para- and orthologues are only weakly inhibited by raloxifene (Figure 52A). Yet, when the substrate concentration is decreased to 125 µM, up to 65 % inhibition (HeteroPhzAB) can be observed at the highest compound concentration of 100 µM (Figure 52B).

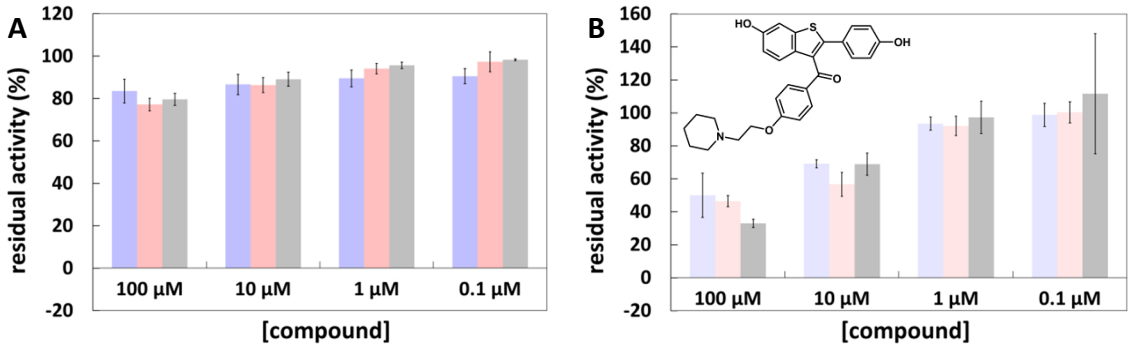

Figure 52: Residual enzymatic activity of different PhzB para- and orthologues in dependency of raloxifene.
The residual enzymatic activity of *Bc*Phz(A)/B ( ), PhzBB ( ), and HeteroPhzAB ( ) on presence of **A** 1 mM or **B** 125 µM DHHA is plotted as dose-response of 0.1, 1, 10, and 100 µM inhibitor. PhzB para- and orthologues as well as the coupled enzyme PhzF were used at 1 mM (dimer) final concentration. After normalization to zero and background correction, data from three independent measurements in 50 mM sodium phosphate pH 7.5, supplemented with 2 % (v/v) DMSO, at 25 °C were averaged. The inset depicts the chemical formula of raloxifene (RAL).

This partially contradicts the results of the recent study, where the authors attributed the reduction of pyocyanin levels in *P. aeruginosa* (PA14 and PAO1 strains) and the attenuated virulence in a *Caenorhabditis elegans* infection model (Ho Sui *et al*., 2012) to

the inhibition of PhzB2 by raloxifene. Indeed, although binding of raloxifene to *Bc*Phz(A)/B could be confirmed by crystal structures, in context of the presented *in vitro* assay the inhibitory potency of raloxifene appears to be weaker than proposed by the authors.

Finally, this *in vitro* study provides solid evidence for the higher inhibitory potency of the newly developed *N*-carboxycycloalkyl anthranilic acid derivatives ("phenazistatins") compared to raloxifene.

6.2.3. *In cellulo* compound screening towards inhibition of pyocyanin production

In order to confirm the low µM-range inhibition potency of some of the "phenazistatins" determined by the *in vitro* study, their *in cellulo* effect was addressed. Initially, the influence on pyocyanin production in bacterial cultures of five "phenazistatins" (WB001, WB011, WB012, WB013, and WB047), seven bioisosteres/prodrugs (WB024, WB025, WB027, WB028, WB031, WB045, and WB050) as well as two "mavericks" (WB014 and WB015) and raloxifene (RAL) was evaluated.

When tested towards inhibition of pyocyanin production in *P. aeruginosa* PA14, only RAL showed up to 30 % inhibition, while other compounds had no effect. Some of them, such as WB011 or WB047, seemingly even induced pyocyanin production (Figure 53). However, a control comprised of the buffer (200 mM TRIS/HCl pH 9.0), in which some ligands (WB011-WB015) were dissolved, showed similar tendencies (B) and thus might have caused this observation, at least to some extent.

As these effects were unexpected and the data (measured as triplicates) exhibited low accuracy, the experiment was repeated including a PqsR inhibitor (HIPS 918), whose IC_{50}-value is 130 nM (internal communication), as reference. Whereas this inhibitor showed the expected effect, namely reduction of pyocyanin levels by 50 % (Figure 44), the other compounds showed similar tendencies as before or even reduced effects as in case of raloxifene. Even when the potential inhibitors were tested against another bacterial strain (PAO1), which, in comparison to PA14, represents a chronic model of infection, no reliable data could be obtained (Figure A28 in appendix A3). Similarly, using a different medium (M63), which is known to enhance pyocyanin production (internal communication), no inhibitory effect on phenazine biosynthesis could be observed either (Figure A29).

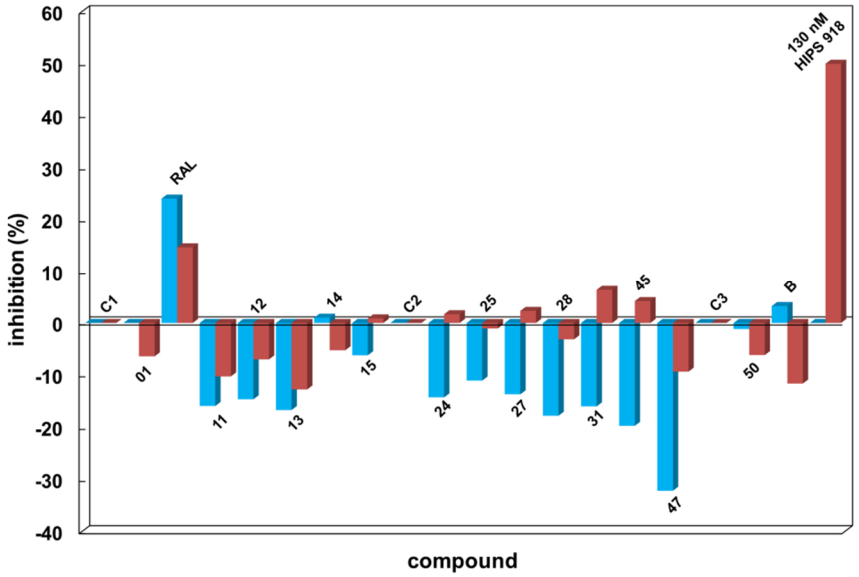

Figure 53: *In cellulo* inhibition studies of pyocyanin production in *P. aeruginosa* PA14.
Phenazine biosynthesis inhibition was analyzed in presence of 100 µM inhibitor by quantification of pyocyanin levels in *P. aeruginosa* PA14 cultures in PPGAS-medium after incubation overnight. After growth correction, data were averaged from triplicates and plotted in relation to a compound free control (C1-3). The numbers represent the individual compounds, *e.g*. 01 = WB001. B represents a buffer control (final concentration: 2 mM TRIS/HCl pH 9.0). Blue and red bars indicate independent replicas (each n = 3). Compound HIPS 918 was used as positive control at its known IC_{50}-value.

One possibility for the absence of *in cellulo* inhibition could be limited membrane permeability caused by the presence of the potentially negatively charged carboxylic acid moieties on the unmodified "phenazistatins" and "mavericks".

Consequently, two additional modified compounds, the prodrug ester WB087 as well as the bioisostere WB090, were tested in parallel to phenazistatin A (WB001) and its simple methyl ester (WB031). In contrast to previous experiments, all tested compounds exhibited detectable reduction of pyocyanin levels in this assay (Figure 54).

However, as the experimental data were very inaccurate, the experiment was repeated twice. Both repetitions showed similar tendencies, but the variance between data from all three measurements (each individual triplicates) was too big to allow reliable quantification. Thus, although it is not possible to draw a definite conclusion, the general trend indicates *in* cellulo inhibition of pyocyanin production by the tested "phenazistatin" derivatives ranging from 30 to 40 % (Figure 54 left).

Moreover, *in cellulo* dose-response experiments for phenazistatin A show a distinct tendency, whereupon higher compound concentrations lead to increased inhibition, with an estimated $IC_{50} \geq 1$ mM. Yet, it should be noted, that these data were also very noisy

and showed high variance when repeated. Furthermore, complete inhibition of pyocyanin production could never be achieved (Figure 54).

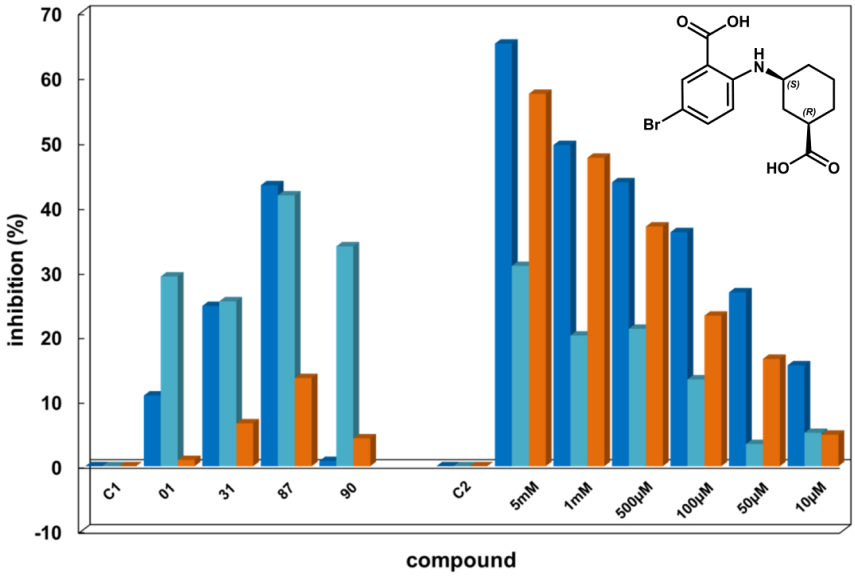

Figure 54: Dose-response inhibition of pyocyanin production in *P. aeruginosa* PA14.
Phenazine biosynthesis inhibition was analyzed in presence of 100 µM inhibitor (left) or as dose-response of phenazistatin A (right) by quantification of pyocyanin levels in *P. aeruginosa* PA14 cultures in PPGAS-medium after incubation overnight. After growth correction, data were averaged from triplicates and plotted in relation to a compound free control (C1-2). The numbers represent the individual compounds, *e.g.* 01 = WB001. Blue, turquoise, and orange bars indicate independent replicas (each triplicates). The inset depicts the structural formula of phenazistatin A (WB001).

Thus, the high inhibitory potency of "phenazistatin" compounds against PhzB observed in the *in vitro* assay could not fully be confirmed regarding pyocyanin production *in cellulo*. Two possible causes of an absent effect in bacterial cell cultures can be hypothesized: either uptake of the potential inhibitors is limited, or they are rapidly exported via multi-drug efflux pumps or other pore-forming proteins. Florian Gräf, who carried out permeability experiments in an artificial membrane transwell system, addressed the first hypothesis. It could be shown that all three tested compounds (WB001, WB050, and WB090) are able to cross the bacterial outer membrane barrier (Figure A30). He further observed that the substance flux (J) for the "phenazistatin" bioisostere carrying two methylsulfonylamides (WB090) instead of carboxylic acid moieties was exceeding the ones of WB050 (with two tetrazole-moieties) and the original compound, carrying two free acids (WB001) (J = 14.8 ± 3.6, 13.2 ± 2.8 and 7.2 ± 2.4 µg cm^{-2} h respectively). Nevertheless, these data should be considered with caution as strong solubility and adsorption issues were observed.

Altogether, "phenazistatins" appear to be inhibitors of phenazine biosynthesis even *in cellulo*, although further optimization of the ligand as well as of the assay will have to be performed to achieve satisfying potency not only *in vitro* but in bacterial cell cultures as well.

6.3. Conclusion

Phenazines are important virulence factors in human infections caused by phenazine producing pathogens such as *Pseudomonas aeruginosa*. For this reason, their biosynthesis seems to be a promising drug target.

PhzB, an enzyme of the core biosynthetic pathway, was chosen as target for its special role in phenazine biosynthesis. In fact, previous data revealed that PhzB is not necessary for phenazine production *in vitro*. However, it seems to accelerate biosynthesis *in vivo.* This peculiarity renders PhzB a promising target for antibiotic or anti-infective development (Scheme 18).

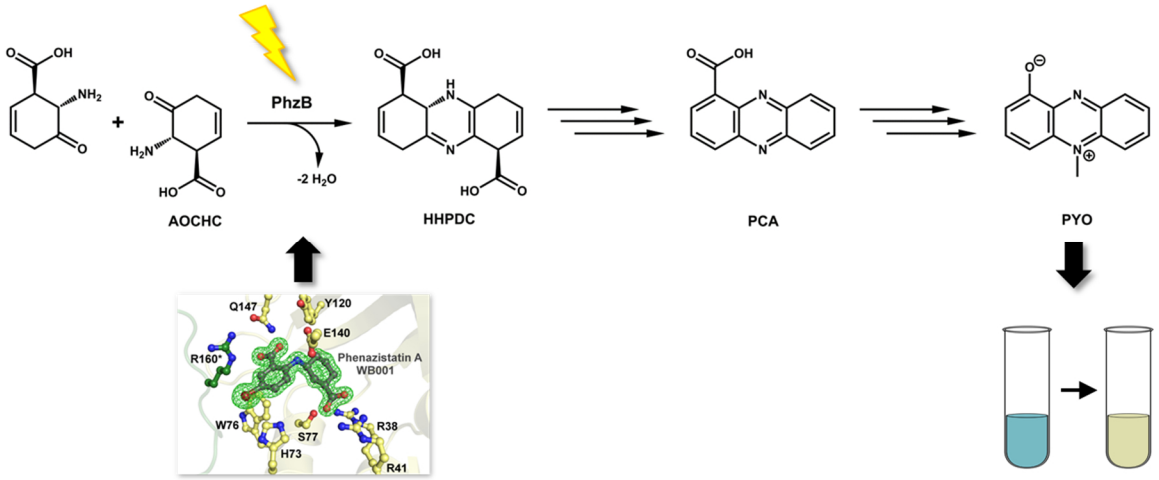

Scheme 18: Simplified representation of the anticipated mode of PhzB-inhibition by synthetic product analogs. PhzB catalyzes the symmetrical head-to-tail condensation of two identical ketamine precursors (AOCHC). The reaction product HHPDC is further converted to the product of core phenazine biosynthesis, PCA. In *Pseudomonas aeruginosa*, additional Phz-enzymes convert PCA further into the virulence factor pyocyanin (PYO). The synthetic product analogs, here represented by a crystal structure of *Bc*Phz(A)/B in complex with phenazistatin A (PDB entry 3JUM, Mentel *et al.*, 2009a), are proposed to inhibit PhzB catalysis and, in turn, lead to reduction of pyocyanin levels and finally reduced virulence.

The first strategy focuses on triggering bacterial self-intoxication via the activity of the ketamine substrate, which can potentially react with primary amines, such as the N_{ζ}-group of lysine. In contrast, the latter anti-infective approach aims at impairing virulence rather than killing the pathogen and consequently avoiding rapid occurrence of antibiotic resistance.

Previous ITC experiments by Matthias Mentel yielded promising inhibitor candidates. Here, these compounds were further characterized regarding their inhibitory potency *in vitro* and *in cellulo*. Additionally, a new library of synthetic PhzB product analogs was synthesized (Jakob Pletz). Based on the chemical structure of a previously determined strong PhzB binder, phenazistatin A (WB001), different modifications on the central anthranilic acid core were introduced (Scheme 19). These modifications were mainly comprised either of the exchange of the bromine group at position five (M1) or alterations of the *N*-linked moiety (M2) with different ring-systems, leading to a variety of likewise potent yet structurally different "phenazistatins". For future potential *in vivo* application, bioisosteres and prodrugs of phenazistatin A were synthesized as well (M3 and M4).

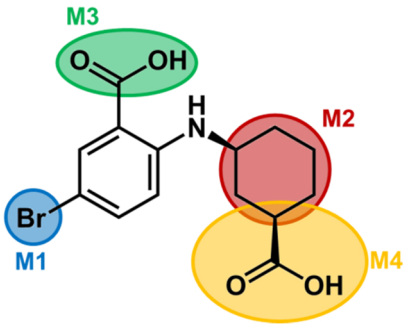

Scheme 19: Chemical structure of phenazistatin A (WB001) as starting point for further inhibitor development. Synthetically introduced modifications are highlighted in different colors.

In addition to investigation of the binding affinities of roughly 30 new compounds belonging to either the group of "phenazistatins" or a second, structurally related group (*N*-piperidinyl anthranilic acids, so-called "mavericks"), 25 complex structures of different ligands could be obtained. Moreover, overall 81 compounds were tested towards their inhibitory potency *in vitro*. Together, these results allowed a detailed analysis of structure activity relationships. The data revealed that two carboxylic acid moieties that are also found in the substrates/product of PhzB, are crucial for binding and consequently for function. These two groups mainly mediate hydrogen bonding to active site residues and waters, docking the ligand tightly to the active site. This explains why the majority of *N*-carboxycycloalkyl-derived compounds ("phenazistatins") are very strong binders up to nM-affinity. Furthermore, "phenazistatins" turned out to be potent inhibitors of PhzB *in vitro*. With few exceptions, all "phenazistatins" exhibit IC_{50}-values in low µM-range, *e.g.* phenazistatin A, one of the tightest PhzB binders, inhibits the homodimeric enzymes from *B. cepacia* and *P. fluorescens* with an IC_{50} of 1.9 and 13.9 µM respectively (6.9 µM for the heterodimer of the latter bacterium).

In contrast, the *N*-piperidinyl anthranilic acid derivatives ("mavericks") turned out to be weak binders in ITC experiments and exhibited no inhibition *in vitro*. These observations

can be explained by the lack of the second carboxylic acid moiety attached to the cycloalkyl-ring in "phenazistatins". Another peculiarity of this ligand class was the endothermic binding behavior of large fused "mavericks" in isothermal titration experiments.

Surprisingly, also "phenazistatin" derivatives with different stereochemical configuration than the original compound (*cis*-/*trans*-isomers) or bioisosteres, such as tetrazole-phenazistatins, exhibited high binding affinity and inhibitory potency against Phz(A)/B from *B. cepacia* R18194 (Figure 55).

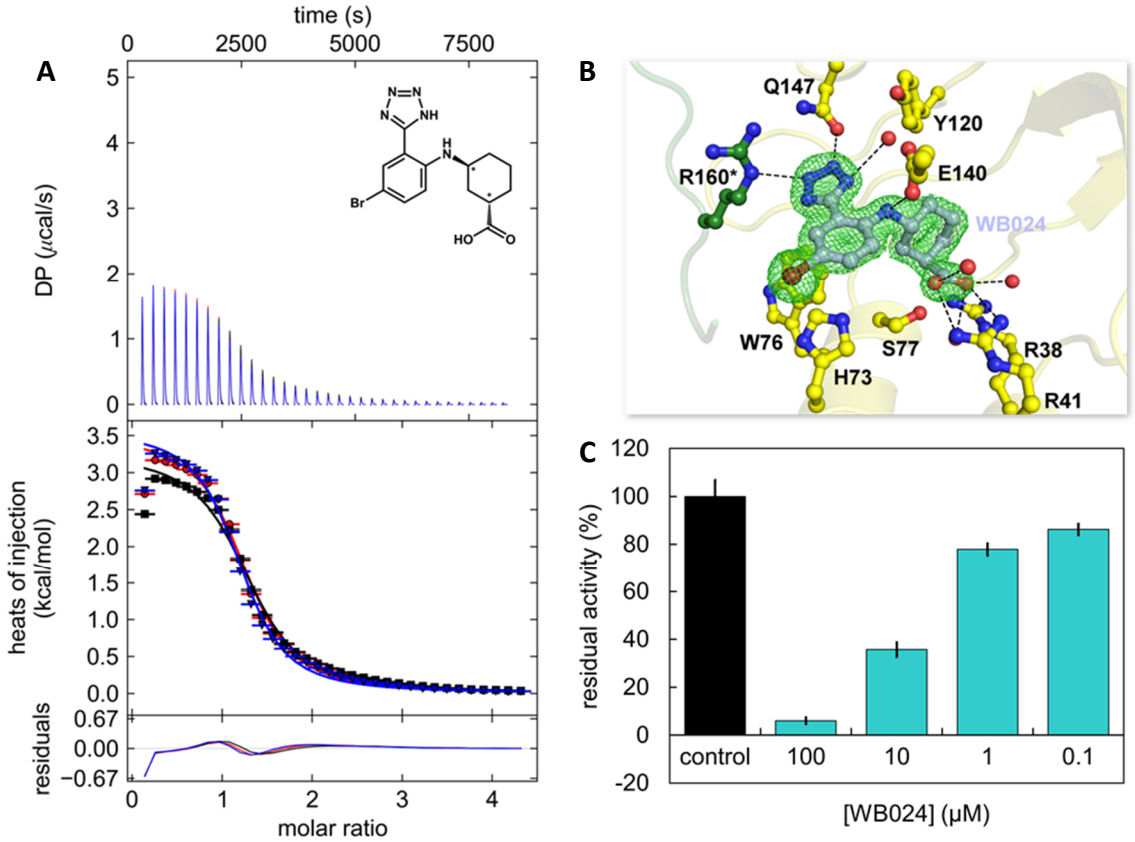

Figure 55: Overview of the individual steps of the experimental characterization of synthetic product analogs towards their inhibitory potency of PhzB catalysis.
A Measuring macromolecule-ligand affinity with isothermal titration calorimetry for *trans*-tetrazole-phenazistatin (WB024) and *Bc*Phz(A)/B. **B** Complex structure determination between WB024 and *Bc*Phz(A)/B after overnight soaking of the ligand using X-ray crystallography. **C** Dose-dependent enzyme inhibition assay for evaluation of the inhibitory potency of WB024 towards PhzB (here *Bc*Phz(A)/B) catalysis *in vitro*.

The latter compounds even showed an altered binding mode to the enzyme, leading to endothermic thermograms and binding profiles in ITC measurements. Analysis of the corresponding crystal structures revealed that PhzB is very flexible and can adopt even larger ligands in its active site. This observation is additionally supported by crystal structures with a previously reported PhzB2 inhibitor, raloxifene. This ligand is not only

much larger than typical product analogs, but also binds mainly via hydrophobic interactions. Despite the distinct structural differences of raloxifene and the inhibitors derived from product analogs ("phenazistatins"), a common structural benzaldehyde motif could be identified, which seems to represent the pharmacophore. Based on this observation, ligand chimeras, combining features of both ligands and sharing the conserved benzaldehyde moiety, ought to be generated (Scheme 20).

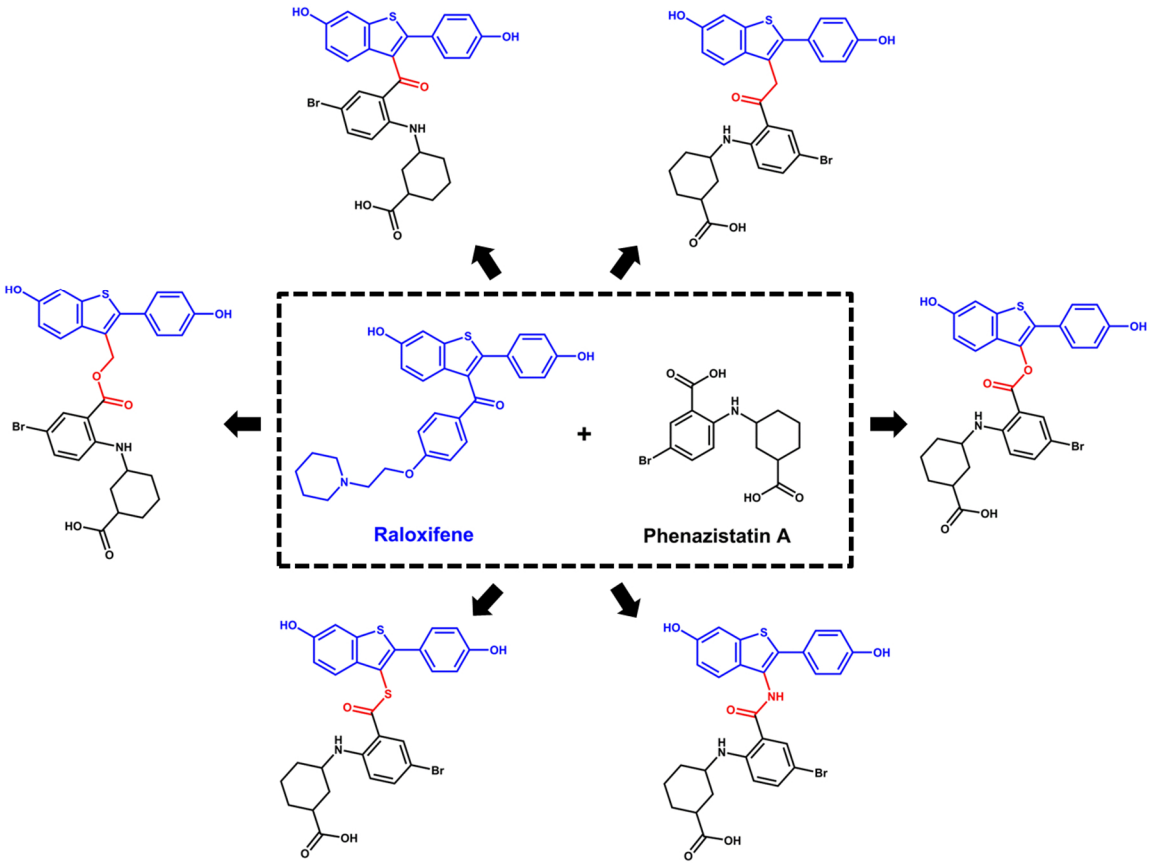

Scheme 20: Graphical overview of potential ligand chimeras derived from raloxifene and phenazistatin A.
The central part of this scheme shows the two original compounds, raloxifene (**blue**) and phenazistatin A (**black**), surrounded by potential chimeras, carrying characteristic elements of both parental compounds (highlighted in corresponding colors). The essential carbonyl moiety together with different linker elements is highlighted in **red**.

It is anticipated that, due to their size, these chimeras will increase ligand specificity and hence inhibitory potency against PhzB. However, this hypothesis requires experimental validation.

Some of the most potent *in vitro* inhibitors were additionally characterized *in cellulo*. However, these experiments turned out to be challenging, as for most ligands no distinct inhibition effect could be demonstrated in liquid bacterial culture. This might be owed to the high variance in experimental data or in fact to intrinsic properties of the ligands and/or the tested bacteria (*P. aeruginosa* PA14). First, it was hypothesized that ligand

uptake is inefficient, however additional membrane permeability studies (Florian Gräf) rendered this hypothesis unlikely. The absent (or weak) inhibitory effect *in cellulo* might thus be related to an unspecific efflux of the compounds by highly efficient multidrug efflux pumps, which are known to be abundantly present in *P. aeruginosa.*

Yet, additional experiments using *e.g*. transposon mutants or knockout strains of *P. aeruginosa*, which lack one or more of these pumps, are necessary to confirm this assumption. Furthermore, continuative rational drug development is needed to optimize the inhibitors especially regarding *in cellulo* efficacy.

7. Summary & Outlook

7.1. Summary

The present study aimed at gaining a deeper understanding of the fundamental biosynthesis pathway of phenazines. The small nitrogen-containing pigments exhibit multifaceted roles not only in the producing microorganisms themselves but also in their hosts. For instance, phenazines, in particular the blue pigment pyocyanin produced by the human pathogen *P. aeruginosa*, were identified to be important virulence factors in human infectious diseases. As such, understanding their biosynthesis is crucial to be able to target and inhibit this important metabolic pathway.

Two enzymes, PhzF and PhzB were selected and their catalytic reactions analyzed in detail. The isomerase PhzF catalyzes the conversion of DHHA to the reactive amino ketone AOCHC. Initially different pathways were hypothesized for this catalysis, one following classic acid-base catalysis, the second proceeding via a concerted pericyclic [1,5]-hydrogen shift, not observed for any enzyme so far. Furthermore, it was suggested that the enzyme assists in the subsequent tautomerization yielding the final reaction product AOCHC as well. In this work, enzyme kinetics were employed to measure kinetic isotope effects, which allow identification of the rate-limiting step of a reaction and thus potentially to distinguish between different catalytic mechanisms. Indeed, following the PhzF-catalyzed reaction using either the natural substrate DHHA or a specifically synthesized deuterated substrate analog revealed a significant rate difference in their enzymatic turnover (Figure 56A). The relative kinetic isotope effect was determined to 9.5 regarding k_{cat}, which strongly indicates that the first step of DHHA isomerization, namely the proton abstraction, is in fact rate limiting and even suggests that proton tunneling might play an important role in catalysis. Yet, these data alone do not allow an unequivocal proposition for the mechanism. For this reason, collaborators employed QC/MM calculations to simulate different reaction paths and to determine the activation energy of the individual steps. In doing so, an acid-base catalyzed proton abstraction with E45 acting as proton shuttle, which is first abstracting the proton from the C3-atom of the substrate and then redonating it to the C1-atom, turned out to be energetically most favorable (Figure 56C).

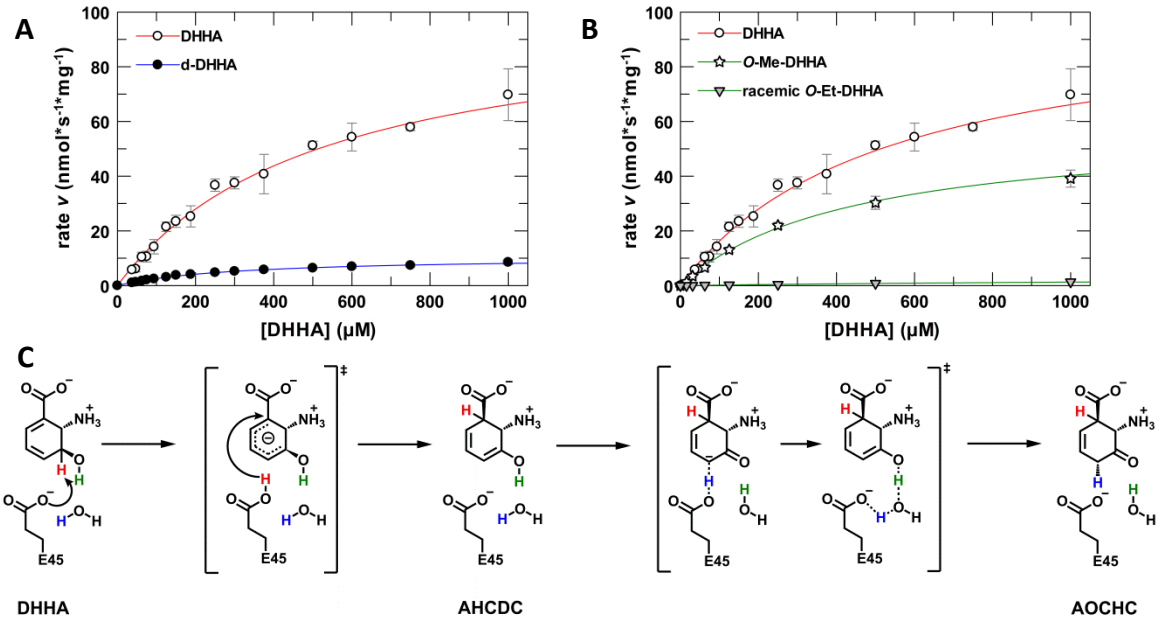

Figure 56: Mechanistic studies of the phenazine biosynthesis protein PhzF.
Kinetic plots showing **A** the turnover of the natural, light substrate DHHA (○) and of the heavy isotopologue d-DHHA (●) or **B** the turnover of DHHA (○), *trans*-2*S*,3*S*-*O*-methylated DHHA (*O*-Me-DHHA, ✿), and racemic *O*-ethylated DHHA (*O*-Et-DHHA, ▽) by PhzF. **C** Overall catalytic mechanism of PhzF. The zwitterionic DHHA is converted into AOCHC via a two-step mechanism: an initial base-catalyzed proton abstraction from position C3 (**H**) leads to formation of an anionic intermediate, which, after reprotonation, yields the reaction intermediate AHCDC. In the next step, this intermediate undergoes enzyme-catalyzed keto-enol tautomerization facilitated via an E45-water relay (**H** and **H**) to yield the final reaction product AOCHC. Figure adapted from Diederich *et al.*, 2017.

The nature of the enzymatic assay did not allow direct addressing of the subsequent tautomerization either. Therefore, this pathway was computationally simulated as well and these calculations favored a tautomerization that involves PhzF in form of a proton relay between the substrate, a conserved active site water and E45 (Figure 56C). The enzymatic assay that was developed in this study, however, allowed further investigations of the pH-, temperature or buffer dependency of the kinetic parameters and shed more light on the isomerization reaction catalyzed by PhzF. Moreover, by using several synthetic substrate analogs insights into the specificity of the enzyme could be obtained. It could notably be shown that the size of the C3-alkoxy group directs enzymatic specificity, as larger groups such as ethoxy- or propyloxy yield poor or no substrates respectively (Figure 56B). A crystal structure with *O*-ethylated DHHA confirmed that the spatial requirements of these larger substrates are incompatible with the topology of the active site. A substrate analog that could not be converted by PhzF turned out to be a weak inhibitor of the enzyme and as such represents a promising starting point for further inhibitor development.

The second main project of this study concerned downstream conversion of the reactive ketamine product of PhzF, AOCHC. Despite its ability to undergo self-condensation *in vitro*, previous studies indicated that PhzB catalyzes and thereby accelerates the reaction *in vivo*. Since AOCHC is a highly reactive ketamine, which potentially can react with other free amines, *e.g*. in proteins, and thus lead to self-intoxication *in vivo*, PhzB may be an attractive drug target.

Particularly relevant to human health, pseudomonads carry a second copy of the *phzB*-gene in their biosynthesis operon. The product of this gene, termed PhzA, however, is not able to accelerate the condensation reaction due to two active site mutations. Although it could be shown that, after heterologous co-expression in *E. coli*, a heterodimer consisting of PhzA and PhzB can be isolated and even crystallized (Figure 57A), the role of this dimer remained unclear. To this aim, a specific activity assay was developed, which allowed determination and comparison of the kinetic parameters of the different dimers. This demonstrates that PhzAB dimers are as efficient as PhzBB homodimers (Figure 57B); at low substrate concentrations, heterodimers might even outperform homodimers.

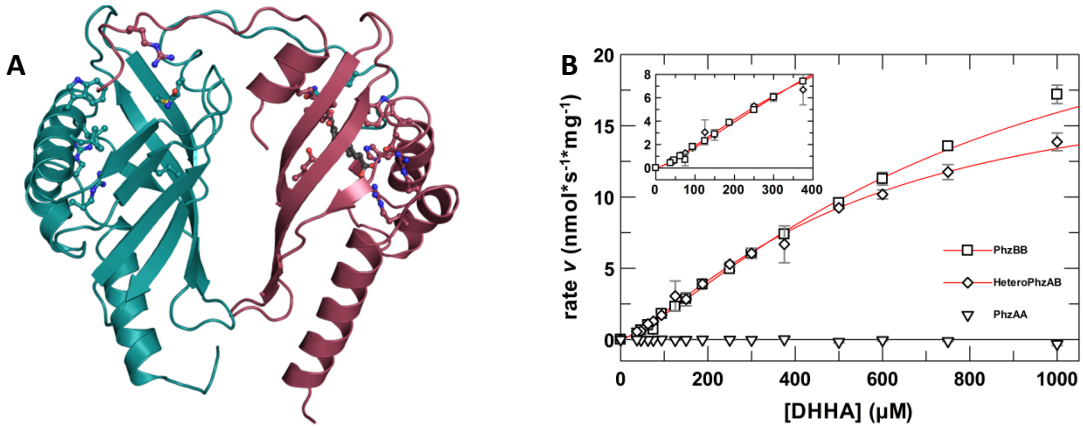

Figure 57: Relevance of PhzAB heterodimerization.
A Overall structure of the PhzAB heterodimer from *P. fluorescens* 2-79 with the inactive and active monomers, PhzA and PhzB, shown in deepteal and raspberry respectively. The co-crystallized ligand (gray) is found only in the active B-subunit. **B** Specific activity of PhzAA and PhzBB homodimers compared to the one of PhzAB heterodimers. PhzAA homodimers are inactive, while PhzBB homodimers and heterodimers show similar activity up to approximately 400 µM substrate.

Since dimer stability was also shown to be very similar, these results strongly support the physiological relevance of PhzAB heterodimerization, which might be of particular importance under environmental conditions when substrate availability is limited.

Prior to this study, PhzB was already investigated as potential drug target and synthetic substrate and product analogs, used for mechanistic studies, demonstrated µM-affinities

towards the enzyme from *B. cepacia*. However, no activity assay was available to screen the inhibitory potency of these compounds and newly synthesized analogs *in vitro*. To this aim, a specific coupled enzymatic assay for PhzB was developed and used for screening of approximately 80 compounds. In addition, ITC experiments and X-ray crystallography were employed to enable full investigation of the compounds' structure-activity relationships. Of the tested compounds, one class, the so-called "phenazistatins", comprised of very tight binders with up to nM-affinities, which were also very potent *in vitro* inhibitors of the PhzB-catalyzed reaction (Figure 58).

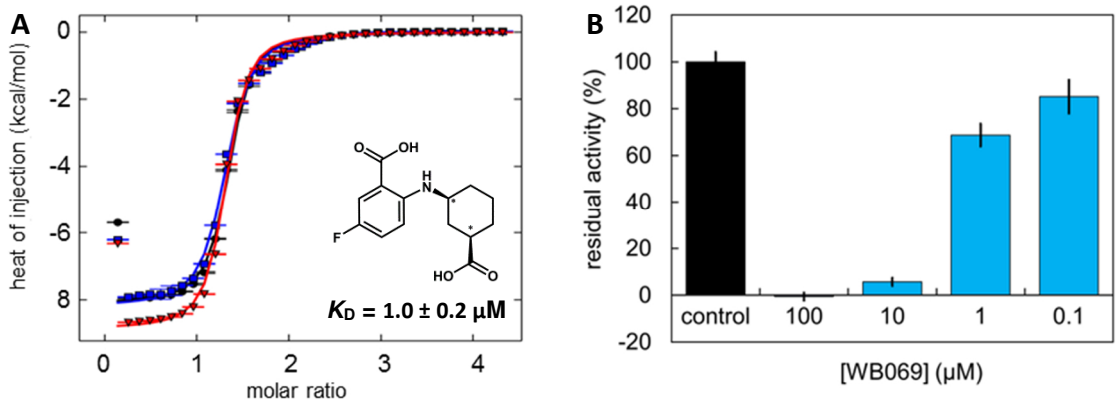

Figure 58: Development and characterization of PhzB-inhibitors.
A Affinity titration of WB069 (*cis*-fluoro-phenazistatin) to *Bc*Phz(A)/B obtained by ITC. The ligand binds with a K_D of 1.0 ± 0.2 µM. **B** Dose-dependent enzyme inhibition assay of WB069 towards *Bc*Phz(A)/B *in vitro*. The IC_{50} can be estimated between 1 and 10 µM.

Some of these promising candidates were tested *in cellulo* against *P. aeruginosa* as well. Although a positive tendency towards inhibition of phenazine biosynthesis could be observed, none of the tested ligands proved to be particularly potent under the tested conditions, emphasizing the need for further ligand development especially regarding compound uptake and bioavailability.

By combining binding measurements, X-ray crystallography and enzyme activity assays, this study provides a detailed description of various PhzB-inhibitors. For the first time endothermic PhzB binders were identified and it could furthermore be shown that "phenazistatins" can bind in different stereoconfigurations, *i.e.* in *cis*- and *trans*-configuration. Future drug-development projects will benefit from these new insights into PhzB-inhibition.

Altogether, this study provided a deeper understanding of two unique mechanisms within the phenazine biosynthesis pathway. The work greatly benefited from the combination of

multiple methods and from the collaboration with organic chemists, who synthesized tailor-made mechanistic probes and ligands, and with theoretical biochemists, who provided decisive complementary information to the kinetic experiments.

7.2. Outlook

As this study aimed at exploring the basic mechanistics of the "core" phenazine biosynthesis pathway, in particular, the unique steps catalyzed by the isomerase PhzF and the subsequent enzyme PhzB, the acquired knowledge may allow targeting and thus controlling this important metabolic pathway. This work contributed to the evaluation of the druggability of important catalytic intermediates that are required for production of the building blocks of all strain specific phenazines. This is of special interest in pathogenic phenazine producers, such as *P. aeruginosa*.

In general, two ways for the druggability of phenazine biosynthesis are possible, the first being the reduction of the virulence factor production by inhibiting essential regulatory or synthetic routes. This method will primarily disarm the bacteria rather than killing them and hence might be an interesting approach for combination therapy with other already established antibiotics. The second idea, particularly interesting in terms of PhzB catalysis, is aiming at directly killing the bacteria by triggering self-intoxication. However, since phenazines play multiple important roles in their producers, resistance towards these drugs might develop rapidly.

By making use of the new insights into the catalytic mechanism of PhzF, enzyme specific inhibitors/modulators could be developed. PhzF catalysis generates the highly reactive and potentially toxic intermediate AOCHC, hence modulating this enzyme might allow control over AOCHC production and thus of the overall phenazine biosynthesis. The approach could be used to inhibit PhzF, leading to complete abortion of phenazine biosynthesis and thus virulence factor production. In general, it might also be possible to enhance AOCHC production and consequently increase the intracellular levels of this toxic intermediate, which could potentially cause negative side effects harming the bacteria. The substrate analog *ent*-H_2-DHHA used in this study shows a decent inhibitory potency and could be further developed into more-potent inhibitors. In addition, screening for other PhzF specific inhibitors, which are chemically not directly related to the substrate or

product of the reaction, represents a potential future perspective. The assay developed in this work allows a semi high-throughput method to screen a large number of candidates in a time- and material-efficient way.

Prior to this work, PhzB was already considered a potential drug target. Yet, the newly identified and characterized inhibitors require further development. Some ligands with µM-affinities were found to be very potent inhibitors *in vitro* but failed to inhibit phenazine biosynthesis *in vivo,* probably due to limited bioavailability or metabolic degradation. Hence, the *in cellulo* efficiency needs further investigation. Drug delivery, in particular, seems to require optimization. This might be achieved by further varying/optimizing the ester groups of the prodrugs or by development of specific carriers or chaperones that are able to transport the inhibitors efficiently across the bacterial membrane. In addition, if further optimization of these substrate/product analogs fails, generation of chimeras with other known PhzB-inhibitors, such as raloxifene, might be a possibility to overcome metabolization or unspecific efflux by phenazine transporting pumps.

Finally, the regulation of PhzB catalysis, especially the actual abundance and role of PhzAB heterodimerization *in vivo* needs to be evaluated in further detail. This knowledge could be used to adapt inhibitor development to certain environmental conditions, such as biofilm formation, or to link it to potential stress induced responses.

8. Side projects

In parallel to the main projects presented in the previous chapters of this thesis, three additional side projects were pursued. All three projects constituted the *de novo*-structure determination of bacterial proteins:

— The antibacterial type VI secretion effector Tse1 from *P. aeruginosa* PA7
— The novel halohydrin dehalogenase HheG from *I. coccineus* YM16-304
— Two lignin-degrading enzymes, the β-etherase LigF2 from *N. aromaticivorans* DSM1244 and the glutathione-lyase LigG2 from *T. denitrificans* ATCC 25259.

The latter projects were carried out in collaboration with Julia Koopmeiners and Hauke Voß from the group of Prof. Dr. Anett Schallmey of the Technical University Braunschweig. In the following paragraphs, a brief overview of the topic and major achievements regarding structural biology for each of these projects is presented.

8.1. Atomic resolution structure of the bacteriolytic effector protein Tse1 from *Pseudomonas aeruginosa* PA7‡

Introduction

Like many Gram-negative and Gram-positive bacteria, the opportunistic human pathogen *Pseudomonas aeruginosa* features up to seven different secretion systems (type I-VII) for the export of diverse biomolecules. These systems are characterized either by their effector/substrate specificity, their target, or by the efficacy of substrate delivery (Chou *et al*., 2012). Upon human infection they are involved in host colonization; in competition with other bacteria they provide a fitness advantage (Kapitein and Mogk, 2013). One of them, the type VI secretion system (T6SS), discovered by Mekalanos and co-workers in *Vibrio cholerae*, provides bacteria with the ability to deliver specific bacteriocins to other prokaryotic cells via direct translocation (Pukatzki *et al*., 2007; Hood *et al*., 2010; Chou *et al*., 2012). The architecture of this secretion system is comparable to bacteriophage infection proteins or R-type pyocins (Cascales and Cambillau, 2012). Haemolysin co-regulated proteins (Hcp) and valine-glycine repeat proteins G (VgrG) assemble to form a contractile phage-tail-like apparatus for effector delivery (Leiman *et al*., 2009). Initially, three delivered proteins, all secreted under post-translational control, were identified and

called type VI secretion exported proteins 1 – 3 (Tse1-3) accordingly (Hood *et al*., 2010). Nowadays, additional secreted effectors such as Tse4-6 are known (Whitney *et al*., 2014). In order to prevent intercellular self-intoxication by an active secretion machinery, the bacteria co-express an immunity protein from the same bicistronic operon as the effector. Inhibition of the effector is accomplished by a physical association with the cognate immunity protein (type VI secretion immunity proteins 1-6 = Tsi1-6; Hood *et al*., 2010).

In order to elucidate the distinct roles of these effector/immunity protein systems in pathogenicity and interbacterial competition, this project aimed at the structural characterization of the individual proteins as well as their corresponding complexes. As a start, the structure determination of the bacteriolytic effector Tse1 was attempted. This bacteriocin is secreted into the periplasm of other Gram-negative bacteria where it hydrolyzes peptidoglycan and thus induces cell lysis (Russell *et al*., 2011).

Results and Discussion

The recombinantly expressed wild type protein from *P. aeruginosa* PA7 (UniProt-entry: A6V6X3 (A6V6X3_PSEA7)) could be obtained in high purity following standard purification procedures (as described in paragraph 3.2.3.) and crystallized from 0.1 - 0.25 M NaF and 14 – 16 % (w/v) PEG 3350 at 20 °C via hanging-drop vapor diffusion method. Crystals of two different morphologies grew to a maximum size of 140*15*15 µm (rod-shaped, WT-1) or 300*150*150 µm (diamond-shaped, WT-2) within a few days (Figure 59 insets A and B). Diffraction data to a resolution of 1.64 Å and 1.16 Å could be collected for each crystal form respectively. The crystals belonged to the same orthorhombic space group $P2_12_12_1$, but exhibited different unit-cell parameters.

Since no significantly similar protein structures could be found in the protein data bank (PDB), experimental phasing using the SIRAS (single isomorphous replacement with anomalous signal) method was employed. To this aim, a native, rod-shaped crystal was soaked with 1 mM mercury chloride and diffraction data to a resolution of 2 Å were collected. Initial phases for the WT-1 crystal form were obtained using the data of the mercury derivative in combination with the native dataset in *PHENIX AutoSol* (Terwilliger *et al*., 2009). The program located two heavy atom sites and built an initial model with 55 % of the residues that was later completed to 98 % by automatic model building with ARP/wARP (Langer *et al*., 2008). The model was completed and optimized by alternating

rounds of manual adjustment in COOT (Emsley *et al.*, 2010) and maximum-likelihood refinement by phenix.refine (Afonine *et al.*, 2012). Subsequently, it was used as an initial search model to solve the structure of the WT-2 crystal form by molecular replacement using Phaser (McCoy *et al.*, 2007) of the PHENIX software suite (Adams *et al.*, 2010).

While in the WT-1 crystal form, one monomer per asymmetric unit is present, the asymmetric unit of the WT-2 form contains three monomers, all exhibiting very similar conformation compared to the monomer found in the first form (r.m.s.d. 0.19 – 0.26; Figure 59). Yet, the near atomic resolution of 1.16 Å allowed a more detailed analysis of the structure.

The overall structure of Tse1 is characterized by a central, slightly twisted, six-stranded anti-parallel β-sheet, surrounded by α-helices. Three α-helices (α_1-α_3) flank the central sheet on one side, α-helix 4 on the other side. An additional small α-helix (α_5) as well as two 3_{10}-helices (η_1 and η_2) span diagonal across the central sheet (Figure 59A).

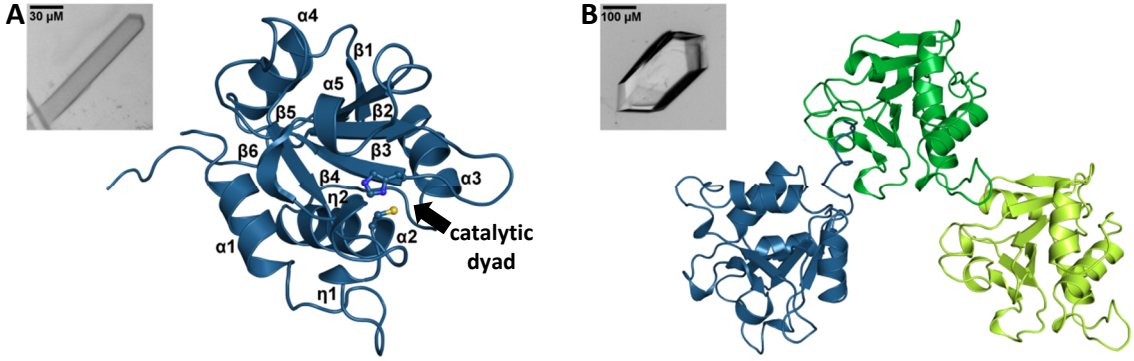

Figure 59: Structure of the bacteriolytic effector protein Tse1 from *P. aeruginosa* PA7 in two crystal forms.
A Overall topology of the Tse1 monomer with its secondary structure elements in cartoon representation (skyblue). The catalytic dyad comprised of cysteine 30 and histidine 93 is highlighted as balls and sticks. **Inset A:** Rod-shaped crystal of Tse1 that diffracted to 1.64 Å resolution and contains one monomer per asymmetric unit. **B** Atomic resolution structure of Tse1 in cartoon representation. The structure was obtained from a diamond-shaped crystal (**inset B**) that diffracted to 1.16 Å and comprised three protein chains per asymmetric unit (chain A = skyblue, chain B = green and chain C = limon).

A structural alignment related this fold, the αβ-papain-like amidase fold, to proteins of the N1pC/P60-peptidase family and hence identifies Tse1 as a cysteine peptidase. Yet, in comparison to other related proteins, Tse1 consists of a single domain only.

The active site is located at the interface between α_2 and β_3, which are conserved structural elements among this family. The catalytic dyad, residues C30 and H93, are both part of two highly conserved amino acid patterns, CSGF and HV, and the thiol-group of the cysteine is further stabilized by the positive helix dipole of α_2. The active site of Tse1 seems

to be much more accessible for the substrate compared to other proteins of similar fold, which might be due to the higher flexibility of surrounding loops. However, attempts to obtain complexes of wild type Tse1 or a catalytically inactive variant with a substrate analog, the muramyl tripeptide M-TriDAP, or the cognate immunity protein remained unsuccessful.

Conclusion

Since, a variety of structures of T6S effector/immunity protein complexes from different bacteria were solved by other groups including the complex of Tse1/Tsi1 (Benz *et al*., 2012; Ding *et al*., 2012; Shang *et al*., 2012). Furthermore, additional effector/immunity protein systems transported by the T6SS were discovered (reviewed by Benz and Meinhart, 2014). The variety of structural data, including the work presented here, provides a comprehensive insight in the structure and function of bacteriolytic effectors delivered by the T6SS and hence bacterial competition and pathogenicity. This knowledge might allow the development of specific small molecule compounds that modulate the activity of this machinery and possibly fight infectious diseases caused by different bacteria.

‡Diederich, C. & Blankenfeldt, W.: Tse1 - Kristallstruktur eines bakteriolytischen Effektorproteins aus *Pseudomonas aeruginosa* (Talk). 30. Rabensteiner Kolleg Pottenstein, Germany, June 2012

‡Diederich, C. & Blankenfeldt, W.: Atomic resolution structure of the bacteriolytic effector protein Tse1 from *Pseudomonas aeruginosa* PA7 (Poster). 5th BZMB-PhD-Symposium, Selb, Germany, October 2012

8.2. Crystal structure determination of the novel halohydrin dehalogenase HheG from *Ilumatobacter coccineus* YM16-304*

Introduction

Halohydrin dehalogenases (HHDHs) are a rare class of bacterial enzymes that catalyze the reversible dehalogenation of β-haloalcohols via epoxide formation (Janssen *et al*., 2006; You *et al*., 2013). Their natural role is the degradation of toxic halogenated compounds such as epichlorhydrin or 1,3-dichloro-3-propanol. Originally, three different phylogenetic subtypes (type A-C), all belonging to the short-chain dehydrogenase/ reductase (SDR) superfamily, were classified based on sequence identities and activity profiles of known HHDHs (van Hylckama Vlieg *et al.*, 2001; Kavanagh *et al*., 2008). Within each subtype, the members share over 90 % sequence identity on the protein level, however between the

subtypes the similarity decreases below 30 % (van Hylckama Vlieg *et al*., 2001). In 2014, Schallmey and co-workers identified 37 novel HHDHs using sequence database mining based on the two conserved motifs $SX_{12}YX_3R$, the residues forming the catalytic triad, and $TX_4(F/Y)XG$. Beside this consensus sequence, the overall sequence identity to known HHDHs was very low (below 30 %). As some of the new enzymes exhibited broader substrate spectra than previously known members of this class or demonstrated enhanced thermostability, the authors subsequently attributed these novel enzymes to four new subtypes, type D-G (Schallmey *et al*., 2014).

The particular catalytic activity of HHDHs renders them promising candidates for biotechnology applications like the production of diverse enantiopure vicinal haloalcohols or epoxides, especially since, beside halides, a variety of other nucleophiles such as cyanide, azide, nitrite (Fuchs *et al.,* 2009) or formate (Hasnaoui-Dijoux *et al*., 2008) can be employed for epoxide ring-opening. This allows industrial production of β-azidoalcohols, which are precursors for β-aminoalcohols, or of the important statin precursor (*R*)-4-cyano-3-hydroxybutyrate (Schallmey and Schallmey, 2016).

Among the HHDHs newly identified by Schallmey and co-workers, one enzyme, the single member of the G-subtype, HheG from *Ilumatobacter coccineus* YM16-304, exhibited higher activities on the conversion of cyclic epoxides or haloalcohols in contrast to other tested halohydrin dehalogenases. In order to understand this catalytic peculiarity and to obtain deeper insights into substrate binding and conversion, X-ray structure determination of HheG was pursued.

Results and Discussion

Hexagonal-shaped crystals of native N-terminally hexahistidine-tagged HheG, which belonged to the trigonal space group $P3_121$, were obtained from a condition containing 0.1 M sodium acetate pH 4.5 and 1 M ammonium phosphate dibasic. Since phasing of the structure using molecular replacement remained unsuccessful, the structure was solved by SAD (single wavelength anomalous dispersion) experimental phasing using a selenomethionine derivative. The moderate resolution of 2.7 Å and the high number of protein chains in the asymmetric unit complicated structure determination, yet collection of a very high redundancy dataset (5760 degree) and the identification of 108 selenium sites by SHELXD (Sheldrick, 2010) eventually yielded a reasonable solution. Moreover, the

derivatized crystals were isomorphous to the native ones, allowing phase extension of the anomalous data to a maximum resolution of 2.3 Å.

Ten copies of the protein constitute the asymmetric unit by forming either a complete tetramer (chain ABCD; Figure 60A) or three individual dimers (chain EF, GH and IJ). In the latter case, the biological assembly of the tetramer is reconstituted by crystallographic two-fold symmetry.

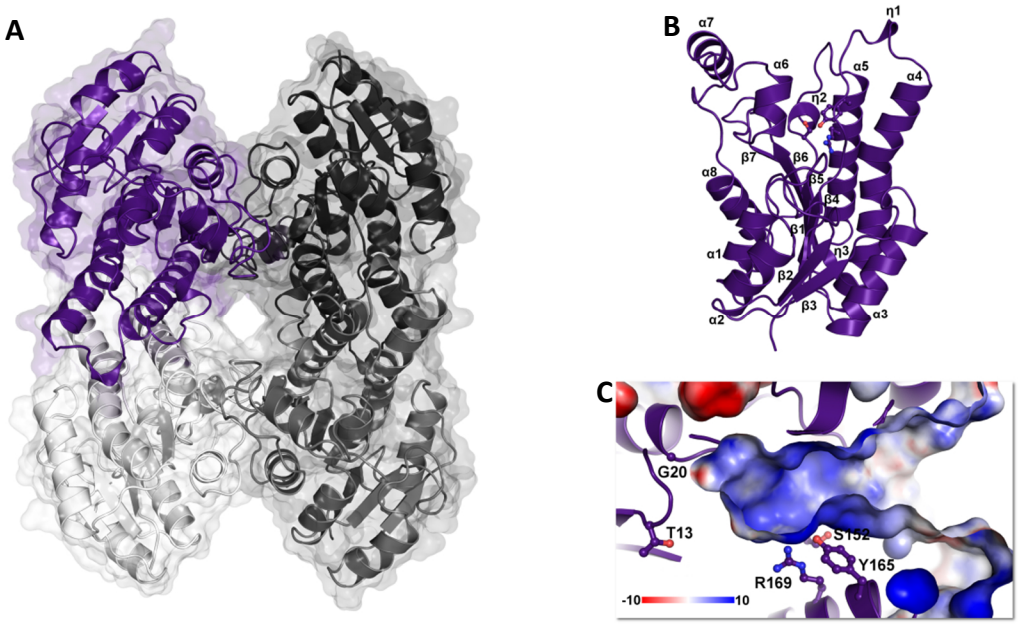

Figure 60: Structure of the novel halohydrin dehalogenase HheG from *I. coccineus* YM16-304.
A Overall topology of the tetrameric biological assembly of HheG shown as cartoon and surface (transparent) representation. The individual chains are colored in **dark purple** (chain A), **dark gray** (chain B), **gray** (chain C) and **white** (chain D) respectively. **B** The HheG monomer depicted with its secondary structure elements. The residues of the catalytic triad are highlighted as balls and sticks. **C** Close-up on the electropositive active site cleft of HheG. The electrostatic potential was calculated using the ABPS plugin (Baker *et al.*, 2001) of PyMOL (The PyMOL Molecular Graphics System, Version 1.8, Schrödinger, LLC.) and is represented on the molecular surface with a scale ranging from -10 (**red**) to 10 (**blue**) KbT/Ec. The residues of the catalytic triad S152, Y165 and R169, as well as the conserved residues T13 and G20 are shown as balls and sticks.

Within a HheG monomer, six α-helices arrange around a central, twisted, seven-stranded parallel β-sheet (β_1-β_7); the three helices α_1, α_2 and α_8 are found on one side, another small (α_3) as well as two longer α-helices (α_4 and α_5) on the other side. Two additional α-helices (α_6 and α_7) and three 3_{10}-helices (η_1-η_3) are located on top of the β-sheet. HheG, like other HHDHs, exhibits a Rossmann-fold like architecture (Figure 60B). The active site is comprised of the catalytic triad S152, Y165 and R169 and is located at the bottom of a long and partially electropositive cleft adjacent to the halide binding site, which is occupied by a water molecule (Figure 60C).

HheG was crystallized in absence of any ligand, nevertheless residual electron density was

observed in the active site (data not shown), indicating a covalent modification of S152. However, the quality of the data did not allow unambiguous attribution of this density to a specific substrate.

A structural comparison of HheG with other previously published halohydrin dehalogenases/lyases (Jong *et al*., 2006; Schallmey *et al*., 2015; Watanabe *et al*., 2015) revealed that HheG features a large open active site cleft, while other HHDHs have narrow substrate tunnels leading to the active site. This large cleft suggests that HheG is able to accommodate larger substrate molecules and hence explain why this enzyme preferentially converts cyclic epoxides/haloalcohols over smaller aliphatic substrates.

Conclusion

The newly determined structure of the first member of the G-subtype of halohydrin dehalogenases, HheG from *I. coccineus*, revealed a distinct difference in the accessibility and volume of the active site compared to known HHDHs such as HheA2 from *Arthrobacter sp*. strain AD2 (Jong *et al*., 2006) or HheC from *Agrobacterium tumefaciens* (Jong *et al*., 2003). The ability to accommodate and convert more bulky, cyclic substrates does not only distinguish HheG from other members of this class, but also opens new biocatalytic routes for industrial applications, including synthesis of chiral tertiary or cyclic haloalcohols. Furthermore, the detailed structural insight enables additional protein engineering of HheG and thus potential further expansion of the product range.

*Koopmeiners, J., Diederich, C., Solarczek, J., Voß, H., Mayer, J., Blankenfeldt, W. & Schallmey, A.: HheG, a Halohydrin Dehalogenase with Activity on Cyclic Epoxides. *ACS Catal.* **2017**, 7 (10), pp 6877–6886.

8.3. Structural studies of the two bacterial lignin-degrading enzymes LigF2 from *Novosphingobium aromaticivorans* DSM1244 and LigG2 from *Thiobacillus denitrificans* ATCC 25259

Introduction

The heterogeneous aromatic biopolymer lignin is assembled from three different monolignols, *p*-coumarylalcohol (H), coniferylalcohol (G) and sinapylalcohol (S) via oxidative coupling and, together with other biopolymers such as cellulose, hemicellulose or pectic polysaccharides, lignin composes the cell wall of plants (Hendriks and Zeeman, 2009). As such, it constitutes one-third of all non-fossil organic carbon on earth (Austin

and Ballaré, 2010). At present, it is mainly used as heat and energy source being a byproduct in paper industry (Zakzeski *et al*., 2010). However, carrying different aromatic building blocks, lignin is considered a potential source for production of biofuel or aromatic fine chemicals (De los Santos Ramos *et al*., 2009). Still, its exploitation and the development of specific catalysts is challenging due to the complexity of this heteropolymer. Typically, industrial lignin depolymerization is achieved by chemical methods like thermolysis or chemical oxidation that have the disadvantage of yielding a complex mixture of degraded and partially repolymerized products (Pandey and Kim, 2011). Therefore, enzymatic routes for selective lignin depolymerization are investigated. In fact, some fungi and bacteria, in particular sphingomonads, possess enzymes for lignin degradation, including peroxidases, laccases and β-etherases. While the former employ unselective radical-based mechanisms, β-etherases offer the possibility to generate pure enantiomeric low-molecular mass aromatics from the "achiral" lignin polymer using an unusual non-radical glutathione-dependent reductive catalytic mechanism to cleave β-O-4-aryl ether bonds (Picart *et al*., 2015). Natural β-etherases, termed LigE, LigF, or LigP, cleave β-aryl ether adjacent to a carbonyl group under chirality inversion using glutathione (GSH) as co-substrate. Whilst LigE and LigP selectively cleave the *R*-enantiomer of a model compound (β-guaiacyl-α-veratrylglycerone, β-GVG), LigF exclusively cleaves the *S*-enantiomer yielding the inverse product enantiomers as GSH-adducts (GS-β-(*S*/*R*)-VG). Subsequently, the highly selective GSH-lyase LigG processes the *R*-enantiomer of the GSH-adduct yielding oxidized glutathione (GSSG) and veratrylglycerone (VG). In nature, stereospecific NADH-dependent alcohol dehydrogenases initially have to oxidize the α-hydroxy group adjacent to the β-aryl ether to yield a ketone that is essential for β-etherase activity. Furthermore, yet uncharacterized racemases are suggested to convert the products of LigE and LigP into substrates for LigG (Masai *et al*., 2003; Gall *et al*., 2014).

The β-O-4-aryl ether bond represents up to two-thirds of all linkages in lignin, hence bacterial β-etherases and the associated enzymes constitute promising candidates for valuable biomass degradation under mild conditions. To understand the molecular details of enzymatic lignin depolymerization better, this work aimed at the crystal structure determination of two novel enzymes involved in lignin degradation, the β-etherase LigF2

from *N. aromaticivorans* DSM1244 and the GSH-lyase LigG2 from *T. denitrificans* ATCC 25259.

Results and Discussion

After size-exclusion chromatography the purified N-terminally hexahistidine-tagged proteins LigF2 and LigG2 were subjected to crystallization in presence or absence of 10 mM reduced glutathione. Diffraction quality crystals of both enzymes could be obtained within a week from conditions containing 0.1 M HEPES pH 7.5, 2 M ammonium sulfate and 2 % (v/v) PEG 400 or 0.1 M TRIS/HCl pH 7.6 – 7.8, 10 – 12 % (w/v) PEG 8000 and 0.2 mM $MgCl_2$ for LigF2 and LigG2 respectively. Whilst for LigF2 only a single crystal, belonging to the trigonal space group $P3_221$ with two monomers in the asymmetric unit, could be obtained in presence of GSH, LigG2 crystallized from conditions with or without GSH present. Both crystals contained six monomers per asymmetric unit, but belonged to two different orthorhombic space groups, namely $P22_12_1$ and $P2_12_12_1$ for apo- and GSH-bound LigG2 respectively.

Diffraction data to 3.1 Å for LigF2 or 2.13 Å (apo) and 2.8 Å (GSH-complex) for LigG2 could be collected. Since homologous structures for both proteins were available from the PDB, structure determination was done via molecular replacement using PDB entry 4XT0 (59 % sequence identity to LigF2) or 4G10 (51 % sequence identity to LigG2) as initial models. The GSH-complex of LigG2 was solved using the apo-structure as model. Model optimization was carried out by alternating rounds of manual adjustment in COOT (Emsley *et al*., 2010) and maximum-likelihood refinement by phenix.refine (Afonine *et al*., 2012). Both proteins form homodimers (Figure 61) and exhibit a typical glutathione S-transferase (GST)-fold with an N-terminal thioredoxin-like domain and a C-terminal α-helical domain comprised of 5 (α_4 - α_8; LigG2) or 8 α-helices (α_4 - α_{11}; LigF2). The former domain is comprised of a central, four-stranded mixed β-sheet (β_1-β_4) packing against parallel α-helices (α_1 and α_3) and is completed by an additional small α- (α_2) as well as a 3_{10}-helix (η_1).

Similar to the published structure from *Sphingobium sp*. SYK-6 and GSTs of the ω-class (Meux *et al*., 2012), LigG2 has an additional long loop at its C-terminus, which, due to its flexibility might be involved in substrate binding and product release. However, no distinct

structural differences could be observed between apo- and GSH-bound LigG2 to support this hypothesis.

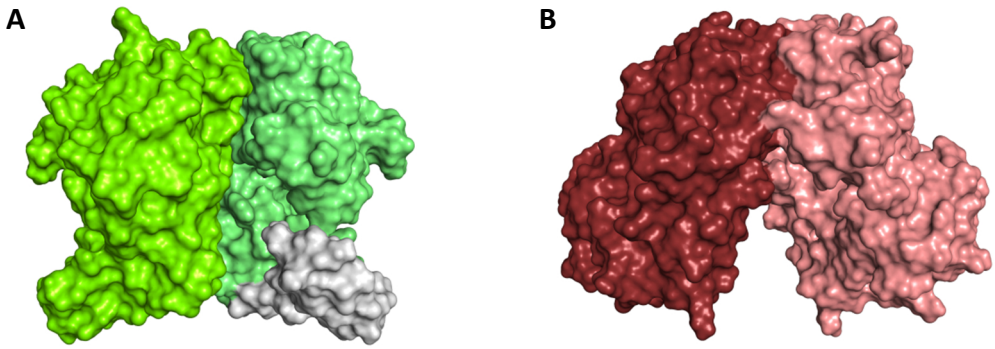

Figure 61: Crystal structures of the two novel lignin-degrading enzymes LigF2 from *N. aromaticivorans* DSM1244 and LigG2 from *T. denitrificans* ATCC 25259.
Overall topology of the homodimeric biological assembly of the β-etherase LigF2 (**A**) and the GSH-lyase LigG2 (**B**) shown as surface representation. The individual chains are colored in light green (chain A) and lime (chain B; the gray region, poorly defined in the electron density maps, was modelled based on the other monomer) or ruby (chain A) and salmon (chain B) for LigF2 and LigG2 respectively. Both proteins exhibit a typical glutathione S-transferase fold and could be crystallized in presence of the co-factor GSH.

Structure determination and analysis of LigF2 turned out to be challenging due to the moderate resolution of 3.1 Å. Nevertheless, a reasonable model could ultimately be obtained. The most striking difference to a previously published LigF-structure (Helmich *et al*., 2016) is the orientation of the helix-loop-helix motif involving α_5 and α_6, which is flipped out and hence opens the active site in LigF2. However, at this point no conclusive statement can be made, since this region is poorly defined in the structure, especially in chain B.

Conclusion

In this work, the crystal structures of two novel lignin-degrading enzymes, LigF2 and LigG2, could be determined. Although, in particular for the former, improvement of the crystals might be necessary before obtaining further potential substrate complex structures, the data on LigF2 and LigG2 give valuable structural insights and, together with biochemical data from collaborators, allow for a better understanding of the enzymes activities and specificities as well as provide a rational for future protein engineering.

9. Bibliography

Abken, H.-J., Tietze, M., Brodersen, J., Bäumer, S., Beifuss, U., and Deppenmeier, U. (1998). Isolation and Characterization of Methanophenazine and Function of Phenazines in Membrane-Bound Electron Transport ofMethanosarcina mazei Gö1. J. Bacteriol. *180*, 2027–2032.

Adams, P.D., Afonine, P.V., Bunkóczi, G., Chen, V.B., Davis, I.W., Echols, N., Headd, J.J., Hung, L.-W., Kapral, G.J., Grosse-Kunstleve, R.W., et al. (2010). PHENIX: a comprehensive Python-based system for macromolecular structure solution. Acta Crystallogr. D Biol. Crystallogr. *66*, 213–221.

Afonine, P.V., Grosse-Kunstleve, R.W., Echols, N., Headd, J.J., Moriarty, N.W., Mustyakimov, M., Terwilliger, T.C., Urzhumtsev, A., Zwart, P.H., and Adams, P.D. (2012). Towards automated crystallographic structure refinement with phenix.refine. Acta Crystallogr. D Biol. Crystallogr. *68*, 352–367.

Afonine, P.V., Moriarty, N.W., Mustyakimov, M., Sobolev, O.V., Terwilliger, T.C., Turk, D., Urzhumtsev, A., and Adams, P.D. (2015). FEM: feature-enhanced map. Acta Crystallogr. D Biol. Crystallogr. *71*, 646–666.

Ahuja, E.G. (2007). Towards elucidation of the phenazine biosynthesis pathway of Pseudomonas with the structural and functional analysis of the enzymes PhzA, B, G and BcepA. Dissertation. Technische Universität Dortmund.

Ahuja, E.G., Mavrodi, D.V., Thomashow, L.S., and Blankenfeldt, W. (2004). Overexpression, purification and crystallization of PhzA, the first enzyme of the phenazine biosynthesis pathway of Pseudomonas fluorescens 2-79. Acta Crystallogr. D Biol. Crystallogr. *60*, 1129–1131.

Ahuja, E.G., Janning, P., Mentel, M., Graebsch, A., Breinbauer, R., Hiller, W., Costisella, B., Thomashow, L.S., Mavrodi, D.V., and Blankenfeldt, W. (2008). PhzA/B Catalyzes the Formation of the Tricycle in Phenazine Biosynthesis. J Am Chem Soc *130*, 17053–17061.

Allemann, R.K., and Scrutton, N.S. (2009). Quantum Tunnelling in Enzyme-Catalysed Reactions (The Royal Society of Chemistry).

Arrhenius, S. (1889). On the reaction rate of the inversion of non-refined sugar upon souring. Z. Für Phys. Chem. *4*, 226–248.

Austin, A.T., and Ballaré, C.L. (2010). Dual role of lignin in plant litter decomposition in terrestrial ecosystems. Proc. Natl. Acad. Sci. *107*, 4618–4622.

Baker, N.A., Sept, D., Joseph, S., Holst, M.J., and McCammon, J.A. (2001). Electrostatics of nanosystems: Application to microtubules and the ribosome. Proc. Natl. Acad. Sci. *98*, 10037–10041.

Bell, R.P. (1980). The Tunnel Effect in Chemistry (Boston, MA: Springer US).

Benz, J., and Meinhart, A. (2014). Antibacterial effector/immunity systems: it's just the tip of the iceberg. Curr. Opin. Microbiol. *17*, 1–10.

Benz, J., Sendlmeier, C., Barends, T.R.M., and Meinhart, A. (2012). Structural Insights into the Effector – Immunity System Tse1/Tsi1 from Pseudomonas aeruginosa. PLoS ONE *7*, e40453.

Berman, H.M., Westbrook, J., Feng, Z., Gilliland, G., Bhat, T.N., Weissig, H., Shindyalov, I.N., and Bourne, P.E. (2000). The Protein Data Bank. Nucleic Acids Res. *28*, 235–242.

Blankenfeldt, W., and Parsons, J.F. (2014). The structural biology of phenazine biosynthesis. Curr. Opin. Struct. Biol. *29*, 26–33.

Blankenfeldt, W., Kuzin, A.P., Skarina, T., Korniyenko, Y., Tong, L., Bayer, P., Janning, P., Thomashow, L.S., and Mavrodi, D.V. (2004). Structure and function of the phenazine biosynthetic protein PhzF from Pseudomonas fluorescens. Proc. Natl. Acad. Sci. U. S. A. *101*, 16431–16436.

Brautigam, C.A. (2015). Chapter Five - Calculations and Publication-Quality Illustrations for Analytical Ultracentrifugation Data. In Methods in Enzymology, J.L. Cole, ed. (Academic Press), pp. 109–133.

Brautigam, C.A., Zhao, H., Vargas, C., Keller, S., and Schuck, P. (2016). Integration and global analysis of isothermal titration calorimetry data for studying macromolecular interactions. Nat. Protoc. *11*, 882–894.

Broglie, L. de (1970). The reinterpretation of wave mechanics. Found. Phys. *1*, 5–15.

Bulheller, B.M., Rodger, A., and Hirst, J.D. (2007). Circular and linear dichroism of proteins. Phys. Chem. Chem. Phys. *9*, 2020–2035.

Burschowsky, D., Eerde, A. van, Ökvist, M., Kienhöfer, A., Kast, P., Hilvert, D., and Krengel, U. (2014). Electrostatic transition state stabilization rather than reactant destabilization provides the chemical basis for efficient chorismate mutase catalysis. Proc. Natl. Acad. Sci. *111*, 17516–17521.

Calhoun, D.H., Carson, M., and Jensen, R.A. (1972). The Branch Point Metabolite for Pyocyanine Biosynthesis in Pseudomonas aeruginosa. Microbiology *72*, 581–583.

Carmody, W.R. (1961). Easily prepared wide range buffer series. J. Chem. Educ. *38*, 559.

Cascales, E., and Cambillau, C. (2012). Structural biology of type VI secretion systems. Phil Trans R Soc B *367*, 1102–1111.

Chen, V.B., Arendall, W.B., III, Headd, J.J., Keedy, D.A., Immormino, R.M., Kapral, G.J., Murray, L.W., Richardson, J.S., and Richardson, D.C. (2010). MolProbity: all-atom structure validation for macromolecular crystallography. Acta Crystallogr. Sect. D *66*, 12–21.

Chin-A-Woeng, T.F., Thomas-Oates, J.E., Lugtenberg, B.J., and Bloemberg, G.V. (2001a). Introduction of the phzH gene of Pseudomonas chlororaphis PCL1391 extends the range of biocontrol ability of phenazine-1-carboxylic acid-producing Pseudomonas spp. strains. Mol. Plant-Microbe Interact. MPMI *14*, 1006–1015.

Chin-A-Woeng, T.F., van den Broek, D., de Voer, G., van der Drift, K.M., Tuinman, S., Thomas-Oates, J.E., Lugtenberg, B.J., and Bloemberg, G.V. (2001b). Phenazine-1-carboxamide production in the biocontrol strain Pseudomonas chlororaphis PCL1391 is regulated by multiple factors secreted into the growth medium. Mol. Plant-Microbe Interact. MPMI *14*, 969–979.

Chou, S., Bui, N.K., Russell, A.B., Lexa, K.W., Gardiner, T.E., LeRoux, M., Vollmer, W., and Mougous, J.D. (2012). Structure of a Peptidoglycan Amidase Effector Targeted to Gram-Negative Bacteria by the Type VI Secretion System. Cell Rep. *1*, 656–664.

Cirilli, M., Zheng, R., Scapin, G., and Blanchard, J.S. (1998). Structural Symmetry: The Three-Dimensional Structure of Haemophilus Influenzae Diaminopimelate Epimerase,. Biochemistry (Mosc.) *37*, 16452–16458.

Cox, C.D. (1986). Role of pyocyanin in the acquisition of iron from transferrin. Infect. Immun. *52*, 263–270.

Cui, Q., Lv, H., Qi, Z., Jiang, B., Xiao, B., Liu, L., Ge, Y., and Hu, X. (2016). Cross-Regulation between the phz1 and phz2 Operons Maintain a Balanced Level of Phenazine Biosynthesis in Pseudomonas aeruginosa PAO1. PLOS ONE *11*, e0144447.

De los Santos Ramos, W., Poznyak, T., Chairez, I., and Córdova R., I. (2009). Remediation of lignin and its derivatives from pulp and paper industry wastewater by the combination of chemical precipitation and ozonation. J. Hazard. Mater. *169*, 428–434.

DeClue, M.S., Baldridge, K.K., Künzler, D.E., Kast, P., and Hilvert, D. (2005). Isochorismate Pyruvate Lyase: A Pericyclic Reaction Mechanism? J. Am. Chem. Soc. *127*, 15002–15003.

Delaney, S.M., Mavrodi, D.V., Bonsall, R.F., and Thomashow, L.S. (2001). phzO, a gene for biosynthesis of 2-hydroxylated phenazine compounds in Pseudomonas aureofaciens 30-84. J. Bacteriol. *183*, 318–327.

Deppenmeier, U., Johann, A., Hartsch, T., Merkl, R., Schmitz, R.A., Martinez-Arias, R., Henne, A., Wiezer, A., Bäumer, S., Jacobi, C., et al. (2002). The genome of Methanosarcina mazei: evidence for lateral gene transfer between bacteria and archaea. J. Mol. Microbiol. Biotechnol. *4*, 453–461.

Diederich, C., Leypold, M., Culka, M., Weber, H., Breinbauer, R., Ullmann, G.M., and Blankenfeldt, W. (2017). Mechanisms and Specificity of Phenazine Biosynthesis Protein PhzF. Sci. Rep. *7*, 6272.

Diederichs, K., and Karplus, P.A. (1997). Improved R-factors for diffraction data analysis in macromolecular crystallography. Nat. Struct. Mol. Biol. *4*, 269–275.

Dietrich, L.E.P., Price-Whelan, A., Petersen, A., Whiteley, M., and Newman, D.K. (2006). The phenazine pyocyanin is a terminal signalling factor in the quorum sensing network of Pseudomonas aeruginosa. Mol. Microbiol. *61*, 1308–1321.

Ding, J., Wang, W., Feng, H., Zhang, Y., and Wang, D.-C. (2012). Structural insights into the Pseudomonas aeruginosa type VI virulence effector Tse1 bacteriolysis and self-protection mechanisms. J. Biol. Chem.

Emsley, P., Lohkamp, B., Scott, W.G., and Cowtan, K. (2010). Features and development of Coot. Acta Crystallogr. D Biol. Crystallogr. *66*, 486–501.

Essar, D.W., Eberly, L., Hadero, A., and Crawford, I.P. (1990). Identification and characterization of genes for a second anthranilate synthase in Pseudomonas aeruginosa: interchangeability of the two anthranilate synthases and evolutionary implications. J. Bacteriol. *172*, 884–900.

Evans, P.R., and Murshudov, G.N. (2013). How good are my data and what is the resolution? Acta Crystallogr. D Biol. Crystallogr. *69*, 1204–1214.

Feiler, C. (2010). PhzAA / PhzBB - Homo - und PhzAB - Heterodimere in der Phenazinbiosynthese von Pseudomonas. Master (M.Sc.) Thesis. Technische Universität Dortmund.

Fokkens, J., and Klebe, G. (2006). A Simple Protocol To Estimate Differences in Protein Binding Affinity for Enantiomers without Prior Resolution of Racemates. Angew. Chem. Int. Ed. *45*, 985–989.

Fordos, M.-J. (1859). Recherches sur la matière colorante des suppurations bleues: pyocyanine. Rec Trav Soc d'Émul Sci Pharm 30.

Fuchs, S. (2006). Untersuchungen zu Sequenz-Aktivitäts-Beziehungen von PhzA und PhzB aus Pseudomonas fluorescens 2-79. Bachelor (B.Sc.) Thesis. Technische Universität Dortmund.

Fuchs, M., Simeo, Y., Ueberbacher, B.T., Mautner, B., Netscher, T., and Faber, K. (2009). Enantiocomplementary Chemoenzymatic Asymmetric Synthesis of (R)- and (S)-Chromanemethanol. Eur. J. Org. Chem. *2009*, 833–840.

Fuqua, W.C., Winans, S.C., and Greenberg, E.P. (1994). Quorum sensing in bacteria: the LuxR-LuxI family of cell density-responsive transcriptional regulators. J. Bacteriol. *176*, 269–275.

Gall, D.L., Kim, H., Lu, F., Donohue, T.J., Noguera, D.R., and Ralph, J. (2014). Stereochemical Features of Glutathione-dependent Enzymes in the Sphingobium sp. Strain SYK-6 β-Aryl Etherase Pathway. J. Biol. Chem. *289*, 8656–8667.

Garab, G., and van Amerongen, H. (2009). Linear dichroism and circular dichroism in photosynthesis research. Photosynth. Res. *101*, 135–146.

Gessard, C. (1882). Thèse pour le Doctorat en Médecine: De la pyocyanine et de son microbe. Colorations qui en dépendant dans les liquides organiques (pus et sérosités, sueur, liquides des culture).). Faculté de Médecine de Paris.

Giddens, S.R., Feng, Y., and Mahanty, H.K. (2002). Characterization of a novel phenazine antibiotic gene cluster in Erwinia herbicola Eh1087. Mol. Microbiol. *45*, 769–783.

Gohain, N., Thomashow, L.S., Mavrodi, D.V., and Blankenfeldt, W. (2006). The purification, crystallization and preliminary structural characterization of FAD-dependent monooxygenase PhzS, a phenazine-modifying enzyme from Pseudomonas aeruginosa. Acta Crystallograph. Sect. F Struct. Biol. Cryst. Commun. *62*, 989–992.

Greenhagen, B.T., Shi, K., Robinson, H., Gamage, S., Bera, A.K., Ladner, J.E., and Parsons, J.F. (2008). Crystal structure of the pyocyanin biosynthetic protein PhzS. Biochemistry (Mosc.) *47*, 5281–5289.

Grocholski, T., Koskiniemi, H., Lindqvist, Y., Mäntsälä, P., Niemi, J., and Schneider, G. (2010). Crystal Structure of the Cofactor-Independent Monooxygenase SnoaB from Streptomyces nogalater: Implications for the Reaction Mechanism. Biochemistry (Mosc.) *49*, 934–944.

Hasnaoui-Dijoux, G., Majerić Elenkov, M., Lutje Spelberg, J.H., Hauer, B., and Janssen, D.B. (2008). Catalytic Promiscuity of Halohydrin Dehalogenase and its Application in Enantioselective Epoxide Ring Opening. ChemBioChem *9*, 1048–1051.

Heisenberg, W. (1927). Über den anschaulichen Inhalt der quantentheoretischen Kinematik und Mechanik. Z. Für Phys. *43*, 172–198.

Helmich, K.E., Pereira, J.H., Gall, D.L., Heins, R.A., McAndrew, R.P., Bingman, C., Deng, K., Holland, K.C., Noguera, D.R., Simmons, B.A., et al. (2016). Structural Basis of Stereospecificity in the Bacterial Enzymatic Cleavage of β-Aryl Ether Bonds in Lignin. J. Biol. Chem. *291*, 5234–5246.

Hendriks, A.T.W.M., and Zeeman, G. (2009). Pretreatments to enhance the digestibility of lignocellulosic biomass. Bioresour. Technol. *100*, 10–18.

Hernandez, M.E., Kappler, A., and Newman, D.K. (2004). Phenazines and Other Redox-Active Antibiotics Promote Microbial Mineral Reduction. Appl. Environ. Microbiol. *70*, 921–928.

Hillemann, H. (1938). Beiträge zur Kenntnis des Phenazins, III. Mitteil.: Über die Stellung der Methylgruppe im Pyocyanin. und über Versuche zur Synthese von Isopyocyanin. Berichte Dtsch. Chem. Ges. B Ser. *71*, 46–52.

Ho Sui, S.J., Lo, R., Fernandes, A.R., Caulfield, M.D.G., Lerman, J.A., Xie, L., Bourne, P.E., Baillie, D.L., and Brinkman, F.S.L. (2012). Raloxifene attenuates Pseudomonas aeruginosa pyocyanin production and virulence. Int. J. Antimicrob. Agents *40*, 246–251.

Hofmeister, F. (1888). Zur Lehre von der Wirkung der Salze. Arch. Exp. Pathol. Pharmakol. *24*, 247–260.

Hood, R.D., Singh, P., Hsu, F., Güvener, T., Carl, M.A., Trinidad, R.R.S., Silverman, J.M., Ohlson, B.B., Hicks, K.G., Plemel, R.L., et al. (2010). A Type VI Secretion System of Pseudomonas aeruginosa Targets a Toxin to Bacteria. Cell Host Microbe *7*, 25–37.

Hor, L., Dobson, R.C.J., Downton, M.T., Wagner, J., Hutton, C.A., and Perugini, M.A. (2013). Dimerization of Bacterial Diaminopimelate Epimerase Is Essential for Catalysis. J. Biol. Chem. *288*, 9238–9248.

Houtman, J.C.D., Brown, P.H., Bowden, B., Yamaguchi, H., Appella, E., Samelson, L.E., and Schuck, P. (2007). Studying multisite binary and ternary protein interactions by global analysis of isothermal titration calorimetry data in SEDPHAT: Application to adaptor protein complexes in cell signaling. Protein Sci. *16*, 30–42.

https://en.wikipedia.org/wiki/Circular_polarization (2017). Circular polarization.

Hübner, K. (2006). 150 Jahre Mauvein. Chem. Unserer Zeit *40*, 274–275.

van Hylckama Vlieg, J.E.T., Tang, L., Spelberg, J.H.L., Smilda, T., Poelarends, G.J., Bosma, T., Merode, A.E.J. van, Fraaije, M.W., and Janssen, D.B. (2001). Halohydrin Dehalogenases Are Structurally and Mechanistically Related to Short-Chain Dehydrogenases/Reductases. J. Bacteriol. *183*, 5058–5066.

Ingledew, W.M., and Campbell, J.J. (1969). Evaluation of shikimic acid as a precursor of pyocyanine. Can. J. Microbiol. *15*, 535–541.

Janssen, D.B., Majerić-Elenkov, M., Hasnaoui, G., Hauer, B., and Spelberg, J.H.L. (2006). Enantioselective formation and ring-opening of epoxides catalysed by halohydrin dehalogenases. Biochem. Soc. Trans. *34*, 291–295.

Jerabek-Willemsen, M., Wienken, C.J., Braun, D., Baaske, P., and Duhr, S. (2011). Molecular Interaction Studies Using Microscale Thermophoresis. Assay Drug Dev. Technol. *9*, 342–353.

Jimenez, P.N., Koch, G., Thompson, J.A., Xavier, K.B., Cool, R.H., and Quax, W.J. (2012). The Multiple Signaling Systems Regulating Virulence in Pseudomonas aeruginosa. Microbiol. Mol. Biol. Rev. *76*, 46–65.

Jong, R.M. de, Tiesinga, J.J.W., Rozeboom, H.J., Kalk, K.H., Tang, L., Janssen, D.B., and Dijkstra, B.W. (2003). Structure and mechanism of a bacterial haloalcohol dehalogenase: a new variation of the short-chain dehydrogenase/reductase fold without an NAD(P)H binding site. EMBO J. *22*, 4933–4944.

Jong, R.M. de, Kalk, K.H., Tang, L., Janssen, D.B., and Dijkstra, B.W. (2006). The X-Ray Structure of the Haloalcohol Dehalogenase HheA from Arthrobacter sp. Strain AD2: Insight into Enantioselectivity and Halide Binding in the Haloalcohol Dehalogenase Family. J. Bacteriol. *188*, 4051–4056.

Kabsch, W. (2010). XDS. Acta Crystallogr. D Biol. Crystallogr. *66*, 125–132.

Kapitein, N., and Mogk, A. (2013). Deadly syringes: type VI secretion system activities in pathogenicity and interbacterial competition. Curr. Opin. Microbiol. *16*, 52–58.

Karplus, P.A., and Diederichs, K. (2012). Linking Crystallographic Model and Data Quality. Science *336*, 1030–1033.

Karsten, W.E., Lai, C.-J., and Cook, P.F. (1995). Inverse Solvent Isotope Effects in the NAD-Malic Enzyme Reaction Are the Result of the Viscosity Difference between D2O and H2O: Implications for Solvent Isotope Effect Studies. J. Am. Chem. Soc. *117*, 5914–5918.

Kavanagh, K.L., Jörnvall, H., Persson, B., and Oppermann, U. (2008). Medium- and short-chain dehydrogenase/reductase gene and protein families. Cell. Mol. Life Sci. *65*, 3895–3906.

Keller, S., Vargas, C., Zhao, H., Piszczek, G., Brautigam, C.A., and Schuck, P. (2012). High-Precision Isothermal Titration Calorimetry with Automated Peak-Shape Analysis. Anal. Chem. *84*, 5066–5073.

Kibbe, W.A. (2007). OligoCalc: an online oligonucleotide properties calculator. Nucleic Acids Res. *35*, W43–W46.

Klein, T., Henn, C., de Jong, J.C., Zimmer, C., Kirsch, B., Maurer, C.K., Pistorius, D., Müller, R., Steinbach, A., and Hartmann, R.W. (2012). Identification of Small-Molecule Antagonists of the Pseudomonas aeruginosa Transcriptional Regulator PqsR: Biophysically Guided Hit Discovery and Optimization. ACS Chem. Biol. *7*, 1496–1501.

Kohen, A., and Klinman, J.P. (1999). Hydrogen tunneling in biology. Chem. Biol. *6*, R191–R198.

Kunz, W., Henle, J., and Ninham, B.W. (2004). "Zur Lehre von der Wirkung der Salze" (about the science of the effect of salts): Franz Hofmeister's historical papers. Curr. Opin. Colloid Interface Sci. *9*, 19–37.

Langer, G., Cohen, S.X., Lamzin, V.S., and Perrakis, A. (2008). Automated macromolecular model building for X-ray crystallography using ARP/wARP version 7. Nat. Protoc. *3*, 1171–1179.

Lau, G.W., Hassett, D.J., Ran, H., and Kong, F. (2004). The role of pyocyanin in Pseudomonas aeruginosa infection. Trends Mol. Med. *10*, 599–606.

Laursen, J.B., and Nielsen, J. (2004). Phenazine Natural Products: Biosynthesis, Synthetic Analogues, and Biological Activity. Chem. Rev. *104*, 1663–1686.

Lee, J., and Zhang, L. (2015). The hierarchy quorum sensing network in Pseudomonas aeruginosa. Protein Cell *6*, 26–41.

Leiman, P.G., Basler, M., Ramagopal, U.A., Bonanno, J.B., Sauder, J.M., Pukatzki, S., Burley, S.K., Almo, S.C., and Mekalanos, J.J. (2009). Type VI secretion apparatus and phage tail-associated protein complexes share a common evolutionary origin. Proc. Natl. Acad. Sci. *106*, 4154–4159.

Li, Q.-A., Mavrodi, D.V., Thomashow, L.S., Roessle, M., and Blankenfeldt, W. (2011). Ligand Binding Induces an Ammonia Channel in 2-Amino-2-desoxyisochorismate (ADIC) Synthase PhzE. J. Biol. Chem. *286*, 18213–18221.

Lloyd, A.J., Huyton, T., Turkenburg, J., and Roper, D.I. (2004). Refinement of Haemophilus influenzae diaminopimelic acid epimerase (DapF) at 1.75 A resolution suggests a mechanism for stereocontrol during catalysis. Acta Crystallogr. D Biol. Crystallogr. *60*, 397–400.

Longley, R.P., Halliwell, J.E., Campbell, J.J.R., and Ingledew, W.M. (1972). The branchpoint of pyocyanine biosynthesis. Can. J. Microbiol. *18*, 1357–1363.

Masai, E., Ichimura, A., Sato, Y., Miyauchi, K., Katayama, Y., and Fukuda, M. (2003). Roles of the Enantioselective Glutathione S-Transferases in Cleavage of β-Aryl Ether. J. Bacteriol. *185*, 1768–1775.

Mavrodi, D.V., Ksenzenko, V.N., Bonsall, R.F., Cook, R.J., Boronin, A.M., and Thomashow, L.S. (1998). A Seven-Gene Locus for Synthesis of Phenazine-1-Carboxylic Acid by Pseudomonas fluorescens 2-79. J. Bacteriol. *180*, 2541–2548.

Mavrodi, D.V., Bleimling, N., Thomashow, L.S., and Blankenfeldt, W. (2003). The purification, crystallization and preliminary structural characterization of PhzF, a key enzyme in the phenazine-biosynthesis pathway from Pseudomonas fluorescens 2-79. Acta Crystallogr. D Biol. Crystallogr. *60*, 184–186.

McCoy, A.J., Grosse-Kunstleve, R.W., Adams, P.D., Winn, M.D., Storoni, L.C., and Read, R.J. (2007). Phaser crystallographic software. J. Appl. Crystallogr. *40*, 658–674.

McDonald, M., Mavrodi, D.V., Thomashow, L.S., and Floss, H.G. (2001). Phenazine biosynthesis in Pseudomonas fluorescens: branchpoint from the primary shikimate biosynthetic pathway and role of phenazine-1,6-dicarboxylic acid. J. Am. Chem. Soc. *123*, 9459–9460.

Melander, L., and Saunders, W.H. (1987). Reaction Rates of Isotopic Molecules. R.E. Krieger, Boca Raton, Florida.

Mentel, M. (2008). Walking Nature's Pathways Tool Compounds for Chemical Biology. Dissertation. Universität Leipzig.

Mentel, M., Blankenfeldt, W., and Breinbauer, R. (2009a). The Active Site of an Enzyme Can Host Both Enantiomers of a Racemic Ligand Simultaneously. Angew. Chem. Int. Ed. *48*, 9084–9087.

Mentel, M., Ahuja, E.G., Mavrodi, D.V., Breinbauer, R., Thomashow, L.S., and Blankenfeldt, W. (2009b). Of Two Make One: The Biosynthesis of Phenazines. ChemBioChem *10*, 2295–2304.

Meux, E., Prosper, P., Masai, E., Mulliert, G., Dumarçay, S., Morel, M., Didierjean, C., Gelhaye, E., and Favier, F. (2012). Sphingobium sp. SYK-6 LigG involved in lignin degradation is structurally and biochemically related to the glutathione transferase omega class. FEBS Lett. *586*, 3944–3950.

Moriarty, N.W., Grosse-Kunstleve, R.W., and Adams, P.D. (2009). electronic Ligand Builder and Optimization Workbench (eLBOW): a tool for ligand coordinate and restraint generation. Acta Crystallogr. D Biol. Crystallogr. *65*, 1074–1080.

Nerbl, Y. (2012). Das Dimerisierungsverhalten von PhzA und PhzB aus Pseudomonas fluorescens 2-79. Master (M.Sc.) Thesis. Universität Bayreuth.

Oliveira, S.H., Ferraz, F.A., Honorato, R.V., Xavier-Neto, J., Sobreira, T.J., and de Oliveira, P.S. (2014). KVFinder: steered identification of protein cavities as a PyMOL plugin. BMC Bioinformatics *15*, 197.

Pandey, M.P., and Kim, C.S. (2011). Lignin Depolymerization and Conversion: A Review of Thermochemical Methods. Chem. Eng. Technol. *34*, 29–41.

Papenfort, K., and Bassler, B.L. (2016). Quorum sensing signal-response systems in Gram-negative bacteria. Nat. Rev. Microbiol. *14*, 576–588.

Parsons, J.F., Calabrese, K., Eisenstein, E., and Ladner, J.E. (2003). Structure and Mechanism of Pseudomonas aeruginosa PhzD, an Isochorismatase from the Phenazine Biosynthetic Pathway. Biochemistry (Mosc.) *42*, 5684–5693.

Parsons, J.F., Song, F., Parsons, L., Calabrese, K., Eisenstein, E., and Ladner, J.E. (2004a). Structure and Function of the Phenazine Biosynthesis Protein PhzF from Pseudomonas fluorescens 2-79. Biochemistry (Mosc.) *43*, 12427–12435.

Parsons, J.F., Calabrese, K., Eisenstein, E., and Ladner, J.E. (2004b). Structure of the phenazine biosynthesis enzyme PhzG. Acta Crystallogr. D Biol. Crystallogr. *60*, 2110–2113.

Pei, J., and Grishin, N.V. (2007). PROMALS: towards accurate multiple sequence alignments of distantly related proteins. Bioinformatics *23*, 802–808.

Picart, P., Domínguez de María, P., and Schallmey, A. (2015). From gene to biorefinery: microbial β-etherases as promising biocatalysts for lignin valorization. Front. Microbiol. *6*.

Pierson, L.S., and Pierson, E.A. (1996). Phenazine antibiotic production in Pseudomonas aureofaciens: role in rhizosphere ecology and pathogen suppression. FEMS Microbiol. Lett. *136*, 101–108.

Pierson, L.S., and Pierson, E.A. (2010). Metabolism and function of phenazines in bacteria: impacts on the behavior of bacteria in the environment and biotechnological processes. Appl. Microbiol. Biotechnol. *86*, 1659–1670.

Pierson, L.S., and Thomashow, L.S. (1992). Cloning and heterologous expression of the phenazine biosynthetic locus from Pseudomonas aureofaciens 30-84. Mol. Plant-Microbe Interact. MPMI *5*, 330–339.

Pierson, L.S., Keppenne, V.D., and Wood, D.W. (1994). Phenazine antibiotic biosynthesis in Pseudomonas aureofaciens 30-84 is regulated by PhzR in response to cell density. J. Bacteriol. *176*, 3966–3974.

Porfetye, A. (2009). Strukturuntersuchung an PhzB, einem Phenazinbiosyntheseenzym aus Pseudomonas fluorescens 2-79. Master (M.Sc.) Thesis. Technische Universität Dortmund.

Price-Whelan, A., Dietrich, L.E.P., and Newman, D.K. (2007). Pyocyanin Alters Redox Homeostasis and Carbon Flux through Central Metabolic Pathways in Pseudomonas aeruginosa PA14. J. Bacteriol. *189*, 6372–6381.

Pukatzki, S., Ma, A.T., Revel, A.T., Sturtevant, D., and Mekalanos, J.J. (2007). Type VI secretion system translocates a phage tail spike-like protein into target cells where it cross-links actin. Proc. Natl. Acad. Sci. *104*, 15508–15513.

Rada, B., and Leto, T.L. (2013). Pyocyanin effects on respiratory epithelium: relevance in Pseudomonas aeruginosa airway infections. Trends Microbiol. *21*, 73–81.

Rupp, B. (2009). Biomolecular Crystallography: Principles, Practice, and Application to Structural Biology (New York: Garland Science).

Russell, A.B., Hood, R.D., Bui, N.K., LeRoux, M., Vollmer, W., and Mougous, J.D. (2011). Type VI secretion delivers bacteriolytic effectors to target cells. Nature *475*, 343–347.

Sakhtah, H., Koyama, L., Zhang, Y., Morales, D.K., Fields, B.L., Price-Whelan, A., Hogan, D.A., Shepard, K., and Dietrich, L.E.P. (2016). The Pseudomonas aeruginosa efflux pump MexGHI-OpmD transports a natural phenazine that controls gene expression and biofilm development. Proc. Natl. Acad. Sci. *113*, E3538–E3547.

Schallmey, A., and Schallmey, M. (2016). Recent advances on halohydrin dehalogenases—from enzyme identification to novel biocatalytic applications. Appl. Microbiol. Biotechnol. *100*, 7827–7839.

Schallmey, M., Koopmeiners, J., Wells, E., Wardenga, R., and Schallmey, A. (2014). Expanding the Halohydrin Dehalogenase Enzyme Family: Identification of Novel Enzymes by Database Mining. Appl. Environ. Microbiol. *80*, 7303–7315.

Schallmey, M., Jekel, P., Tang, L., Majerić Elenkov, M., Höffken, H.W., Hauer, B., and Janssen, D.B. (2015). A single point mutation enhances hydroxynitrile synthesis by halohydrin dehalogenase. Enzyme Microb. Technol. *70*, 50–57.

Scheuermann, T.H., and Brautigam, C.A. (2015). High-precision, automated integration of multiple isothermal titration calorimetric thermograms: New features of NITPIC. Methods *76*, 87–98.

Scheuring, J., and Schramm, V.L. (1997). Kinetic Isotope Effect Characterization of the Transition State for Oxidized Nicotinamide Adenine Dinucleotide Hydrolysis by Pertussis Toxin. Biochemistry (Mosc.) *36*, 4526–4534.

Schomaker, V., and Trueblood, K.N. (1968). On the rigid-body motion of molecules in crystals. Acta Crystallogr. B *24*, 63–76.

Shang, G., Liu, X., Lu, D., Zhang, J., Li, N., Zhu, C., Liu, S., Yu, Q., Zhao, Y., Zhang, H., et al. (2012). Structural insight into how Pseudomonas aeruginosa peptidoglycanhydrolase Tse1 and its immunity protein Tsi1 function. Biochem. J. *448*, 201–211.

Sheldrick, G.M. (2010). Experimental phasing with *SHELXC* / *D* / *E* : combining chain tracing with density modification. Acta Crystallogr. D Biol. Crystallogr. *66*, 479–485.

Terwilliger, T.C., Adams, P.D., Read, R.J., McCoy, A.J., Moriarty, N.W., Grosse-Kunstleve, R.W., Afonine, P.V., Zwart, P.H., and Hung, L.-W. (2009). Decision-making in structure solution using Bayesian estimates of map quality: the PHENIX AutoSol wizard. Acta Crystallogr. D Biol. Crystallogr. *65*, 582–601.

Toohey, J.I., Nelson, C.D., and Krotkov, G. (1965). Toxicity of Phenazine Carboxylic Acids to Some Bacteria, Algae, Higher Plants, and Animals. Can. J. Bot. *43*, 1151–1155.

Turner, J.M., and Messenger, A.J. (1986). Occurrence, biochemistry and physiology of phenazine pigment production. Adv. Microb. Physiol. *27*, 211–275.

Watanabe, F., Yu, F., Ohtaki, A., Yamanaka, Y., Noguchi, K., Yohda, M., and Odaka, M. (2015). Crystal structures of halohydrin hydrogen-halide-lyases from Corynebacterium sp. N-1074. Proteins Struct. Funct. Bioinforma. *83*, 2230–2239.

Weikart, N. (2006). Untersuchungen zur Heterodimerisierung von PhzA und PhzB aus Pseudomonas fluorescens 2-79. Bachelor (B.Sc.) Thesis. Technische Universität Dortmund.

Weiss, M.S. (2001). Global indicators of X-ray data quality. J. Appl. Crystallogr. *34*, 130–135.

Whitmore, L., and Wallace, B.A. (2008). Protein secondary structure analyses from circular dichroism spectroscopy: Methods and reference databases. Biopolymers *89*, 392–400.

Whitney, J.C., Beck, C.M., Goo, Y.A., Russell, A.B., Harding, B.N., De Leon, J.A., Cunningham, D.A., Tran, B.Q., Low, D.A., Goodlett, D.R., et al. (2014). Genetically distinct pathways guide effector export through the type VI secretion system. Mol. Microbiol. *92*, 529–542.

Wienken, C.J., Baaske, P., Rothbauer, U., Braun, D., and Duhr, S. (2010). Protein-binding assays in biological liquids using microscale thermophoresis. Nat. Commun. *1*, 100.

Wigner, E.P. (1932). Z. Für Phys. Chem. *B19*, 203.

Winn, M.D., Ballard, C.C., Cowtan, K.D., Dodson, E.J., Emsley, P., Evans, P.R., Keegan, R.M., Krissinel, E.B., Leslie, A.G.W., McCoy, A., et al. (2011). Overview of the CCP4 suite and current developments. Acta Crystallogr. D Biol. Crystallogr. *67*, 235–242.

Wood, D.W., Gong, F., Daykin, M.M., Williams, P., and Pierson, L.S. (1997). N-acyl-homoserine lactone-mediated regulation of phenazine gene expression by Pseudomonas aureofaciens 30-84 in the wheat rhizosphere. J. Bacteriol. *179*, 7663–7670.

Wrede, F., and Strack, E. (1924). Über das Pyocyanin, den blauen Farbstoff des Bacillus pyocyaneus. II. Hoppe Seylers Z Physiol Chem 103–119.

Xu, N., Ahuja, E.G., Janning, P., Mavrodi, D.V., Thomashow, L.S., and Blankenfeldt, W. (2013). Trapped intermediates in crystals of the FMN-dependent oxidase PhzG provide insight into the final steps of phenazine biosynthesis. Acta Crystallogr. D Biol. Crystallogr. *69*, 1403–1413.

You, Z.-Y., Liu, Z.-Q., and Zheng, Y.-G. (2013). Properties and biotechnological applications of halohydrin dehalogenases: current state and future perspectives. Appl. Microbiol. Biotechnol. *97*, 9–21.

Yu, S., Vit, A., Devenish, S., Mahanty, H.K., Itzen, A., Goody, R.S., and Blankenfeldt, W. (2011). Atomic resolution structure of EhpR: phenazine resistance in Enterobacter agglomerans Eh1087 follows principles of bleomycin/mitomycin C resistance in other bacteria. BMC Struct. Biol. *11*, 33.

Zakzeski, J., Bruijnincx, P.C.A., Jongerius, A.L., and Weckhuysen, B.M. (2010). The Catalytic Valorization of Lignin for the Production of Renewable Chemicals. Chem. Rev. *110*, 3552–3599.

Zhao, H. (2016). Protein stabilization and enzyme activation in ionic liquids: specific ion effects. J. Chem. Technol. Biotechnol. *91*, 25–50.

Zhao, H., Piszczek, G., and Schuck, P. (2015). SEDPHAT – A platform for global ITC analysis and global multi-method analysis of molecular interactions. Methods *76*, 137–148.

Appendices

A1. Additional results for PhzF

A1.1. Additional figures

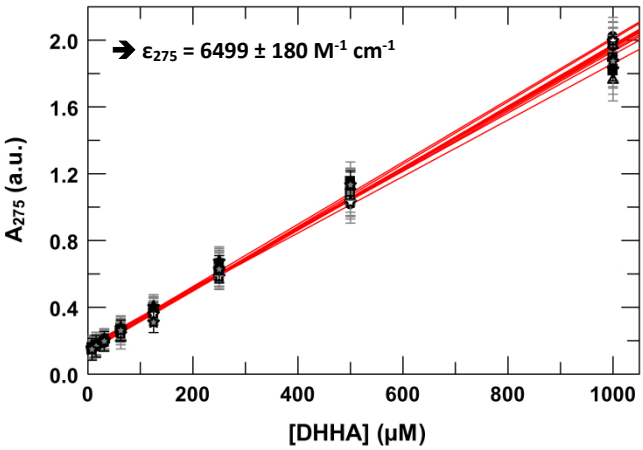

Figure A1: Standard curve for determination of the extinction coefficient of DHHA in aqueous buffer at 275 nm.
Serial dilutions of 1 mM of the two substrate isotopologues DHHA and d-DHHA in both, standard assay and crystallization buffer were prepared and the absorption at 275 nm of each dilution measured in an Infinite® M200 microplate reader (Tecan Group Ltd.) using a five point readout per well. The plotted absorption values are average data from every readout with the corresponding error. Each of the four dilution series was measured in triplicates and individually fitted by linear regression using GraFit 5. The slopes from each regression curve were averaged and yielded an extinction coefficient of 6499 ± 180 M^{-1} cm^{-1}.

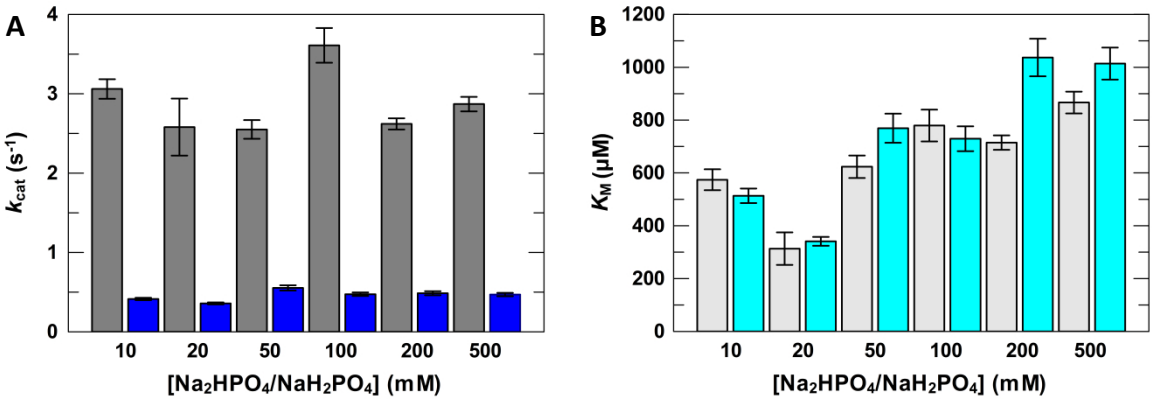

Figure A2: PhzF-catalyzed DHHA/d-DHHA isomerization in dependency of increasing concentrations of sodium phosphate.
A The turnover number k_{cat} (■ = DHHA, ■ = d-DHHA) and **B** the Michaelis-constant K_M (□ = DHHA, □ = d-DHHA) were plotted against different sodium phosphate concentrations ranging from 10 to 500 mM. The plotted values were derived by fitting normalized, background corrected, and averaged data of three independent measurements to a Michaelis-Menten model using GraFit 5. All data were obtained at 25 °C.

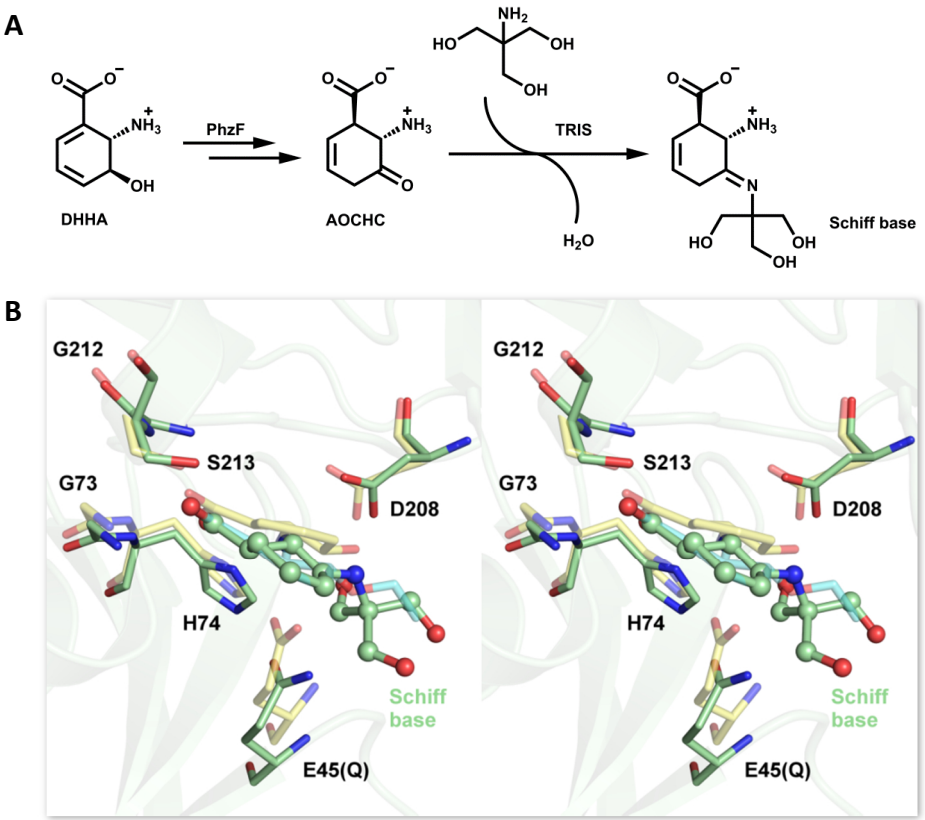

Figure A3: Schiff base formation - a potential spontaneous side reaction that the highly reactive amino ketone AOCHC, as product of DHHA isomerization, could undergo in TRIS buffer.
A PhzF catalyzed DHHA isomerization leads to formation of AOCHC. This amino ketone can react with the primary amine of TRIS and after water elimination an imine derivative, a so-called Schiff base, is formed. **B** Stereoscopic view of the potential binding mode of the Schiff base, synthesized from AOCHC and TRIS, to the active site of PhzF (*P. fl* 2-79). The molecule was modelled in an open structure of PhzF E45Q in complex with *O*-ethylated DHHA (PDB entry 5IWE, this study) and superimposed with the active complex PhzF/DHHA (PDB entry 1U1X, Blankenfeldt *et al*., 2004). The active site residues of the model as well as the ligand are shown in palegreen, while the original ligand *O*-Et-DHHA is shown in aquamarine. The active site residues and ligand of the DHHA complex are shown in palegoldenrod. The Schiff base is shown as balls and sticks, all other residues only as stick representation.

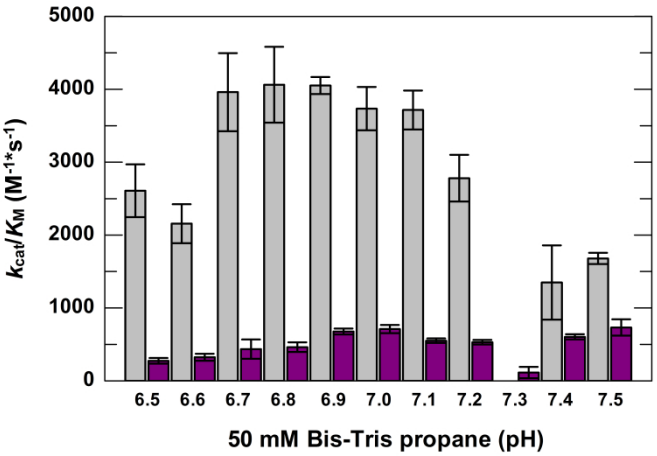

Figure A4: pH-dependency of PhzF-catalyzed DHHA/d-DHHA isomerization in 50 mM Bis-TRIS propane buffer.
The overall catalytic efficiency k_{cat}/K_M (= DHHA, = d-DHHA) is plotted against different pH-values ranging from pH 6.5 to 7.5 in steps of 0.1 pH-units. The plotted values were derived by fitting normalized, background corrected, and averaged data of three independent measurements to a Michaelis-Menten model using GraFit 5. All data were obtained at 25 °C.

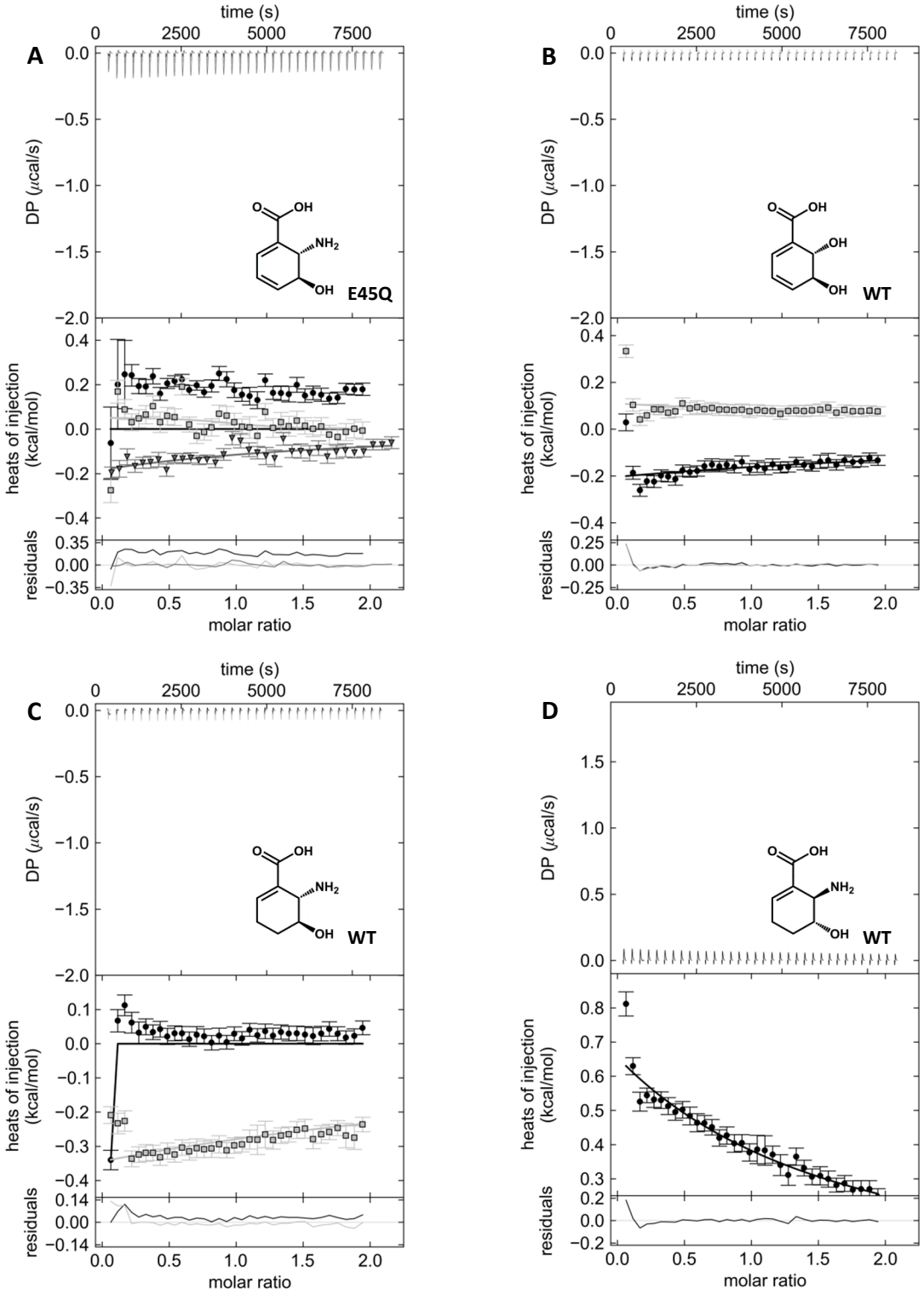

Figure A5: ITC profiles for affinity titrations of different PhzF substrates, substrate analogs, and inhibitors against wild type PhzF or variant E45Q.

The individual plots show the generated heat per injection at different time points (upper panel), the fitted binding curves for individual titration experiments (middle panel), and the quality of the fit (lower panel). **A** shows profiles for individual titrations of 450 µM (● and □) or 1 mM (▽) DHHA to 50 or 100 µM PhzF E45Q respectively. The three other plots show titrations of 450 µM of either DHHS (**B**: ● and □), H_2-DHHA (**C**: ● and □), and *ent*-H_2-DHHA (**D**: ●) to 50 µM PhzF WT. No binding event could be observed for any of the titrated compounds. All data were analyzed and fitted using the programs NITPIC (Keller *et al.*, 2012) and SEDPHAT (Houtman *et al.*, 2007; Zhao *et al.*, 2015) and plotted using the program GUSSI (Brautigam, 2015).

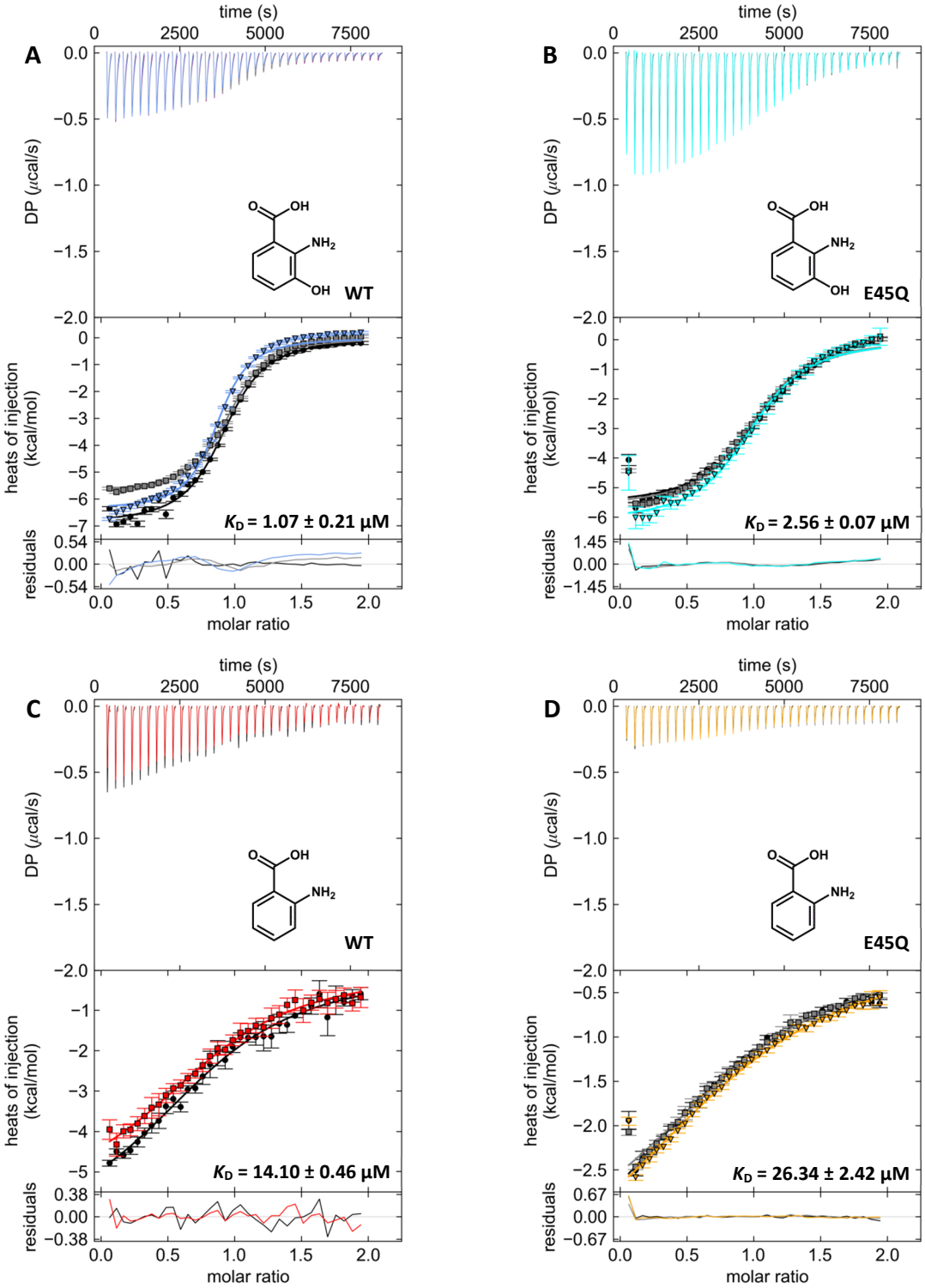

Figure A6: ITC profiles for affinity titrations of 3OHAA and AA against wild type PhzF and variant E45Q.
The individual plots show the generated heat per injection at different time points (upper panel), the fitted binding curves for individual titration experiments (middle panel), and the quality of the fit (lower panel). Upper profiles: Titration of 450 µM 3OHAA to **A** 50 µM wild type PhzF (●, ■, and ▼ for individual experiments) and **B** variant E45Q (●, ■, and ▼). Binding of 3OHAA to PhzF WT and E45Q was exothermic, with 1:1 stoichiometry and occurred with K_D values of 1.07 ± 0.21 µM and 2.56 ± 0.07 µM respectively. Lower profiles: Titration of 450 µM AA to **C** 50 µM wild type PhzF (● and ■) and **D** variant E45Q (●, ■, and ▼). Binding of AA to PhzF WT and E45Q was exothermic, with 1:1 stoichiometry and occurred with K_D values of 14.10 ± 0.46 µM and 26.34 ± 2.42 µM respectively. All data were analyzed and fitted using the programs NITPIC (Keller *et al.*, 2012; Scheuermann and Brautigam, 2015) and SEDPHAT (Houtman *et al.*, 2007; Zhao *et al.*, 2015) and plotted using the program GUSSI (Brautigam, 2015).

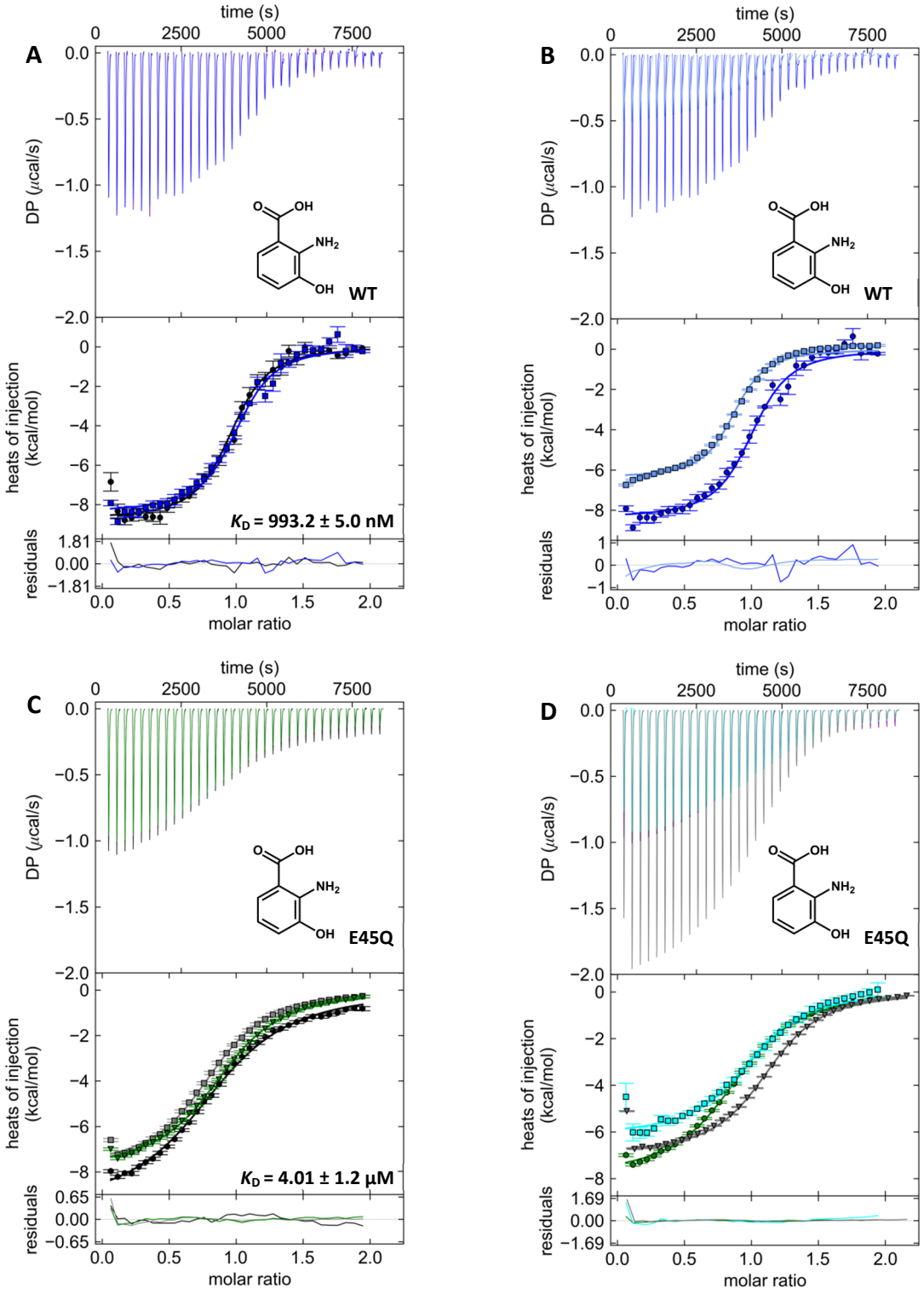

Figure A7: ITC profiles for affinity titrations of 3OHAA against wild type PhzF and variant E45Q.
The individual plots show the generated heat per injection at different time points (upper panel), the fitted binding curves for individual titration experiments (middle panel), and the quality of the fit (lower panel). **A** and **C** show profiles for titrations of 450 µM 3OHAA to PhzF WT (**A**: ● and ■ for individual experiments) or E45Q (**C**: ●, ■, and ▼). Binding is exothermic, with 1:1 stoichiometry and affinities of 993.2 ± 5.0 nM (WT) and 4.0 ± 1.2 µM (E45Q). **B** and **D**: Comparison of binding curves from different subsets of titration experiments showing reproducibility of the binding event. **B** 450 µM 3OHAA to 50 µM PhzF WT (● and ■ for a single experiment of each subset), **D** 450 µM (●, ■) or 1 mM 3OHAA (▼) to 50 µM or 100 µM PhzF E45Q respectively. All data were analyzed and fitted using the programs NITPIC (Keller *et al.*, 2012) and SEDPHAT (Houtman *et al.*, 2007; Zhao *et al.*, 2015) and plotted using the program GUSSI (Brautigam, 2015).

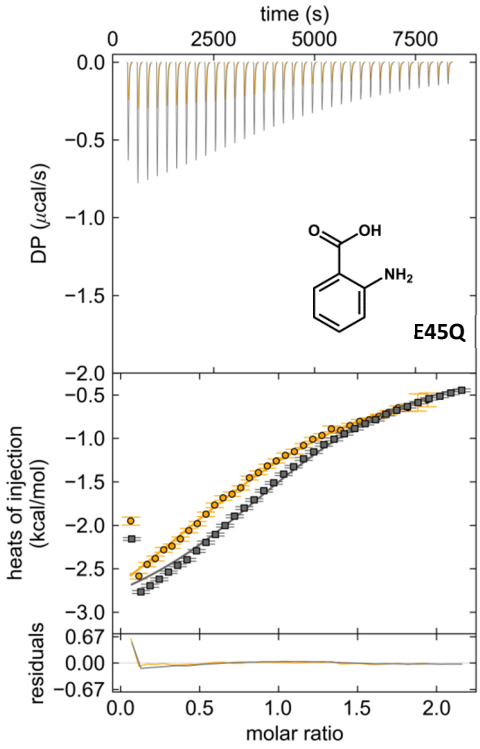

Figure A8: ITC profile for affinity titrations of AA against PhzF variant E45Q.
The individual plots show the generated heat per injection at different time points (upper panel), the fitted binding curves for individual titration experiments (middle panel), and the quality of the fit (lower panel). Comparison of binding curves from different titration experiments of 450 µM (○, single subset) and 1 mM (■) AA to 50 µM or 100 µM PhzF E45Q respectively, showing reproducibility of the binding event. The data were analyzed and fitted using the programs NITPIC (Keller *et al.*, 2012) and SEDPHAT (Houtman *et al.*, 2007; Zhao *et al.*, 2015) and plotted using the program GUSSI (Brautigam, 2015).

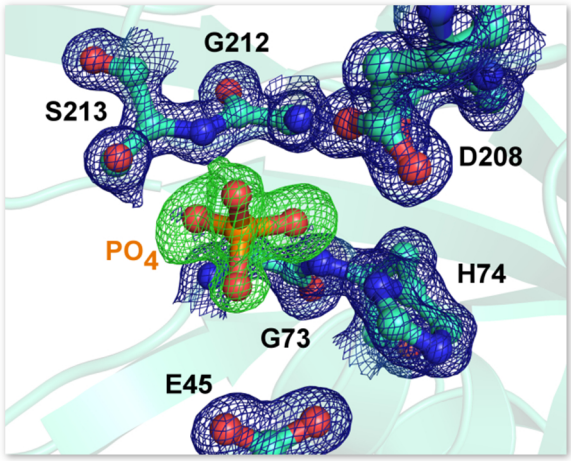

Figure A9: Active site of PhzF (*P. fl* 2-79) at near atomic resolution of 1.18 Å.
Close-up on the active site of wild type PhzF in its open conformation with the active site residues shown as balls and sticks in their $2mF_o$-DF_c density map, contoured at 1σ. The protein was crystallized in presence of H_2-DHHA, however the displayed Fourier difference density (mF_o-DF_c) omit map contoured at 3σ cannot unambiguously be attributed to the co-crystallized ligand. Instead, residual **phosphate** from the purification buffer was built.

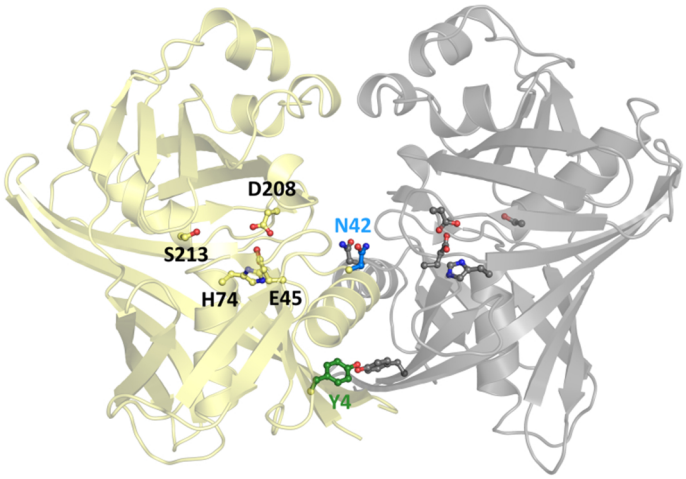

Figure A10: Amino acids at the dimer interface as targets for mutagenesis to probe the influence of dimerization on PhzF activity.

Cartoon representation of a PhzF dimer in paleyellow (chain A) and gray (chain B). The active site residues E45, H74, D208 and S213 as well as the dimer interface residues Y4 and N42 are shown as balls and sticks. In chain A, the active site residues are depicted in paleyellow, while Y4 and N42 are highlighted in **green** and **blue** respectively. Their counterparts in chain B are shown in gray. Y4 and N42 mediate important hydrogen-bonding interactions with the corresponding amino acid of the second chain. Exchange of these interface residues with a smaller amino acid, *e.g.* alanine, is supposed to impede dimerization and thus potentially influence catalytic activity. N42 is particularly interesting as it is located in close proximity to the active site cleft of PhzF.

A1.2. Additional tables

Table A1: Enzyme kinetic parameters for the conversion of the heavy substrate isotopologue d-DHHA by PhzF (*P. fl* 2-79) in presence of increasing sodium phosphate concentrations.*

sodium phosphate pH 7.5	k_{cat} (s^{-1})	K_M (µM)	k_{cat}/K_M ($M^{-1}s^{-1}$)
10 mM	0.41 ± 0.01	513 ± 27	804 ± 52
20 mM	0.36 ± 0.01	341 ± 17	1050 ± 63
50 mM	0.55 ± 0.03	769 ± 55	720± 67
100 mM	0.47 ± 0.02	729 ± 47	650± 52
200 mM	0.49 ± 0.03	1037 ± 71	469 ± 41
500 mM	0.47 ± 0.02	1014 ± 60	462 ± 35

* The obtained values are averaged data of three independent measurements fitted to a Michaelis-Menten model. All data were obtained in the respective buffer at 25 °C, normalized to zero, and background corrected.

Table A2: Primary kinetic isotope effects (KIE) for the DHHA isomerization catalyzed by PhzF (*P. fl* 2-79) in dependency of increasing sodium phosphate concentrations.*

sodium phosphate pH 7.5	KIE_{app} (k_{cat})	KIE_{app} (k_{cat}/K_M)
10 mM	7.4 ± 0.4	6.6 ± 0.7
20 mM	7.2 ± 1.0	7.9 ± 1.9
50 mM	4.6 ± 0.3	5.7 ± 0.7
100 mM	7.6 ± 0.6	7.1 ± 0.9
200 mM	5.4 ± 0.3	7.8 ± 0.8
500 mM	6.1 ± 0.3	7.2 ± 0.7

* The obtained values are averaged data of three independent measurements fitted to a Michaelis-Menten model. All data were obtained in the respective buffer at 25 °C, normalized to zero, and background corrected.

Table A3: Enzyme kinetic parameters for the conversion of light (DHHA) and heavy substrate isotopologue (d-DHHA) by PhzF (*P. fl* 2-79) in 50 mM sodium phosphate buffer at different pH-values.*

50 mM sodium phosphate		k_{cat} (s^{-1})	K_M (µM)	k_{cat}/K_M ($M^{-1}s^{-1}$)	KIE_{app} (k_{cat})	KIE_{app} (k_{cat}/K_M)
pH 6.5	DHHA	1.06 ± 0.09	442 ± 115	2402 ± 658	-	-
	d-DHHA	-	-	-		
pH 6.75	DHHA	4.88 ± 0.89	2800 ± 640	1743 ± 510	5.7 ± 1.2	9.8 ± 3.4
	d-DHHA	0.86 ± 0.10	4839 ± 660	178 ± 32		
pH 7.0	DHHA	5.00 ± 0.20	1411 ± 75	3539 ± 237	8.1 ± 0.5	6.9 ± 0.8
	d-DHHA	0.62 ± 0.03	1203 ± 94	512 ± 46		
pH 7.25	DHHA	4.80 ± 0.78	1379 ± 248	3485 ± 845	13.3 ± 2.2	4.5 ± 1.1
	d-DHHA	0.36 ± 0.01	461 ± 19	780 ± 40		
pH 7.5	DHHA	2.83 ± 0.30	532 ± 68	5329 ± 888	6.3 ± 0.8	11.2 ± 2.1
	d-DHHA	0.45 ± 0.03	945 ± 63	475 ± 43		
pH 7.75	DHHA	3.42 ± 0.37	632 ± 83	5407 ± 918	7.4 ± 0.9	4.9 ± 1.0
	d-DHHA	0.46 ± 0.03	419 ± 34	1095 ± 113		
pH 8.0	DHHA	3.13 ± 0.42	893 ± 159	3506 ± 784	5.7 ± 1.0	3.4 ± 1.0
	d-DHHA	0.55 ± 0.07	536 ± 79	1023 ± 196		

* The obtained values are averaged data of three independent measurements fitted to a Michaelis-Menten model. All data were obtained in the respective buffer at 25 °C, normalized to zero, and background corrected.

Table A4: Enzyme kinetic parameters for the conversion of light (DHHA) and heavy substrate isotopologue (d-DHHA) by PhzF (*P. fl* 2-79) in 50 mM Bis-TRIS propane buffer at different pH-values.*

50 mM Bis-TRIS propane		k_{cat} (s^{-1})	K_M (µM)	k_{cat}/K_M ($M^{-1}s^{-1}$)	KIE_{app} (k_{cat})	KIE_{app} (k_{cat}/K_M)
pH 6.5	DHHA	2.11 ± 0.17	810 ± 93	2608 ± 363	5.6 ± 0.7	9.5 ± 1.9
	d-DHHA	0.38 ± 0.03	1382 ± 157	274 ± 39		
pH 6.6	DHHA	2.41 ± 0.17	1117 ± 113	2156 ± 267	7.0 ± 0.7	6.7 ± 1.3
	d-DHHA	0.34 ± 0.03	1059 ± 136	324 ± 48		
pH 6.7	DHHA	2.82 ± 0.21	713 ± 81	3961 ± 535	3.9 ± 0.9	9.1 ± 3.0
	d-DHHA	0.72 ± 0.15	1659 ± 366	435 ± 132		
pH 6.8	DHHA	2.85 ± 0.19	701 ± 76	4062 ± 521	7.5 ± 0.8	8.8 ± 1.7
	d-DHHA	0.38 ± 0.03	821 ± 92	462 ± 66		
pH 6.9	DHHA	2.26 ± 0.03	558 ± 15	4052 ± 117	7.1 ± 0.2	6.0 ± 0.4
	d-DHHA	0.32 ± 0.01	471 ± 24	677 ± 41		
pH 7.0	DHHA	2.41 ± 0.09	646 ± 46	3735 ± 297	7.6 ± 0.4	5.3 ± 0.6
	d-DHHA	0.32 ± 0.01	448 ± 31	710 ± 56		
pH 7.1	DHHA	2.45 ± 0.11	659 ± 36	3716 ± 267	8.4 ± 0.5	6.8 ± 0.6
	d-DHHA	0.29 ± 0.01	531 ± 24	550 ± 31		
pH 7.2	DHHA	1.68 ± 0.07	603 ± 65	2780 ± 320	5.2 ± 0.3	5.2 ± 0.7
	d-DHHA	0.32 ± 0.01	605 ± 30	530 ± 32		
pH 7.3	DHHA	-	-	-	-	-
	d-DHHA	0.26 ± 0.11	2235 ± 1160	114 ± 78		
pH 7.4	DHHA	3.57 ± 0.92	2647 ± 731	1349 ± 510	12.0 ± 3.1	2.2 ± 0.9
	d-DHHA	0.30 ± 0.01	494 ± 23	603 ± 36		
pH 7.5	DHHA	3.07 ± 0.09	1826 ± 66	1679 ± 77	9.2 ± 1.0	2.3 ± 0.4
	d-DHHA	0.33 ± 0.03	453 ± 53	732 ± 112		

* The obtained values are averaged data of three independent measurements fitted to a Michaelis-Menten model. All data were obtained in the respective buffer at 25 °C, normalized to zero, and background corrected.

Table A5: Data collection and preliminary refinement statistics for a wild type PhzF (*P. fl* 2-79) dataset at near atomic resolution.‡

	putative complex with H_2-DHHA[1]
Data collection[2]	
Beamline†	X06DA (PXIII), SLS
Wavelength (Å)	1.00002
Resolution range (Å)	77.97 – 1.18 (1.20 – 1. 18)
Space group	$P3_221$
unit cell dimensions	
a, b, c (Å)	56.29, 56.29, 155.95
α, β, γ (°)	90, 90, 120
Mosaicity (°)‡	0.10
Measured reflections	1791273 (71681)
Unique reflections	95255 (4676)
Multiplicity	18.8 (15.3)
Mean *I*/σ*(I)*	27.2 (2.0)
$CC_{1/2}$*	1.000 (0.621)
Completeness (%)	100.0 (99.9)
R_{meas}§	6.0 (157.5)
$R_{p.i.m.}$¶	1.4 (39.9)
Refinement[3]	
Resolution range (Å)	51.98 – 1.18 (1.19 – 1.18)
R_{cryst} (%)	12.50 (23.48)
R_{free} (%)	14.44 (23.52)
No. of non H-atoms	
Protein	2194
Ligand / Ion	5
Water	273
Average B-factors (Å²)	
Protein	16.4
Ligand / Ion	20.4
Water	30.9
R.m.s deviations	
Bond lengths (Å)	0.009
Bond angles (°)	1.071
Ramachandran plot (%)	
Favored regions	98.2
Outliers	0
MolProbity score #	0.87

‡Values in parentheses are for the highest resolution shell. -

[1] Careful inspection of the electron density map in the active site did not convincingly support the presence of the ligand, but rather suggests that a phosphate ion from the purification buffer is bound to the active site.

[2] The dataset was collected from a single crystal.

† SLS: Swiss Light Source, Paul Scherrer Institute (PSI), Villigen, Switzerland.

‡ Mosaicity values reported by *XDS* (Kabsch, 2010).

* $CC_{1/2}$ is the correlation coefficient between two random half datasets (Karplus and Diederichs, 2012)

§ $R_{meas} = \sum_{hkl}\{N(hkl)/[N(hkl)-1]\}^{1/2}\sum_i|I_i(hkl) - \langle I(hkl)\rangle| \,/\, \sum_{hkl}\sum_i I_i\,(hkl)$, where *N(hkl* is the number of observations of the reflection with index *hkl* and $I_i(hkl)$ is the intensity of its *i*th observation (Diederichs and Karplus, 1997);

¶ $R_{p.i.m.} = \sum_{hkl}\{1/[N(hkl)-1]\}^{1/2}\sum_i|I_i(hkl) - \langle I(hkl)\rangle|/\sum_{hkl}\sum_i I_i(hkl)$ (Weiss, 2001)

[3] Refinement was not conducted until final convergence.

As reported by *MolProbity* (http://molprobity.biochem.duke.edu/ (Chen *et al.*, 2010)

A2. Additional results for the PhzAB heterodimerization

A2.1. Additional figures

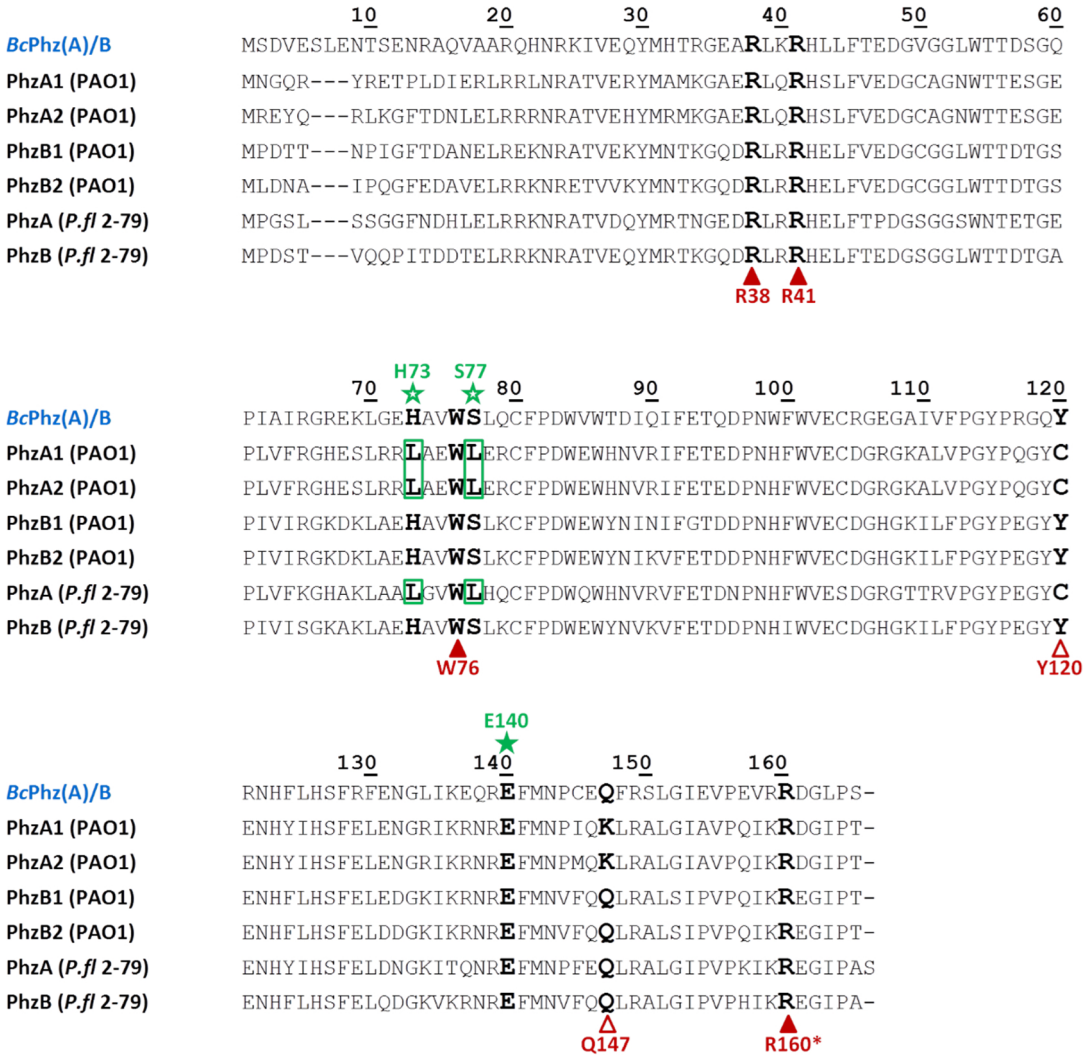

Figure A11: Sequence alignment of PhzB para- and orthologues from different phenazine producing species. Using the enzyme from *Burkholderia cepacia* R18194 (*Bc*Phz(A)/B) as reference, the orthologous proteins PhzA and PhzB from two *Pseudomonas spp.*, *P. fluorescens* 2-79 (*P. fl* 2-79) and *P. aeruginosa* PAO1 (PhzA/B1 and PhzA/B2) were compared regarding their sequence identity. Residues important for ligand binding (▲) or catalysis (★) are highlighted. Filled symbols represent strict conservation, whilst empty symbols indicate single amino acid mutations, which impede activity and/or binding. The alignment was generated using PROMALS3d (Pei and Grishin, 2007).

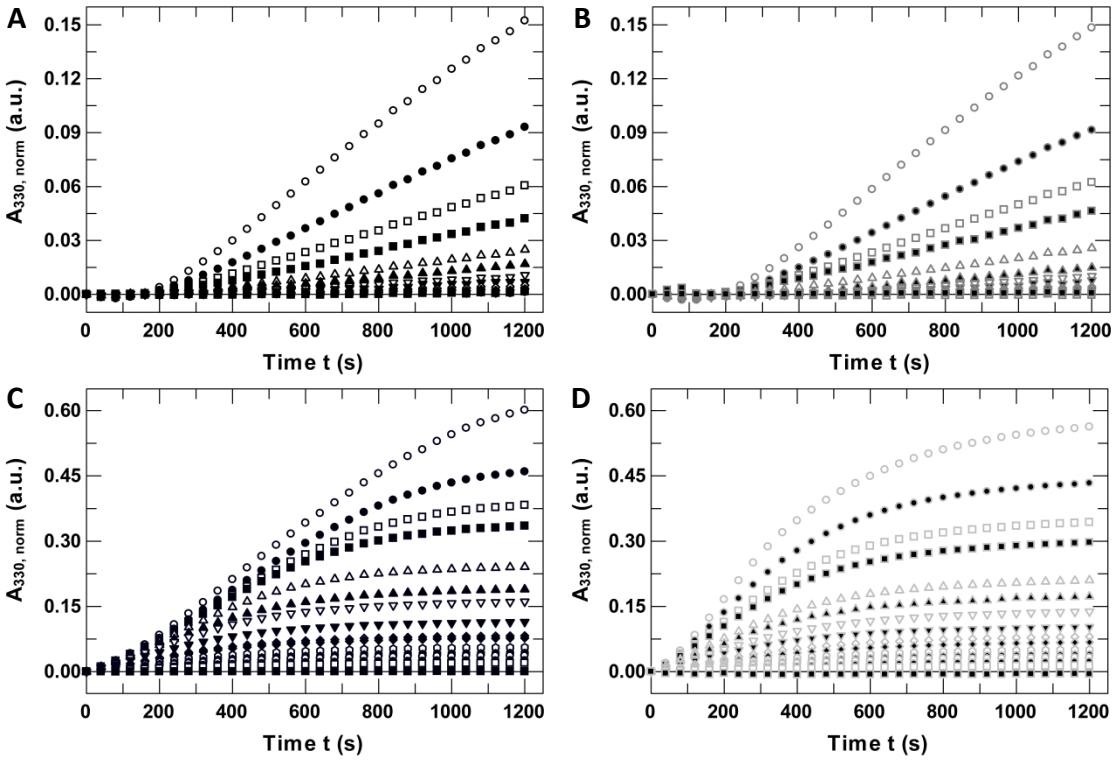

Figure A12: Time traces of the PhzB catalyzed condensation of AOCHC.
The time traces of **A** the uncatalyzed reaction and **B**-**D** the reaction using 1 µM of the respective dimer (**B**: PhzAA; **C**: *Bc*Phz(A)/B and **D**: PhzBB) in presence of 1 µM PhzF dimer as coupled enzyme are shown at different substrate concentrations ranging from ■ = 0 mM to ○ = 1 mM DHHA. Formation of a downstream product of the condensation was followed at 330 nm. All data were obtained in 50 mM sodium phosphate buffer at 25 °C and normalized to zero.

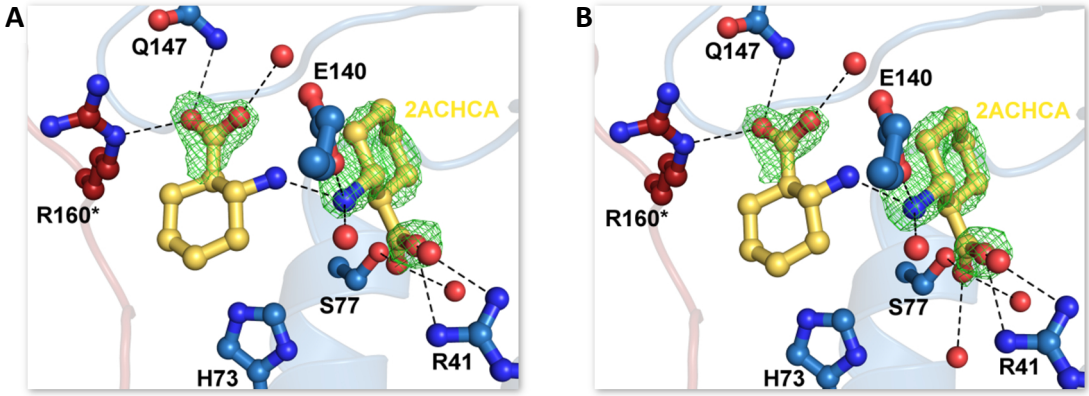

Figure A13: Crystal structures of *Bc*Phz(A)/B in complex with 2ACHCA after soaking with different concentrations.
Close-ups on the active site (chain B) of two different *Bc*Phz(A)/B complex structures each with two molecules of the substrate analog 2ACHCA bound to the active site. The complex structures of *Bc*Phz(A)/B and the analog were obtained after soaking with **A** 5 mM or **B** 50 mM of the ligand overnight. The ligands as well as the coordinating active site residues are shown as ball and stick representation (* indicates that this residue is belonging to the second protein chain). The ligands are additionally depicted in their Fourier difference density (mF_o-DF_c) omit map contoured at 3σ in green. Hydrogen bonds (- - -) and coordinating water (red balls) are highlighted as well.

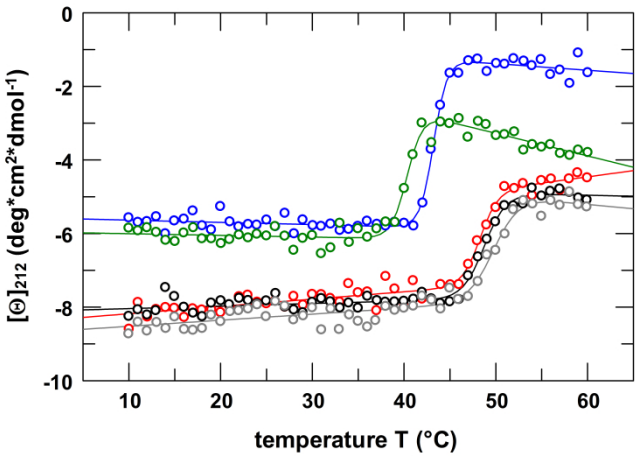

Figure A14: Temperature dependent unfolding transitions of different PhzB para- and orthologues.
The melting curves of *Bc*Phz(A)/B (O), HeteroPhzAB with (O) and without N-terminal hexahistidine-tag (O), PhzBB (O) as well as PhzAA (O) were recorded within a temperature range from 10 to 60 °C using the CD signal at 212 nm and converted to mean residue ellipticity $[\Theta]_{MRW}$.

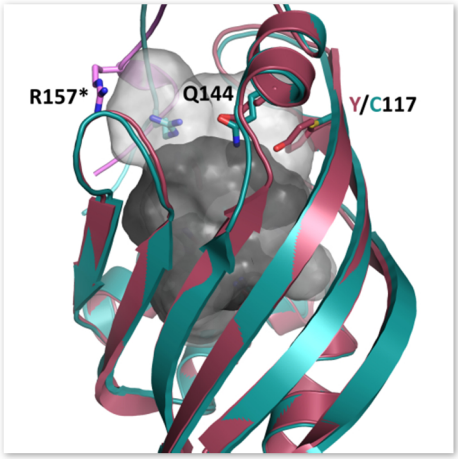

Figure A15: Comparison of the "active site" pockets of HeteroPhzAB.
Overlay of the two chains (**PhzA** and **PhzB**) of the PhzAB heterodimer. The volumes of their active site/binding cavities were calculated using the program KVFinder (Oliveira *et al*., 2014), which yielded volumes of 765 Å³ and 500 Å³ for PhzA (light gray) and PhzB (dark gray) respectively. The extension of the pocket in the A-monomer is caused by mutation of tyrosine 117 (PhzB) to cysteine, a residue bearing a smaller side chain. Furthermore, the displacement of the C-terminus of the second monomer that - via arm-exchange - provides a residue (R157*) to the binding pocket leads to an opening of the pocket.

A2.2. Additional tables

Table A6: Overview of the refined occupancy and temperature factors for the crystal structures of *Bc*Phz(A)/B in complex with different concentrations of two substrate analogs, 3OCHCA and 2ACHCA*

3OCHCA		**chain A high**	**chain A low**	**chain B high**	**chain B low**
50 mM	occupancy	1.00	0.99	1.00	1.00
	average B-factor (Å²)	22.8	46.2	23.7	37.1
20 mM	occupancy	1.00	0.89	1.00	0.99
	average B-factor (Å²)	25.7	52.7	25.5	40.3
10 mM	occupancy	0.92	0.89	1.00	0.96
	average B-factor (Å²)	29.4	58.2	28.0	46.6
5 mM	occupancy	0.93	0.94	0.94	0.89
	average B-factor (Å²)	32.1	58.9	30.9	47.9
2ACHCA					
50 mM	occupancy	0.85	0.67	0.84	0.66
	average B-factor (Å²)	21.7	48.2	25.9	40.5
20 mM	occupancy	0.92	0.86	1.00	0.76
	average B-factor (Å²)	20.2	49.7	27.0	39.0
10 mM	occupancy	1.00	0.67	1.00	0.72
	average B-factor (Å²)	24.4	82.6	33.8	63.6
5 mM	occupancy	0.94	0.71	0.90	0.80
	average B-factor (Å²)	29.5	64.0	29.5	56.4

*Data refinement was carried out using phenix.refine (Afonine *et al.*, 2012) of the PHENIX software suite (Adams *et al.*, 2010). The occupancy was analyzed in coot (Emsley *et al.*, 2010) and the temperature factors calculated with the program BAVERGAE implemented in the CCP4 suite (Winn *et al.*, 2011).

Table A7: Data collection and refinement statistics for complex structures of *Bc*Phz(A)/B co-crystallized with different concentrations of the substrate analogue 3OCHCA. [‡]

	Complex with 50mM 3OCHCA	Complex with 20mM 3OCHCA	Complex with 10mM 3OCHCA	Complex with 5mM 3OCHCA
Data collection[1]				
Beamline[†]	PXIII (X06DA), SLS	PXIII (X06DA), SLS	PXIII (X06DA), SLS	PXIII (X06DA), SLS
Wavelength (Å)	1.00003	1.00003	1.00003	1.00003
Resolution range (Å)	80.69 – 1.65 (1.68 – 1.65)	80.71 – 1.73 (1.76 – 1.73)	80.52 – 1.65 (1.68 – 1.65)	80.44 – 1.53 (1.56 – 1.53)
Space group	$P3_221$	$P3_221$	$P3_221$	$P3_221$
unit cell dimensions				
a, b, c (Å)	64.71, 64.71, 161.37	64.78, 64.78, 161.43	64.61, 64.61, 161.04	64.52, 64.52, 160.88
α, β, γ (°)	90, 90, 120	90, 90, 120	90, 90, 120	90, 90, 120
Mosaicity (°)[‡]	0.08	0.21	0.15	0.09
Measured reflections	315251 (14068)	321202 (17259)	523486 (26212)	653405 (30545)
Unique reflections	48087 (2320)	41959 (2260)	47866 (2304)	59581 (2890)
Multiplicity	6.6 (6.1)	7.7 (7.6)	10.9 (11.4)	11.0 (10.6)
Mean $I/\sigma(I)$	21.0 (2.0)	20.1 (2.0)	23.0 (2.2)	27.3 (2.1)
$CC_{1/2}$*	0.999 (0.643)	0.999 (0.713)	1.000 (0.700)	1.000 (0.656)
Completeness (%)	100.0 (100.0)	100.0 (100.0)	100.0 (100.0)	100.0 (100.0)
R_{meas}[§]	7.3 (101.0)	9.0 (109.8)	8.8 (129.1)	6.2 (130.6)
$R_{p.i.m.}$[¶]	2.8 (40.7)	3.2 (39.5)	2.6 (38.1)	1.9 (39.8)
Refinement				
Resolution range (Å)	53.79 – 1.65 (1.67 – 1.65)	56.10 – 1.73 (1-75 – 1.73)	55.96 – 1.65 (1.67 – 1.65)	55.88 – 1.53 (1.55 – 1.53)
R_{cryst} (%)	15.87 (28.81)	15.80 (27.63)	15.69 (26.48)	15.40 (28.57)
R_{free} (%)	18.26 (33.47)	18.31 (33.08)	17.95 (29.01)	17.18 (34.02)
No. of non H-atoms				
Protein	2636	2656	2654	2674
Ligand / Ion	51	58	58	58
Water	334	342	353	366
Average B-factors (Å²)				
Protein	24.2	24.4	24.6	25.8
Ligand / Ion	35.0	37.2	40.2	42.0
Water	39.9	39.7	41.3	42.9
R.m.s deviations				
Bond lengths (Å)	0.007	0.005	0.005	0.008
Bond angles (°)	0.878	0.738	0.772	0.916
Ramachandran plot (%)				
Favored regions	98.8	98.8	98.8	98.8
Outliers	0	0	0	0
MolProbity score [#]	0.93	0.95	1.05	1.08

[†]Values in parentheses are for the highest resolution shell. [1] All data sets were collected from a single crystal. [†] Swiss light source (SLS) at the Paul Scherrer Institute (PSI), Villigen, Switzerland. [‡] Mosaicity values reported by *XDS* (Kabsch, 2010). * $CC_{1/2}$ is the correlation coefficient between two random half data sets (Karplus and Diederichs, 2012). [§] $R_{meas} = \sum_{hkl}\{N(hkl)/[N(hkl)-1]\}^{1/2}\sum_i|I_i(hkl) - \langle I(hkl)\rangle| / \sum_{hkl}\sum_i I_i(hkl)$, where *N(hkl* is the number of observations of the reflection with index *hkl* and $I_i(hkl)$ is the intensity of its *i*th observation (Diederichs and Karplus, 1997). [¶] $R_{p.i.m.} = \sum_{hkl}\{1/[N(hkl)-1]\}^{1/2}\sum_i|I_i(hkl) - \langle I(hkl)\rangle|/\sum_{hkl}\sum_i I_i(hkl)$ (Weiss, 2001); [#] As reported by *MolProbity* (http://molprobity.biochem.duke.edu/ (Chen *et al.*, 2010).

Table A8: Data collection and refinement statistics for complex structures of *Bc*Phz(A)/B co-crystallized with different concentrations of the substrate analogue 2ACHCA.[‡]

	Complex with 50mM 2ACHCA	Complex with 20mM 2ACHCA	Complex with 10mM 2ACHCA	Complex with 5mM 2ACHCA
Data collection[1]				
Beamline[†]	PXIII (X06DA), SLS	PXIII (X06DA), SLS	PXIII (X06DA), SLS	PXIII (X06DA), SLS
Wavelength (Å)	1.00003	1.00003	1.00003	1.00003
Resolution range (Å)	80.36 – 1.76 (1.79 – 1.76)	80.44 – 1.56 (1.59 – 1.56)	80.22 – 1.66 (1.69 – 1.66)	80.62 – 1.72 (1.75 – 1.72)
Space group	$P3_221$	$P3_221$	$P3_221$	$P3_221$
unit cell dimensions				
a, b, c (Å)	64.57, 64.57, 160.72	64.51, 64.51, 160.89	64.42, 64.42, 160.44	64.80, 64.80, 161.24
α, β, γ (°)	90, 90, 120	90, 90, 120	90, 90, 120	90, 90, 120
Mosaicity (°)[‡]	0.26	0.14	0.21	0.21
Measured reflections	401025 (21104)	432138 (29645)	441882 (21027)	490933 (25691)
Unique reflections	39484 (2238)	40463 (2750)	46861 (2269)	42683 (2278)
Multiplicity	10.2 (9.4)	10.7 (10.8)	9.4 (9.3)	11.5 (11.3)
Mean $I/\sigma(I)$	15.3 (2.0)	36.7 (2.1)	20.4 (2.0)	21.0 (2.0)
$CC_{1/2}$*	0.998 (0.687)	1.000 (0.701)	0.999 (0.678)	0.999 (0.710)
Completeness (%)	100.0 (100.0)	71.7 (99.9)[ᵖ]	100.0 (100.0)	100.0 (100.0)
R_{meas}[§]	15.0 (135.8)	5.4 (124.7)	8.2 (124.2)	10.2 (133.6)
$R_{p.i.m.}$[¶]	4.6 (43.4)	1.6 (37.2)	2.6 (40.4)	3.0 (39.3)
Refinement				
Resolution range (Å)	55.92– 1.76 (1.78 – 1.76)	55.87 – 1.56 (1.58 – 1.56)	55.97 – 1.66 (1.68 - 1.66)	56.12 – 1.72 (1.74 – 1.72)
R_{cryst} (%)	17.58 (27.65)	15.97 (26.10)	15.64 (28.21)	15.47 (27.17)
R_{free} (%)	20.14 (26.70)	19.06 (28.88)	19.09 (33.89)	18.17 (30.48)
No. of non H-atoms				
Protein	2627	2634	2635	2654
Ligand / Ion	51	55	55	55
Water	359	290	354	334
Average B-factors (Å²)				
Protein	22.4	24.7	28.3	25.7
Ligand / Ion	33.6	33.3	48.9	43.2
Water	37.1	38.6	41.6	39.9
R.m.s deviations				
Bond lengths (Å)	0.003	0.009	0.017	0.009
Bond angles (°)	0624	1.000	1.356	0.942
Ramachandran plot (%)				
Favored regions	98.7	98.7	99.0	98.7
Outliers	0	0	0	0
MolProbity score [#]	1.10	1.26	1.26	1.06

[‡]Values in parentheses are for the highest resolution shell. [1] All data sets were collected from a single crystal. [†] Swiss light source (SLS) at the Paul Scherrer Institute (PSI), Villigen, Switzerland. [‡] Mosaicity values reported by *XDS* (Kabsch, 2010). * $CC_{1/2}$ is the correlation coefficient between two random half data sets (Karplus and Diederichs, 2012). [ᵖ] The diffraction data suffer from the presence of ice-tings, especially at low resolution; therefore the overall completeness of the data is very low. [§] $R_{meas} = \sum_{hkl}\{N(hkl)/[N(hkl)-1]\}^{1/2}\sum_i|I_i(hkl) - \langle I(hkl)\rangle| \,/\, \sum_{hkl}\sum_i I_i\,(hkl)$, where *N(hkl* is the number of observations of the reflection with index *hkl* and $I_i(hkl)$ is the intensity of its *i*th observation (Diederichs and Karplus, 1997). [¶] $R_{p.i.m.} = \sum_{hkl}\{1/[N(hkl)-1]\}^{1/2}\sum_i|I_i(hkl) - \langle I(hkl)\rangle|/\sum_{hkl}\sum_i I_i(hkl)$ (Weiss, 2001); [#] As reported by *MolProbity* (http://molprobity.biochem.duke.edu/ (Chen *et al.*, 2010).

A3. Additional results for PhzB-inhibitors

A3.1. Additional figures and schemes

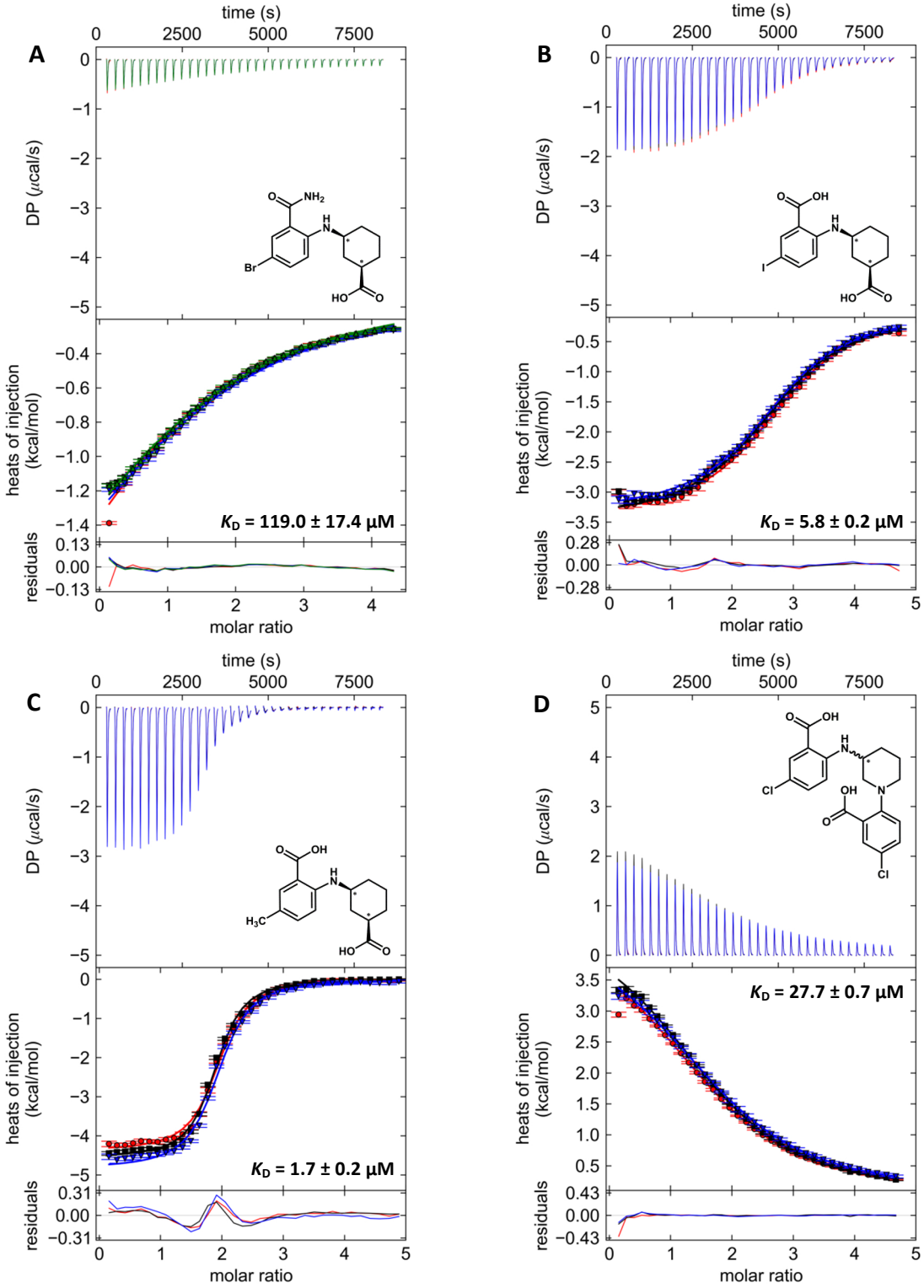

Figure A16: ITC profiles for affinity titrations of WB003 (A), WB012 (B), WB013 (C), and WB014 (D) against *Bc*Phz(A)/B. For a detailed description of these plots please refer to the legend of Figure A17.

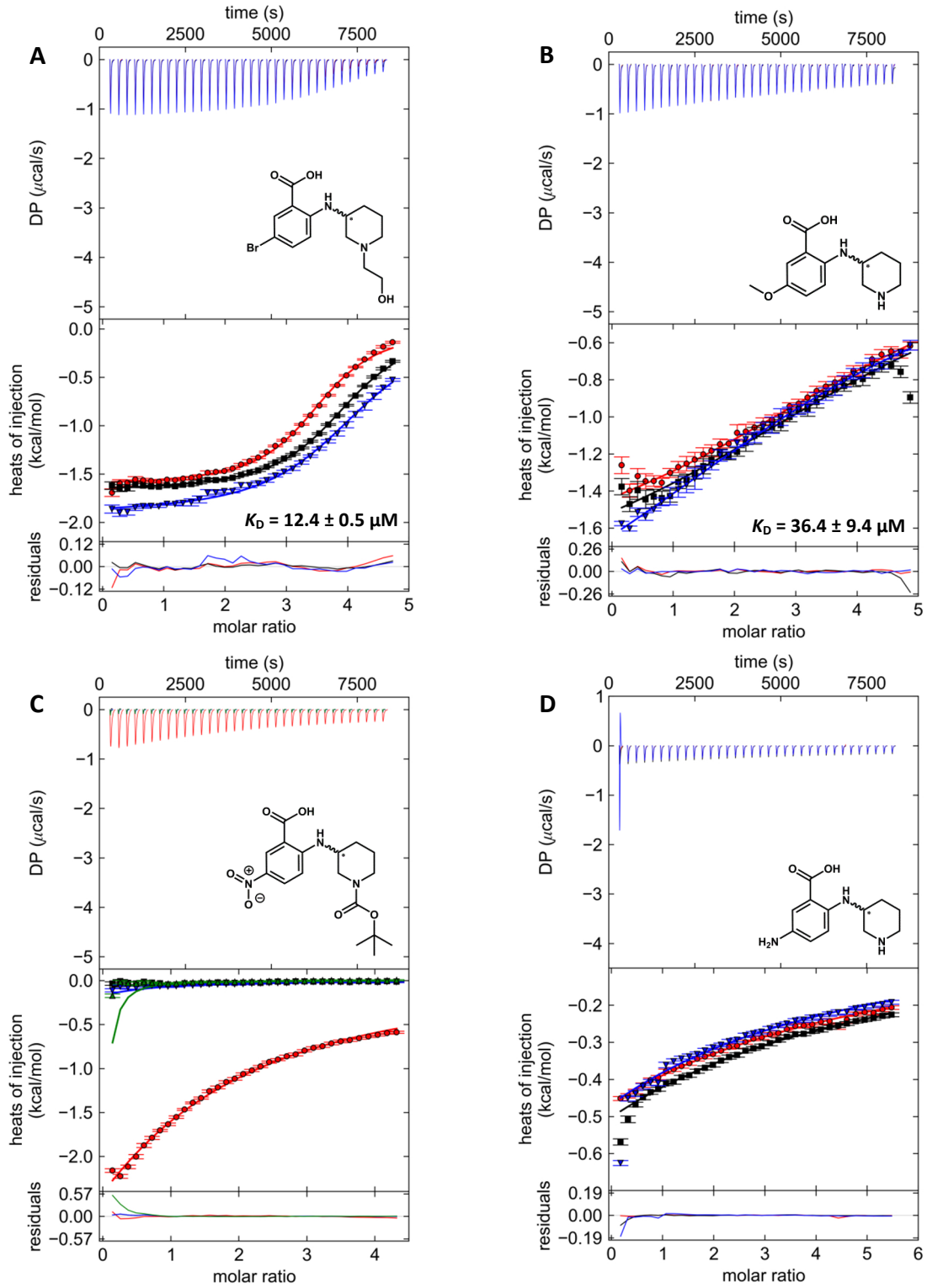

Figure A17: ITC profiles for affinity titrations of WB015 (A), WB018 (B), WB019 (C), and WB020 (D) against *Bc*Phz(A)/B. The individual plots show the generated heat per injection at different time points (upper panel), the fitted binding curves for individual titration experiments (middle panel), and the quality of the fit (lower panel). All profiles represent titrations of 2 mM of the respective analog to 100 µM *Bc*Phz(A)/B. Binding is exothermic for all titrated ligands in Figure **A16** and Figure A17 except for WB014 in Figure A16**D**, which exhibits an endothermic binding curve. The corresponding binding affinities are depicted in the plots unless fitting of the data failed, *e.g.* Figure A17**C** and **D**. The symbols ●, ■ and ▼ (and ▲) represent individual experiments All data were analyzed and fitted using the programs NITPIC (Keller *et al.*, 2012; Scheuermann and Brautigam, 2015) and SEDPHAT (Houtman *et al.*, 2007; Zhao *et al.*, 2015) and plotted using the program GUSSI (Brautigam, 2015).

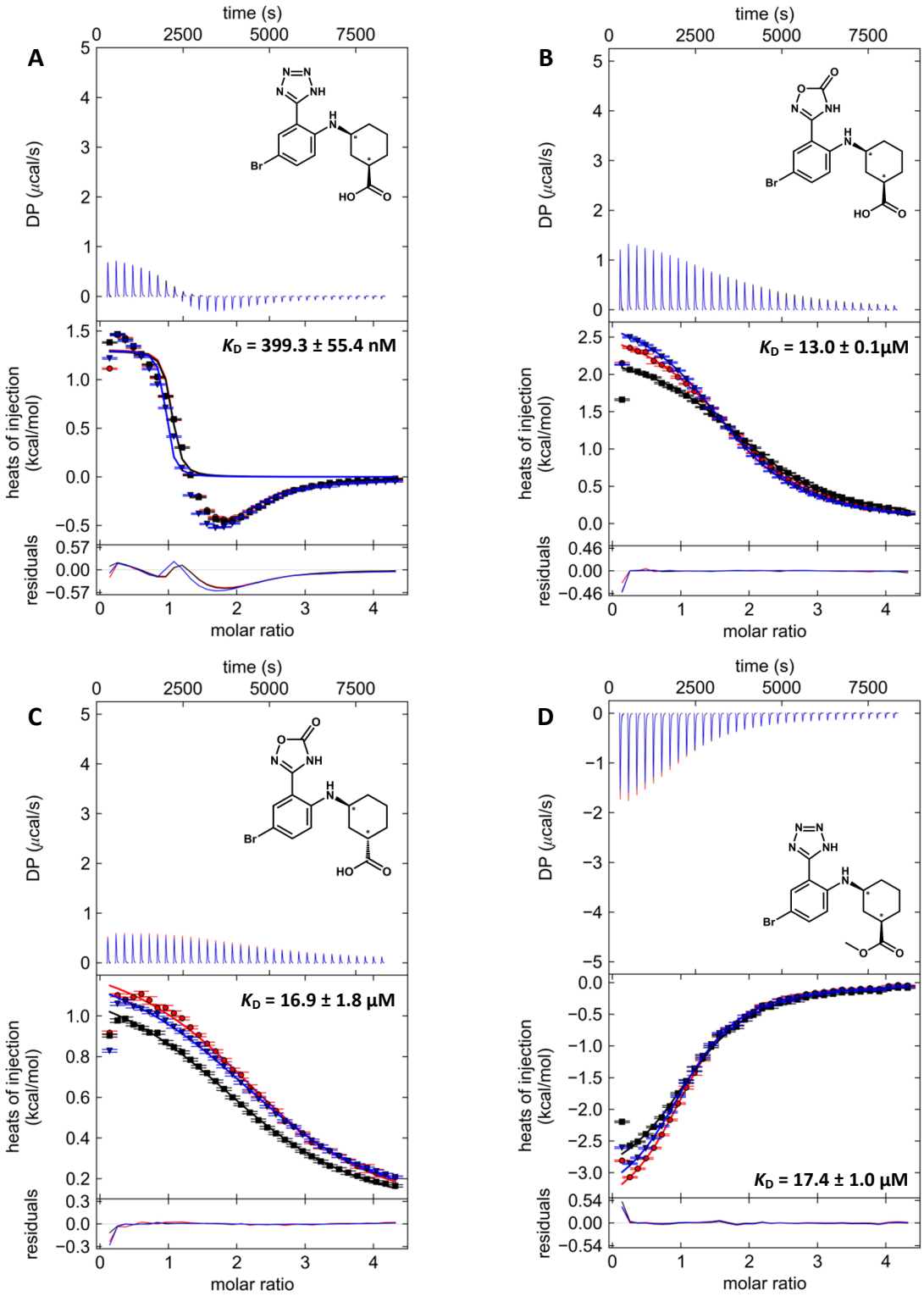

Figure A18: ITC profiles for affinity titrations of WB025 (A), WB027 (B), WB026 (C), and WB028 (D) against *Bc*Phz(A)/B. The individual plots show the generated heat per injection at different time points (upper panel), the fitted binding curves for individual titration experiments (middle panel), and the quality of the fit (lower panel). All profiles represent titrations of 2 mM of the respective analog to 100 µM *Bc*Phz(A)/B. Binding is endothermic for all titrated ligands except for WB028 (**D**), which exhibits an exothermic binding curve. The corresponding binding affinities are depicted in the plots. The symbols ●, ■, and ▼ represent individual experiments All data were analyzed and fitted using the programs NITPIC (Keller *et al*., 2012; Scheuermann and Brautigam, 2015) and SEDPHAT (Houtman *et al*., 2007; Zhao *et al*., 2015) and plotted using the program GUSSI (Brautigam, 2015).

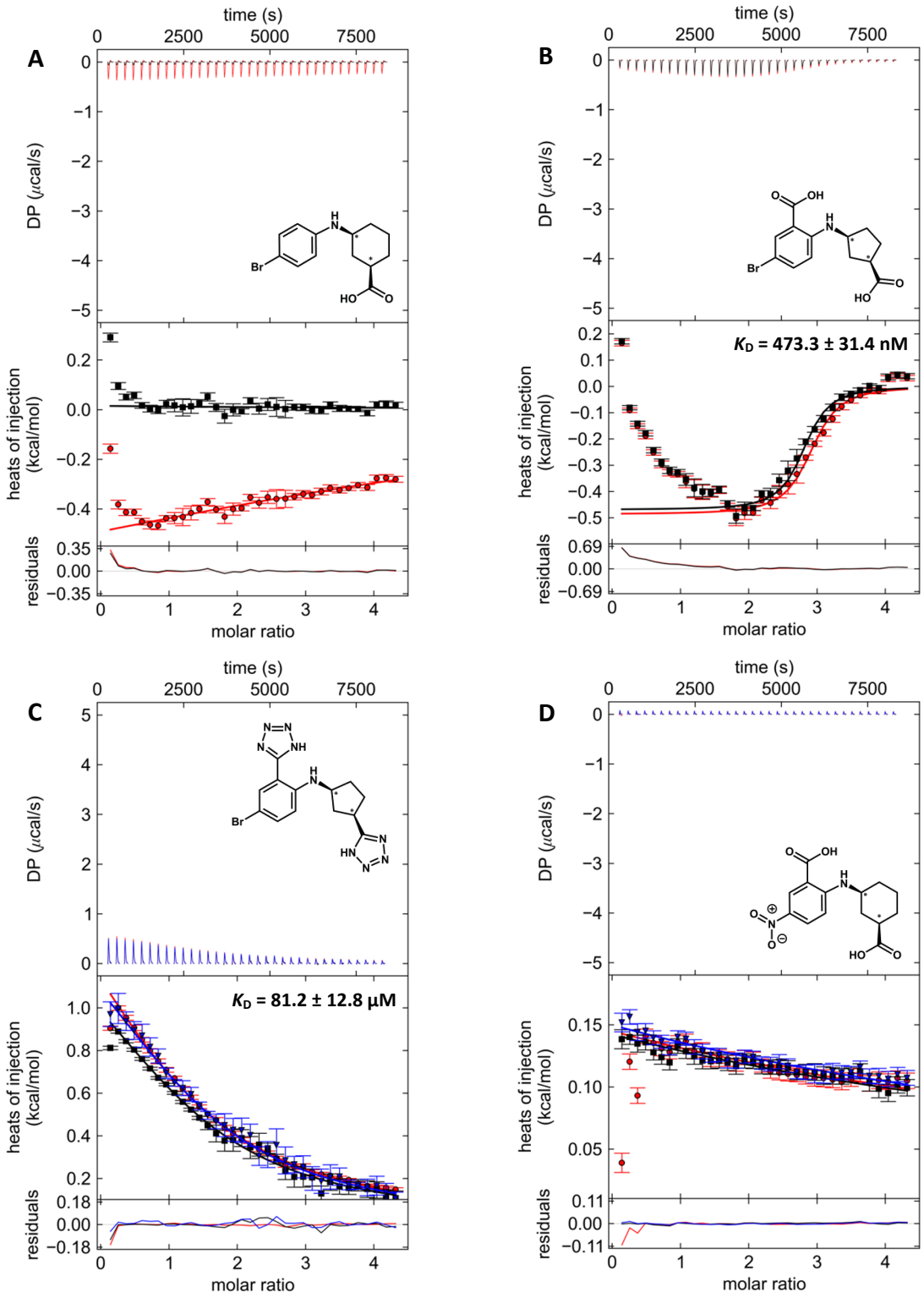

Figure A19: ITC profiles for affinity titrations of WB035 (A), WB047 (B), WB050 (C), and WB067 (D) against *Bc*Phz(A)/B. The individual plots show the generated heat per injection at different time points (upper panel), the fitted binding curves for individual titration experiments (middle panel), and the quality of the fit (lower panel). All profiles represent titrations of 2 mM of the respective analog to 100 µM *Bc*Phz(A)/B. Binding is exothermic for WB047 (**B**) and endothermic for WB050 (**C**), although the former ligand exhibits an unusual binding curve. The corresponding binding affinities are depicted in the plots unless fitting of the data failed, *e.g.* WB035 (**A**) and WB067 (**D**). The symbols ●, ■, and ▼ represent individual experiments All data were analyzed and fitted using the programs NITPIC (Keller *et al.*, 2012; Scheuermann and Brautigam, 2015) and SEDPHAT (Houtman *et al.*, 2007; Zhao *et al.*, 2015) and plotted using the program GUSSI (Brautigam, 2015).

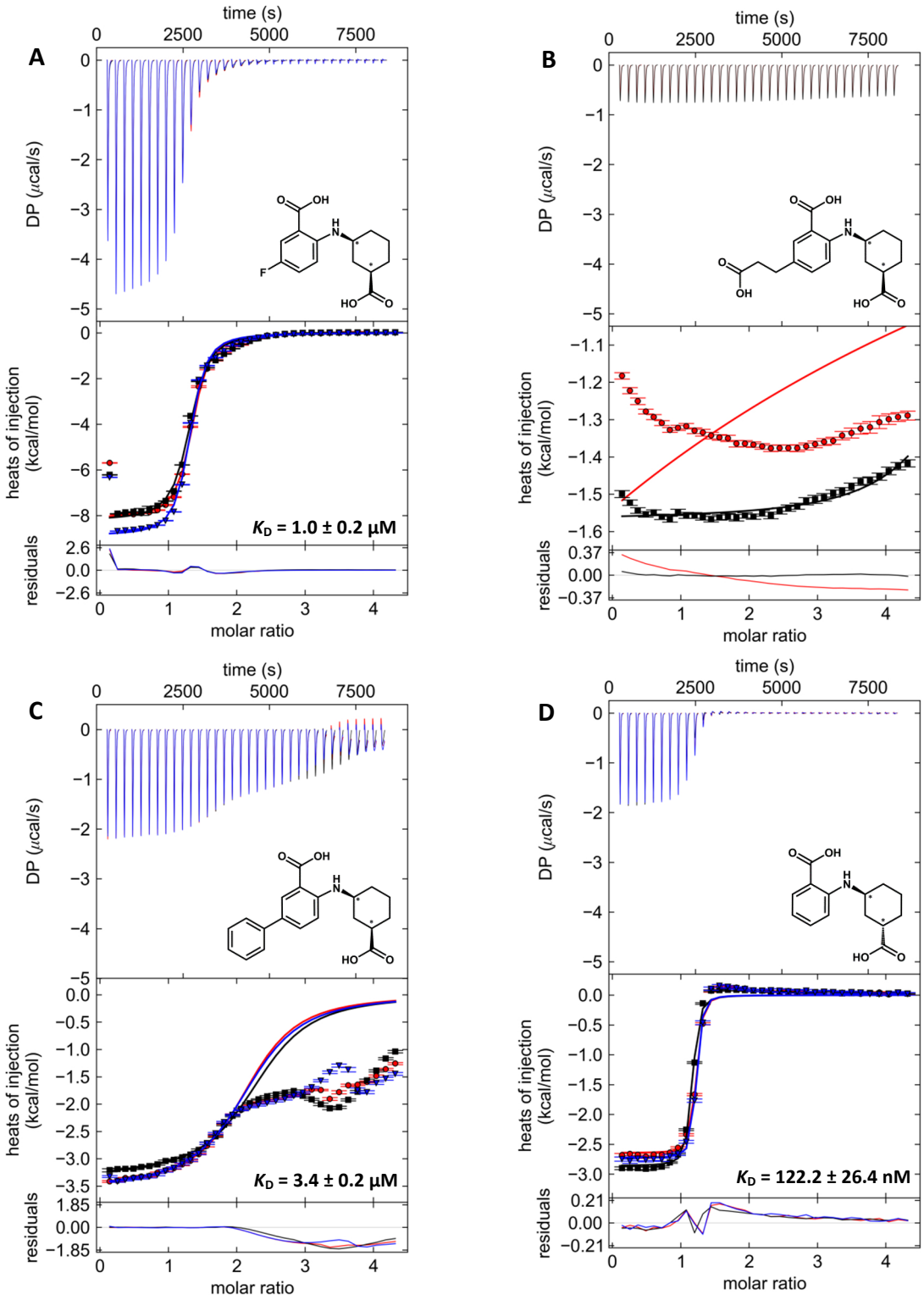

Figure A20: ITC profiles for affinity titrations of WB069 (A), WB071 (B), WB073 (C), and WB083 (D) against *Bc*Phz(A)/B. The individual plots show the generated heat per injection at different time points (upper panel), the fitted binding curves for individual titration experiments (middle panel), and the quality of the fit (lower panel). All profiles represent titrations of 2 mM of the respective analog to 100 µM *Bc*Phz(A)/B. Binding is exothermic for all tested compounds, except WB071 (**B**) where no binding could be detected. The corresponding binding affinities are depicted in the plots unless fitting of the data failed, *e.g.* WB071 (**B**). The symbols ●, ■, and ▼ represent individual experiments All data were analyzed and fitted using the programs NITPIC (Keller *et al.*, 2012; Scheuermann and Brautigam, 2015) and SEDPHAT (Houtman *et al.*, 2007; Zhao *et al.*, 2015) and plotted using the program GUSSI (Brautigam, 2015).

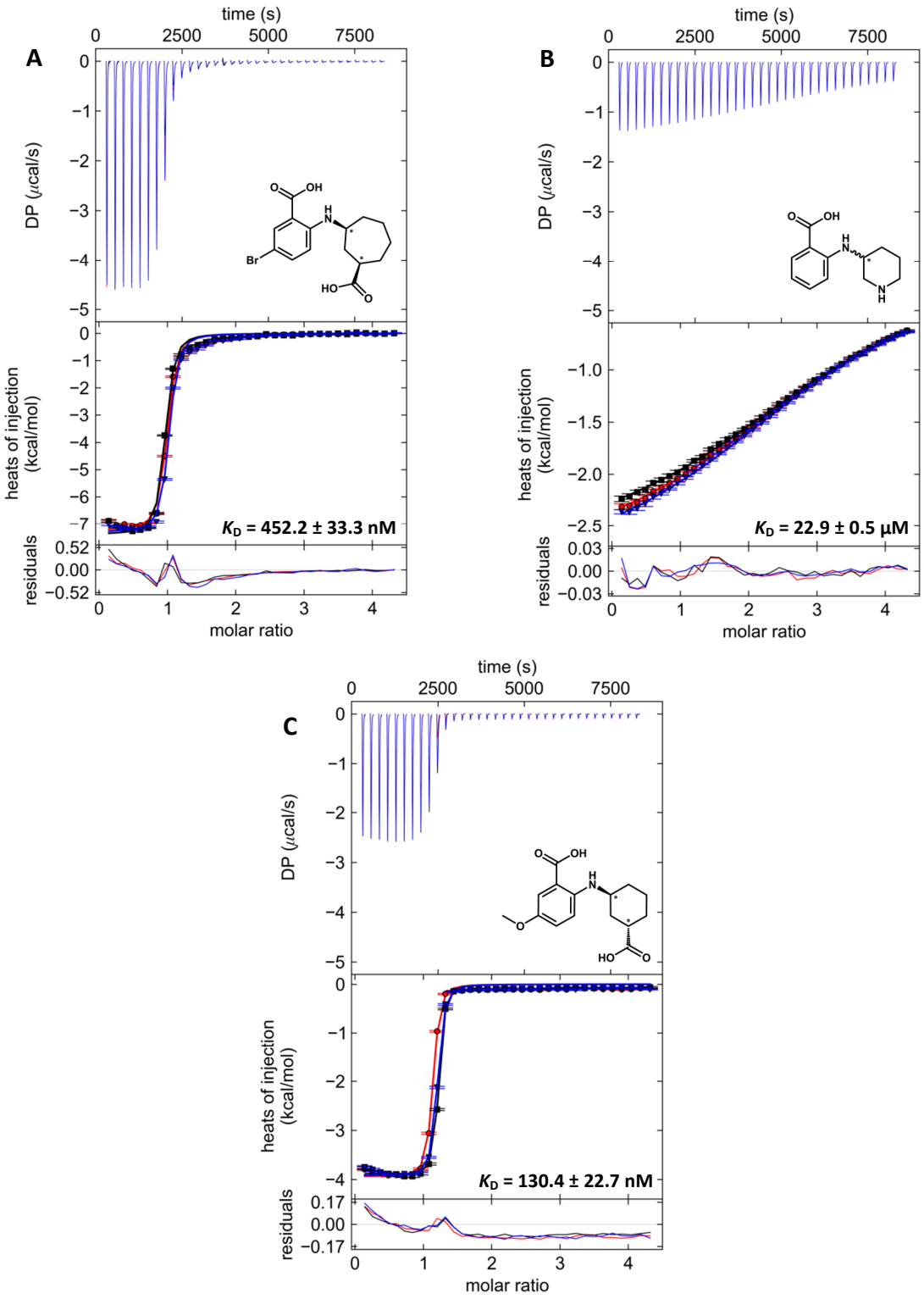

Figure A21: ITC profiles for affinity titrations of WB084 (A), WB086 (B), and WB089 (C) against *Bc*Phz(A)/B.
The individual plots show the generated heat per injection at different time points (upper panel), the fitted binding curves for individual titration experiments (middle panel), and the quality of the fit (lower panel). All profiles represent titrations of 2 mM of the respective analog to 100 µM *Bc*Phz(A)/B. Binding is exothermic for all tested compounds and the corresponding binding affinities are depicted in the plots. The symbols ●, ■, and ▼ represent individual experiments All data were analyzed and fitted using the programs NITPIC (Keller *et al.*, 2012; Scheuermann and Brautigam, 2015) and SEDPHAT (Houtman *et al.*, 2007; Zhao *et al.*, 2015) and plotted using the program GUSSI (Brautigam, 2015).

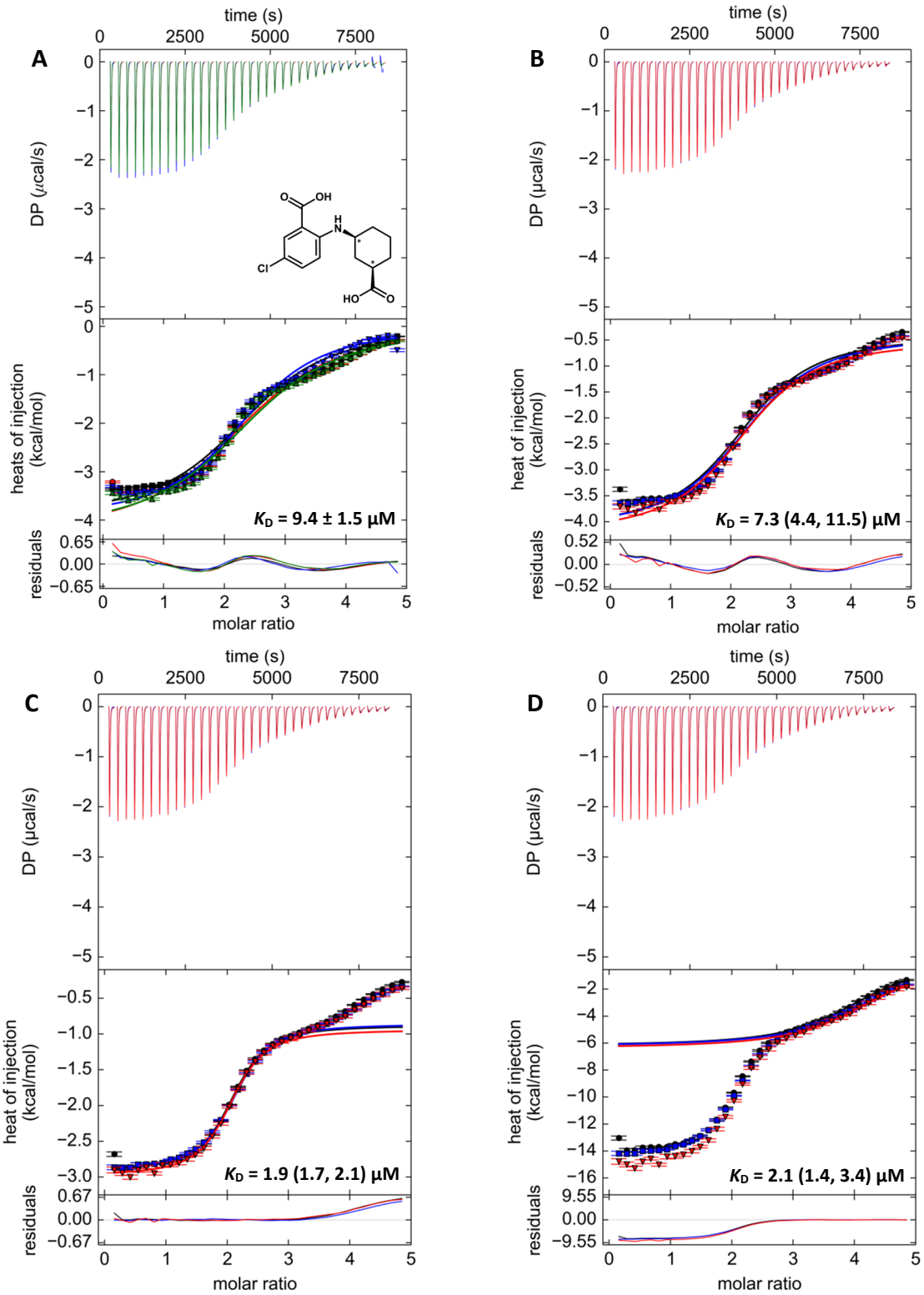

Figure A22: ITC profiles for the individual fits of affinity titrations of WB011 against *Bc*Phz(A)/B.
The individual plots show the generated heat per injection at different time points (upper panel), the fitted binding curves for (individual) titration experiments (middle panel), and the quality of the fit (lower panel). Titrations of 2 mM WB011 to 100 µM *Bc*Phz(A)/B reveal an exothermic binding behavior of the compound. The curves in **A** were all fitted individually and the associated binding constants averaged. In the plots **B**-**D**, the data from three individual titrations (triplicate) were fitted together, either as single (**B**) or as individual transition curves (**C** and **D**). The corresponding binding affinities with the standard deviation (**A**) or a confidence level, *i.e.* an affinity range (**B**-**D**) are depicted in the plots. The symbols ●, ■, and ▼ represent individual experiments All data were analyzed and fitted using the programs NITPIC (Keller *et al.*, 2012; Scheuermann and Brautigam, 2015) and SEDPHAT (Houtman *et al.*, 2007; Zhao *et al.*, 2015) and plotted using the program GUSSI (Brautigam, 2015).

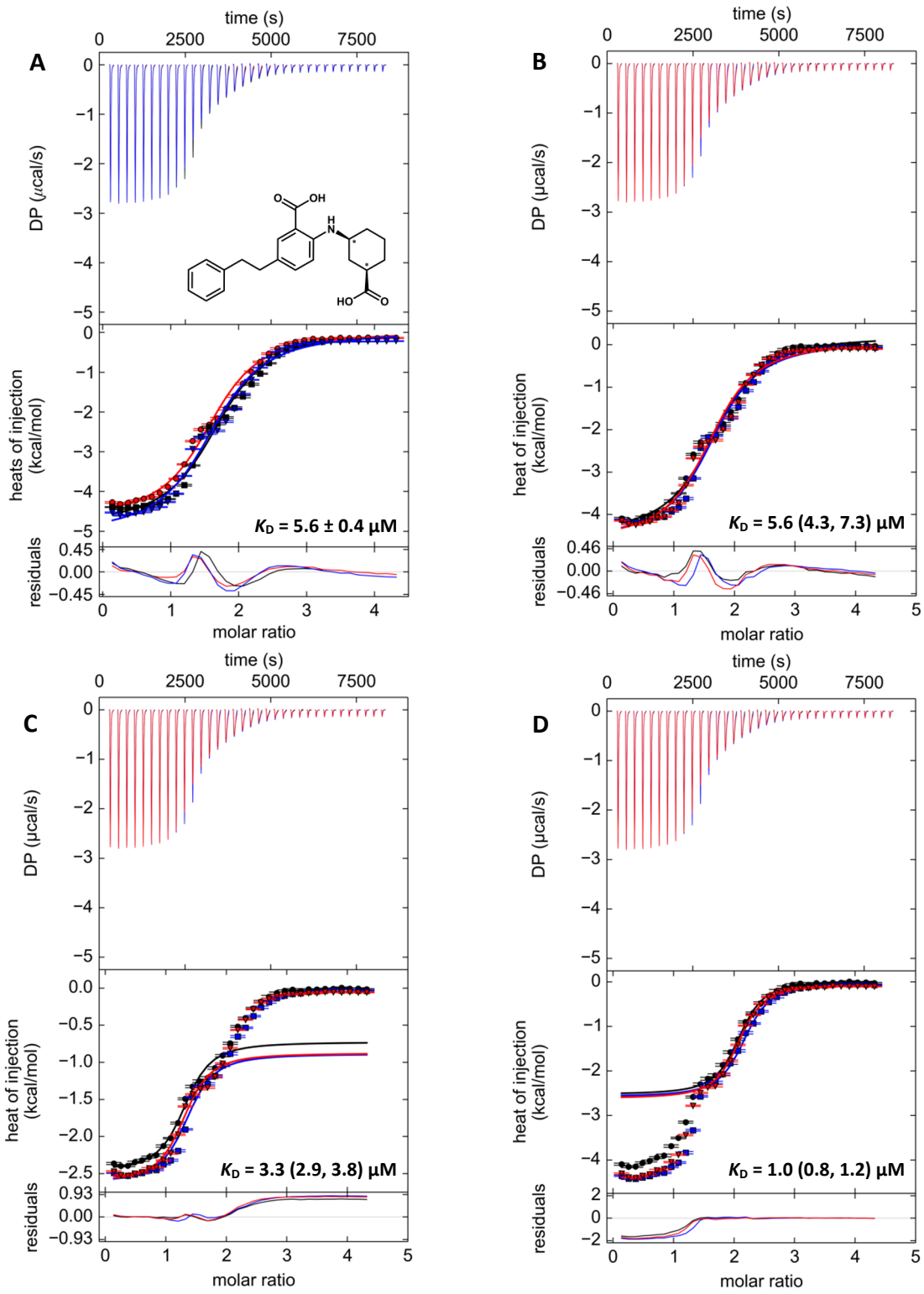

Figure A23: ITC profiles for the individual fits of affinity titrations of WB077 against *Bc*Phz(A)/B.
The individual plots show the generated heat per injection at different time points (upper panel), the fitted binding curves for (individual) titration experiments (middle panel), and the quality of the fit (lower panel). Titrations of 2 mM WB077 to 100 µM *Bc*Phz(A)/B reveal an exothermic binding behavior of the compound. The curves in **A** were all fitted individually and the associated binding constants averaged. In the plots **B**-**D**, the data from three individual titrations (triplicate) were fitted together, either as single (**B**) or as individual transition curves (**C** and **D**). The corresponding binding affinities with the standard deviation (**A**) or a confidence level, *i.e.* an affinity range (**B**-**D**) are depicted in the plots. The symbols ●, ■, and ▼ represent individual experiments All data were analyzed and fitted using the programs NITPIC (Keller *et al.*, 2012; Scheuermann and Brautigam, 2015) and SEDPHAT (Houtman *et al.*, 2007; Zhao *et al.*, 2015) and plotted using the program GUSSI (Brautigam, 2015).

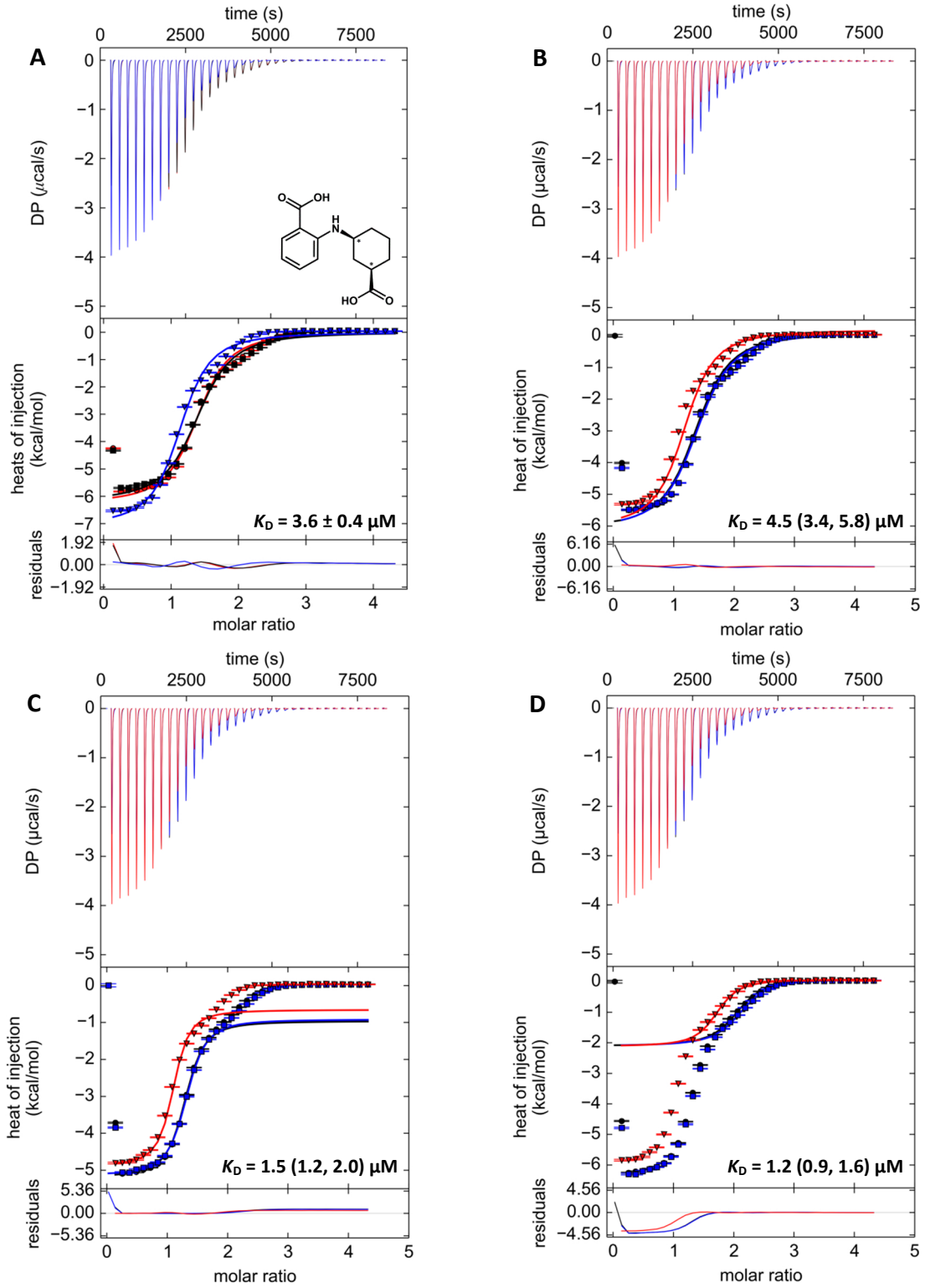

Figure A24: ITC profiles for the individual fits of affinity titrations of WB082 against *Bc*Phz(A)/B.
The individual plots show the generated heat per injection at different time points (upper panel), the fitted binding curves for (individual) titration experiments (middle panel), and the quality of the fit (lower panel). Titrations of 2 mM WB082 to 100 µM *Bc*Phz(A)/B reveal an exothermic binding behavior of the compound. The curves in **A** were all fitted individually and the associated binding constants averaged. In the plots **B**-**D**, the data from three individual titrations (triplicate) were fitted together, either as single (**B**) or as individual transition curves (**C** and **D**). The corresponding binding affinities with the standard deviation (**A**) or a confidence level, *i.e.* an affinity range (**B**-**D**) are depicted in the plots. The symbols ●, ■, and ▼ represent individual experiments All data were analyzed and fitted using the programs NITPIC (Keller *et al*., 2012; Scheuermann and Brautigam, 2015) and SEDPHAT (Houtman *et al*., 2007; Zhao *et al*., 2015) and plotted using the program GUSSI (Brautigam, 2015).

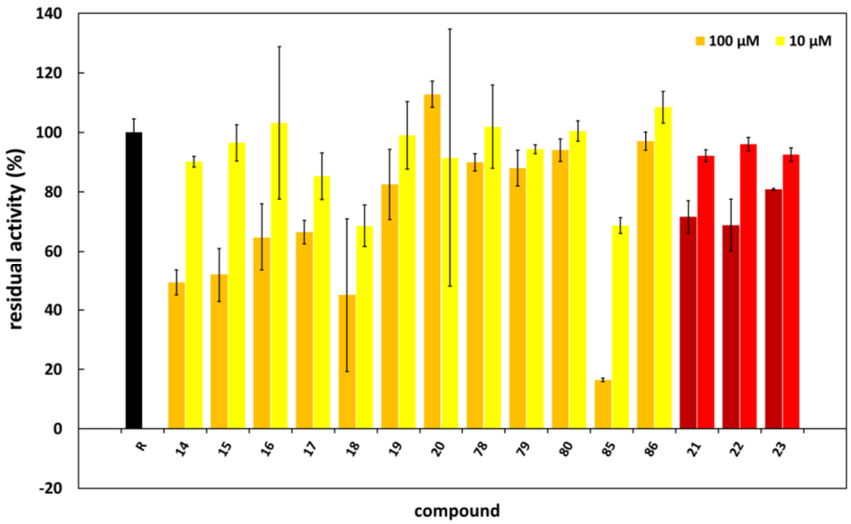

Figure A25: Residual enzymatic activity of *Bc*Phz(A)/B in presence of *N*-piperidinyl or *N*-phenyl anthranilic acid-derived inhibitors and 125 µM DHHA.
The plot shows the residual enzymatic activity of Phz(A)/B from *B. cepacia* in presence of 125 µM DHHA and either 10 (light colors) or 100 µM (dark colors) inhibitor compared to the uninhibited reaction (R). The numbers represent the individual compound, *e.g.* 14 = WB014. *Bc*Phz(A)/B and the coupled enzyme PhzF were used at 1 mM (dimer) final concentration in all assays. The data, obtained in 50 mM sodium phosphate buffer pH 7.5, supplemented with 2 % (v/v) DMSO, at 25 °C, were normalized to zero, corrected, and averaged from three independent measurements.

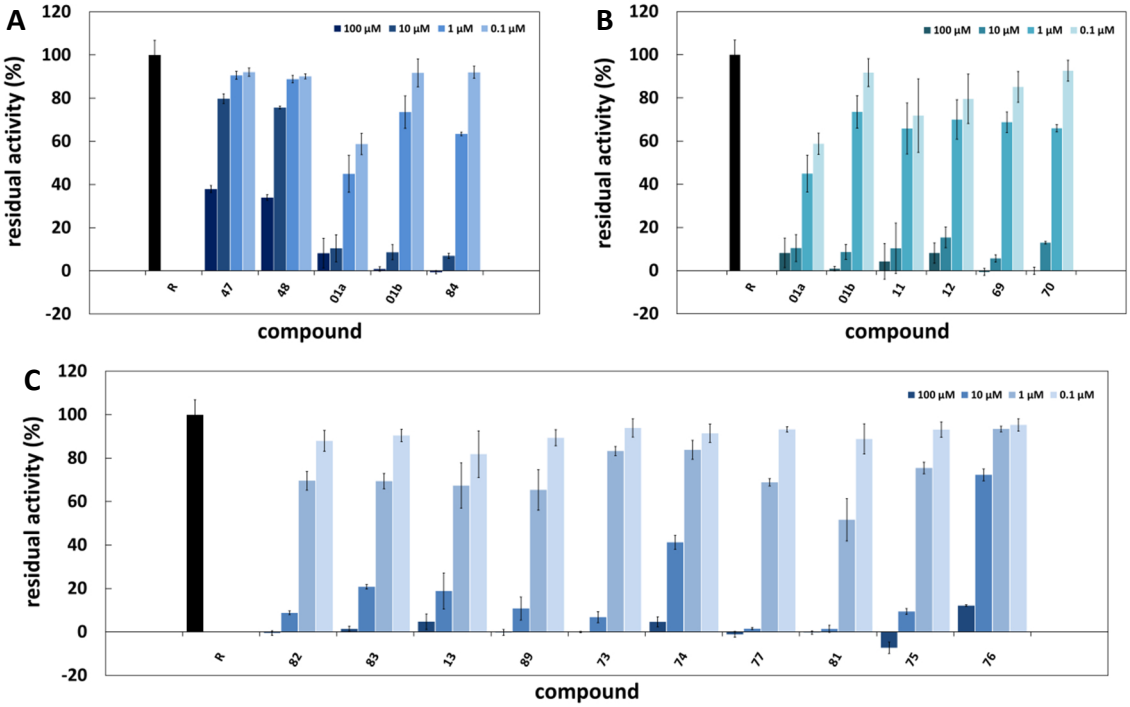

Figure A26: Residual enzymatic activity of *Bc*Phz(A)/B in presence of different concentrations of *N*-carboxycycloalkyl anthranilic acid-derived inhibitors.
The plot shows the residual enzymatic activity of Phz(A)/B from *B. cepacia* in presence of 1 mM DHHA and inhibitor concentrations from 0.1 – 100 µM (from light to dark colors) compared to the uninhibited reaction (R) allowing approximation of the corresponding IC_{50}-values. The numbers represent the individual compound, *e.g.* 47 = WB047. *Bc*Phz(A)/B and the coupled enzyme PhzF were used at 1 mM (dimer) final concentration in all assays. The data, obtained in 50 mM sodium phosphate buffer pH 7.5, supplemented with 2 % (v/v) DMSO, at 25 °C, were normalized to zero, corrected, and averaged from three independent measurements.

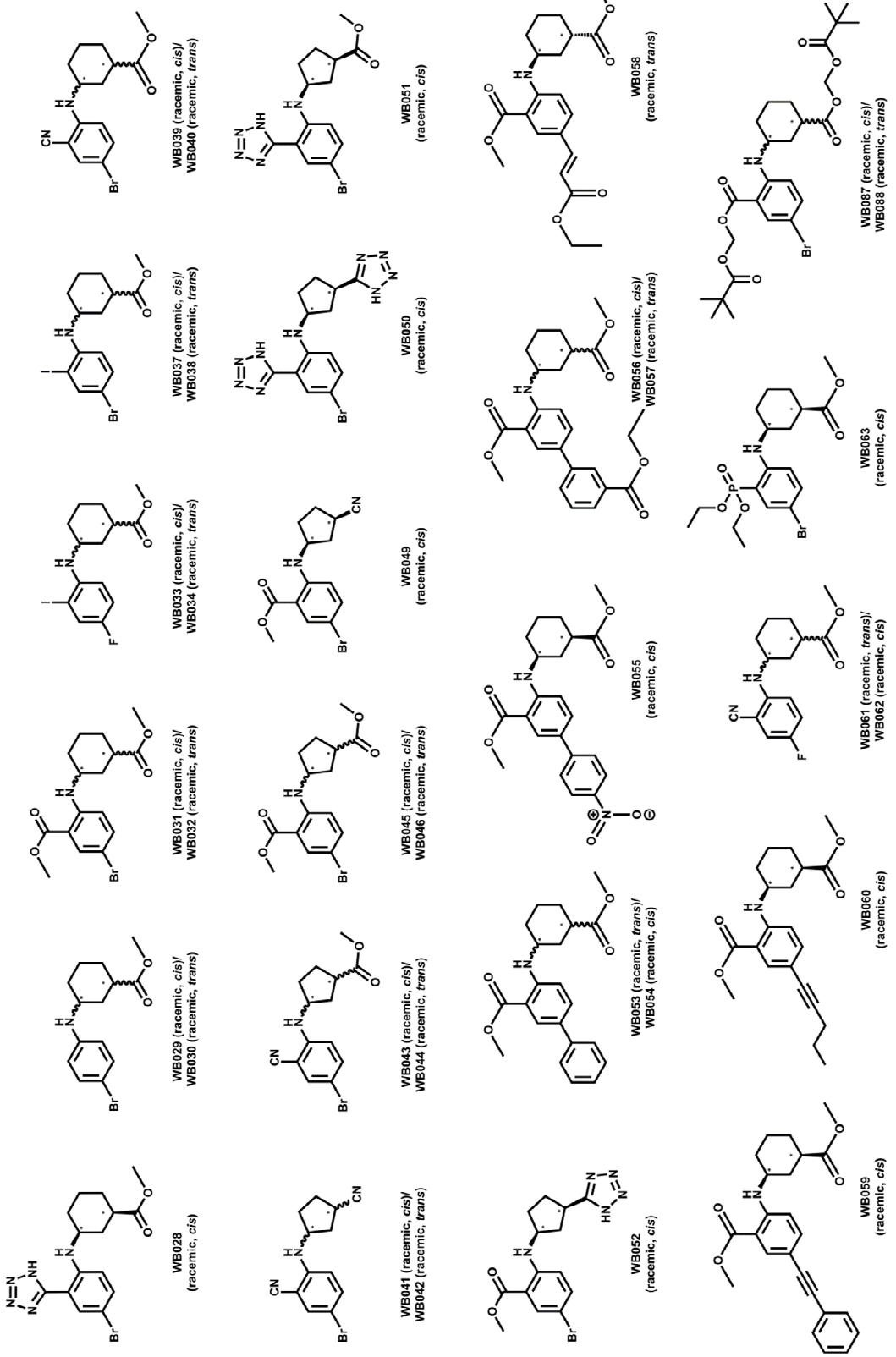

Scheme A1: Chemical structures of bioisosteres and prodrug esters of the *N*-carboxycycloalkyl anthranilic acid-derived compounds ("phenazistatins").

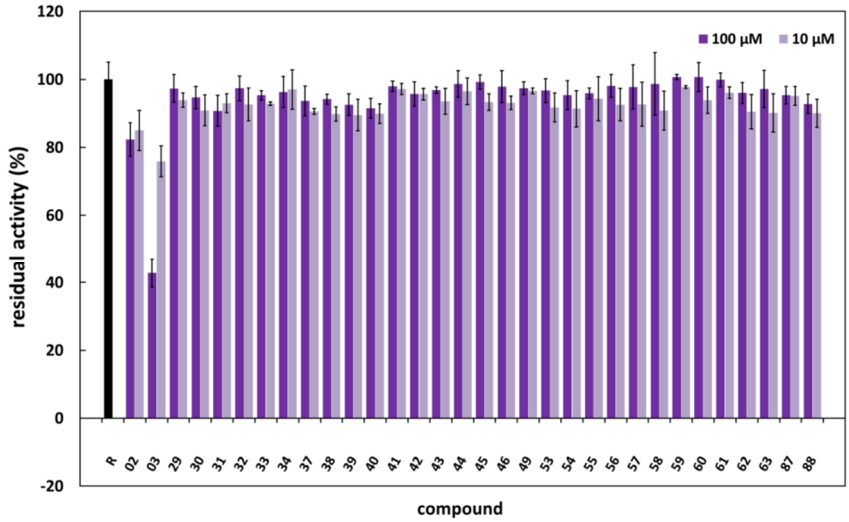

Figure A27: Residual enzymatic activity of *Bc*Phz(A)/B in presence of bioisosteres and prodrug esters of *N*-carboxy-cycloalky anthranilic acid-derived inhibitors.
The plot shows the residual enzymatic activity of Phz(A)/B from *B. cepacia* in presence of 1 mM DHHA and either 10 (light colors) or 100 µM (dark colors) inhibitor compared to the uninhibited reaction (R). The numbers represent the individual compound, *e.g.* 02 = WB002. *Bc*Phz(A)/B and the coupled enzyme PhzF were used at 1 mM (dimer) final concentration in all assays. The data, obtained in 50 mM sodium phosphate buffer pH 7.5, supplemented with 2 % (v/v) DMSO, at 25 °C, were normalized to zero, corrected, and averaged from three independent measurements.

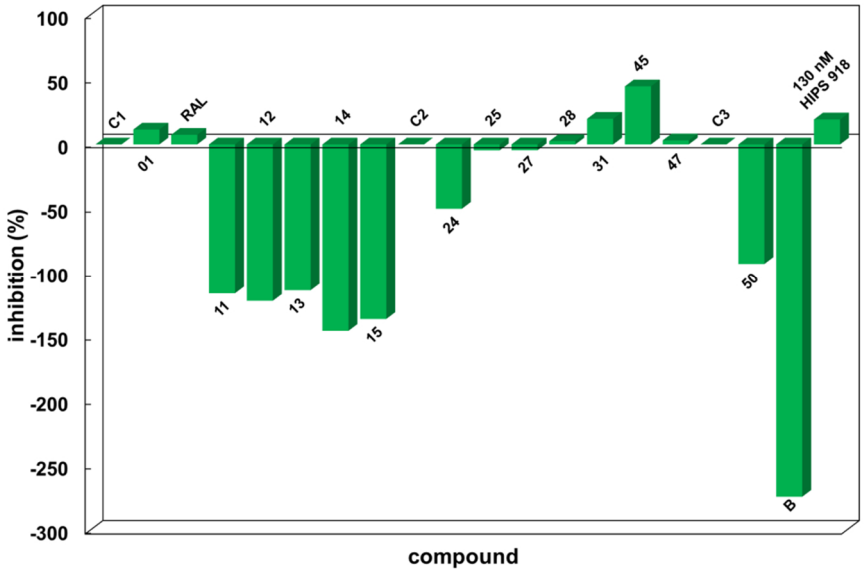

Figure A28: *In cellulo* inhibition studies of pyocyanin production in *P. aeruginosa* PAO1.
Phenazine biosynthesis inhibition was analyzed in presence of 100 µM inhibitor by quantification of pyocyanin levels in *P. aeruginosa* PAO1 cultures in PPGAS-medium after incubation overnight. After growth correction, data were averaged from triplicates and plotted in relation to a compound free control (C1-3). The numbers represent the individual compounds, *e.g.* 01 = WB001. B represents a buffer control (final concentration: 2 mM TRIS/HCl pH 9.0). Each bar indicates an independent replica (each n = 3). Compound HIPS 918 was used as positive control at its known IC_{50}-value (determined against *P. aeruginosa* PA14 in PPGAS-medium, internal communication).

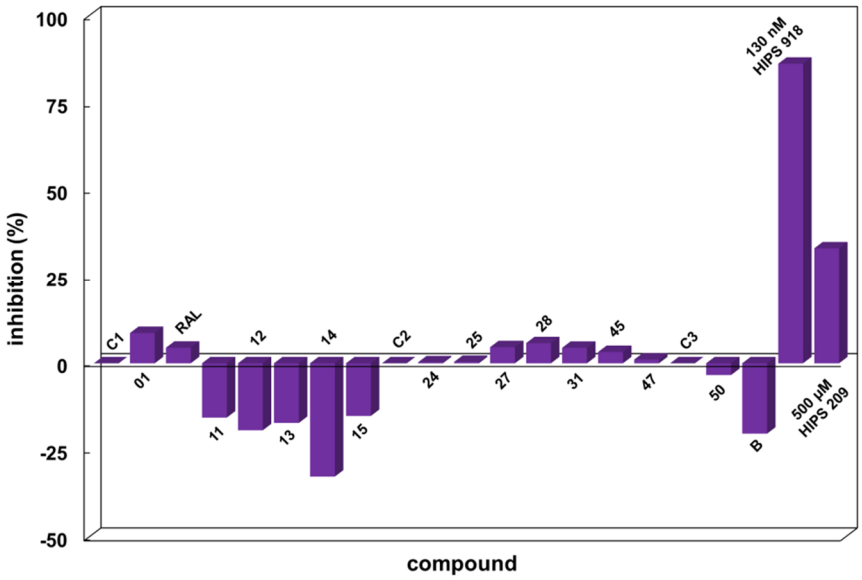

Figure A29: *In cellulo* inhibition studies of pyocyanin production in *P. aeruginosa* PA14 in M63-medium.
Phenazine biosynthesis inhibition was analyzed in presence of 100 µM inhibitor by quantification of pyocyanin levels in *P. aeruginosa* PA14 cultures in M63-medium after incubation overnight. After growth correction, data were averaged from triplicates and plotted in relation to a compound free control (C1-3). The numbers represent the individual compounds, *e.g*. 01 = WB001. B represents a buffer control (final concentration: 2 mM TRIS/HCl pH 9.0). Each bar indicates an independent replica (each n = 3). The compounds HIPS 918 and HIPS 209 were used as positive control at their known IC_{50}-value (determined against *P. aeruginosa* PA14 in PPGAS- or M63-medium for HIPS 918 and HIPS 209 respectively; internal communication).

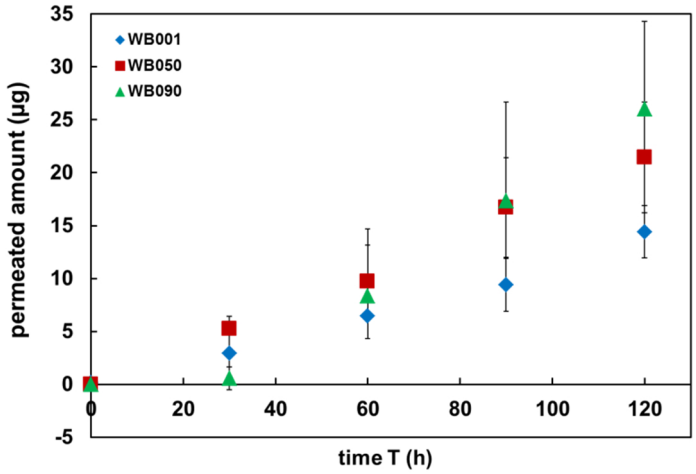

Figure A30: Kinetically resolved permeability of three "phenazistatin"-derivatives using an *in vitro* permeation model.
Membrane permeability of three "phenazistatin"-derivatives, WB001 (◆), WB050 (■), WB090 (▲), was evaluated in a specifically coated Transwell®-filter system mimicking the bacterial outer membrane. The substance flux J was quantified using the UV-signal of the compounds on an UHPLC-system and amounted to 7.2 ± 2.4, 13.2 ± 2.8, and 14.8 ± 3.6 µg cm^{-2} h^{-1} for WB001, WB050, and WB090 respectively. All permeability measurements were performed by Florian Gräf (Helmholtz Institute for Pharmaceutical Research Saarland, Saarbrücken).

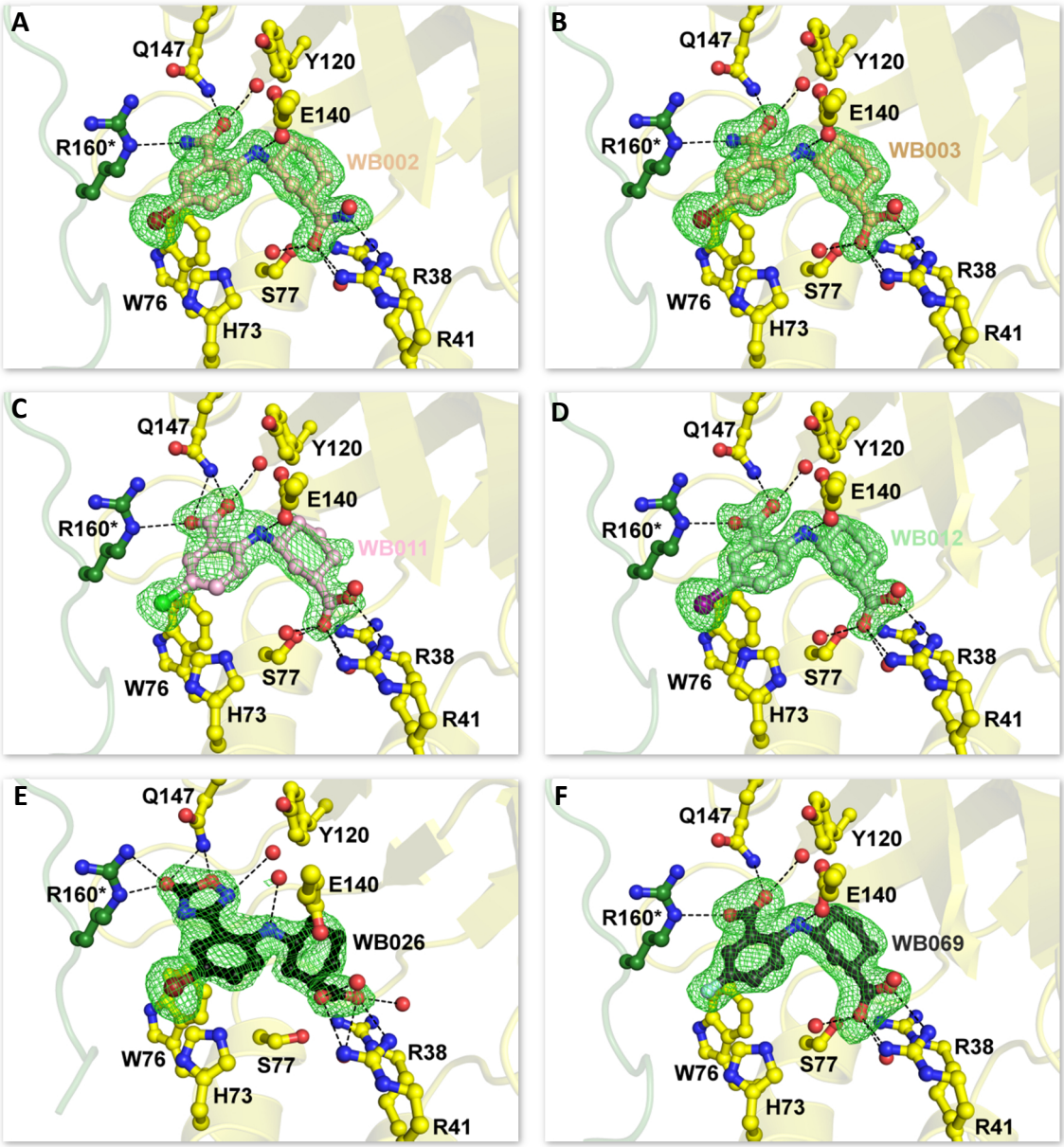

Figure A31: Crystal structures of *Bc*Phz(A)/B in complex with different synthetic "phenazistatin" derivatives.
Close-ups on the active site (chain A or B) of different *Bc*Phz(A)/B complex structures with potential PhzB-inhibitors of the "phenazistatin"-class after soaking with 10 mM of the respective ligand overnight. The ligands are highlighted as balls and sticks in different colors and depicted in their Fourier difference density (mF_o-DF_c) omit map contoured at 3σ in green: **A** WB002, **B** WB003, **C** *cis*-chloro-phenazistatin (WB011), **D** *cis*-iodo-phenazistatin (WB012), **E** *trans*-oxadiazolone-phenazistatin (WB026), and **F**: *cis*-fluoro-phenazistatin (WB069). The protein is shown as cartoon and the coordinating active site residues as balls and sticks colored in **yellow** and **forest** (for residues belonging to the second chain, depicted with *). Hydrogen bonds (- - -) and coordinating water (red balls) are highlighted as well.

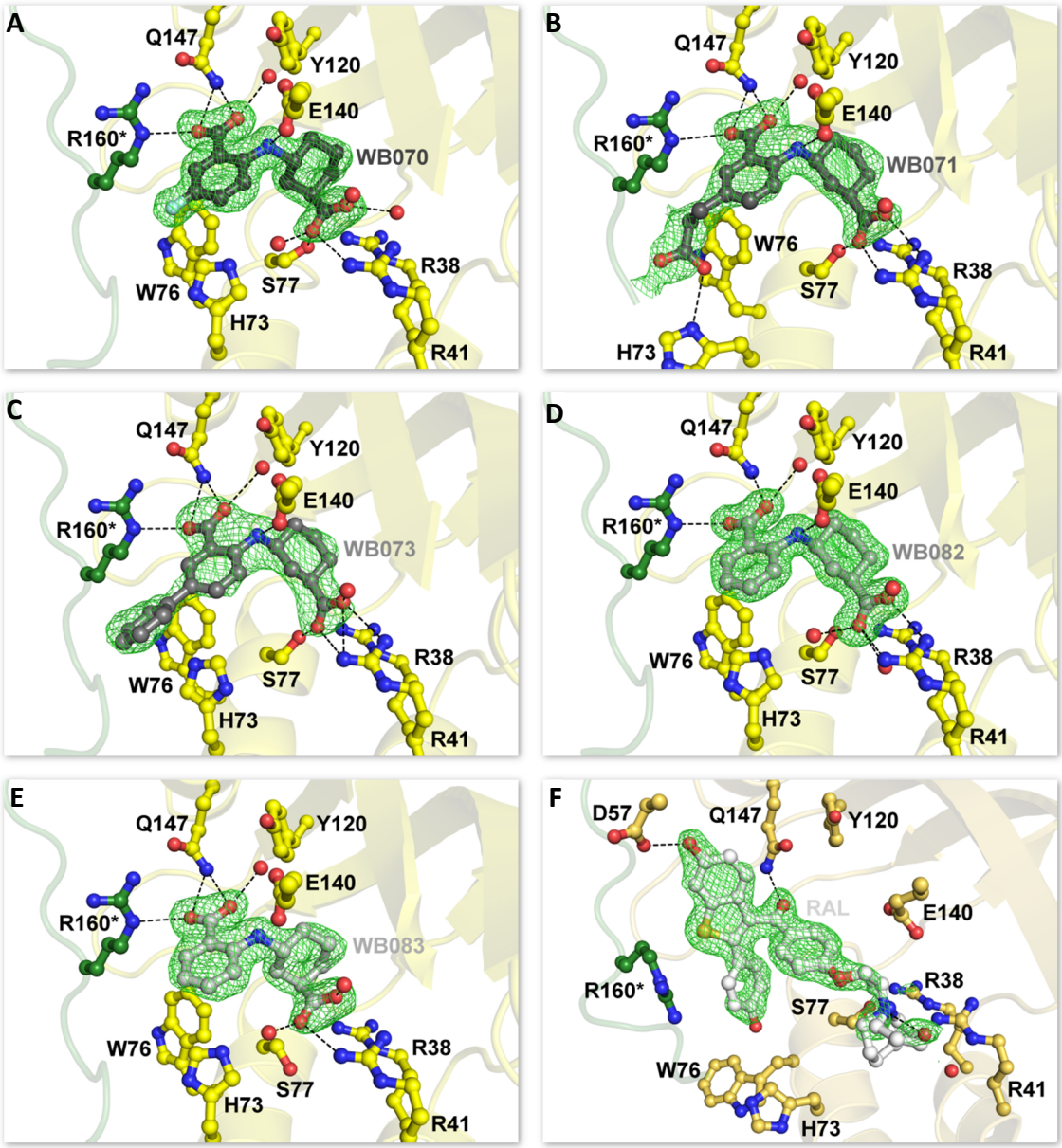

Figure A32: Crystal structures of *Bc*Phz(A)/B in complex with different synthetic "phenazistatin" derivatives or raloxifene .

Close-ups on the active site (chain A or B) of different *Bc*Phz(A)/B complex structures with potential PhzB-inhibitors of the "phenazistatin"-class or raloxifene after soaking with 10 mM of the respective ligand overnight. The ligands are highlighted as balls and sticks in different colors and depicted in their Fourier difference density (mF_o-DF_c) omit map contoured at 3σ in green: **A** *trans*-fluoro-phenazistatin (WB070), **B** *cis*-carboxyethyl-phenazistatin (WB071), **C** *cis*-phenyl-phenazistatin (WB073), **D** *cis*-hydro-phenazistatin (WB082), **E** *trans*-hydro-phenazistatin (WB083), and **F**: raloxifene (RAL). The protein is shown as cartoon and the coordinating active site residues as balls and sticks colored in yellow (gold for raloxifene in **F**) and forest (for residues belonging to the second chain, depicted with *). Hydrogen bonds (- - -) and coordinating water (red balls) are highlighted as well.

A3.2. Additional tables

Table A9: Overview over thermodynamic binding parameters obtained from ITC affinity titrations against *Bc*Phz(A)/B for a variety of newly synthesized PhzB ligands.[#]

Ligand	K_D (µM)	ΔG (kcal mol^{-1})	ΔH (kcal mol^{-1})	-T*ΔS (kcal mol^{-1})	*N*	c
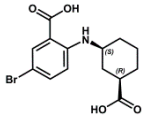 **WB001 (*cis*)**	6.4 ± 1.1 • 10^{-2}	-9.8 ± 0.1	-10.3 ± 0.2	0.5 ± 0.2	1.8 ± 0.1	1610.6 ± 242.7
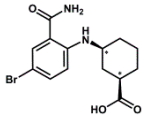 **WB003 (racemic, *cis*)**	119.0 ± 17.4	-5.4 ± 0.1	-4.2 ± 0.1	-1.2 ± 0.2	1.5 ± 0.3	0.9 ± 0.1
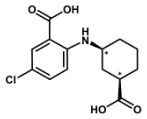 **WB011 (racemic, *cis*)**	9.4 ± 1.5 7.3 (4.8, 11.5)	-6.9 ± 0.1 -7.0	-10.2 ± 0.5 -8.4	3.4 ± 0.6 -1.4	2.4 ± 0.0 2.3	10.9 ± 1.8 13.7
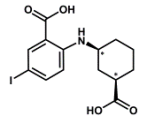 **WB012 (racemic, *cis*)**	5.8 ± 0.2	-7.1 ± 0.0	-9.4 ± 0.2	2.3 ± 0.2	2.8 ± 0.0	17.3 ± 0.7
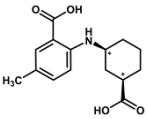 **WB013 (racemic, *cis*)**	1.7 ± 0.2	-7.9 ± 0.1	-8.7 ± 0.4	0.8 ± 0.4	1.9 ± 0.0	58.4 ± 5.8
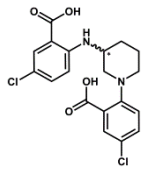 **WB014 (racemic)**	27.7 ± 0.7	-6.2 ± 0.0	8.1 ± 0.2	-14.3 ± 0.2	1.8 ± 0.0	3.6 ± 0.1
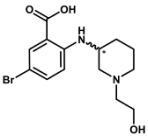 **WB015 (racemic)**	2.4 ± 0.5	-7.7 ± 0.1	-6.7 ± 0.9	-1.0 ± 1.0	4.2 ± 0.5	43.1 ± 8.0
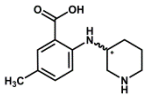 **WB017 (racemic)**	11.3 ± 0.1	-6.7 ± 0.0	-10.8 ± 0.1	4.0 ± 0.1	2.6 ± 0.1	8.8 ± 0.1

Ligand	K_D (µM)	ΔG (kcal mol^{-1})	ΔH (kcal mol^{-1})	-T*ΔS (kcal mol^{-1})	*N*	c
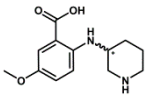 **WB018 (racemic)**	36.4 ± 9.4	-6.1 ± 0.1	-9.5 ± 0.6	3.5 ± 0.8	3.7 ± 0.9	2.9 ± 0.7
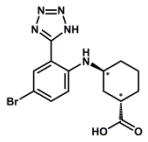 **WB024 (racemic, *trans*)**	5.1 ± 0.4	-7.2 ± 0.0	4.3 ± 0.1	-11.5 ± 0.1	1.3 ± 0.0	19.7 ± 1.5
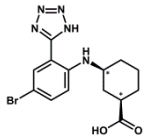 **WB025 (racemic, *cis*)**	4.0 ± 0.6 • 10^{-1}	-8.7 ± 0.1	1.3 ± 0.0	-10.0 ± 0.1	1.0 ± 0.0	255.8 ± 39.0
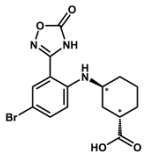 **WB026 (racemic, *trans*)**	13.0 ± 0.1	-6.7 ± 0.0	5.0 ± 0.0	-11.7 ± 0.0	1.9 ± 0.2	7.7 ± 0.1
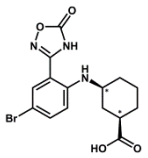 **WB027 (racemic, *cis*)**	16.9 ± 1.8	-6.5 ± 0.1	3.3 ± 0.2	-9.8 ± 0.3	2.4 ± 0.1	6.0 ± 0.7
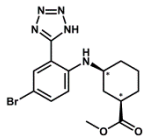 **WB028 (racemic, *cis*)**	17.4 ± 1.0	-6.5 ± 0.0	-4.1 ± 0.1	-2.4 ± 0.0	1.2 ± 0.1	5.8 ± 0.3
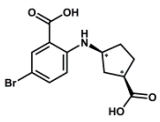 **WB047 (racemic, *cis*)**	4.7 ± 0.3 • 10^{-1}	-8.6 ± 0.0	-1.3 ± 0.0	-7.3 ± 0.1	3.0 ± 0.1	212.2 ± 14.1
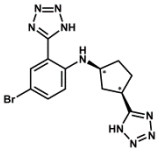 **WB050 (racemic, *cis*)**	81.2 ± 12.8	-5.6 ± 0.1	2.6 ± 0.2	-8.2 ± 0.1	1.6 ± 0.1	1.3 ± 0.2
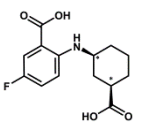 **WB069 (racemic, *cis*)**	1.0 ± 0.2	-8.2 ± 0.1	-10.8 ± 0.4	2.6 ± 0.3	1.3 ± 0.0	103.7 ± 16.2

Ligand	K_D (μM)	ΔG (kcal mol^{-1})	ΔH (kcal mol^{-1})	-T*ΔS (kcal mol^{-1})	*N*	c
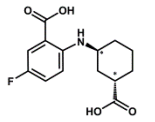 **WB070 (racemic, *trans*)**	4.7 ± 0.1 • 10^{-2}	-10.0 ± 0.0	-5.0 ± 0.3	-5.0 ± 0.3	1.1 ± 0.1	2126.1 ± 41.9
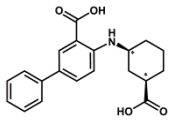 **WB073 (racemic, *cis*)**	3.4 ± 0.2	-7.5 ± 0.0	-7.6 ± 0.0	0.2 ± 0.1	1.8 ± 0.0	29.7 ± 1.6
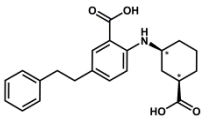 **WB077 (racemic, *cis*)**	5.6 ± 0.4 5.6 (4.3, 7.3)	-7.2 ± 0.0 -7.2	-8.0 ± 0.4 -8.0	0.9 ± 0.4 0.8	1.7 ± 0.0 1.7	17.9 ± 1.2 17.8
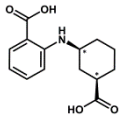 **WB082 (racemic, *cis*)**	3.6 ± 0.4 4.5 (3.4, 5.8)	-7.4 ± 0.1 -7.3	-8.4 ± 0.3 -9.0	1.0 ± 0.3 1.7	1.3 ± 0.1 1.3	28.5 ± 3.4 22.3
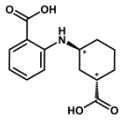 **WB083 (racemic, *trans*)**	1.2 ± 0.3 • 10^{-1}	-9.4 ± 0.1	-3.2 ± 0.0	-6.3 ± 0.1	1.2 ± 0.0	855.8 ± 176.9
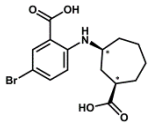 **WB084 (racemic, *cis*)**	4.5 ± 0.3 • 10^{-1}	-8.7 ± 0.0	-7.3 ± 0.1	-1.3 ± 0.1	0.9 ± 0.0	222.3 ± 16.0
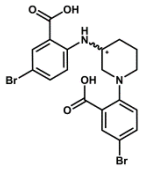 **WB085 (racemic)**	6.1 ± 0.2	-7.1 ± 0.0	4.7 ± 0.1	-11.9 ± 0.1	1.7 ± 0.1	16.5 ± 0.5
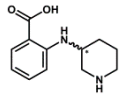 **WB086 (racemic)**	22.9 ± 0.5	-6.3 ± 0.0	-8.9 ± 0.1	2.6 ± 0.2	3.3 ± 0.1	4.4 ± 0.1
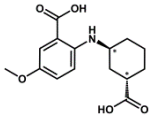 **WB089 (racemic, *trans*)**	1.3 ± 0.2 • 10^{-1}	-9.4 ± 0.1	-4.5 ± 0.1	-4.9 ± 0.1	1.1 ± 0.0	793.6 ± 151.9

[#] All ITC experiments were carried out at 25 °C in 20 mM TRIS/HCl pH 8.0, 150 mM NaCl (if necessary supplemented with up to 1 % DMSO). 2 mM of the respective compound were titrated to 100 μM *Bc*Phz(A)/B. The data are averaged from at least two independent measurements.

Table A10: Individual thermodynamic binding parameters for double transition binding curves obtained from ITC affinity titrations against *Bc*Phz(A)/B for the Phenazistatin derivatives WB011, WB077, and WB082.[#]

Ligand	K_D (µM)	ΔG (kcal mol^{-1})	ΔH (kcal mol^{-1})	-T*ΔS (kcal mol^{-1})	*N*	c
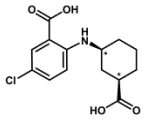 WB011 (racemic*, cis*)	7.3 (4.8, 11.5)	-7.0	-8.4	1.4		13.7
	1.9 (1.7, 2.1)	-7.8	-5.1	-2.7	2.3	52.4
	2.1 (1.4, 3.4)	-7.8	-6.3	-1.5		48.6
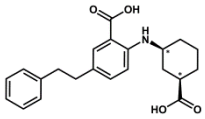 WB077 (racemic, *cis*)	5.6 (4.3, 7.3)	-7.2	-8.0	0.8		17.8
	3.3 (2.9, 3.8)	-7.5	-7.0	-0.5	1.7	30.7
	1.0 (0.8, 1.2)	-8.2	-5.3	-3.0		101.9
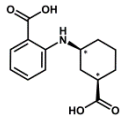 WB082 (racemic, *cis*)	4.5 (3.4, 5.8)	-7.3	-9.0	1.7		22.3
	1.5 (1.2, 2.0)	-7.9	-6.1	-1.8	1.3	64.6
	1.2 (0.9, 1.6)	-8.1	-4.1	-4.0		84.2

[#] All ITC experiments were carried out at 25 °C in 20 mM TRIS/HCl pH 8.0, 150 mM NaCl (if necessary supplemented with up to 1 % DMSO). 2 mM of the respective compound were titrated to 100 µM *Bc*Phz(A)/B. The data are averaged from at least two independent measurements.

Table A11: Data collection and refinement statistics for complex structures of *Bc*Phz(A)/B soaked with different *N*-carboxycycloalkyl anthranilic acid derivatives ("phenazistatins")[‡]

	Complex with WB002	Complex with WB003	Complex with WB011	Complex with WB012
Data collection[1]				
Beamline[†]	MX BL14.1, BESSY II	MX BL14.1, BESSY II	MX BL14.1, BESSY II	MX BL14.1, BESSY II
Wavelength (Å)	0.91841	0.91841	0.91841	0.91841
Resolution range (Å)	55.96 – 1.73 (1.76 – 1.73)	55.88 – 1.70 (1.73 – 1.70)	55.73 – 2.20 (2.27 – 2.20)	55.80 – 1.72 (1.75 – 1.72)
Space group	$P3_221$	$P3_221$	$P3_221$	$P3_221$
unit cell dimensions				
a, b, c (Å)	64.61, 64.61, 160.62	64.53, 64.53, 160.40	64.35, 64.35, 160.08	64.43, 64.43, 160.16
α, β, γ (°)	90, 90, 120	90, 90, 120	90, 90, 120	90, 90, 120
Mosaicity (°)[‡]	0.15	0.17	0.60	0.09
Measured reflections	149096 (8300)	184287 (9709)	95850 (6771)	244260 (13198)
Unique reflections	41031 (2255)	43077 (2219)	20251 (1751)	41849 (2173)
Multiplicity	3.6 (3.7)	4.3 (4.4)	4.7 (3.9)	5.8 (6.1)
Mean $I/\sigma(I)$	14.3 (2.0)	12.2 (1.9)	8.6 (1.8)	12.7 (2.0)
$CC_{1/2}$*	0.998 (0.667)	0.997 (0.622)	0.995 (0.658)	0.998 (0.675)
Completeness (%)	99.1 (99.2)	99.3 (99.6)	99.8 (99.9)	99.9 (99.9)
R_{meas}[§]	7.3 (73.7)	9.1 (90.3)	13.1 (76.3)	11.6 (130.6)
$R_{p.i.m.}$[¶]	3.7 (37.3)	4.2 (42.0)	7.8 (37.8)	4.7 (51.5)
Refinement				
Resolution range (Å)	52.84 – 1.73 (1.75 – 1.73)	52.77 – 1.70 (1.72 – 1.70)	53.26 – 2.20 (2.26 – 2.20)	55.80 – 1.72 (1.74– 1.72)
R_{cryst} (%)	16.29 (27.51)	17.75 (29.97)	20.72 (30.36)	18.82 (28.33)
R_{free} (%)	18.70 (28.11)	20.36 (36.99)	25.44 (34.12)	21.20 (30.05)
No. of non H-atoms				
Protein	2644	2679	2609	2672
Ligand / Ion	40	40	40	40
Water	372	337	158	233
Average B-factors (Å²)				
Protein	26.2	27.2	40.8	31.0
Ligand / Ion	18.6	21.0	33.9	27.8
Water	39.5	38.2	46.3	44.4
R.m.s deviations				
Bond lengths (Å)	0.009	0.007	0.002	0.012
Bond angles (°)	0.946	0.797	0.465	1.035
Ramachandran plot (%)				
Favored regions	98.8	98.8	98.7	98.8
Outliers	0	0	0	0
MolProbity score [#]	1.03	0.99	0.90	1.13

[†]Values in parentheses are for the highest resolution shell. [1] All data sets were collected from a single crystal. [†] BESSY II: Berlin Electron Storage Ring Society for Synchrotron Radiation, Helmholtz Centre Berlin, Berlin, Germany. [‡] Mosaicity values reported by *XDS* (Kabsch, 2010). * $CC_{1/2}$ is the correlation coefficient between two random half data sets (Karplus and Diederichs, 2012). [§] $R_{meas} = \sum_{hkl}\{N(hkl)/[N(hkl)-1]\}^{1/2}\sum_i|I_i(hkl) - \langle I(hkl)\rangle| / \sum_{hkl}\sum_i I_i(hkl)$, where *N(hkl* is the number of observations of the reflection with index *hkl* and $I_i(hkl)$ is the intensity of its *i*th observation (Diederichs and Karplus, 1997). [¶] $R_{p.i.m.} = \sum_{hkl}\{1/[N(hkl)-1]\}^{1/2}\sum_i|I_i(hkl) - \langle I(hkl)\rangle| / \sum_{hkl}\sum_i I_i(hkl)$ (Weiss, 2001); [#] As reported by *MolProbity* (http://molprobity.biochem.duke.edu/ (Chen *et al.*, 2010).

Table A12: Data collection and refinement statistics for complex structures of *Bc*Phz(A)/B soaked with different *N*-carboxycycloalkyl anthranilic acid derivatives ("phenazistatins")[‡]

	Complex with WB013	Complex with WB024	Complex with WB025	Complex with WB026
Data collection[1]				
Beamline[†]	MX BL14.1, BESSY II	MX BL14.1, BESSY II	MX BL14.1, BESSY II	MX BL14.1, BESSY II
Wavelength (Å)	0.91841	0.91841	0.91841	0.91841
Resolution range (Å)	53.44 – 1.51 (1.54 – 1.51)	56.02 – 1.64 (1.67 – 1.64)	56.09 – 1.86 (1.90 – 1.86)	46.05 – 1.85(1.89 – 1.85)
Space group	$P3_221$	$P3_221$	$P3_221$	$P3_221$
unit cell dimensions				
a, b, c (Å)	64.52, 64.52, 160.31	64.69, 64.69, 161.16	64.77, 64.77, 161.22	64.75, 64.75, 161.48
α, β, γ (°)	90, 90, 120	90, 90, 120	90, 90, 120	90, 90, 120
Mosaicity (°)[‡]	0.08	0.08	0.15	0.22
Measured reflections	335338 (16748)	717282 (34798)	350442 (13628)	333621 (21165)
Unique reflections	61644 (3023)	48893 (2392)	33749 (1993)	33850 (2028)
Multiplicity	5.4 (5.5)	14.7 (14.5)	10.4 (6.8)	9.9 (10.4)
Mean $I/\sigma(I)$	14.8 (1.9)	18.1 (2.1)	18.9 (2.0)	14.9 (2.0)
$CC_{1/2}$*	0.999 (0.658)	0.999 (0.740)	0.999 (0.474)	0.998 (0.655)
Completeness (%)	99.9 (100.0)	100.0 (100.0)	99.7 (96.6)	98.9 (98.2)
R_{meas}[§]	7.0 (94.0)	9.6 (135.4)	11.5 (98.7)	12.4 (120.3)
$R_{p.i.m.}$[¶]	3.0 (39.5)	2.5 (35.3)	3.5 (37.1)	3.9 (36.8.)
Refinement				
Resolution range (Å)	53.44 – 1.51 (1.53 – 1.51)	53.72 – 1.64 (1.66 – 1.64)	56.09 – 1.86 (1.89 – 1.86)	46.06 – 1.85 (1.88– 1.85)
R_{cryst} (%)	15.76 (28.86)	17.66 (26.90)	16.26 (27.88)	17.98 (27.08)
R_{free} (%)	17.36 (30.17)	19.11 (26.34)	19.39 (30.64)	20.11 (31.66)
No. of non H-atoms				
Protein	2676	2610	2615	2648
Ligand / Ion	40	44	50	50
Water	378	290	304	258
Average B-factors (Å²)				
Protein	25.7	28.1	27.0	30.5
Ligand / Ion	17.6	29.0	33.9	33.8
Water	40.0	42.5	42.2	43.0
R.m.s deviations				
Bond lengths (Å)	0.004	0.003	0.012	0.003
Bond angles (°)	0.688	0.635	1.010	0.646
Ramachandran plot (%)				
Favored regions	98.8	99.1	98.7	99.4
Outliers	0	0	0	0
MolProbity score [#]	0.78	1.05	1.10	1.20

[†]Values in parentheses are for the highest resolution shell. [1] All data sets were collected from a single crystal. [†] BESSY II: Berlin Electron Storage Ring Society for Synchrotron Radiation, Helmholtz Centre Berlin, Berlin, Germany. [‡] Mosaicity values reported by *XDS* (Kabsch, 2010). * $CC_{1/2}$ is the correlation coefficient between two random half data sets (Karplus and Diederichs, 2012). [§] $R_{meas} = \sum_{hkl}\{N(hkl)/[N(hkl)-1]\}^{1/2}\sum_i|I_i(hkl) - \langle I(hkl)\rangle| / \sum_{hkl}\sum_i I_i(hkl)$, where *N(hkl* is the number of observations of the reflection with index *hkl* and $I_i(hkl)$ is the intensity of its *i*th observation (Diederichs and Karplus, 1997). [¶] $R_{p.i.m.} = \sum_{hkl}\{1/[N(hkl)-1]\}^{1/2}\sum_i|I_i(hkl) - \langle I(hkl)\rangle|/\sum_{hkl}\sum_i I_i(hkl)$ (Weiss, 2001); [#] As reported by *MolProbity* (http://molprobity.biochem.duke.edu/ (Chen *et al.*, 2010).

Table A13: Data collection and refinement statistics for complex structures of *Bc*Phz(A)/B soaked with different *N*-carboxycycloalkyl anthranilic acid derivatives ("phenazistatins")[‡]

	Complex with WB047	Complex with WB069	Complex with WB070	Complex with WB071
Data collection[1]				
Beamline[†]	PXIII (X06DA), SLS	PXIII (X06DA), SLS	PXIII (X06DA), SLS	ID30B MAD, ESRF
Wavelength (Å)	1.00003	1.00003	1.00003	0.97625
Resolution range (Å)	80.11 – 1.83 (1.87 – 1.83)	80.24 – 1.68 (1.71 – 1.68)	55.52 – 1.80 (1.84 – 1.80)	80.25 – 2.08 (2.14 – 2.08)
Space group	$P3_221$	$P3_221$	$P3_221$	$P3_221$
unit cell dimensions				
a, b, c (Å)	64.54, 64.54, 160.21	64.50, 64.50, 160.48	64.11, 64.11, 159.52	64.52, 64.52, 160.50
α, β, γ (°)	90, 90, 120	90, 90, 120	90, 90, 120	90, 90, 120
Mosaicity (°)[‡]	0.37	0.30	0.26	0.17
Measured reflections	326098 (16898)	819143 (37933)	292558 (18123)	174327 (13190)
Unique reflections	35065 (2121)	45125 (2286)	36081 (2107)	23904 (1809)
Multiplicity	9.3 (8.0)	18.2 (16.6)	8.1 (8.6)	7.3 (7.3)
Mean $I/\sigma(I)$	26.4 (1.9)	16.2 (2.0)	19.4 (2.0)	17.1 (2.0)
$CC_{1/2}$*	0.999 (0.707)	0.999 (0.787)	0.999 (0.731)	0.999 (0.632)
Completeness (%)	100.0 (100.0)	100.0 (100.0)	99.9 (100.0)	99.4 (100.0)
R_{meas}[§]	8.0 (119.6)	7.6 (112.7)	10.0 (109.3)	6.6 (113.4)
$R_{p.i.m.}$[¶]	2.6 (42.1)	1.8 (27.5)	3.5 (36.9)	2.4 (41.7)
Refinement				
Resolution range (Å)	55.90 – 1.83 (1.86 – 1.83)	55.86 – 1.68 (1.70 – 1.68)	55.52 – 1.80 (1.83 – 1.80)	53.50 – 2.08 (2.13 – 2.08)
R_{cryst} (%)	17.82 (27.72)	17.24 (27.64)	16.24 (25.67)	18.66 (29.95)
R_{free} (%)	21.27 (29.95)	20.09 (33.38)	20.15 (27.53)	21.06 (30.27)
No. of non H-atoms				
Protein	2696	2737	2709	2645
Ligand / Ion	38	48	40	48
Water	360	190	293	91
Average B-factors (Å²)				
Protein	30.5	52.1	28.6	60.5
Ligand / Ion	26.0	62.7	21.7	65.2
Water	43.6	66.0	40.3	61.8
R.m.s deviations				
Bond lengths (Å)	0.005	0.006	0.013	0.002
Bond angles (°)	0.686	0.739	1.098	0.487
Ramachandran plot (%)				
Favored regions	98.8	98.8	98.8	99.4
Outliers	0	0	0	0
MolProbity score [#]	0.97	0.74	0.95	0.93

[†]Values in parentheses are for the highest resolution shell. [1] All data sets were collected from a single crystal. [†] Swiss light source (SLS) at the Paul Scherrer Institute (PSI), Villigen, Switzerland; European Synchrotron Radiation Facility (ESRF), Grenoble, France. [‡] Mosaicity values reported by *XDS* (Kabsch, 2010). * $CC_{1/2}$ is the correlation coefficient between two random half data sets (Karplus and Diederichs, 2012). [§] $R_{meas} = \sum_{hkl}\{N(hkl)/[N(hkl)-1]\}^{1/2}\sum_i|I_i(hkl)-\langle I(hkl)\rangle| / \sum_{hkl}\sum_i I_i(hkl)$, where *N(hkl* is the number of observations of the reflection with index *hkl* and $I_i(hkl)$ is the intensity of its *i*th observation (Diederichs and Karplus, 1997). [¶] $R_{p.i.m.} = \sum_{hkl}\{1/[N(hkl)-1]\}^{1/2}\sum_i|I_i(hkl)-\langle I(hkl)\rangle| / \sum_{hkl}\sum_i I_i(hkl)$ (Weiss, 2001); [#] As reported by *MolProbity* (http://molprobity.biochem.duke.edu/ (Chen *et al.*, 2010).

Table A14: Data collection and refinement statistics for complex structures of *Bc*Phz(A)/B soaked with different *N*-carboxycycloalkyl anthranilic acid derivatives ("phenazistatins")[‡]

	Complex with WB073	Complex with WB077	Complex with WB082	Complex with WB083
Data collection[1]				
Beamline[†]	PXIII (X06DA), SLS	ID30B MAD, ESRF	PXIII (X06DA), SLS	ID30B MAD, ESRF
Wavelength (Å)	1.00003	0.97625	1.00003	0.97625
Resolution range (Å)	80.41 – 2.57 (2.68 – 2.57)	80.39 – 1.92 (1.97 – 1.92)	80.09 – 1.58 (1.61 – 1.58)	80.48 – 2.02 (2.07 – 2.02)
Space group	$P3_221$	$P3_221$	$P3_221$	$P3_221$
unit cell dimensions				
a, b, c (Å)	64.43, 64.43, 160.82	64.79, 64.79, 160.79	64.37, 64.37, 160.18	64.87, 64.87, 160.96
α, β, γ (°)	90, 90, 120	90, 90, 120	90, 90, 120	90, 90, 120
Mosaicity (°)[‡]	0.52	0.35	0.20	0.34
Measured reflections	107334 (12646)	308461 (14826)	463126 (23608)	304321 (18988)
Unique reflections	12970 (1543)	30758 (2056)	53739 (2664)	26564 (1907)
Multiplicity	8.3 (8.2)	10.0 (7.2)	8.6 (8.9)	11.5 (10.0)
Mean $I/\sigma(I)$	8.7 (2.0)	12.9 (1.9)	19.0 (2.1)	17.5 (2.0)
$CC_{1/2}$*	0.994 (0.638)	0.997 (0.654)	1.000 (0.705)	0.998 (0.751)
Completeness (%)	100.0 (100.0)	100.0 (99.9)	100.0 (100.0)	99.9 (99.9)
R_{meas}[§]	20.2 (124.6)	12.4 (104.0)	6.6 (113.4)	13.4 (108.2)
$R_{p.i.m.}$[¶]	6.8 (43.1)	3.7 (36.8)	2.2 (37.9)	3.9 (33.3
Refinement				
Resolution range (Å)	55.80 – 2.57 (2.69 – 2.57)	56.11 – 1.92 (1.95 – 1.92)	55.74 – 1.58 (1.60 – 1.58)	56.18 – 2.02 (2.06 – 2.02)
R_{cryst} (%)	19.97 (28.54)	16.98 (31.78)	14.64 (26.63)	18.20 (26.43)
R_{free} (%)	24.71 (30.92)	19.98 (35.93)	17.48 (28.68)	21.58 (28.06)
No. of non H-atoms				
Protein	2657	2730	2801	2703
Ligand / Ion	50	60	56	44
Water	59	223	352	226
Average B-factors (Å²)				
Protein	61.9	38.6	32.4	29.9
Ligand / Ion	52.8	42.8	31.6	31.4
Water	55.9	45.7	46.3	41.6
R.m.s deviations				
Bond lengths (Å)	0.003	0.004	0.008	0.002
Bond angles (°)	0.524	0.631	0.878	0.487
Ramachandran plot (%)				
Favored regions	99.4	98.8	98.5	98.8
Outliers	0	0	0.3	0
MolProbity score [#]	0.89	0.87	0.95	0.82

[†]Values in parentheses are for the highest resolution shell. [1] All data sets were collected from a single crystal. [†] Swiss light source (SLS) at the Paul Scherrer Institute (PSI), Villigen, Switzerland; European Synchrotron Radiation Facility (ESRF), Grenoble, France. [‡] Mosaicity values reported by *XDS* (Kabsch, 2010). * $CC_{1/2}$ is the correlation coefficient between two random half data sets (Karplus and Diederichs, 2012). [§] $R_{meas} = \sum_{hkl}\{N(hkl)/[N(hkl)-1]\}^{1/2}\sum_i|I_i(hkl) - \langle I(hkl)\rangle| / \sum_{hkl}\sum_i I_i(hkl)$, where $N(hkl)$ is the number of observations of the reflection with index hkl and $I_i(hkl)$ is the intensity of its ith observation (Diederichs and Karplus, 1997). [¶] $R_{p.i.m.} = \sum_{hkl}\{1/[N(hkl)-1]\}^{1/2}\sum_i|I_i(hkl) - \langle I(hkl)\rangle|/\sum_{hkl}\sum_i I_i(hkl)$ (Weiss, 2001); [#] As reported by *MolProbity* (http://molprobity.biochem.duke.edu/ (Chen *et al.*, 2010).

Table A15: Data collection and refinement statistics for complex structures of *Bc*Phz(A)/B soaked or co-crystallized with two different *N*-carboxycycloalkyl anthranilic acid derivatives ("phenazistatins") or raloxifene [‡]

	Complex with WB084	Complex with WB089	Complex with raloxifene (soaked)	Complex with raloxifene (co-cryst.)
Data collection[1]				
Beamline[†]	PXIII (X06DA), SLS	ID30B MAD, ESRF	MX BL14.1, BESSY II	ID23-1 MAD, ESRF
Wavelength (Å)	1.00003	0.97625	0.91841	0.97243
Resolution range (Å)	79.75 – 1.95 (2.00 – 1.95)	80.23 – 1.84 (1.88 – 1.84)	80.73 – 1.93 (1.98 – 1.93)	69.01 – 1.50 (1.53 – 1.50)
Space group	$P3_221$	$P3_221$	$P3_221$	$P2_1$
unit cell dimensions				
a, b, c (Å)	64.07, 64.07, 159.50	64.68, 64.68, 160.45	64.47, 64.47, 161.47	54.07, 69.01, 54.12
α, β, γ (°)	90, 90, 120	90, 90, 120	90, 90, 120	90, 101, 90
Mosaicity (°)[‡]	0.36	0.27	0.13	0.09
Measured reflections	327172 (20717)	439263 (23486)	191391 (12804)	308285 (15924)
Unique reflections	28533 (1975)	34617 (2080)	30146 (1973)	62210 (3074)
Multiplicity	11.5 (10.5)	12.7 (11.3)	6.3 (6.5)	5.0 (5.2)
Mean $I/\sigma(I)$	15.6 (2.0)	26.3 (2.0)	9.6 (2.1)	10.4 (2.0)
$CC_{1/2}$*	0.996 (0.569)	0.999 (0.683)	0.994 (0.702)	0.998 (0.728)
Completeness (%)	100.0 (100.0)	99.9 (99.4)	100.0 (100.0)	99.6 (99.6)
R_{meas} [§]	18.8 (121.2)	6.7 (124.7)	15.1 (103.6)	9.3 (102.7)
$R_{p.i.m.}$ [¶]	5.5 (36.9)	1.8 (35.4)	6.0 (40.5)	4.0 (44.0)
Refinement				
Resolution range (Å)	55.48 – 1.95 (1.99 – 1.95)	53.48 – 1.84 (1.87 – 1.84)	55.83 – 1.93 (1.96 – 1.93)	53.13 – 1.50 (1.52– 1.50)
R_{cryst} (%)	23.06 (32.30)	15.68 (27.62)	17.04 (27.07)	15.17 (26.78)
R_{free} (%)	25.94 (30.38)	18.88 (31.03)	20.42 (29.13)	17.69 (30.49)
No. of non H-atoms				
Protein	2662	2696	2660	2587
Ligand / Ion	42	54	114	114
Water	203	238	204	222
Average B-factors (Å²)				
Protein	20.5	37.0	32.0	24.6
Ligand / Ion	20.8	39.4	40.0	26.0
Water	40.8	50.5	40.3	38.4
R.m.s deviations				
Bond lengths (Å)	0.003	0.007	0.011	0.018
Bond angles (°)	0.629	0.776	1.181	1.610
Ramachandran plot (%)				
Favored regions	98.5	98.8	99.1	99.4
Outliers	0	0	0	0
MolProbity score [#]	1.10	0.92	1.29	1.22

[†]Values in parentheses are for the highest resolution shell. [1] All data sets were collected from a single crystal. [†] Swiss light source (SLS) at the Paul Scherrer Institute (PSI), Villigen, Switzerland; European Synchrotron Radiation Facility (ESRF), Grenoble, France; BESSY II: Berlin Electron Storage Ring Society for Synchrotron Radiation, Helmholtz Centre Berlin, Berlin, Germany. [‡] Mosaicity values reported by *XDS* (Kabsch, 2010). * $CC_{1/2}$ is the correlation coefficient between two random half data sets (Karplus and Diederichs, 2012). [§] $R_{meas} = \sum_{hkl}\{N(hkl)/[N(hkl)-1]\}^{1/2}\sum_i|I_i(hkl) - \langle I(hkl)\rangle| / \sum_{hkl}\sum_i I_i(hkl)$, where *N(hkl* is the number of observations of the reflection with index *hkl* and $I_i(hkl)$ is the intensity of its *i*th observation (Diederichs and Karplus, 1997). [¶] $R_{p.i.m.} = \sum_{hkl}\{1/[N(hkl)-1]\}^{1/2}\sum_i|I_i(hkl) - \langle I(hkl)\rangle|/\sum_{hkl}\sum_i I_i(hkl)$ (Weiss, 2001); [#] As reported by *MolProbity* (http://molprobity.biochem.duke.edu/ (Chen *et al.*, 2010).

Table A16: Data collection and refinement statistics for complex structures of *Bc*Phz(A)/B soaked with different *N*-piperidinyl anthranilic acid derivatives ("mavericks").[‡]

	Complex with WB015	Complex with WB017	Complex with WB019	Complex with WB086
Data collection[1]				
Beamline[†]	MX BL14.1, BESSY II	MX BL14.1, BESSY II	MX BL14.1, BESSY II	PXIII (X06DA), SLS
Wavelength (Å)	0.91841	0.91841	0.91841	1.00003
Resolution range (Å)	80.20 – 2.10 (2.16 – 2.10)	80.05 – 2.00 (2.05 – 2.00)	80.10 – 2.16 (2.23 – 2.16)	80.53 – 1.98 (2.03 – 1.98)
Space group	$P3_221$	$P3_221$	$P3_221$	$P3_221$
unit cell dimensions				
a, b, c (Å)	64.59, 64.59, 160.41	64.29, 64.29, 160.11	64.30, 64.30, 160.20	64.68, 64.68, 161.06
α, β, γ (°)	90, 90, 120	90, 90, 120	90, 90, 120	90, 90, 120
Mosaicity (°)[‡]	0.21	0.24	0.18	0.28
Measured reflections	133800 (9110)	157463 (10824)	172108 (14745)	274153 (18457)
Unique reflections	23405 (1861)	26768 (1944)	21388 (1824)	28092 (1969)
Multiplicity	5.7 (4.9)	5.9 (5.6)	8.0 (8.1)	9.8 (9.4)
Mean $I/\sigma(I)$	14.9 (1.9)	17.8 (1.9)	14.8 (2.0)	19.7 (2.0)
$CC_{1/2}$*	0.999 (0.627)	0.999 (0.685)	0.998 (0.722)	0.999 (0.680)
Completeness (%)	99.7 (98.4)	100.0 (99.9)	100.0 (100.0)	100.0 (100.0)
R_{meas}[§]	7.5 (89.8)	6.8 (98.1)	10.7 (112.2)	8.2 (118.1)
$R_{p.i.m.}$[¶]	3.1 (39.1)	2.8 (41.2)	3.7 (39.3)	2.6 (38.4)
Refinement				
Resolution range (Å)	55.93 – 2.10 (2.15 – 2.10)	55.68 – 2.00 (2.04 – 2.00)	53.40 – 2.16 (2.21 – 2.16)	53.69 – 1.98 (2.02– 1.98)
R_{cryst} (%)	18.83 (30.15)	19.29 (29.77)	20.14 (28.92)	16.95 (28.34)
R_{free} (%)	21.69 (33.19)	22.31 (28.45)	23.59 (32.97)	18.88 (29.77)
No. of non H-atoms				
Protein	2636	2619	2550	2700
Ligand / Ion	40	34	54	44
Water	106	167	129	172
Average B-factors (Å²)				
Protein	49.7	50.3	42.0	43.1
Ligand / Ion	78.6	53.3	70.0	49.2
Water	53.5	56.9	48.9	50.4
R.m.s deviations				
Bond lengths (Å)	0.002	0.002	0.002	0.005
Bond angles (°)	0.511	0.501	0.512	0.655
Ramachandran plot (%)				
Favored regions	99.0	98.8	99.4	98.8
Outliers	0	0	0	0
MolProbity score [#]	0.90	0.90	1.04	0.78

[†]Values in parentheses are for the highest resolution shell. [1] All data sets were collected from a single crystal. [†] BESSY II: Berlin Electron Storage Ring Society for Synchrotron Radiation, Helmholtz Centre Berlin, Berlin, Germany; Swiss light source (SLS) at the Paul Scherrer Institute (PSI), Villigen, Switzerland. [‡] Mosaicity values reported by *XDS* (Kabsch, 2010). * $CC_{1/2}$ is the correlation coefficient between two random half data sets (Karplus and Diederichs, 2012). [§] $R_{meas} = \sum_{hkl}\{N(hkl)/[N(hkl)-1]\}^{1/2}\sum_i|I_i(hkl)-\langle I(hkl)\rangle| / \sum_{hkl}\sum_i I_i(hkl)$, where *N(hkl* is the number of observations of the reflection with index *hkl* and $I_i(hkl)$ is the intensity of its *i*th observation (Diederichs and Karplus, 1997). [¶] $R_{p.i.m.} = \sum_{hkl}\{1/[N(hkl)-1]\}^{1/2}\sum_i|I_i(hkl)-\langle I(hkl)\rangle|/\sum_{hkl}\sum_i I_i(hkl)$ (Weiss, 2001); [#] As reported by *MolProbity* (http://molprobity.biochem.duke.edu/ (Chen *et al.*, 2010).

Danksagung

Hiermit möchte ich mich bei all den Menschen bedanken, die zum Gelingen dieser Doktorarbeit beigetragen haben.

In erster Linie gilt mein Dank meinem Mentor **Prof. Dr. Wulf Blankenfeldt** für die Betreuung und Unterstützung meiner Doktorarbeit. Er hat mir nicht nur ein herausforderndes Thema gestellt, sondern mir auch eine Vielzahl von experimentellen Freiheiten bei dessen Bearbeitung gelassen.

Weiterhin bedanke ich mich bei den übrigen Mitgliedern meiner Promotionskommission, **Prof. Dr. Anett Schallmey** für die Übernahme der Zweitkorrektur und **Prof. Dr. Ralf R. Mendel** für die Übernahme des Vorsitzes der Kommission.
Darüber hinaus danke ich Prof. Dr. Anett Schallmey und ihren beiden Doktoranden, **Julia Koopmeiners** und **Hauke Voß**, für die gute Zusammenarbeit bei unseren Kooperationsprojekten.

Mein besonderer Dank gilt meinem Hauptkooperationspartner **Prof. Dr. Rolf Breinbauer** und seinen Doktoranden, vor allem **Mario Leypold** und **Jakob Pletz**, die nicht nur durch die Synthese wichtiger Liganden, sondern auch durch zahlreiche Diskussionen und Ratschläge maßgeblich zum Erfolg der Projekte und dieser Arbeit beigetragen haben. Zudem danke ich Prof. Dr. Rolf Breinbauer für seine Mitgliedschaft und Unterstützung in meinem Thesis-Komitee, gleiches gilt für **Prof. Dr. Markus Kalesse**.

Des Weiteren danke ich **Prof. Dr. G. Matthias Ullmann** und **Martin Culka** von der Universität Bayreuth, als auch **Prof. Dr. Rolf W. Hartmann** und **Antonio Martins**, sowie **Prof. Dr. Claus-Michael Lehr** und **Florian Gräf** vom Helmholtz-Institut für Pharmazeutische Forschung Saarland und allen weiteren Kooperationspartnern für die gute wissenschaftliche Zusammenarbeit.

Natürlich danke ich auch meinen Kollegen und Freunden von SFPR für die gute (Arbeits)Atmosphäre. Ein besondere Dank gilt **Christian Feiler**, der mich schon während meiner Masterarbeit betreut hat, **Allegra Vit**, die stets für allerlei fachliche und private Diskussionen bereit war, meiner ehemaligen Masterstudentin **Nina Schwemmlein**, sowie **Monika Popp** und **Florian Witzgall.**

Außerdem danke ich **Vanessa Hering**, **Ute Widow** und **Claudia Hanko** für ihre technische Unterstützung bei einigen Experimenten.

Auch danke ich allen weiteren Mitgliedern der **Abteilung SFPR**, meinen ehemaligen Kollegen vom **Lehrstuhl für Biochemie der Universität Bayreuth**, sowie meinen ehemaligen **Bachelor- und Masterstudenten**.

Schließlich möchte ich meiner Familie, besonders **meinen Eltern** von Herzen danken, dass sie während meines Studiums und dieser Doktorarbeit unentwegt an mich geglaubt und mich unterstützt haben.

Nicht zuletzt danke ich **Sébastien** für das Korrekturlesen dieser Arbeit und für die Hilfestellung bei zahlreichen Fragen und Problemen rund um die Kristallographie, vor allem aber für seine bedingungslose Unterstützung, Motivation und den uneingeschränkten Glauben an mich.

DANKE!